The chemical evolution of the Proterozoic biosphere

Katherine Audrey Doyle

Submitted in accordance with the requirements for the degree of
Doctor of Philosophy

The University of Leeds
Earth Surface Science Institute
School of Earth and Environment

June, 2018

The candidate confirms that the work submitted is his/her own and that appropriate credit has been given where reference has been made to the work of others.

Acknowledgements

I would first like to thank my supervisors Simon Poulton and Rob Newton for their incredible support over the last four years. Both of your guidance and encouragement has been unwavering throughout my PhD, and I am incredibly thankful for never turning me away when I had another ridiculous question to ask. Simon, thank you for involving me in incredible projects that have kick-started my passion in the subject. You always heard every idea I brought to the table and helped me whenever asked. Rob, thank you for always providing further guidance and knowledge on the projects, of which I am truly appreciative of.

I would not have been able to complete my PhD without all the people in Cohen, but especially Andy C and Stephen. Andy, you always had time for me even in the most stupid of moments, like taking me to hospital with a potential HF burn and all my accidents in the lab (setting the floor on fire wasn't the best decision!). You made my life in the lab so easy and I am truly thankful for it. Sincere thanks also goes to Stephen. I never would have got all my lab work done in time without your training and also providing bacon sandwiches when times got tough.

My Leeds family have supported me the whole through my PhD and I cannot thank them enough. Evie, Lucy and especially Autumn, you were my home away from home and I'll never forget all our times together. Thank you for listening to my every complaint and coming on every adventure with me, whether a hike, a boozy night out, or watching endless episodes of love island. You all made a home for me that I'll find so hard to leave. To all the others who made my life as a postgrad so much more enjoyable: Mark and Jenny, my scientific family, every day in the lab was not a work day with you guys; to Ais and our many dates; to Andy H for being my lab slave in the end; and to Andy B, James N, Mike S, Allie, Luke, James Witts, Adam, Emma J, Lewis, Alex K, Laura G, Carl, James W, Sam P, Dot, Tim, Andy C, Jed, Andy M, Johan, and Martin, thank you all so much for being a part of it.

And finally to my family and friends back home who supported me moving across the water and encouraging me to finish my PhD the whole way through. To Gill, Ken, Mark and Elaine, thank you for knowing how to cheer me up and motivate me. Your visits to Leeds were always appreciated and likewise all my R&R trips to Donegal. To Sam, you probably arrived in at both the worst and best time, but I definitely believe that you got me through the tough months of writing. You've always been there to lean on, never said no to any trips I

suggested, and kept me level headed through a stressful time. The biggest thank you goes to my Mam and Dad. I'll never be able to pay you back for your undying support and also being your biggest financial burden. Thank you for teaching me how to work for what I want and always being there. The motto that was mentioned every morning of my exams as an undergraduate, and rang through my head in the final months of thesis writing was "Failure is not an option". This might seem extreme to others, but really means just put the work in. I definitely think it was a good motto to live by and helped me through to the end.

Abstract

The chemical evolution of the Proterozoic biosphere is not a well comprehended topic. Major gaps exist in the redox record which documents the ocean's transition from a dominantly ferruginous state throughout most of the Proterozoic, to widespread deep ocean oxygenation during the Late Neoproterozoic. Between ~1.85 – 0.54 Ga, significant developments in biological evolution also occurred with the emergence of macroscopic eukaryotes followed by the radiation of metazoans. A strong link between stably oxygenated marine environments and the radiation of increasingly complex organisms is observed across the literature. However, there is little understood concerning nutrient availability during the Proterozoic, another major governing factor in biological development. Phosphorus is considered the ultimate limiting nutrient for oxygen production over geological timescales through organic carbon burial, and is thus vital to consider in discussing the chemical evolution of the Proterozoic biosphere. Through the application of multiple palaeoredox proxies (iron speciation and trace metal analyses) alongside a newly adapted phosphorus speciation method, this research aims to add to the current record of Proterozoic redox to assess if the chemical evolution of the ocean had a potential effect on the biogeochemical phosphorus cycle, and thus the development of complex organisms. The sedimentary successions from the ~1.8 – 1.4 Ga Yanshan Basin in North China, and the 1.6 – 1.0 Ga Bashkir Meganticlinorium in Russia uncovered dynamically evolving water column chemistry. Their palaeoredox signals contrast to other basins from this time period and highlight the significant spatial and temporal heterogeneity that occurred across the Proterozoic ocean. Analysis of phosphorus-bound phases within marine sediments from the Late Palaeoproterozoic Yanshan Basin and the Ediacaran White Sea (Kel'tma and Kostovo cores), Avalon Peninsula, Cariboo Mountains and the Upper Ungoolya Group, Officer Basin confirmed that water column redox, and a basin's depositional environment, were the dominant controls on the Proterozoic phosphorus cycle. This is the first geochemical record of phosphorus burial mechanisms in Proterozoic marine sediments as all other studies have been modelling based, or focused on BIFs and total phosphorus content. The research presented here provides a crucial insight into the feedbacks between ocean redox and nutrient availability during a dynamic period of Earth's history.

Table of Contents

Chapter 1 Introduction ..... - 1 -
1.1 The rise of atmospheric oxygen ..... - 1 -
1.1.1 The Great Oxygenation Event ..... - 1 -
1.1.2 The Neoproterozoic Oxygenation Event (NOE) ..... - 5 -
1.2 Evolution of Proterozoic ocean redox chemistry ..... - 6 -
1.3 The evolution of the Proterozoic biosphere ..... - 8 -
1.3.1 Eukaryote evolution ..... - 8 -
1.3.2 Metazoan Radiation ..... - 10 -
1.4 Palaeoredox Proxies ..... - 15 -
1.4.1 Iron ..... - 15 -
1.4.2 Manganese ..... - 21 -
1.4.3 Trace Metals ..... - 23 -
1.5 Phosphorus ..... - 27 -
1.5.1 Archaean and Proterozoic Phosphorus studies ..... - 28 -
1.5.2 The global phosphorus cycle ..... - 30 -
1.5.3 Measuring P phases in sediments ..... - 35 -
1.6 Isotope systematics ..... - 36 -
1.6.1 Carbon isotopes ($\delta^{13}C$) ..... - 36 -
1.6.2 Sulfur isotopes ($\delta^{34}S$) ..... - 37 -
1.7 This study ..... - 39 -
1.7.1 Aims and Objectives ..... - 39 -
1.7.2 Thesis Outline ..... - 40 -
Chapter 2 Materials and Methodology ..... - 42 -
2.1 Sample Collection and Preparation ..... - 42 -
2.2 Total Carbon, Total Organic Carbon and Total Inorganic Carbon - 43 -
2.2.1 Total Carbon (TC) ..... - 43 -
2.2.2 Total Organic Carbon (TOC) ..... - 44 -
2.2.3 Total Inorganic Carbon (TIC) ..... - 45 -
2.3 Iron ..... - 45 -
2.3.1 Iron speciation ..... - 45 -
2.3.2 Analysis ..... - 46 -

2.3.3 Iron pyrite ..... - 47 -
2.3.4 Poorly reactive sheet silicate iron (Fe_{PRS}) ..... - 50 -
2.4 Bulk Rock Digestion ..... - 51 -
2.4.1 Major elements (Fe, Al, Mn, P) ..... - 51 -
2.4.2 Trace Metals (Mo, V, U, Cr) ..... - 55 -
2.4.3 Digestion Calculations ..... - 55 -
2.5 Phosphorus Speciation ..... - 56 -
2.5.1 Method ..... - 56 -
2.5.2 Analysis ..... - 58 -
2.5.3 Calculations ..... - 63 -
2.6 Sulfur Isotopes ($\delta^{34}S_{py}$) ..... - 64 -
2.7 Organic Carbon Isotopes ($\delta^{13}C_{org}$) ..... - 65 -
2.8 Assessment of pyrite preservation with optical microscopy and SEM - 65 -

Chapter 3 Shallow water anoxia in the Mesoproterozoic ocean: Evidence from the Bashkir Meganticlinorium, Southern Urals - 68 -

3.1 Introduction ..... - 68 -
3.2 Geological setting ..... - 70 -
3.2.1 Regional geology ..... - 70 -
3.2.2 The Burzyan Group ..... - 74 -
3.2.3 The Yurmatau Group ..... - 75 -
3.2.4 The Karatau Group ..... - 76 -
3.3 Materials and methods ..... - 77 -
3.4 Results ..... - 78 -
3.4.1 Evaluating the effect of secondary weathering ..... - 78 -
3.4.2 Fe-S-C systematics ..... - 79 -
3.4.3 Trace metals ..... - 85 -
3.5 Discussion ..... - 86 -
3.5.1 Ocean redox reconstruction from Fe speciation ..... - 86 -
3.5.2 Redox-sensitive metals ..... - 88 -
3.5.3 Spatial and temporal variability in mid-Proterozoic ocean redox chemistry ..... - 93 -
3.6 Conclusions ..... - 96 -

Chapter 4 Redox and nutrient cycling in the mid-Proterozoic: Evidence from the North China Craton ..... - 97 -

4.1 Introduction ..... - 97 -
4.2 Geological Setting ..... - 98 -

4.2.1 North China Craton Formation ..... - 98 -
4.2.2 Stratigraphy ..... - 100 -
4.3 Materials and Methods ..... - 105 -
4.4 Results ..... - 106 -
4.4.1 TIC & TOC ..... - 106 -
4.4.2 Major Elements (Al, Mn, Fe) ..... - 106 -
4.4.3 Iron Speciation ..... - 107 -
4.4.4 $\delta^{13}C_{org}$ ..... - 107 -
4.4.5 Trace Metals (Mo, V, U, Cr) and Mn ..... - 109 -
4.4.6 Phosphorus Speciation ..... - 109 -
4.5 Discussion ..... - 114 -
4.5.1 Fe-S-C systematics ..... - 114 -
4.5.2 Mn as a Palaeoredox Proxy ..... - 121 -
4.5.3 Trace Metal (TM) Dynamics ..... - 122 -
4.5.4 Controls on the P cycle during the Late Palaeoproterozoic ..... - 126 -
4.5.5 Nutrient Availability in the Yanshan basin ..... - 135 -
4.6 Conclusions ..... - 138 -
Chapter 5 Redox controls on the Ediacaran phosphorus cycle ..... - 141 -
5.1 Introduction ..... - 141 -
5.2 Geological Setting ..... - 143 -
5.2.1 Kel'tma-1 Drill core, Russia ..... - 144 -
5.2.2 Kostovo-13 Drill core, Russia ..... - 147 -
5.2.3 Avalon Peninsula, Newfoundland ..... - 147 -
5.2.4 Cariboo Mountains, Western Canada ..... - 148 -
5.2.5 Narana Formation, Upper Ungoolya Group, Officer Basin, Australia ..... - 148 -
5.3 Methods ..... - 149 -
5.3.1 Organic Carbon ..... - 149 -
5.3.2 Palaeoredox proxy ..... - 149 -
5.3.3 Phosphorus Speciation ..... - 150 -
5.4 Results ..... - 150 -
5.4.1 White Sea ..... - 150 -
5.4.2 Avalon Peninsula ..... - 158 -
5.4.3 Cariboo Mountains ..... - 160 -
5.4.4 Narana Formation, Upper Ungoolya Group ..... - 162 -

5.4.5 Detrital P ..... - 164 -
5.5 Discussion ..... - 167 -
5.5.1 White Sea ..... - 167 -
5.5.2 Avalon Peninsula ..... - 174 -
5.5.3 Cariboo Mountains, Canada ..... - 175 -
5.5.4 Narana Formation, Upper Ungoolya Group ..... - 177 -
5.5.5 The Ediacaran marine P cycle ..... - 178 -
5.5.6 Evolution of the total P content in Neoproterozoic sediments . - 184 -
5.6 Conclusions ..... - 188 -
Chapter 6 Conclusions ..... - 190 -
6.1 Summary ..... - 190 -
6.1.1 The chemical evolution of Proterozoic redox ..... - 190 -
6.1.2 Proterozoic P dynamics ..... - 191 -
6.2 Future work ..... - 192 -
6.2.1 Palaeoredox studies ..... - 192 -
6.2.2 Proterozoic P studies ..... - 193 -
Bibliography ..... - 195 -

List of Tables

Table 2.1 Information regarding sample collection ..... - 43 -

Table 2.2 Statistics for certified standards used for TC analyses for North China and South Ural samples..... - 44 -

Table 2.3 Statistics for certified standards used for TOC analyses for North China and South Ural samples..... - 45 -

Table 2.4 RSD values for new iron speciation data from the South Urals and North China Craton ..... - 47 -

Table 2.5 RSD and recovery values of all elements using standard referencing materials..... - 53 -

Table 2.6 RSD values for replicate analyses of all elements measured from sediment samples chosen from each locality..... - 54 -

Table 2.7 LOD, LOQ and percentage uncertainty for major element analyses on the ICP-OES ..... - 55 -

Table 2.8 LOD, LOQ and percentage uncertainty on trace metal measurements on the ICP-MS ..... - 55 -

Table 2.9 List of acids added to molybdate blue method to keep pH constant during analysis..... - 60 -

Table 2.10 Calibration values for all localities..... - 61 -

Table 2.11 Relative errors and RSD values for replicate analysis of sediment samples from different locations..... - 62 -

Table 3.1 List and location of methods employed for the BMA sedimentary succesion ..... - 77 -

Table 4.1. List and location of methods employed for the North China sedimentary succession ..... - 106 -

Table 5.1 List of sources for iron speciation data used in this project... - 150 -

Table B.1 Iron speciation, TOC, TIC and $\delta^{34}S_{py}$ results for the Bashkir Meganticlinorium sedimentary succession..... - 247 -

Table B.2 Mn, Mo, U and Al results for the Bashkirian Meganticlinorium- 268 -

Table C.1 TOC, TIC, Al, Mn, Fe_T, Fe_{CARB}, Fe_{OX}, Fe_{MAG}, Fe_{PY}, Fe_{PRS} and $\delta^{13}C_{org}$ values for Yanshan Basin, North China..... - 277 -

Table C.2 Trace metal (Mo, V, U, Cr) results for Yanshan Basin in ppm. - 284 -

Table C.3 Phosphorus speciation results for the North China unit - 286 -

Table D.1 Iron speciation, Al and TOC results for the Kel'tma core taken from Johnston et al. (2012) ..... - 289 -

Table D.2 Phosphorus speciation results for the Kel'tma core ..... - 294 -

Table D.3 Kostovo core iron speciation, TOC and Al results supplied by Romain Guilbaud ..... - 297 -

Table D.4 Kostovo core phosphorus speciation results ..... - 302 -

Table D.5 Iron speciation, TOC and Al (wt%) results for the Avalon Peninsula taken from Canfield et al. (2007) ..... - 307 -

Table D.6 Phosphorus speciation results for samples chosen from the Avalon Peninsula ..... - 310 -

Table D.7 Cariboo Mountain iron speciation, TOC and Al results. Taken from Canfield et al. (2008) ..... - 313 -

Table D.8 Cariboo Mountain phosphorus speciation results..... - 316 -

Table D.9 Narana Formation iron speciation and TOC results determined by Rachel Beaumont at University of Leeds. Al results measured in this research ..... - 319 -

Table D.10 Phosphorus speciation results for the Narana Formation, Upper Ungoolya Group, Officer Basin ..... - 323 -

List of Figures

Figure 1.1 Evolution of atmospheric oxygen concentrations through time from Poulton (2017). The blue arrows signify possible whiffs of oxygen that were insufficient to permanently alter atmospheric levels. The dashed blue lines signify the range of atmospheric O_2 predicted to have existed during the Proterozoic. 1 – Zhang et al. (2016); 2 – Planavsky et al. (2014a) ..... - 4 -

Figure 1.2 Timeline for the appearance of eukaryotic crown groups. Taken from (Planavsky et al., 2014a). Black circles are dates from the fossil record; red circles are estimates from molecular clock techniques, and blue circles are from the molecular fossil record. The grey area highlights an interval of eukaryotic radiation. LOEM – Large ornamented Ediacaran microfossils; VSM – vase-shaped microfossils..... - 9 -

Figure 1.3 The use of the Fe_{HR}/Fe_T ratio in distinguishing between different redox states. The Fe_{PY}/Fe_{HR} ratio can further separate anoxia into sulfide-rich (euxinia) or iron-rich (ferruginous). Image modified from Poulton and Canfield (2011)..... - 18 -

Figure 1.4 Schematic diagram for pyrite formation taken from Raiswell and Canfield (2012). Green arrows represent the main reaction pathways for pyrite formation. Orange arrows illustrate pathways using partially or fully oxidised sulfur species. ..... - 20 -

Figure 1.5 Redox zones in a typical sediment marine profile. Taken from Schulz and Zabel (2006) ..... - 22 -

Figure 1.6 Simplified schematic for mechanisms involved in the sequestering of trace metals (Mo, V, U, Cr) under varying redox states. A – Fully oxygenated water column. Molybdate, vanadate, uranyl carbonates and chromates adsorb to Fe-Mn oxyhydroxides particulates which are supplied from rivers to the ocean. U reduction occurs in the sediment at the Fe(II)-Fe(III) boundary. B – Oxic waters overlying ferruginous deeper conditions. Particulates form at the chemocline creating an enhanced shuttle to the sediment. Reductive dissolution can release trace metals back to the water column if not sequestered by other phases in sediment. C – Mo binds to organic matter and Fe sulfides in a euxinic water column. V is also preferentially brought down with organic phases ..... - 25 -

Figure 1.7 Simplified box diagram of the Proterozoic marine P cycle. Sources of P to the marine system are colour-coded in red; P mineral phases in blue; and processes involving the use of P phases are in green. The ultimate sink for P is burial, and shown in black..... - 32 -

Figure 1.8 Schematic of the pre-industrial carbon cycle, taken from Newton and Bottrell (2007)..... - 37 -

Figure 1.9 Schematic of the pre-industrial global S cycle. Figure taken from Newton and Bottrell (2007)..... - 38 -

Figure 2.1 Location of all sample used in this research..... - 42 -

Figure 2.2 Flow chart illustrating the iron speciation method by Poulton and Canfield (2005). Reagents used during the extraction are highlighted in grey..... - 46 -

Figure 2.3 Schematic of the experimental setup for pyrite extractions .. - 49 -

Figure 2.4 Filtering setup following pyrite extraction..... - 50 -

Figure 2.5 Flow chart depicting all steps involved in the modified P speciation sequential extraction by Thompson et al (*in prep*). Reagents used are highlighted in grey, while all washes ($MgCl_2$ or Milli-Q) are shown in blue ..... - 58 -

Figure 3.1 Geological map of the South Urals highlighting the position of the Bashkir Meganticlinorium (B), adapted from Puchkov et al. (2013). The inset illustrates the regional geology of the eastern margin of Baltica where the Urals Mountains developed. The geological map of the BMA is adapted from Kuznetsov et al. (2017a). Sample localities are highlighted by yellow circles 73

Figure 3.2 Stratigraphic column of the BMA sedimentary succession, adapted from Bartley et al. (2007). Sample positions are shown in red. Scale bars denote thickness used for corresponding samples. Zi – Zigalga Formation; ZK – Zigazino-Komarovo Formation; Avzy – Avzyan Formation; Inz – Inzer Formation. In between the Zilmerdak and Inzer Formations is the Katav Formation, which was too small to label in this figure. Dating: A – U-Pb zircon age (Krasnobaev et al., 2013); B – Pb-Pb carbonate age (Kuznetsov et al., 2008); C – U-Pb zircon age (Puchkov et al., 2013); D –Pb-Pb phosphorite age (Ovchinnikova et al., 2013); E – Pb-Pb carbonate age (Kuznetsov et al., 2017b)..... - 75 -

Figure 3.3 Representative SEM images. A: Backscatter image of euhedral pyrite in a carbonate sample from the Inzer Formation. B: Backscatter image showing a single occurrence of a jarosite (oxidized pyrite) band of ~10 µm thickness in a shale sample from the Zigazino-Komarovo Formation. C: EDX spectra of euhedral pyrite found in A. D: EDX spectra of jarosite found in B..... - 79 -

Figure 3.4 Chemostratigraphic section showing TIC, TOC, FeT, Fe_{HR}/Fe_T, Fe_{PY}/Fe_{HR}, $(Fe_{HR}+ Fe_{PRS})/Fe_T$, and $\delta^{34}S_{PY}$. Iron speciation data are colour-coded based on the identified redox state: blue for oxic, yellow for equivocal, and green for anoxic. Fe_{PY}/Fe_{HR} ratios are only shown for anoxic and equivocal samples as this ratio does not provide information on water column chemistry when samples are deposited under oxic water column conditions. The dashed line on the Fe_T plot is at 0.5 wt%, below which samples were not analysed for Fe speciation. Dashed lines on the Fe_{HR}/Fe_T plot distinguish oxic ($Fe_{HR}/Fe_T < 0.22$) from anoxic ($Fe_{HR}/Fe_T > 0.38$) depositional conditions. Dashed line on the Fe_{PY}/Fe_{HR} plot distinguishes ferruginous ($Fe_{PY}/Fe_{HR} < 0.7$) from euxinic ($Fe_{PY}/Fe_{HR} > 0.7$) water column conditions. Dashed lines on the $(Fe_{HR}+ Fe_{PRS})/Fe_T$ plot show the Palaeozoic range (average ± 1 σ) from Raiswell et al. (2008). The range of depositional environments for each formation is also shown and is adapted from Bartley et al. (2007), Maslov et al. (1997), and Maslov (2002, 2004) ..... - 81 -

Figure 3.5 Plot of Fe_{HR} (wt%) versus Al (wt%) and Fe_{ox} (wt%) versus Al for samples from both near-coastal and shallow marine (above SWB) settings ..... - 82 -

Figure 3.6 Histograms depicting the cumulative percentage of the different Fe_{HR} phases (Fe_{CARB}, Fe_{OX}, Fe_{MAG}, Fe_{PY}) in each depositional environment in the BA succession ..... - 83 -

Figure 3.7 Normalized chemostratigraphic plot of Mo/Al, U/Al and Mn/Al. Dashed lines are representative of PAAS values from Taylor and McLennan (1995) and are as follows: Mo/Al – 0.2; U/Al – 0.35; and Mn/Al – 75. Only shales are included in this plot ..... - 86 -

Figure 3.8 Frequency plot of FeHR/FeT ratios for near-shore, shallow marine, and deeper marine samples, binned in terms of oxic, equivocal, and anoxic depositional settings. FeHR/FeT* ratios were used for samples with FePRS/FeT values above the Palaeozoic average shale (for correction procedure see the main text) ..... - 88 -

Figure 3.9 Chemostratigraphic log of Enrichment Factors for Mo, U, and Mn. Dashed lines at 1 represent the PAAS reference (Taylor and McLennan, 1995). Samples are colour coded according to the redox state indicated by iron speciation data; blue for oxic, yellow for equivocal, and green for anoxic. Fe_{HR}/Fe_T* ratios were used for the samples with elevated Fe_{PRS}/Fe_T ratios (for correction procedure see the main text) ..... - 90 -

Figure 3.10 Plot of Mo_{EF} vs. U_{EF} for shales (red circles) from the BMA. The diagram is modified from Algeo and Tribovillard (2009) and Tribovillard et al. (2012) to accommodate for low levels of U (U_{EF}<1) by extending the axis values. The modern seawater molar Mo/U ratio (Mo/U)SW of 3.1 (Tribovillard et al., 2012) is represented by the solid black line. The dashed lines correspond to multiples of the (Mo/U)SW ratio. All redox labels were defined for modern environments in open-marine basins by Tribovillard et al. (2012). The arrow pointing to the particulate shuttle highlights how Mo_{EF} and U_{EF} would evolve as a result of drawdown via an Fe (oxyhydr)oxide particulate shuttle. The yellow field denotes the area established by Tribovillard et al. (2012) as unrestricted marine ..... - 93 -

Figure 4.1 Tectonic map of China illustrating the three Precambrian cratons and Late Neoproterozoic and Palaeozoic fold belts. HY - Himalaya fold belt; KL - Kunlun fold belt; JSS- Jiangshan-Shaoxing suture; QDSL - Qinlin-Dabie-Su-Lu fold belt; QLS - Qilianshan fold belt; TIMD – Tianshan-Inner Mongolia-Daxinganling fold belt. Image taken and adapted from Zhao et al. (2001). B Geological map of Proterozoic sequences exposed in the north of Jixian County, Tianjin. ..... - 101 -

Figure 4.2 Stratigraphic log of the Proterozoic sedimentary succession on the northern margin of the NCC. Changzh - Changzhougou Fm; Chuanlin - Chuanlinggou Fm; Tua - Tuanshanzi Fm; D - Dahongyu Fm. Stratigraphic log adapted from Zhu et al. (2016) & Zhai et al. (2015). Relative age references are as follows: A - Wan et al. (2003); B - Peng et al. (2009); C - Li et al. (1995); D - Lu et al. (2008); E - Lu and Li (1991); F - Li et al. (2010)..... - 104 -

Figure 4.3 Chemostratigraphic log of TIC, TOC, $\delta^{13}C_{org}$, Al, Mn, Fe_T and each iron phase involved in iron speciation (Fe_{CARB}, Fe_{OX}, Fe_{MAG}, Fe_{PY}, Fe_{PRS}). Shales are represented by closed circles, while open circles are carbonates. Dashed lines represent average shale values for the respective elements, taken from Turekian et al. (1961): Al – 8 wt%; Mn – 0.085 wt%; Fe – 4.72 wt%..... - 108 -

Figure 4.4 Chemostratigraphic log of normalized TM concentrations (ppm) to Al for Mo, V, U, and Cr. The dashed lines are indicative of the AS values determined by Turekian et al. (1961). They are: Mo/Al = 0.3; V/Al = 16.25; U/Al = 0.5; and Cr/Al = 11.25. Only shales are shown in this diagram..... - 109 -

Figure 4.5 Graph of P_{Sum} vs. P_{Tot} for all samples used in the sequential extraction from the Yanshan basin ..... - 110 -

Figure 4.6 Plot of the remaining P at the end of the sequential extraction (P_{unx}) versus Al content (wt%) of the sample ..... - 111 -

Figure 4.7 Assessment of trends between P_{det} and P_{reac} against Al for the Changzhougou and Chuanlinggou Formations. P_{det} and P_{reac} are reported as percentages of P_{Tot}. ..... - 112 -

Figure 4.8 Phosphorus speciation results plotted stratigraphically for the Yanshan-Liaoxi Rift basin. P_{Tot} – Total P; P_{Fe} – Fe-bound P; P_{mag} – magnetite-bound P; P_{auth} – authigenic P; P_{det} – detrital P; P_{org} – organic-bound P. The Chuanlinggou is subdivided into units A, B and C. ..... - 114 -

Figure 4.9 Relationship between the pool of Fe_{HR} and the detrital input (Al) for the Changzhougou (A) and Chuanlinggou (B) Formations. - 115 -

Figure 4.10 Bar chart illustrating the differences between the original Fe_{HR}/Fe_T ratio and the new Fe_{HR}/Fe_T* when incorporated into the data set ..... - 117 -

Figure 4.11 Log of TOC, $\delta^{13}C_{org}$, Fe_T/Al, Fe_{HR}/Fe_T, Fe_{PY}/Fe_{HR}, $(Fe_{HR}+Fe_{PRS})/Fe_T$; Mn/Al and Mn/Fe for the Yanshan basin. Samples are colour coded based on Fe_{HR}/Fe_T ratios: oxic – blue; equivocal – yellow; anoxic – green. Closed circles are shales while open circles signify carbonates. The dashed lines are as follows: 0.55 Fe_T/Al (Clarkson et al., 2014); 0.22 and 0.38 Fe_{HR}/Fe_T; 0.7 Fe_{PY}/Fe_{HR} (Poulton and Canfield, 2011); 106 Mn/Al, 11.25 Cr/Al, 0.018 Mn/Fe (Turekian et al., 1961) ..... - 120 -

Figure 4.12 Relationship of Mo v TOC, Mo v Fe_{OX} and Mo v Fe_{PY}. Mo values are expressed in ppm, while TOC, Fe_{OX} and Fe_{PY} are in wt%. Samples are from the Changzhougou and Chuanlinggou Formations only. ..... - 125 -

Figure 4.13 Colour coded iron specition, TOC and phosphorus speciation results. All P phases are reported as a percentage of the total amount of P extracted during the speciation method (P_{sum}). The colour code remains the same as Figure 4.11: oxic – blue; equivocal – yellow; anoxic – green. The section analyzed in the Chuanlinggou Formation is also subdivided into units A, B and C. ..... - 128 -

Figure 4.14 Simplified schematic of P burial mechanisms operating during deposition of the Changzhougou Formation. The proportions of P recovered during the extraction are illustrated next to the diagram to illustrate the dominant phases ..... - 129 -

Figure 4.15 Schematic of redox and P burial mechanisms in subsection A (samples ADS-10 – ADS-23) of the Chuanlinggou Formation - 130 -

Figure 4.16 A: C_{org} v P_{org}. B –C_{org}:P_{reac} plots. Samples are colour coded based on redox: oxic – blue and anoxic – green. Formations are differentiated by diamonds for Changzhougou Fm and circles for Chuanlinggou Fm ..... - 131 -

Figure 4.17 Schematic diagram of P burial mechanisms in unit B (ADS-24 – ADS-31) of the Chuanlinggou Formation. Proportions of each P pool removed during the extraction are illustrated. Iron speciation and Fe_T showed an oxic layer mixing with ferruginous deeper waters across a shallow and dynamic chemocline..... - 132 -

Figure 4.18 Schematic of redox and P burial mechanisms for unit C of the Chuanlinggou Formation. Following mixing of shallow oxic and deeper ferruginous waters, and the drawdown of Fe, oxic conditions push to deeper depths, modifying P burial mechanisms ..... - 134 -

Figure 4.19 A - Evolution of Total P in the sampled units of the Yanshan Basin. The black dashed line represents the AS value at 700 ppm for shales and 400 ppm for carbonates. B – P/Al for samples from the Yanshan Basin. Dashed line is 87.5 ppm. All AS values taken from Turekian et al. (1961). The red dashed lines represent gaps between the formations..... - 138 -

Figure 5.1 Map of localities for each sample site. Ediacaran palaeogeographic map is adapted from Shen et al. (2008)..... - 146 -

Figure 5.2 P_{Sum} vs P_{Tot} for all localities to illustrate P recovery from the sequential extraction. A – Kel'tma Core; B – Kostovo-13 core; C- Avalon Peninsula; D- Cariboo Mountains; E- Narana Formation, Officer Basin ..... - 151 -

Figure 5.3 Relationship between P_{unx} and Al content for all sample localities ..... - 152 -

Figure 5.4 Log of TOC, Fe_T, Al, Fe_{HR}/Fe_T, Fe_{PY}/Fe_{HR}, P_{Tot}, and P speciation results for the Kel'tma Core. All P pools are reported as a percentage of the total amount of P extracted during the method (P_{Sum}). Fe_{HR}/Fe_T dashed lines are: oxic 0-0.22; equivocal 0.22-0.38; and anoxic 0.38-1. Fe_{PY}/Fe_{HR} dashed line at 0.7 is the boundary between ferruginous conditions (<0.7) and euxinic conditions (>0.8). The average shale value for P_{Tot} is 0.08 wt% (Turekian et al., 1961). The sedimentary log for this succession is taken from Johnston et al. (2012a) ..... - 155 -

Figure 5.5 Chemostratigraphic log of TOC, Fe_T, Al, Fe_{HR}/Fe_T, Fe_{PY}/Fe_{HR}, P_{Tot}, and P speciation results for the Kostovo-13 Core. P speciation results are reported as a percentage of the total amount of P extracted during the method (P_{Sum}). The Kotlin-2 horizon is subdivided into units A, B, and C based on varying redox intervals ..... - 157 -

Figure 5.6 Chemostratigraphic log of TOC, Fe_T, Al, Fe_{HR}/Fe_T, Fe_{PY}/Fe_{HR}, P_{Tot}, and P speciation results for the Avalon Peninsula sedimentary succession. Sedimentary log adapted from McCall (2006). P speciation results are reported as a percentage of the total amount of P extracted during the method (P_{Sum}) ..... - 159 -

Figure 5.7 Chemostratigraphic log of TOC, Fe_T, Al, Fe_{HR}/Fe_T, Fe_{PY}/Fe_{HR}, P_{Tot}, and P speciation results for the Cariboo Mountains unit, Canada. The sedimentary log is drawn based on the lithologies recorded during sample collection. P speciation results are reported as a percentage of the total amount of P extracted during the method (P_{Sum}) ..... - 161 -

Figure 5.8 Chemostratigraphic log of TOC, Fe_T, Al, Fe_{HR}/Fe_T, Fe_{PY}/Fe_{HR}, P_{Tot}, and P speciation results for the Narana Formation, Upper Ungoolya Group, Australia. The sedimentary log is drawn based on the lithological divisions of the Munta-1 drill core presented in Arouri et al. (2000). P speciation results are reported as a percentage of the total amount of P extracted during the method (P_{Sum}) ..... - 163 -

Figure 5.9 Assessment of relationship between P_{det} and P_{reac} to Al content from all localities investigated in this study. P_{det} versus P_{Tot} is also shown for each locality. ..... - 166 -

Figure 5.10 Assessment of relationship between detrital content of ironstone samples, represented by Al, versus Fe_{HR} (A), Fe_{OX} (B), and Fe_T (C) for the Kostovo-13 core ..... - 168 -

Figure 5.11 $(C:P)_{org}$ and $C_{org}:P_{reac}$ plots for each locality. Each sample is colour-coded based on redox, with oxic samples in blue ($Fe_{HR}/Fe_T < 0.38$) and anoxic samples in green ($Fe_{HR}/Fe_T > 0.38$). Equivocal samples are not individually categorized due to potential complications when interpreting these scatter plots. Insets in the Avalon Peninsula and Cariboo Mountains show these trends at smaller scales than depicted by the other sites. The Redfield Ratio is indicated by the grey band on each chart. The size of this line is to account for the low values of C_{org}, P_{org} and P_{reac} in these basins, as they are typically much higher in modern settings ..... - 172 -

Figure 5.12 Schematic of the P cycle operating in the Kel'tma core basin. The relative proportions of each P phase is shown next to both the Redkino and Kotlin horizons ..... - 180 -

Figure 5.13 Schematic of the redox state and P burial mechanisms in the Kostovo-13 core basin. Relative proportions of each P phase measured in the extraction are shown beside each stage..... - 180 -

Figure 5.14 A – P_{auth} (wt%) for all samples measured in this study B – P_{auth}/P_{Tot} (%) for each Ediacaran locality..... - 181 -

Figure 5.15 Schematic for the redox mechanisms in the Avalon Peninsula and Cariboo Mountain sedimentary units. Potential P burial mechanisms for each of these sections is also illustrated, with the percentages of each P phase designated next to their appropriate depositional environment..... - 183 -

Figure 5.16 Simplified schematic for water column redox and P burial mechanisms for the Narana Formation ..... - 184 -

Figure 5.17 Plot of the total P content of sediments throughout the Neoproterozoic. Samples in green are taken from Reinhard et al. (2016). Snowball earth ages are taken from Rooney et al. (2015). The black dashed line is representative of the average shale value for phosphorus (0.08 wt%) from Turekian et al. (1961)..... - 187 -

List of Equations

Equation 1 Fe_{HR}/Fe_T* ratio ..... - 87 -
Equation 2 Enrichment factor formula ..... - 88 -

List of Abbreviations

In order of appearance:

Elemental Symbols

Mo	Molybdenum
Re	Rhenium
Se	Selenium
Cr	Chromium
S	Sulfur
Fe	Iron
C	Carbon
O	Oxygen
N	Nitrogen
Mn	Manganese
V	Vanadium
U	Uranium
P	Phosphorus
Al	Aluminium

Others

GOE	Great Oxygenation Event
NOE	Neoproterozoic Oxygenation Event
MIF	Mass Independent Fractionation
MDF	Mass Dependent Fractionation
PAL	Present atmospheric levels
LIP	Large Igneous Province
BIF	Banded Iron Formation
LECA	Last eukaryote common ancestor
DOC	Dissolved organic carbon
Fe_{HR}	Highly reactive iron

Fe_{PRS}	Poorly reactive sheet silicate iron
Fe_{U}	Unreactive iron
Fe_{CARB}	Iron carbonate
Fe_{MAG}	Iron magnetite
Fe_{OX}	Iron (oxyhydr)oxide
Fe_{PY}	Iron pyrite
Fe_{T}	Total iron
BSR	Bacterial sulfate reduction
PIP	Particulate inorganic phosphorus
POP	Particulate organic phosphorus
DIP	Dissolved inorganic phosphorus
DOP	Dissolved organic phosphorus
TC	Total Carbon
TOC	Total Organic Carbon
TIC	Total Inorganic Carbon
P_{org}	Organic phosphorus
P_{auth}	Authigenic phosphorus
CFA	Carbonate Fluorapatite
P_{det}	Detrital phosphorus
P_{Fe}	Iron bound phosphorus
P_{mag}	Magnetite bound phosphorus
P_{reac}	Reactive phosphorus
REE	Rare Earth Element
BMA	Bashkir Meganticlinorium
AS	Average Shale
EF	Enrichment factor
SW	Seawater
NCC	North China Craton
TM	Trace Metals

SE	Snowball Earth
EEP	East European Platform

Chapter 1 Introduction

In terms of our planet's geological history, the Proterozoic Eon (2.5 – 0.54 Ga) hosted many of the most fundamental environmental and evolutionary changes. Across this two billion year period, the following significant revolutions occurred: the first appreciable rise in atmospheric oxygen concentrations; the evolution of life from prokaryotes to eukaryotes, and subsequently metazoans; the formation and disarticulation of two supercontinents, Columbia and Rodinia; a change in deep ocean redox from anoxic to oxic; and the occurrence of Snowball Earth events, with a significant glacial gap of 1.5 Ga between those in the Palaeoproterozoic and the Neoproterozoic Eras. The coupling of all these events biogeochemically shaped our planet and had an irreversible influence on the remainder of Earth's history.

1.1 The rise of atmospheric oxygen

1.1.1 The Great Oxygenation Event

The evolution of atmospheric oxygen has long been considered to have evolved across two stages: the Great Oxygenation Event (GOE) (~2.32 Ga); and the Neoproterozoic Oxygenation Event (NOE) (Figure 1.1). The GOE represents the first long-lasting, appreciable rise of atmospheric oxygen in Earth's history (Holland, 2002). Earlier inferences of atmospheric oxygen production are termed "whiffs" due to their transient nature. Whiff signatures have been identified via trace metal (molybdenum (Mo), rhenium (Re)) enrichments (Anbar et al., 2007), Mo isotopes (Duan et al., 2010) and selenium (Se) isotopes (Stüeken et al., 2015) in the 2501 ± 8 Ma Mt McRae Shale in Australia; trace metal signatures in the Transvaal Supergroup in South Africa (Kendall et al., 2010); and through chromium (Cr) isotopes (Crowe et al., 2013), and sulfur (S) and iron (Fe) isotopes (Eickmann et al., 2018) in the ~3 Ga Pongola Supergroup in South Africa.

1.1.1.1 Evidence

The most compelling evidence for the timing of the GOE stems from the isotopic composition of S in pyrite grains from the 2.32 Ga Rooihoogte and Timeball Hill Formations in South Africa (Farquhar et al., 1997; Bekker et al., 2004). Sediments deposited before 2.32 Ga contain a mass independent fractionation (MIF) signature in S isotopes, while those formed after do not (Holland, 2006). The MIF signal in S isotopes is caused by photolysis reactions between UV radiation and S (SO_2, SO) gases sourced from volcanic eruptions (Farquhar and Wing, 2003). Prior to the GOE, the limited amount of oxygen in the atmosphere coupled with the absence of an ozone layer, allowed sedimentary MIF signatures to develop in S isotopes. When oxygen levels sufficiently rose, the termination of an anoxic (CO_2, CH_4) atmosphere saw the formation of an ozone layer, preventing UV radiation reaching the Earth's surface. Mass Independent Fractionation signatures disappeared from the rock record, and were replaced by mass dependent fractionations (MDF) (Farquhar et al., 2000; Canfield, 2000; Farquhar and Wing, 2003), signifying that a substantial change in the composition of the atmosphere had occurred. Alternative arguments to rising oxygen (O) concentrations as the sole reason for MIF signatures disappearing have also been proposed. They include: the collapse of atmospheric methane as a result of increasing oceanic sulfate concentrations (Zahnle et al., 2006; Papineau et al., 2007); and differing adsorbing S species in the upper atmosphere prior to the development of an ozone layer (Farquhar et al., 2000; Ueno et al., 2009; Zerkle et al., 2012; Claire et al., 2014). Further work on the isotopic composition of carbonate-associated sulfate ($\delta^{34}S_{CAS}$) in the Transvaal Supergroup of South Africa revealed a contemporaneous build-up of sulfate within the basin as MIF vanished (Guo et al., 2009), providing additional substantiation for a large-scale atmospheric oxygenation event. Supplemental evidence for the GOE can be found in the appearance of red, terrestrial sedimentary rocks (red beds), the geochemistry of paleosols (Yang and Holland, 2003), and the termination of detrital uraninite, pyrite and siderite minerals in conglomerates (Canfield, 2005; Holland, 2006; Kump et al., 2013; Johnson et al., 2014; Farquhar et al., 2011).

1.1.1.2 Timing Constraints

Discrepancies exist in dates estimated for the GOE. From the Transvaal Group in South Africa, ages for the GOE range from 2.32 Ga using Re-Os dating and carbon (C) isotope correlations (Bekker et al., 2004; Hannah et al., 2004; Guo et al., 2009), to a U-Pb age of 2.426 Ga (Gumsley et al., 2017). An older age of 2.47 Ga from the Huronian Supergroup in Canada was estimated using records

of MIF-MDF signals (Papineau et al., 2007). Limitations exist in solely using MIF of S to date the GOE. This is due to the crustal memory effect, whereby it would have taken millions of years of continued weathering, burial, and uplift of sedimentary rocks under a mildly oxygenated atmosphere to fully eradicate the MIF signal (Lyons et al., 2014). For the appearance of MDF to be separated by approximately 100 Ma between localities seems questionable, as the rate by which S is transferred from the atmospheric reservoir to sediments is relatively quick, and the well-mixed nature of the troposphere rules out large variations in global atmospheric chemistry at one time (Farquhar et al., 2013; Hannah et al., 2004; Hoffman, 2013).

1.1.1.3 Estimates for past concentrations of atmospheric oxygen

There have been several attempts across the literature to approximate concentrations of atmospheric oxygen following the GOE. Studies utilizing Cr isotopes advocate for levels <0.1% PAL (present atmospheric levels) (Planavsky et al., 2014a; Zhang et al., 2016) to <1% PAL at the base of the Cambrian (Cole et al., 2016; Mills and Canfield, 2014). Modelling approaches based on the carbonate C isotope record ($\delta^{13}C_{carb}$) suggest concentrations remained at approximately 0.1% PAL following the GOE, as at values <0.01% PAL, the C cycle would become unstable (Daines et al., 2017).

1.1.1.4 Causes for the GOE

On the initial discovery of the GOE, two schools of thought emerged concerning the cause for this event. They are: the evolution of oxygenic photosynthesis (Buick, 2008); and a change in the redox state and fugacity of volcanic gasses (Kump and Barley, 2007; Holland, 2002).

1.1.1.4.1 The evolution of oxygenic photosynthesis

The evolutionary timing of organisms (cyanobacteria) capable of oxygenic photosynthesis remains controversial. Molecular fossils discovered in the 2.7 Ga Pilbara Craton in Australia placed the innovation of oxygenic photosynthesis approximately 300 Ma before the GOE (Brocks et al., 1999). However, further work on other cores from this region exposed the issue that surficial contamination had occurred to these biomarkers from hydrocarbons, and thus were not a record of oxygenic photosynthesis (French et al., 2015). Efforts to use lipid biomolecular studies to constrain this evolutionary event are driven by the absence of a robust Archaean fossil record, but are also plagued

with challenges from the thermal maturity of Archaean rocks (Fischer et al., 2016). If oxygenic photosynthesis arose before the GOE, this would reflect a period in Earth's history when the source of oxygen was much greater than its sink, and continued to rise until a new sink capable of balancing the cycle emerged (Farquhar et al., 2011). It could also suggest that oxygen has more than one steady state in nature. Modelling studies have shown that oxygenic photosynthesis can persist simultaneously in two stable state states, and would allow atmospheric concentrations to rise (Goldblatt et al., 2006). Carbon isotope signatures in sediments deposited prior to the GOE (2.7 – 2.5Ga) exhibit extremely depleted values (up to -43‰), and are attributed to prevalent methanotrophic activity. Coupled with S isotope studies, these signals are suggestive of bistability in the atmosphere between an organic (methane-rich) state and anoxic background conditions, and oppositely free from an organic haze (Zerkle et al., 2012; Izon et al., 2015). The capability of the atmosphere to exist in multiple steady states questions the unidirectional transition the atmosphere was theorized to have trajected upon during its oxygenation history.

Evidence for a pre-GOE evolutionary date comes indirectly from geochemical (Riding et al., 2014; Planavsky et al., 2014b; Kendall et al., 2010) and modelling (Olson et al., 2013) evidence for oxygen oases in Archaean surface waters. As indirect proxies are the only current evidence for oxygenic photosynthesis, there remains no overall consensus, with dates ranging from 3.8 Ga (Rosing and Frei, 2004) to an emergence during the GOE (Kirschvink and Kopp, 2008; Rasmussen et al., 2008).

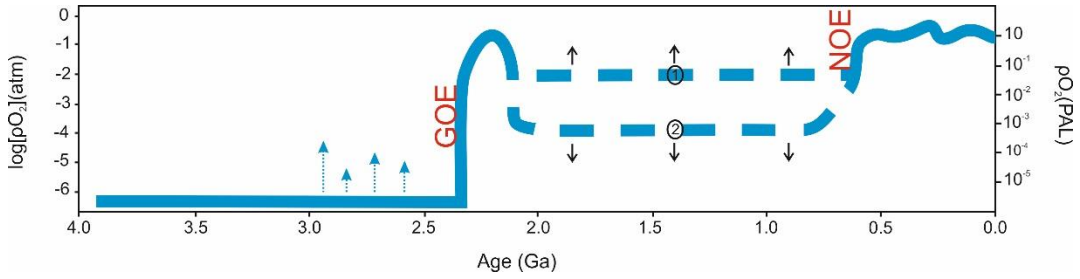

Figure 1.1 Evolution of atmospheric oxygen concentrations through time from Poulton (2017). The blue arrows signify possible whiffs of oxygen that were insufficient to permanently alter atmospheric levels. The dashed blue lines signify the range of atmospheric O_2 predicted to have existed during the Proterozoic. 1 – Zhang et al. (2016); 2 – Planavsky et al. (2014a)

1.1.1.4.2 Changes to volcanism

At the Archaean-Proterozoic boundary, a global decline in sea level accompanied the largest growth of continental crust the Earth would ever see, and ultimately changed the dominant setting for volcanism. Submarine volcanism was prevalent during the Archaean, due to the largely absent continental crust (Kump and Barley, 2007). This enhanced activity in submarine localities is theorized to have acted as a substantial oxygen sink, as submarine volcanism is conceived to be more reducing than subaerial, and could therefore maintain critically low levels of atmospheric oxygen (Kump and Barley, 2007). With the stabilization of the continents, subaerial volcanism became more common alongside the emplacement of Large Igneous Provinces (LIPs). More recent work has invoked differences in the average pressure of volcanic degassing between submarine and subaerial sites to have contributed to oxidizing the atmosphere (Gaillard et al., 2011). However, studies on oxygen fugacity levels (fO_2) in the mantle showed no observable differences between the Archaean mantle redox state and that of the modern (Li and Lee, 2004). A more recent investigation into fO_2 levels of modern volcanoes similarly agreed that a change of over two orders of magnitude would be required for this theory to uphold (Brounce et al., 2017), thus ruling it out as a potential cause for the GOE. The proposed absence of continental crust at this time also strongly objects to the debate for the presence of crust prior to the GOE, and as far back as 4.4 Ga. Evidence for the existence of continental crust during this period stems from: Rb/Sr ratios (Dhuime et al., 2015); hafnium isotope data from zircons (Reimink et al., 2016); O isotopes on detrital zircons (Mojzsis et al., 2001); and U-Pb dating (Iizuka et al., 2006; Wilde et al., 2001). It therefore seems more convincing that the emergence of oxygenic photosynthesis was the leading cause for the GOE.

1.1.2 The Neoproterozoic Oxygenation Event (NOE)

A second important rise in atmospheric oxygen occurred during the Neoproterozoic Era (Figure 1.1), widely termed the NOE. The NOE has formerly been invoked to explain the evolution of animal life during the Ediacaran Period (635 – 542 Ma), as the more biologically complex the organism, the higher amounts of oxygen it requires (Butterfield, 2009; Mills et al., 2014). Support for this event stems from the C cycle. At approximately 800 Ma during the Cryogenian Period, large positive $\delta^{13}C_{carb}$ values of up to 5‰ were suggestive of elevated rates of organic C burial (Shields-Zhou and Och, 2011). These positive isotopic excursions transition to extremely negative values at ~580 Ma, insinuating that a large portion of the dissolved organic C

pool had been oxidized (Och and Shields-Zhou, 2012). Other sources of evidence to support this event include: Re concentrations and Re/Mo ratios (Baldwin et al., 2013); Se isotopes (Pogge von Strandmann et al., 2015), an increase in $^{87}Sr/^{86}Sr$ ratios approaching the Cambrian-Precambrian boundary (Och and Shields-Zhou, 2012); Cr isotopes (Frei et al., 2009); and nitrogen (N) isotopes (Ader et al., 2014). A multi-stage event rather than one discrete rise in atmospheric oxygen concentrations has also been suggested for the NOE, based on the limited range of S isotopes in gypsum deposits deposited prior to the 811 Ma Bitter Springs event (Turner and Bekker, 2016).

The role of animals and their resulting adaptations to the biological pump have also been proposed as drivers for oxygenation and ventilation of the deep ocean during this period. With the advent of filter feeding metazoans, it is suggested widespread anoxia, that was a common feature of Proterozoic oceans, was dampened by moving oxygen demand to deeper waters (Lenton et al., 2014). The spread of oxygenated waters to the deep ocean is suggested to be the result of a stronger biological pump, as faster sinking and larger pellets from metazoan zooplankton reduced oxygen consumption in shallower waters. Such a change coupled with the evolution of filter feeding potentially ventilated the water column (Butterfield, 2009; Lenton et al., 2014). This places animals as a driver in the oxygenation of the deep oceans and not an outcome of such conditions (Butterfield, 2009; Wood et al., 2015). The diversification of metazoans is discussed in further detail in section 1.3.2.

The timing and magnitude of the NOE as a singular event is prominently debated across the literature. This is the outcome of the heterogeneous redox state of the ocean during this period, further discussed in 1.2, whereby there was no global transition in the deep ocean to an oxygenated state. Just as the ocean lagged behind after the GOE, it is not unexpected that diverse conditions initially prevailed following the NOE.

1.2 Evolution of Proterozoic ocean redox chemistry

Though a general consensus has been reached regarding atmospheric oxygen concentrations rising over two separate events, the evolution of the redox state of the deeper ocean remains unsolved. An initial change in ocean redox was pinpointed at 1.8 Ga with the disappearance of banded iron formations (BIFs) from the rock record (Holland, 1984). Banded Iron Formations are sediments which consist of alternating iron-rich and silica-rich layers, and are widespread

throughout the Archaean and Early-Mid Proterozoic (Posth et al., 2014; Song et al., 2017). They are hypothesized to have precipitated in a ferruginous (iron-rich) global ocean, where the main source of iron (Fe^{2+}) was derived from hydrothermal inputs, as well as terrestrial runoff and iron diffusively released from sediments during diagenesis (Canfield et al., 2008). With the loss of BIF deposits from the rock record at 1.8 Ga, a change in ocean chemistry was envisaged from anoxic, ferruginous conditions to completely oxygenated (Cloud, 1968). This hypothesis of appreciable amounts of oxygen removing large quantities of iron from the deep ocean was upheld for many decades. Rather than the deep ocean becoming oxygenated, it was later proposed that the ocean remained anoxic, but existed in a sulfide-rich (euxinic) state, rather than iron-rich (Canfield, 1998). A large increase in sulfide production via bacterial sulfate reduction (BSR) was the main factor believed to have caused the disappearance of BIFs (Canfield, 1998; Canfield and Raiswell, 1999; Poulton, et al., 2004a).

An upheaval of the long-standing theory concerning oxygenation of the Proterozoic ocean influenced an enormous amount of geochemical research into sedimentary successions from this time interval. Further eluding on the theory of a completely sulfidic deep ocean with a mildly oxygenated surface layer, was the discovery that euxinic conditions were not widespread, but confined to productive continental margins and certain epicontinental basins (Beghin et al., 2017; Boyle et al., 2013; Cox et al., 2016b; Gilleaudeau and Kah, 2013; Guilbaud et al., 2015; Kendall et al., 2011; Planavsky et al., 2011; Poulton et al., 2010; Poulton and Canfield, 2011; Reinhard et al., 2013; Shen et al., 2002, 2003). The current understanding of ocean chemistry found throughout many different Late Palaeoproterozoic to Mesoproterozoic (1.8 – 1.0 Ga) successions across the literature is a ferruginous deep ocean overlain by oxygenated shallow waters (Arnold et al., 2004; Diamond et al., 2018; Gilleaudeau and Kah, 2015; Hardisty et al., 2017; Li et al., 2015a; Lyons et al., 2014; Planavsky et al., 2011; Poulton and Canfield, 2011; Sperling et al., 2015; Wang et al., 2017a). However, there have been several arguments for deep ocean oxygenation during this time (Sperling et al., 2014; Zhang et al., 2016; Planavsky et al., 2018), implying that the history of mid-Proterozoic redox was more spatially and temporally heterogeneous than previously envisaged.

It still remains unclear when deep ocean oxygenation precisely occurred in the Late Neoproterozoic, but what has been uncovered is that there was no global transition to an oxic state. Evidence for deep ocean oxygenation during the Ediacaran Period (630 – 542 Ma) was initially discovered in the ~580 Ma Mistaken Point Formation on the Avalon Peninsula in Newfoundland (Canfield

et al., 2007). A later Ediacaran succession from the East European Platform also advocated for deep ocean oxygenation at ~550 Ma (Johnston et al., 2012a). Similar to the Mesoproterozoic, the initial discovery of deep ocean oxygenation prompted massive investigations into other basins from this time period, and also demonstrated that the Ediacaran ocean was a period of significant heterogeneity in ocean redox, with ferruginous deep oceans remaining prevalent during this dynamic period (Bowyer et al., 2017; Canfield et al., 2008; Lang et al., 2016; Li et al., 2010, 2015b; Sahoo et al., 2016; Song et al., 2017; Sperling et al., 2013; Tostevin et al., 2016; Wood et al., 2015; Xiao et al., 2012). This again highlighted the lack of understanding concerning the evolution of Proterozoic ocean redox.

1.3 The evolution of the Proterozoic biosphere

The Proterozoic Eon hosted the most important stages for the evolution of life: the transition from single-celled organisms (prokaryotes) to macroscopic multicellular (eukaryotes) in the Mesoproterozoic, and to soft-bodied animals (metazoans) in the Ediacaran Period. The definition of a eukaryotic organism is an organism with a membrane-bound nucleus, whereas prokaryotic organisms lack a nucleus and cytoskeleton (Stanier and Niel, 1962). As previously stated in section 1.1, the emergence of oxygenic photosynthetic cyanobacteria is strongly linked to the GOE, and postulated to have occurred at ~3 Ga (Buick, 2008), with a larger body of evidence pointing towards their definitive presence by 2.7 Ga. Evidence for this date stems from: Cr isotopes (Crowe et al., 2013); redox sensitive metals (Robbins et al., 2016); molecular clock estimates (Shih et al., 2016); and stromatolite facies and C isotopes (Buick, 1992).

1.3.1 Eukaryote evolution

Dating the emergence of eukaryotic organisms is complicated by three factors: differences in molecular clock estimates, a lack of preservation in the fossil record, and the absence of a clear palaeobiological boundary between a prokaryote-dominated world and a eukaryote-dominated body fossil one (Knoll, 2015). Current dates using the fossil record, both body fossils and the molecular record, and molecular clock estimates are shown in Figure 1.2. However as previously mentioned, the molecular record was found to be contaminated (French et al., 2015), and thus not appropriate for discussion. Molecular clocks use phylogenies to quantify the timing of crown group

divergence or the last eukaryote common ancestor (LECA). Recovering phylogenetic relationships from deep time is a difficult task. Molecular clocks are very useful in dating LECA but are heavily influenced by the model used and its associated fossil calibrations (Eme et al., 2014), causing large differences between individual dates. Estimates for eukaryotic diversification range from 1007 (943 – 1102) Ga to 1898 (1655 – 2094) Ga (Douzery et al., 2004; Eme et al., 2014). With these large differences in mind, there are two schools of thought on whether eukaryotes diversified rapidly within the appearance of LECA (Eme et al., 2014; Chernikova et al., 2011), or whether they endured several 100 Ma of hidden evolution with no physical record left behind (Hedges et al., 2004; Parfrey et al., 2011).

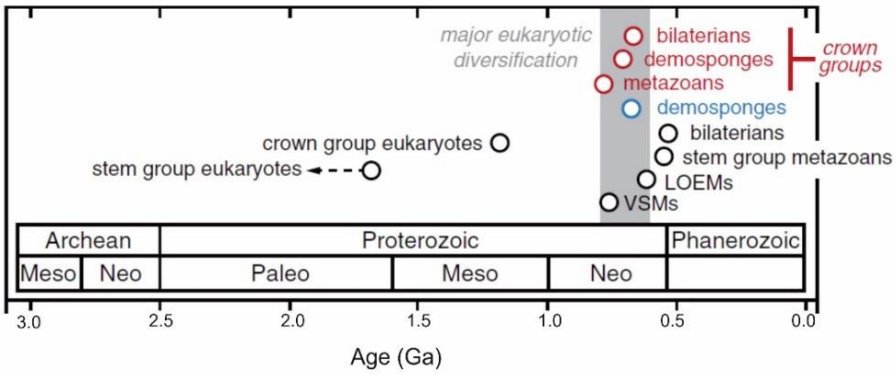

Figure 1.2 Timeline for the appearance of eukaryotic crown groups. Taken from (Planavsky et al., 2014a). Black circles are dates from the fossil record; red circles are estimates from molecular clock techniques, and blue circles are from the molecular fossil record. The grey area highlights an interval of eukaryotic radiation. LOEM – Large ornamented Ediacaran microfossils; VSM – vase-shaped microfossils

Gaps in the fossil record during this interval have complicated estimates of eukaryote radiation. Multicellular filaments (*Bangiomorpha pubescens*) in the 1.2 Ga Hunting Formation in arctic Canada, were identified as red algae and long believed to mark the onset of eukaryote diversification (Butterfield, 2000). However, newly emerging discoveries continually push this date further back into Earth's history. In the 1.4 – 1.5 Ga Roper Group in Australia, an intermediate assemblage of both protistan and microscopic eukaryotes were endorsed as the bridge between the gap in the body fossil and molecular biomarker record (Javaux et al., 2004). Decimetre-scale macrofossils in the 1.56 Ga Chuanlinggou Formation in North China provide strong evidence that multicellular life had evolved to macroscopic forms by the Mesoproterozoic Era

(Zhu et al., 2016). This discovery contradicts previous beliefs that the Mesoproterozoic was an interval of biological stasis (Holland, 2006), and sheds doubt on its nickname as the “Boring Billion”. Other palaeontological and geochemical evidence has moved eukaryote evolution further back to the Palaeoproterozoic Era. Centimetre-sized structures, interpreted as colonial organisms, in the 2.1 Ga Francevillian B Formation in Gabon are proposed as evidence for multicellularity, pre-dating molecular clock estimates (Albani et al., 2010).

What is agreed upon in the literature is the timing of a later Neoproterozoic surge in eukaryote diversification. At the beginning of the Cryogenian Period, ornamented microfossils become more abundant in the rock record, aiding an understanding in multicellular evolution. The Chuar Group in Arizona has a diverse assemblage of stromatolites, acritarchs, vase-shaped microfossils and biomarkers dated to ~742 Ma (Nagy et al., 2009; Porter et al., 2003). This basin endured episodic incursions of euxinia amid a dominant ferruginous state (Johnston et al., 2010), but still played host to an assortment of organisms. Recent work on microfossil assemblages in cap carbonates deposited after the Sturtian Snowball Earth (~717 – 660 Ma) from different palaeo-continents, revealed that similar types of microbial eukaryotes were distributed globally (Moore et al., 2017), aiding the resolution of the fossil record from this time. A biomarker record of sterane/hopane ratios throughout the Proterozoic has demonstrated, for the first time, that algal dominance occurred between the Sturtian and Marinoan glacial periods (659 – 645 Ma) (Brocks et al., 2017). The emergence of marine planktonic algae resulted in the development of food webs, potentially expanding the marine ecosystem and driving the evolution of more complex organisms. This theory is complemented by modelling studies (e.g. Lenton et al., 2014) which suggest a shift from a cyanobacteria-dominated biological pump to a eukaryote-dominated one moved oxygen demand from shallow waters to deeper depths by the generation of larger, faster-sinking organic carbon, and aided in the radiation of metazoans.

1.3.2 Metazoan Radiation

The final stage of the evolution of the Proterozoic biosphere was the advent of soft-bodied metazoans in the Late Neoproterozoic. The hydrocarbon biomarker sterane, produced by demosponge, was discovered in the >635 Ma strata of the Huqf Supergroup in the South Oman Salt Basin, suggesting metazoan radiation occurred in shallow marine waters during the Cryogenian (Love et al.,

2009). More recent phylogenetic evidence from the Ediacaran macro-biota *Stromatoveris* places the Ediacaran genera within the Metazoa clade, establishing them as animals but also dating metazoan radiation to a minimum of 558 – 571 Ma (Hoyal Cuthill and Han, 2018). Molecular clock estimates have dated this diversification to ~800 Ma, signifying a lag between their emergence and subsequent ecological success in the Ediacaran (Erwin et al., 2011). A major gap therefore exists between molecular clock estimates and preserved metazoans in the fossil record. The first documented appearance of the *Ediacaran Biota* fossils were found in the deep marine sedimentary succession at Mistaken Point, Avalon Peninsula (Gehling et al., 2000; Narbonne, 2005; Clapham et al., 2003; Narbonne and Gehling, 2003). Other fossil localities are more commonly found in shallow marine environments, complimenting previous hydrocarbon biomarker evidence: the Nama Group, Namibia (Jensen et al., 2000; Wood et al., 2015; Penny et al., 2014; Wood et al., 2017); the White Sea, Russia (Fedonkin and Waggoner, 1997; Fedonkin, 2003; Martin, 2000; Fedonkin et al., 2007); the Flinders Range in Australia (Gehling and Droser, 2009; Gehling and Rigby, 1996; Xiao et al., 2013; Mapstone and McIlroy, 2006) , the Khatyspyt Formation, Siberia (Rogov et al., 2012; Brasier et al., 2013) and the Doushantuo Formation in South China (Xiao and Knoll, 2000; Yin et al., 2007; McFadden et al., 2008; Sperling et al., 2011).

Three Lagerstätten in the Doushantuo Formation (635 – 551 Ma) in South China host assemblages of complex acritarchs, filamentous and coccoidal cyanobacteria (McFadden et al., 2008), and multicellular algae and animal embryos (Xiao and Knoll, 2000; Yin et al., 2007). Detailed studies of the organic matter preserved in chert nodules from this section show evidence for a diverse microbial ecosystem operating at this time (Qu et al., 2017). This strongly implies that early marine ecosystems were much more complex than previously envisaged. Geochemical proxies applied to these sediments give evidence for oxic waters bracketing euxinic conditions (Wang et al., 2012; Wagner et al., 2017; McFadden et al., 2008), further solidifying the argument of a complex ecosystem operating in stressful environments. Investigations into the redox state of the Nama Group's basin, has since shown that areas with low levels of oxygen prevailed between the anoxic deep sea and well-oxygenated shallow marine environment, but did not contain any skeletal organisms occupying these dysoxic zones (Tostevin et al., 2016). The Nama Group hosts a remarkably preserved succession of soft-bodied animals, as well as documenting the emergence of skeletal metazoans across the Cambrian boundary (550 – 541 Ma) (Wood et al., 2015). Complex trace fossils in this

locality aged ca. 548 – 545 Ma also provide evidence for the presence of bilaterian motile animals in the Proterozoic (Jensen et al., 2000).

1.3.2.1 Bioturbation

With the advent of motile animals came the evolutionary adaptation of shallow bioturbation, the physical and chemical mixing of sediments as a result of animal activity. For the first time in Earth's history, sediment deposited on the seafloor was disturbed by the movement of animals. Evidence for shallow bioturbation originates from trace fossils, with the oldest record of bioturbation from burrows in the ~550 Ma Khatyspyt Formation in arctic Siberia (Rogov et al., 2012). However, just as with trace fossil identification in younger rocks, their nature as records of animal activity are debated (Brasier et al., 2013). In the 555.3 ± 0.3 Ma White Sea succession (Martin, 2000), scratches potentially made by *Kimberella,* called *Radulichnus*, are hypothesized to originate from the organism grazing on microbial mats (Seilacher et al., 2003; Fedonkin et al., 2007). Microbial mats can bind the underlying sediment, with any disturbance to them affecting their structural stability for the formation of biogenic structures e.g. stromatolites (Crimes and Fedonkin, 1994). Other trace fossils which further elucidate the feeding styles of the *Ediacaran biota* can be found on the ~555 Ma Winter Coast of the White Sea, Russia (Grazhdankin, 2004; Ivantsov and Malakhovskaya, 2002) and at Mistaken Point (575 – 565 Ma) in Newfoundland (Liu et al., 2010).

The innovation of bioturbation is considered an important evolutionary tool for its associated impacts on seawater chemistry. Modelling studies have suggested that sediment mixing induced by the emergence of mobile animals caused a several-fold rise in seawater sulfate concentrations, and the first global-scale deposition of sulfate evaporate minerals at the Precambrian-Cambrian boundary (Canfield and Farquhar, 2009). The biogeochemical cycling of phosphorus (P), C and O have also been hypothesized to have been affected by bioturbation. By increasing the exposure of marine sediments to oxygenated waters through bioturbation and bioirrigation, a decrease in marine phosphate levels and the size of the global ocean oxygen reservoir are suggested to have transpired (Boyle et al., 2014). Continued exposure is also posited to have reduced the large scale excursions, typical of the Precambrian, in the $\delta^{13}C_{carb}$ record through authigenic carbonate precipitation or methanogenesis (Boyle et al., 2018). These theories are, however, all sourced from modelling approaches and lack support from geochemical evidence. There is strong opposition to shallow bioturbation exerting a major control on

sedimentary and marine geochemistry in the Ediacaran and Cambrian Periods. Ichnological, sedimentological and taphonomic data from trace fossils suggest bioturbation did not develop a sediment mixed layer until the Late Silurian (Tarhan et al., 2015; Tarhan, 2018). This implies there was a ~120 Ma lag between the emergence of sediment colonization and prevalent sediment mixing.

Just as the evolution of macroscopic eukaryotes in the Mesoproterozoic is potentially linked to stable oxic conditions (Zhang et al., 2018a), the emergence of metazoans is similarly connected to oxygenated settings. Briefly discussed in 1.2 was the initial discovery of deep ocean oxygenation in the Mistaken Point unit (Canfield et al., 2007), a famous locality for the preservation of the *Ediacaran Biota* (Narbonne and Gehling, 2003). Oxygen and complex life are intertwined due to the chemical properties of oxygen. During reduction, oxygen gives the largest amount of free energy per electron transfer, where its bonding ensures it is sufficiently stable for metabolic use (Catling et al., 2005). To be clear, it is not solely the presence of free molecular oxygen which acted as a trigger for animal evolution, but rather its increasing availability creating a habitable environment (Knoll, 1999; Mills and Canfield, 2014; Reinhard et al., 2016b). Ocean oxygenation is increasingly put forward as a trigger for the radiation of animals but also due to its connection to the Shuram Excursion, the largest known negative $\delta^{13}C_{carb}$ excursion in Earth's history. The excursion predates the Gaskiers Glaciation (~580 Ma) in the Ediacaran Period, and was initially found in the Huqf Supergroup of Oman (Fike et al., 2006). Lasting 5 Ma with values reaching -12‰ within a few hundred metres of section (Grotzinger et al., 2011; Lee et al., 2015; Husson et al., 2015), this major excursion was thought to signify oxidation and remineralization of an usually large oceanic dissolved organic carbon (DOC) reservoir (Rothman et al., 2003; Fike et al., 2006). As the $\delta^{13}C_{carb}$ values fall below the mantle value (-6‰), typical fractionation processes such as C fixation or organic C burial could not be used to explain the magnitude of the negative excursion. Diagenesis has been proposed as a potential cause for such a signal (Knauth and Kennedy, 2009; Derry, 2010), but due to the global correlation of this excursion across multiple continents (Burns and Matter, 1993) and through petrographic and geochemical analysis of these sections (Cui et al., 2017; Bjerrum and Canfield, 2011; Fike et al., 2006), diagenesis has been ruled out. The proposal for oxidation of a large DOC reservoir was based on the relationship between carbonate and marine organic C isotopic signatures, as they did not follow typical steady state behaviour and showed no evidence for covariation (Rothman et al., 2003), the typical signal between the pair. If the pools of

organic C and dissolved inorganic C were coupled during this stage in the Ediacaran, a parallel negative excursion in $\delta^{13}C_{org}$ would be expected, as this dissolved inorganic C pool is the source for C fixation in organic matter (Fike et al., 2006). A vast DOC reservoir is hypothesized to have buffered coexisting $\delta^{13}C_{org}$ via adsorption to siliciclastic particles and carbonate precipitation, and thus masking the signal of continued depletion of primary organic matter (Fike et al., 2006). It is also suggested to originate from the advent of rapidly sinking particulate organic matter (faecal pellets) as a result of metazoan evolution (Logan et al., 1995; Rothman et al., 2003).

There have been alternative proposals for the Shuram excursion including: a stratified ocean (Ader et al., 2009); the release of methane hydrates (Bjerrum and Canfield, 2011); perturbations to the surface C cycle (Johnston et al., 2012b); and authigenic carbonate produced during early diagenesis in pore fluids (Schrag et al., 2013). The suggestion for authigenic carbonate as an important sink in the Proterozoic carbonate cycle is an important hypothesis, as if correct, requires an overhaul of the current understanding of the $\delta^{13}C_{carb}$ record. Authigenic carbonate is a minor sink in the modern, highly oxygenated, C cycle. Under much lower concentrations of atmospheric oxygen and in a widely anoxic ocean, changes to this sink could potentially explain major C isotope excursions as the isotopic mass balances require a strong relationship between the oxidation state of the Earth's surface and the C cycle (Schrag et al., 2013).

Ocean redox and changes to the DOC reservoir as a result of increasing atmospheric oxygen concentrations have commonly been invoked as triggers for animal evolution. However, there is an ongoing debate on whether the emergence of animals appeared prior to the NOE, and therefore contributed to ocean oxygenation. Modelling approaches have demonstrated that the biological pump shifted oxygen demand further into deeper waters as a result of larger organisms evolving and generating higher quantities of organic matter (Lenton et al., 2014). The development of aquatic propulsion in animals is also considered a major factor in controlling redox dynamics due to: turbulent mixing generated by their movement; and filter feeding clearing DOC in a water column (Butterfield, 2018; Butterfield, 2009).

The evolution of life from simple to more complicated forms has a convoluted history, but with increasingly more work focused on unravelling this story, a clearer perspective exists on why they emerged than ever before.

1.4 Palaeoredox Proxies

To effectively document the evolution of ocean redox during the Proterozoic, proxies must be applied to ancient sediments. For this research, the main palaeoredox proxies used are: iron, manganese (Mn) and the trace metals Mo, vanadium (V), uranium (U) and Cr. Each of these elements are redox-sensitive, exhibiting different behaviours in varying conditions, of which will be discussed in the following section.

1.4.1 Iron

Understanding the iron cycle plays a key role in unravelling the Earth's chemical past as it is redox sensitive, exists in both dissolved and particulate phases, and is involved in a whole host of biogeochemical reactions. The recognition of iron's ability to limit primary productivity (Martin, 1990) kick-started a berth of research into the iron cycle and the chemical and physical parameters behind it. The biogeochemical cycle of iron consists of three main reservoirs: the ocean, the atmosphere and the crust (Raiswell and Canfield, 2012). The main source of iron to the modern marine system is via riverine delivery, but also from hydrothermal vents, aeolian dust, icebergs, and diagenetic recycling in sediments (Poulton and Raiswell, 2002; Raiswell et al., 2006; Poulton and Canfield, 2011; Anderson and Raiswell, 2004). Its physical size fractions determine the chemical form of Fe present, whether in a dissolved (filterable through 0.4 or 0.2 µm; Klunder et al., 2012; Klar et al., 2018; Rijkenberg et al., 2014) or particulate phase (>0.2 or 0.4 µm; Boye et al., 2010), and can be separated using standard filtration methods. The pore size of 0.2 – 0.4 µm is used to separate photoautotrophic and heterotrophic bacteria from the dissolved iron phase, with a 0.2 µm size the more current size used to guarantee the complete separation of bacteria within the samples.

Within the riverine supply, particulate phases are dominated by Fe (oxyhydr)oxides (e.g. ferrihydrite, lepidocrocite, goethite, haematite; Poulton and Raiswell (2005)), but also consist of dissolved organic iron complexes (Powell and Wilson-Finelli, 2003), and iron-binding colloids (Krachler et al., 2005). The majority of the particulate fraction is removed during transport through estuary systems via flocculation or precipitation. The dissolved phase is estimated to be approximately three orders of magnitude lower than that of particulates (Poulton and Raiswell, 2002).

1.4.1.1 Iron redox sensitivity

Iron has two thermodynamically stable phases, a reduced form as ferrous (Fe^{2+}) iron, and an oxidized state as ferric (Fe^{3+}) iron. In modern oceans, iron is typically in the ferric state due to the oxygenated nature of most terrestrial and marine waters. Ferrous iron originates from hydrothermal vents and upon encountering sulfide forms pyrite in close proximity to the vents, or oxidizes further way to ferric (oxyhydr)oxides. During early diagenesis in marine sediments, reductive dissolution releases Fe(II) from ferric (oxyhydr)oxides to the interstitial porewaters and to an overlying aerobic water column, where it will be oxidized and redeposited to the sediments (Poulton and Canfield, 2011). In ancient oceans where deep ocean anoxia was common, such as during the Proterozoic Era, iron would have predominantly existed in its ferrous state. Fe(II) released from the above sources (hydrothermal vents and diagenetic recycling) would have not been oxidized in the water column. Following upwelling from deep sea sediments to continental margins, Fe(II) would remain stable until necessary conditions existed for precipitation and deposition (Poulton and Canfield, 2011). Controversy surrounds the mechanism behind Fe(II) oxidation within a dominantly anoxic ocean and consequently the precipitation of ferric (oxyhydr)oxides. There are currently three main hypothesises: the direct generation of ferric iron by photoferrotrophy or chemolithoautotrophic iron oxidation (Konhauser et al., 2002; Crowe et al., 2008); abiotic photodissociation of $FeOH^+$ (Cairns-Smith, 1978; François, 1986); and the release of dissolved oxygen during cyanobacterial oxygenic photosynthesis, abiotically or microbially catalysing the reaction of Fe(II) (Cloud, 1968).

Sedimentary highly reactive iron (Fe_{HR}) enrichments occur under both ferruginous and euxinic conditions, but via different mechanisms. Highly reactive iron is defined as the sum of the iron carbonate (Fe_{CARB}), iron oxide (Fe_{OX}), magnetite (Fe_{MAG}) and pyrite (Fe_{PY}) pools in ancient sediments. In an iron-rich, ferruginous ocean, unsulfidized iron minerals can form directly from the water column, such as ferrous carbonates (e.g. siderite) and ferric (oxyhydr)oxides from the Fe(II) upwelled from deeper sediment porewaters and hydrothermal vents. In order for anoxic waters to persist in a ferruginous state, the flux of sulfide to the deep ocean must be less than half of the Fe_{HR} input, based on the molar ratios of iron and sulfur in pyrite (FeS_2) (Canfield, 1998; Canfield et al., 2008). Studies on the Black Sea demonstrated that the iron shuttle is the main method of Fe_{HR} enrichment under ancient euxinic settings. This is the intrabasinal mobilization of Fe(II) released from the reductive dissolution of iron (oxyhydr)oxides in shelf sediments during early diagenesis

and subsequently transferred to the deep basin (Canfield et al., 1996; Lyons and Severmann, 2006). A fraction of this Fe is re-oxidized before it passes the chemocline and is continually recycled in the water column. A significant portion of the original Fe(II) diffusively released from sediments is moved to deeper waters by lateral transport mechanisms, either bound to organic ligands or in colloidal form (Kondo and Moffett, 2015; Scholz, 2018). This Fe(II) in a euxinic column precipitates as pyrite and is ultimately buried in the sediments (Anderson & Raiswell, 2004), where iron deposition in deep sediments is ultimately balanced by the flux of dissolved Fe^{2+} from shelf sediments (Wijisman et al. 2001).

1.4.1.2 Measuring iron in ancient sediments

Sedimentary iron does not solely consist of Fe_{HR} phases but also of poorly reactive sheet silicate phases (Fe_{PRS} e.g. hornblende, chlorite, biotite, garnet; half-life with respect to sulfidation of 84,000 years) and unreactive iron ($Fe_{U;}$ residual sheet silicates; half-life with respect to sulfidation of $2\text{-}4x10^6$ years). The classification of iron into different reactive pools was initially determined in modern marine sediments based on the reactivity of iron minerals towards the presence of dissolved sulfide (Canfield et al., 1992; Raiswell and Canfield, 1996). It was also found that different dissolution techniques were required to efficiently separate the iron oxide and sheet silicate pools via a buffered dithionite and boiling 12 M HCl extraction respectively (Raiswell et al., 1994).

The importance of Fe_{CARB} and Fe_{MAG} as constituents of ancient, anoxic sediments, as well as Fe_{OX}, led to the formation of the most recent iron speciation method. This sequential extraction by Poulton and Canfield (2005) targets the biogeochemically reactive iron-bound phases in sediments (Fe_{CARB}, Fe_{OX}, Fe_{MAG}). Pyrite (Fe_{PY}) is also an important constituent of Fe_{HR}, but is measured via a chromous chloride distillation extraction (Canfield et al., 1986). This distillation determines the reduced inorganic sulfur species within the sediment sample (pyrite, acid volatile sulfur (AVS), and elemental sulfur) by decomposing in a hot chromous chloride solution to H_2S and forming a AgS precipitate. The significance of separating the total concentration of one element into its relative fractions was previously identified by Tessier et al. (1979), on the premise that each fraction was separately influenced by environmental conditions. The redox state of a water column affects the behaviour of iron and forms the basis for this iron speciation technique as a redox indicator. The Fe_{HR} pool is the sum of the separate iron phases (Fe_{CARB}, Fe_{OX}, Fe_{MAG}, Fe_{PY}) and when measured against the total amount of iron (Fe_T)

within the sample, can further elude on the redox state of the water column as shown in Figure 1.3. Ratios of Fe_{HR}/Fe_T less than 0.22 are generally indicative of oxic water column conditions, while those greater than 0.38 are considered anoxic. The term equivocal is given to samples with a ratio between 0.22 – 0.38, and may be due to oxic deposition, or to anoxic settings where Fe_{HR} enrichments are masked by either high sedimentation rates, or the diagenetic transfer of Fe_{HR} into Fe_{PRS} if insufficient free sulfide is available to form pyrite (Canfield et al., 1992; Poulton and Canfield, 2011). Iron speciation goes one step further in identifying the type of anoxia i.e. ferruginous or euxinic, through the use of the Fe_{PY}/Fe_{HR} ratio (Poulton et al., 2004a). Ferruginous conditions are identified by Fe_{PY}/Fe_{HR} ratios less than 0.7, with values greater than 0.8 indicative of a euxinic state (Anderson and Raiswell, 2004; Poulton et al., 2004a; Poulton and Canfield, 2011; März et al., 2008).

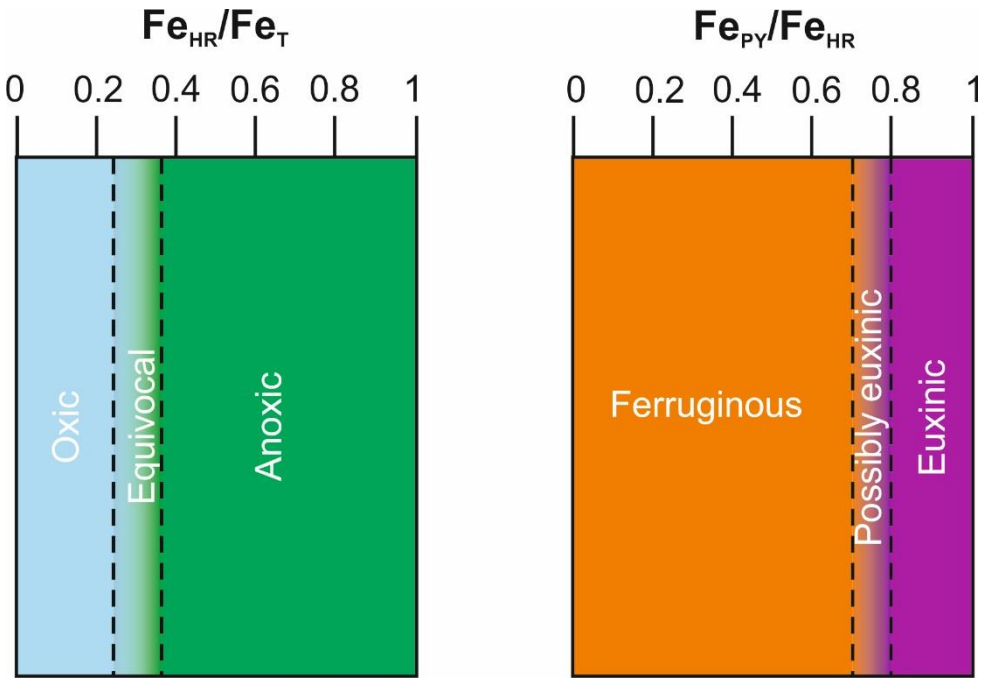

Figure 1.3 The use of the Fe_{HR}/Fe_T ratio in distinguishing between different redox states. The Fe_{PY}/Fe_{HR} ratio can further separate anoxia into sulfide-rich (euxinia) or iron-rich (ferruginous). Image modified from Poulton and Canfield (2011)

Iron speciation offers a comprehensive understanding of iron mineralogy in ancient marine sediments and is one of the most robust palaeoredox techniques used throughout the literature. Just as with any palaeoproxy, there are limitations to this method. Care needs to be taken when utilizing iron speciation in carbonate-rich rocks, as those with low Fe_T and low organic C can give deceptively high Fe_{HR}/Fe_T ratios. It was ascertained that values below 0.5 wt% Fe_T may give incorrect results (Clarkson et al., 2014) and this threshold acts as a constraint when dealing with carbonate-rich samples. As briefly

mentioned, redox equivocal results (Fe_{HR}/Fe_T 0.22 – 0.38) can result from the transformation of unsulfidized Fe_{HR} to Fe_{PRS} during early diagenesis if there is insufficient free sulfide available to form pyrite (Canfield et al., 1992; Poulton and Canfield, 2011). A boiling 12 M HCl method can quantify this pool, but further issues may be introduced on the origin of the sheet silicate minerals from an oxic or anoxic water column. The bulk measurement of Fe_T/Al (Al; aluminium) is typically used to manage this complication. Ratios above the average oxic Phanerozoic shale value (0.53 $\pm$ 0.11 wt%) are indicative of anoxic settings, and are not influenced by the post-depositional transformation of iron (Lyons and Severmann, 2006; Raiswell et al., 2008; Clarkson et al., 2014). As the Fe_T/Al ratio does not distinguish between anoxic ferruginous and euxinic conditions, using the two measurements of iron together can give a more thorough understanding of the sedimentary behaviour of iron in ancient settings.

1.4.1.3 Pyrite formation

The Proterozoic Era saw both ferruginous and euxinic conditions play an important role in seawater chemistry. It is thus vital to consider the mechanisms and controls on pyrite formation, an iron sulfide mineral. Increases in atmospheric oxygen concentrations are linked to the formation of sedimentary pyrite through the burial of organic matter. Elevated rates of organic matter burial are suggestive that photosynthetic production is outpacing respiration (Berner, 1982). Organic matter is used as an energy source for bacterial sulfate reduction (BSR), and therefore limits the formation of pyrite and the removal of sulfate from the oceanic reservoir (Berner, 1970; Bottrell and Newton, 2006).

All pathways and sources for pyrite formation are illustrated in Figure 1.4.

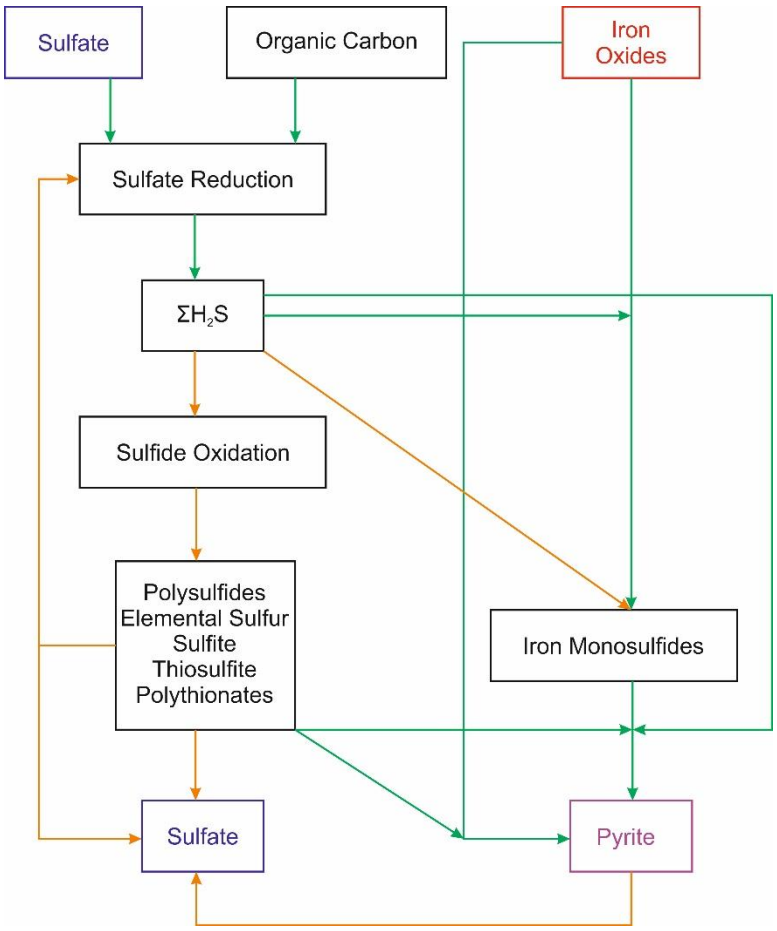

Figure 1.4 Schematic diagram for pyrite formation taken from Raiswell and Canfield (2012). Green arrows represent the main reaction pathways for pyrite formation. Orange arrows illustrate pathways using partially or fully oxidised sulfur species.

Berner (1970) first defined the three major steps in sedimentary pyrite formation: BSR to provide the principal source of sulfide; the reaction of iron minerals with hydrogen sulfide (H_2S) to form metastable iron monosulfide phases (FeS; e.g. mackinawite); and the final reaction of FeS with elemental sulfur to form pyrite (FeS_2). If pyrite forms directly from metastable FeS forms, there are three main pathways for this reaction to proceed: conversion via S addition using S as an electron acceptor; conversion with a non-S electron acceptor; and via iron loss with an electron acceptor (Schoonen, 2004). As there are multiple methods for pyrite to form in both the sediment and water column, the mechanisms behind its formation and their role in the S cycle remain poorly understood due to their complex relationships. What is apparent is the main limiting factors behind pyrite's growth. They are sulfate (SO_4), organic matter and iron oxides (Berner, 1964; Berner, 1970; Berner, 1982; Canfield, 1989; Poulton and Raiswell, 2002; Poulton et al., 2004b; Anderson and Raiswell, 2004; Schippers and Jorgensen, 2002; Rickard and Luther, 2007). Within a sediment profile, dissolved sulfide may only accumulate once all Fe_{OX} are exhausted (Canfield et al., 1992). This can occur by both abiotic

and biotic mechanisms, such as reductive dissolution during anoxic diagenesis, and microbial iron reduction respectively (Canfield, 1989). Further work has shown that the rate of pyrite formation is not controlled by the oxidation rate of sulfide, but by the dissolution of Fe_{OX} in surface sediments (Poulton et al., 2004b; Raiswell et al., 1994), solidifying the importance of Fe_{OX} within marine sediments for pyrite growth. As previously discussed, the mineralization and burial of organic matter is a primary control on atmospheric oxygen concentrations (Berner, 1982). The most significant pathway for organic matter mineralization is respiration during BSR, thus linking pyrite formation and burial to organic matter availability. There are two forms of pyrite that can contribute to this buried fraction. Diagenetic pyrite forms in typical marine sediments underlying oxygenated bottom waters during post-depositional processes. Syngenetic pyrite is that which forms in the water column when sufficient H_2S and reactive Fe is present (Rickard and Luther, 2007). This type of pyrite was important in Proterozoic settings where euxinic conditions developed along productive continental margins (Poulton et al., 2004a; Scott et al., 2008; Lyons et al., 2009; Poulton et al., 2010; Kendall et al., 2011).

1.4.2 Manganese

Manganese (Mn) behaves chemically similarly to Fe. In oxic seawater, Mn exists in the metastable Mn(III) and stable Mn(IV) oxidation states as insoluble (oxyhydr)oxides (MnO_2 and MnOOH) (Burdige, 1993; Calvert and Pedersen, 1996). In oxic-deficient settings, Mn(IV) is reduced to the soluble Mn(II). The reductive dissolution of Mn (oxyhydr)oxides also occurs in aquatic sediments chemically by anoxic diagenesis or biologically via dissimilatory iron reduction (Lovley, 2000). However, Mn reduction occurs before Fe and is the reason why dissolved Mn(II) can appear in a sediment profile at a shallower depth than Fe(II). This is illustrated in the typical redox zonation of marine sediment in Figure 1.5. Each zone is based on the vertical sequence of electron acceptors used in organic matter degradation with depth (Sorensen and Jorgensen, 1987).

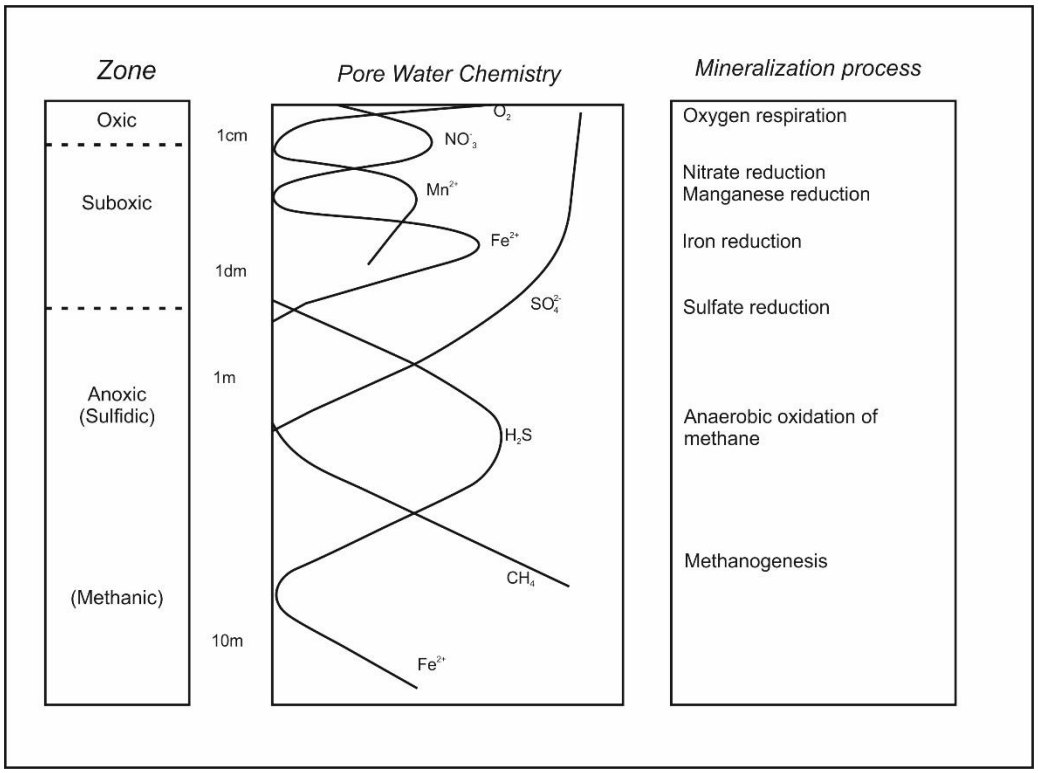

Figure 1.5 Redox zones in a typical sediment marine profile. Taken from Schulz and Zabel (2006)

Though both the Mn and Fe biogeochemical cycles are tightly coupled, there are some key differences in their behaviour in anoxic sediments. In general, dissolved Mn(II) is stable in the presence of dissolved sulfide, unlike Fe(II), and will only precipitate if sufficiently high levels of sulfide are present (Nealson and Saffarini, 1994; Perkins and Mason, 2015). The oxidized form of Mn (MnO_2) is however, far more susceptible to the presence of sulfide, and reacts at a quicker rate.

Manganese is also not typically taken up by organic complexes, allowing it to diffuse up and down in a reducing sediment column where it will either recycle back to the water column, or form authigenic Mn carbonates ($MnCO_3$, rhodochrosite) and (oxyhydr)oxides (Huerta-Diaz and Morse, 1992; Algeo and Maynard, 2004; Tribovillard et al., 2006). Because of its mobile nature, Mn was long considered to be ineffective as a palaeoredox proxy (Calvert and Pedersen, 1993; Calvert et al., 1996; Tribovillard et al., 2006). Instead its main role was seen as a mechanism for the transfer of trace metals to the sediment. Similarly to Fe (oxyhydr)oxide particulates, Mn (oxyhydr)oxides have complexed charged surfaces, and are efficient at binding other trace metals (German et al., 1991; Nealson and Saffarini, 1994; Morford and Emerson, 1999; Morford et al., 2005; Scott and Lyons, 2012; Dellwig et al., 2010; Scholz et al., 2013; Little et al., 2015). It was later recognized that as Mn reduction

occurs at a higher redox potential than Fe, it could be used to identify significant oxygenation in the water column through the precipitation of Mn (oxyhydr)oxides, and thus intermediate redox states (Burdige, 1993; Calvert and Pedersen, 1996; Jackson, 2015). The measurement of Mn can be used as an indicator for suboxic conditions by utilizing the Mn/Fe ratio. This ratio is considered to act as a proxy for the oxidation-reduction potential of a sediment during deposition, whereby the higher the ratio, the more oxidizing the depositional environment was (Jackson, 2015). This technique has been applied to other ancient environments to assist in redox interpretations (e.g. Tostevin et al., 2016). Problems can be encountered when using this ratio if the depositional setting is restricted and cut off from deep water circulation which continually replenishes the seawater elemental inventory (Hetzel et al., 2009; Goldberg et al., 2016). In modern settings where short-term redox changes are captured within the sediments, this can also affect the Mn/Fe ratio (Lewis and Landing, 1991; Dellwig et al., 2010).

1.4.3 Trace Metals

1.4.3.1 Molybdenum

In oxic seawater, Mo(VI) exists as the molybdate anion (MoO_4^{2-}) (Bertine and Turekian, 1973) and is largely unreactive, causing it to be the most abundant transition metal in today's oceans (Morris, 1975; Emerson and Huested, 1991; Morford and Emerson, 1999). Molybdate adsorbs to Mn-Fe (oxyhydr)oxides entering the aquatic system from riverine sources, and through sedimentation, subsequently falls to the sediment-water interface (Figure 1.6A). In a ferruginous system, the Fe-Mn (oxyhydr)oxide shuttle is enhanced through the formation of these particulates at the chemocline, which brings down more Mo at a quicker rate than in oxic settings. Upon reductive dissolution of the particulates in the sediment, molybdate is released back into the water column or into the sediment where it is scavenged by other phases (Figure 1.6B) (Adelson et al., 2001; Tribovillard et al., 2004). Scavenging of molybdate within the sediment accelerates the accumulation of authigenic Mo relative to other trace metals, such as uranium (U), that are not readily adsorbed onto Mn-Fe-oxyhydroxides (Algeo and Tribovillard, 2009; Little et al., 2015). However this behaviour may not transpire if depositional settings are restricted, such as in an intracontinental basin or containing other palaeogeographic barriers such as a sill, where deep water renewal of such elements are constrained. Depleted trace metal inventories have been documented in localities during Ocean

Anoxic Event 2 (OAE-2) as a result of restricted depositional settings (Hetzel et al., 2009; Goldberg et al., 2016).

Molybdenum behaves in a different manner in euxinic settings than ferruginous, as molybdate is converted to thiomolybdate ($MoO_xS_{4-x}^{2-}$, x = 0 - 3) and becomes particle reactive (Erickson and Helz, 2000). A greater proportion of thiomolybdate is drawn down through adsorption to organic matter (Meyers, 2007; Scott et al., 2008; Algeo and Rowe, 2012; Dahl et al., 2016; Wagner et al., 2017) or sulfide phases in solid solutions e.g. pyrite (Helz et al., 1996; Erickson and Helz, 2000; Adelson et al., 2001; Algeo and Lyons, 2006; Tribovillard et al., 2004), resulting in greater sedimentary Mo enrichments than in other redox settings (Figure 1.6C).

Molybdenum is commonly used in Proterozoic studies, and is applied through a variety of methods such as in: the bulk concentrations of Mo (Cox et al., 2016b; Dahl et al., 2011; Gilleaudeau and Kah, 2015; Miller et al., 2017; Reinhard et al., 2013; Sahoo et al., 2012; Scott et al., 2008; Sperling et al., 2014; Spinks et al., 2016; Zhang et al., 2016); its isotopic composition ($\delta^{98}Mo$) in sediments (Arnold et al., 2004; Baldwin et al., 2013; Duan et al., 2010; Kendall et al., 2011; Kurzweil et al., 2015, 2016, Planavsky et al., 2014b, 2018); and its relationship to organic carbon (Wilde et al., 2004; Algeo and Lyons, 2006; Lyons et al., 2009) to gain further understanding on the chemistry of ancient oceans.

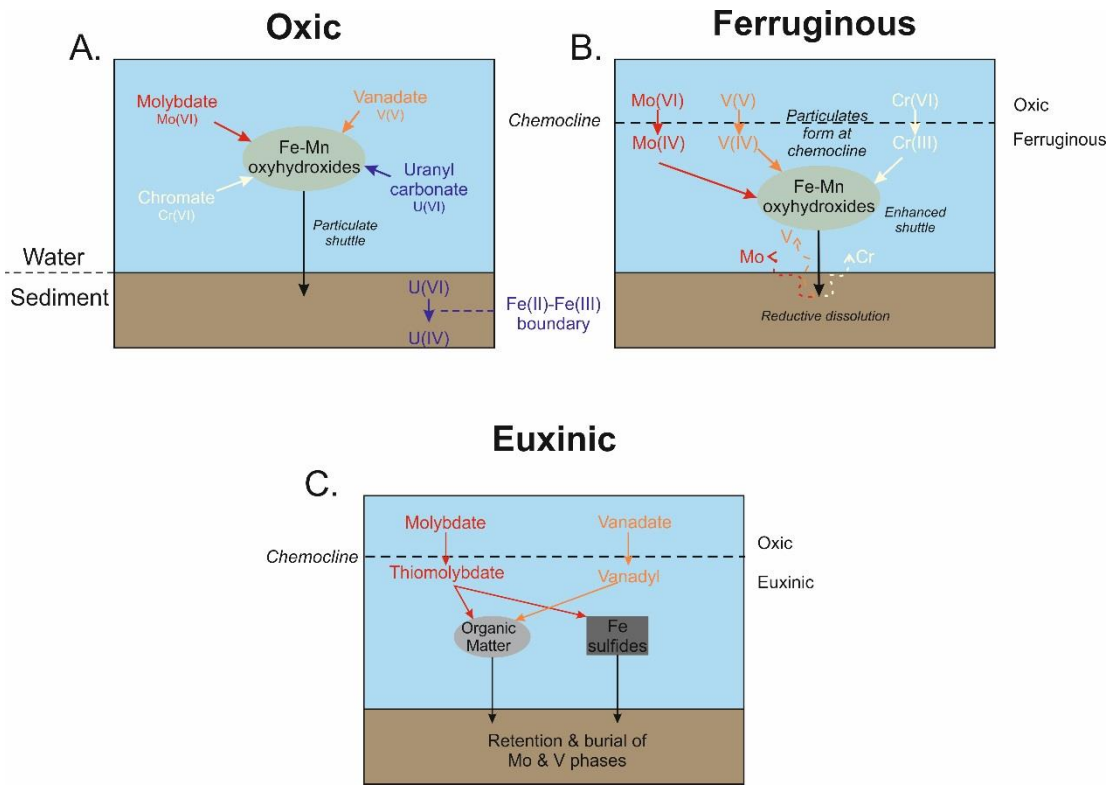

Figure 1.6 Simplified schematic for mechanisms involved in the sequestering of trace metals (Mo, V, U, Cr) under varying redox states. A – Fully oxygenated water column. Molybdate, vanadate, uranyl carbonates and chromates adsorb to Fe-Mn oxyhydroxides particulates which are supplied from rivers to the ocean. U reduction occurs in the sediment at the Fe(II)-Fe(III) boundary. B – Oxic waters overlying ferruginous deeper conditions. Particulates form at the chemocline creating an enhanced shuttle to the sediment. Reductive dissolution can release trace metals back to the water column if not sequestered by other phases in sediment. C – Mo binds to organic matter and Fe sulfides in a euxinic water column. V is also preferentially brought down with organic phases

1.4.3.2 Vanadium

Vanadium (V), though widely applied for Phanerozoic palaeoredox studies, is the least researched trace metal in Proterozoic sediments across the literature. This is potentially due to its semi-conservative behaviour in shallow waters (Emerson and Huested, 1991) as a result of: biological uptake; deposition of associated particles and Fe-Mn particulates; and altering sedimentary or fluvial input (Wang et al., 2009). Vanadium also has a shorter seawater residence time compared to Mo and U, suggesting that it is removed from the water column at a faster rate (Algeo and Maynard, 2008). In oxic conditions, V(V) exists as the vanadate oxyanion (HVO_4^{2-}) and similarly to Mo, slowly adsorbs to Fe-Mn oxyhydroxides (Figure 1.6A). In mildly reducing conditions V(V) reduces to V(IV), a vanadyl ion (VO^{2-}) and other insoluble hydroxides (Tribovillard et al., 2006). V is therefore strongly coupled to Mn cycling due to its transformation at

mildly reducing conditions (Morford et al., 2005; Beck et al., 2008). The behaviour of V is similar to that of Mo in its adsorption to particulates (Emerson and Huested, 1991; Morford and Emerson, 1999) and hyper-enrichments in sediments with elevated H_2S concentrations (Scott et al., 2017), but its main difference lies in its strong affinity to organic matter where organic complexes can form (Figure 1.6C) (Wanty and Goldhaber, 1992; Algeo and Maynard, 2008; Wang et al., 2009; Beck et al., 2008). Bulk concentrations of V have been applied as a palaeoredox tool in other Proterozoic studies (e.g. Shields-Zhou and Och, 2011; Och and Shields-Zhou, 2012; Sperling et al., 2013; Gilleaudeau and Kah, 2013; Sperling et al., 2014; Sahoo et al., 2012; Zhang et al., 2016; Cox et al., 2016; Miller et al., 2017; Diamond et al., 2018).

1.4.3.3 Uranium

In oxic to suboxic waters, the stable state of U is U(VI), which forms uranyl carbonate complexes ($UO_2(CO_3)_3^{4-}$) and is largely unreactive. Similarly to Mo and V, U is adsorbed to Mn-Fe (oxyhydr)oxides in well-oxygenated marine settings, and is also associated with particulate matter in the water column (Dunk et al., 2002; Och et al., 2016). As discussed in 1.4.3.1, Mo is preferentially scavenged by Mn-Fe particulates in comparison to U in the sediment, and can result in a net loss of U back to the water column.

The main source of U to the marine system is riverine delivery, and its ultimate sink is burial in organic-rich, oxygen poor sediments via diffusion across the sediment-water interface (Emerson and Huested, 1991; Morford and Emerson, 1999; Dunk et al., 2002). Uranium reduction typically occurs in the sediment at the same redox boundary where Fe(III) reduces to Fe(II). The more soluble reduced form (U(IV); uranyl iron) precipitates as uraninite, or associates with carbonate and phosphate phases (Morin et al., 2016; Algeo and Tribovillard, 2009). As there is a strong coupling between U and Fe redox cycles, U reduction is largely mediated by microbial reduction (i.e. BSR) (Morford et al., 2009; Algeo and Tribovillard, 2009; Tribovillard et al., 2012). Uranium is a useful palaeoredox proxy and can signal different reduction mechanisms than that of other redox-sensitive trace metals. Both the bulk concentrations of U and its stable isotope ($\delta^{238}U$) have been applied to Proterozoic sedimentary successions (e.g. Partin et al., 2013; Anbar et al., 2007; Asael et al., 2013; Och and Shields-Zhou, 2012; Sperling et al., 2015; Cox et al., 2016a; Zhang et al., 2016; Xiang et al., 2017; Lau et al., 2017; Yang et al., 2017; Miller et al., 2017).

1.4.3.4 Chromium

Chromium is transported as part of the clastic fraction of terrestrial material in rivers to the marine system (Tribovillard et al., 2006). In oxic conditions, Cr(VI) exists as the unreactive chromate anion (CrO_4^{2-}). Reduction to Cr(III) occurs in mildly denitrifying conditions, and can form aquahydroxyl or hydroxyl cations (Algeo and Maynard, 2004). Water column pH influences which insoluble phase of Cr(III) precipitates, with $Cr(OH)_3$ or Cr_2O_3 forming at high pH and $Cr(OH)_2^+$ under low pH conditions, adsorbing to Fe-Mn oxyhydroxides or complexing with humic or fulvic acids (Algeo and Maynard, 2004). Chromium behaves in a similar fashion to U, in that the presence of free sulfide is not required for its reduction. Because of this, Cr can be lost to the water column during diagenesis as it is not readily sequestered by sulfide during organic matter remineralization (Tribovillard et al., 2006). Another complication Cr concentrations can give is its large detrital flux entering the ocean as chromite, clay minerals, or in ferromagnesian minerals where Cr readily substitutes for magnesium (Tribovillard et al., 2006; Miller et al., 2017). Precautions need to be taken in interpreting Cr concentrations by normalizing them to common detrital minerals e.g. Al, Ti (Lyons and Severmann, 2006) to show the true authigenic Cr component without a detrital influence.

Chromium isotopes ($\delta^{53}Cr$) are a much more commonly used palaeoredox tool than Cr concentrations in Proterozoic studies. They have been widely applied in an attempt to estimate past atmospheric oxygen concentrations throughout the Proterozoic (Reinhard et al., 2014; Cole et al., 2016; Planavsky et al., 2014b; Crowe et al., 2013) and have also been measured in BIFs to further constrain the date for the GOE (Frei et al., 2009; Konhauser et al., 2011).

1.5 Phosphorus

When conducting research concerning the evolution of a habitable planet, it is crucial to consider phosphorus (P). Phosphorus, along with sugars, forms the structure of DNA and RNA, is the main mineral component in vertebrate bones as apatite, and is also responsible for the transfer of metabolic energy in organisms. It also behaves significantly differently to other biogenic elements (C, H, O, N, S), in that it has no major volatile phase and only one oxidation state under normal terrestrial conditions (Pasek et al., 2017). This behaviour, coupled with the incompatible nature of phosphate with mantle mineralogy,

contributes to a high crustal abundance of P in continental rocks (~700 ppm, Taylor and McLennan (1995)).

Phosphorus is considered one, if not the ultimate, limiting nutrient for life on this planet (Redfield, 1958; Tyrrell, 1999). Decades of research have pitted N and P against each other for the title of “ultimate limiting nutrient” over geological timescales. There are several reasons to defend P as the ultimate limiting nutrient. The first is its long oceanic residence time at 10,000 – 20,000 years (Filippelli and Delaney, 1996). Riverine delivery is the only major source of P to the oceans, as its atmospheric input is too small to have a significant impact on nutrient availability (Froelich et al., 1982). In open waters far from continental shelves, processes such as upwelling, vertical eddy diffusivity and turbulent motions circulate P into surface waters (Berner, 1990; Ingall and Van Cappellen, 1990; Ruttenberg and Berner, 1993; Filippelli and Delaney, 1996; Karl, 2014). Both the ocean and the atmosphere are large reservoirs of N, and if open ocean surface waters become depleted in N, it will eventually be restored through nitrogen fixation on shorter timescales from the atmosphere (Saltzman, 2005). The operation of N-fixing microorganisms in open waters is also another reason why P is deemed the ultimate limiting nutrient. If nitrate becomes depleted, organisms which fix N_2 from the atmosphere (diazotrophs) will become more abundant. This algal growth fuelled by atmospheric N availability will eventually return nitrate and ammonia to the water column following decomposition, increasing the ratio of nitrate to phosphate (Tyrrell, 1999).

1.5.1 Archaean and Proterozoic Phosphorus studies

This research recognizes the importance of understanding the marine P cycle across the Proterozoic Eon, as it is the ultimate limiting nutrient for oxygen production by means of organic C burial on geological timescales (Betts and Holland, 1991). As this period saw major changes to atmospheric oxygen concentrations, it is crucial to decipher how the P cycle functioned as a response to both biological and environmental evolutions. Past studies can be grouped into two areas where attention has been focused: estimating seawater phosphate concentrations; and modelling the P cycle as a consequence of changing ocean redox and the emergence of increasingly complex life during this period.

There is a divide in the literature over estimates for past phosphate concentrations from BIFs. Some have suggested that extremely low levels

(0.04 – 0.6 µM) compared to modern levels (2.3 µM) would have limited photosynthetic production of organic C, and thus long term oxygen production (Bjerrum and Canfield, 2002; Jones et al., 2015). Disagreements with these estimates propose similar levels as the modern, but advocate that high levels of dissolved silica competed against phosphate for adsorption sites on iron (oxyhydr)oxides, preventing P from being drawn down to the sediment-water interface (Konhauser et al., 2007). A peak in phosphate levels were uncovered in iron formations deposited after the Cryogenian Snowball Earth glaciations. These have been used to infer an elevated postglacial flux of nutrients to the marine system with potential links to increased concentrations of atmospheric oxygen and the emergence of metazoans (Planavsky et al., 2010). The limitation with these approaches is their sole application to BIFs and not shales. They provide some understanding of the P cycle under intensely ferruginous waters, but do not capture the typical conditions of the Proterozoic ocean. Banded Iron Formations disappear from the rock record at 1.85 Ga, and their reappearance in the Neoproterozoic (~0.8 – 0.6 Ga) is much more spatially constrained and found only in association with glaciomarine deposits (Klein, 2005). In normal marine sediments with oxygenated surface waters, new mechanisms for P sequestration would be introduced, such as with organic matter. Estimations for phosphate concentrations would thus be complicated by a more advanced P cycle. These investigations are the most current empirical attempts to assess P burial dynamics from the rock record. However, they do not capture P burial mechanisms during periods of significant biological evolution i.e. the Mesoproterozoic Era and Ediacaran Period, leaving a significant gap in the understanding of the role of the ultimate limiting nutrient during this time.

Recent modelling approaches have attempted to reconstruct the Proterozoic P cycle. Reinhard et al. (2016a) used a comprehensive dataset (sample n>7000) to model total P content in shales across geological time. The authors document a rapid increase in total P during the Neoproterozoic, and proposed this event signalled a change in sediments predominantly consisting of detrital-bound P phases, to authigenic phases. A shift in ocean redox, to more oxygenated environments from formerly ferruginous settings, is hypothesized as the major cause behind this upheaval due to the removal of the water column Fe_{OX} sink as the ocean's chemistry transitioned. An assumption made by this study is that the total P content of sediments tracks bioavailable P through time. This hypothesis is incorrect as only reactive P phases, such as organic and iron-bound P, are bioavailable while detrital is not. Also discounted is the importance of P recycling. P burial occurs under

ferruginous conditions, but with euxinic conditions becoming increasingly more common following the GOE, sulfide availability in sedimentary porewaters promotes P recycling back to the water column (März et al., 2008). The conclusion that a surge in sedimentary P concentrations is also based on a small number of samples from the Doushantuo Formation, a known phosphorite deposit. This introduces restrictions to the findings of this modelling study, as phosphorites require unique conditions for formation (discussed in 1.5.2.2) and are not common throughout this period.

Other modelling studies have related changes in the P cycle during the Ediacaran Period (635 – 542 Ma) to the radiation of animals, as well as ocean oxygenation. The findings of Lenton et al. (2014) theorized that a positive feedback was established between the spread of oxic waters and P burial, whereby the continued removal of P under an oxic water column limited primary production and allowed increasingly complex organisms to evolve. Similarly to Reinhard et al. (2016a), this study also assumed constant P recycling under ferruginous conditions prior to the Ediacaran, thereby creating a simplified version of the P cycle during this period.

With the evolution and subsequent radiation of animals, came the effects of bioturbation on marine sediments. Evidence for bioturbation is discussed in detail in section 1.3.2.1. Attempts have been made by modelling studies to analyse how the introduction of bioturbation into the marine system affected the P cycle. Increased rates of bioturbation were found to decrease the ocean oxygen reservoir through the continued burial of organic P, creating a negative feedback between oxygen availability and this biological innovation (Boyle et al., 2014). A problem with the model used in this study is the removal of Fe-bound P burial under anoxic conditions, which contradicts the studies listed above (e.g. Bjerrum and Canfield, 2002; Konhauser et al., 2007; Planavsky et al., 2010; Jones et al., 2015). This is an important mechanism for both the shuttling of P to the sediment-water interface, and the scavenging of phosphate during diagenesis. The removal of this pathway similarly simplifies the operations behind the Proterozoic P cycle as other modelling studies have. A geochemical investigation capable of analysing all reactive P phases within marine sediments is thus required to gain a full understanding of the Proterozoic P cycle. This technique is further discussed in section 1.5.3.

1.5.2 The global phosphorus cycle

1.5.2.1 Sources of phosphorus

A simplified box diagram of the Proterozoic marine P cycle is illustrated in Figure 1.7. Phosphorus is primarily supplied to the oceans by rivers in both particulate and dissolved forms, which include: particulate inorganic P (PIP), particulate organic P (POP), dissolved inorganic P (DIP), and dissolved organic P (DOP). Particulate phases are the dominant forms as P is particle reactive, with their associated chemical form dependent upon the local bedrock, drainage basin geology, weathering rate and the geomorphology of the river (Ruttenberg, 2003). Particulate inorganic P mainly exists as apatite or P bound to ferric (oxyhydr)oxides. Atmospheric input of P to the ocean is currently believed to be an inefficient source when comparing to terrestrial runoff (Duce et al., 1991; Karl, 2014). The flux of DIP and DOP to the ocean can be altered as a result of: biological uptake; remineralization; adsorption/desorption to or from particle surfaces; changes in weathering; and redox reactions influencing PIP and POP dissolution (Froelich et al., 1982; Benitez-Nelson, 2000). There are three natural states of DIP or phosphate, whereby in seawater at pH 8, the main species is HPO_4^{2-}, with minor amounts as PO_4^{3-} and $H_2PO_4^-$ (Ruttenberg, 2003). A recent study by Cox et al. (2018) analysed the P content of igneous rocks across geological time and showed that increases in the total P content of continental igneous rocks were accompanied by similar rises in total P in the sedimentary rock record. From this finding they proposed that bedrock weathering was a much more important factor to the P budget than sedimentary recycling and has further implications for the role of mantle cooling on the continental P inventory.

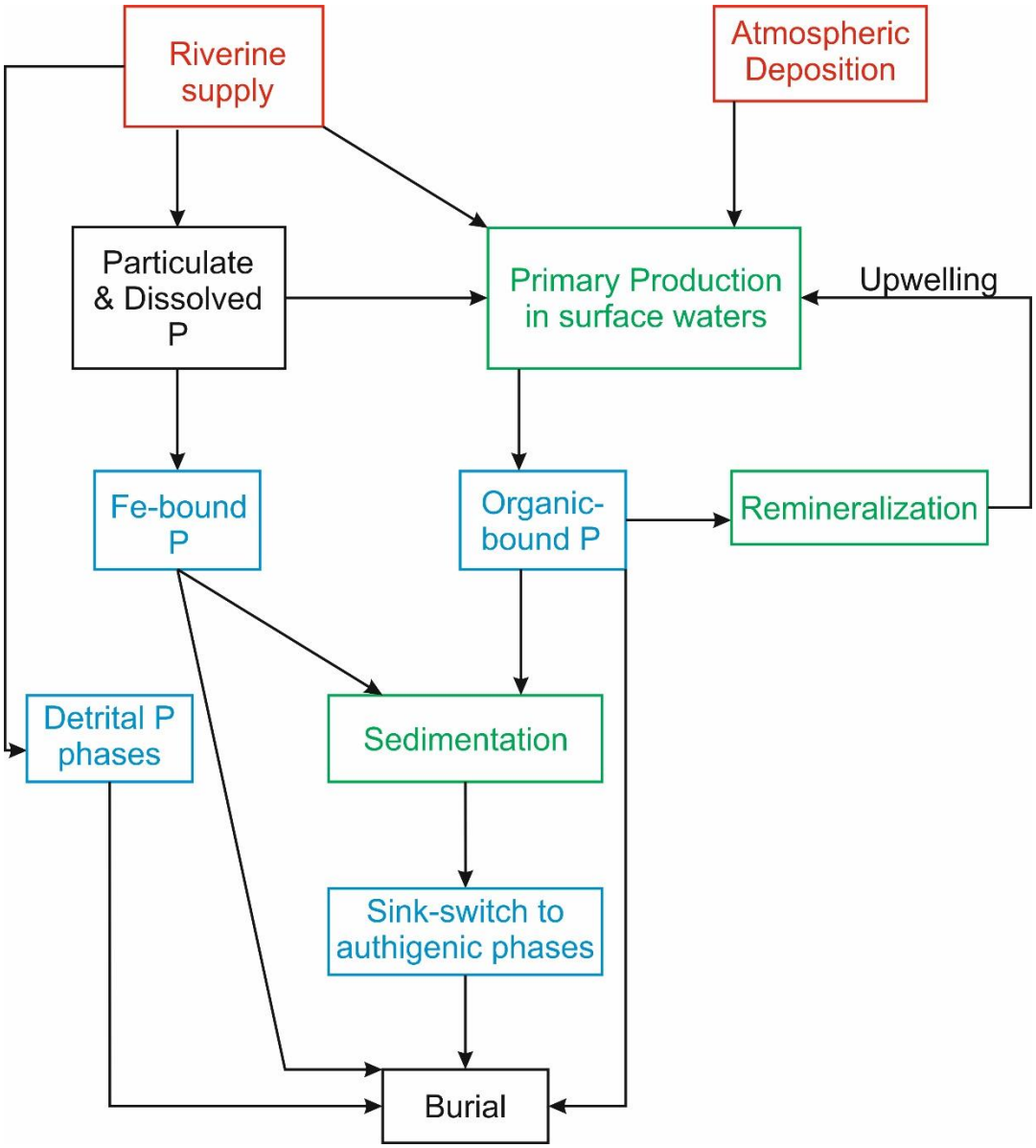

Figure 1.7 Simplified box diagram of the Proterozoic marine P cycle. Sources of P to the marine system are colour-coded in red; P mineral phases in blue; and processes involving the use of P phases are in green. The ultimate sink for P is burial, and shown in black.

1.5.2.2 Phosphorus sinks

The ultimate sink for P is burial in marine sediments, as P has no stable gaseous form. Estimates for the amount of P removed from its marine cycle and sequestered into sediments stands at <1% (Benitez-Nelson, 2000). There are a variety of mechanisms by which this can occur, and are listed in order of importance:

1.5.2.2.1 Organic Matter burial

Phosphorus adsorbed to sinking organic matter (P_{org}) is the dominant mechanism involved in transporting P to the sediment-water interface (Froelich et al., 1982; Tyrrell, 1999). Phosphorus, as well as N and C, are used by phytoplankton during primary production. The Redfield Ratio defines the relative quantities of each element in settling organic matter on the seafloor (P:N:C 1:16:106; Redfield (1958)). This simple formula has gained overwhelming recognition in the field of marine biogeochemistry, and the ratios of organic C to P have been widely applied to assess if P is preferentially stored or recycled in sediments under differing redox conditions (Ingall and Van Cappellen, 1990; Ingall et al., 1993; Anderson et al., 2001; Faul et al., 2005; Algeo and Ingall, 2007; Jilbert et al., 2011). The absolute values of the elements in the Redfield Ratio are now believed to be substantially more complex based on the role of dissolved organic nutrients, metabolic activity and biological growth rate (Geider and La Roche, 2002; Karl, 2014). It is also hypothesized that the Redfield Ratio may have been different in ancient oceans, based on the dominance of cyanobacteria and their ability to thrive in nutrient-limited environments in comparison to the modern environment (Planavsky, 2014; Reinhard et al., 2016a).

Organic matter decomposition begins in the water column (Martin et al., 1987), and on reaching the sediment-water interface releases the previously adsorbed phosphate to the interstitial sediment porewaters (Krom and Berner, 1981; Filippelli and Delaney, 1996). Under an oxic water column, this phosphate is commonly significantly retained within the sediments and if buried to sufficient depths transforms, or “sink-switches”, to authigenic P (P_{auth}) phases, typically carbonate fluorapatite (CFA) (Ruttenberg and Berner, 1993; Ingall et al., 1993). If the correct conditions are met, the continued burial of P may generate phosphorite deposits. Phosphorites are sedimentary rocks with greater than 15 wt% P_2O_5 (Papineau, 2010). Though they contain significantly more P than that of shales, the abundance of shales in the geological record compared to the episodic occurrence of phosphorites means they are not the most significance source of P (Ruttenberg and Berner, 1993). Their formation has been linked to: OAEs; high primary production with an accompanying elevated organic matter burial flux; and sea level changes (Ruttenberg, 2003; Filippelli, 2011). The occurrence of phosphorite deposits at both ends of the Proterozoic Eon is hypothesized to relate to the two events in rising atmospheric oxygen levels, the GOE and NOE (Papineau, 2010).

Upwards diffusing phosphate may also be scavenged by Fe (oxyhydr)oxides in the surface sediment layer, acting as a barrier and preventing the escape of P back to the water column (Slomp et al., 1996a).

This mechanism is discussed in further detail in section 1.5.2.2.2. If sedimentation rates are sufficiently high (~1 cm/yr; Ingall and Van Cappellen, 1990), P_{org} can escape diagenesis and be sequestered in its original form (Lenton and Watson, 2000).

Different processes can govern P burial mechanisms under anoxic conditions. Earlier studies suggest that under anoxic waters, phosphate is lost from the sediments and recycled back to the water column, fuelling primary productivity (Calvert et al., 1996; Ingall et al., 1993; Jilbert et al., 2011; Kraal et al., 2010, 2012; Mort et al., 2010; Slomp et al., 2004; Sundby et al., 1992). However, other authors have advocated that the type of anoxia is imperative to whether P is recycled or stored, as recycling more readily occurs under euxinic environments (März et al., 2008; Poulton et al., 2015). Sedimentation rates also exert a major control on P accumulation in sediments, where higher rates in continental margins promote P storage compared to deep ocean sediments (Filippelli, 1997; Ingall and Van Cappellen, 1990).

1.5.2.2.2 Phosphorus adsorption to Fe (oxyhydr)oxides

The adsorption of P to Fe (oxyhydr)oxides is also an important mechanism for the shuttling of P to the sediments (Berner, 1973). This can occur in both the water column, where the particulates form at the chemocline and P is adsorbed to (Jones et al., 2015), or in the sediment. The latter is considered where the majority of P adsorption occurs and similarly to the burial of organic matter, is dependent upon redox. Hydrothermal activity is an important source of Fe(II) to the marine system, and when vent fluids mix with seawater, hydrous ferric (oxyhydr)oxides form (Wheat et al., 1996; 2003). Again, P binds to these Fe (oxyhydr)oxides, and become incorporated in sediments away from the vent system as hydrothermal plume fallout (Poulton and Canfield, 2006).

During organic matter degradation, some of the phosphate released can adsorb to Fe (oxyhydr)oxides within the sediment (Slomp, et al. 1996a; Van Cappellen and Ingall, 1996). If the overlying waters are sufficiently oxygenated, keeping the oxic-anoxic redox boundary within the sediment, Fe (oxyhydr)oxides in the upper oxic layer will act as a barrier and prevent phosphate from escaping back to the water column (Slomp et al., 1996a; Lenton and Watson, 2000; Algeo and Ingall, 2007). If reductive dissolution occurs to the Fe (oxyhydr)oxides, both the Fe and phosphate bound to the particulate are diffusively released back to the porewaters. Fe-bound P (P_{Fe}), if sequestered in the sediment for a sufficiently long period, will undergo diagenetic recycling where phosphate is desorbed from the iron particulate and

used in the formation of authigenic phases (Anderson et al., 2001; Algeo and Ingall, 2007). Sulfidic conditions in the sediment would also cause the reductive dissolution of P_{Fe}, but would retain the Fe through the formation of iron-sulfide products, such as pyrite (Colman and Holland, 2000; Kraal and Slomp, 2014).

Authigenic iron phosphate minerals can also be important constituents of the sedimentary P pool. If Fe (oxyhydr)oxides are buried below the zone of dissimilatory iron reduction in sediments, such as on continental margins with high sedimentation rates, the Fe (oxyhydr)oxides and associated phosphate phases can be buried into subsurface sediments and escape surficial diagenetic processes (Hensen et al., 2003; März et al., 2008). These phases then endure diagenetic processes deep in the sediment profile at the sulfate-methane transition zone. Here, the anaerobic oxidation of methane generates free HS^-, and subsequently reductively dissolves the Fe (oxyhydr)oxides buried to this depth. Similarly to the reductive dissolution of Fe (oxyhydr)oxides in shallower depths, the phosphate adsorbed to these phases diffuses up and down the sedimentary profile. It is the downward diffusing phosphate into the methanic zone that can ultimately form authigenic phases, such as vivianite (Egger et al., 2015; März et al., 2018; Dijkstra et al., 2016).

1.5.3 Measuring P phases in sediments

Phosphorus speciation, termed SEDEX (sedimentary extraction), was developed by Ruttenberg (1992) and is the main experimental method used to assess the different reactive phases of P within modern sediments: loosely-sorbed; ferric iron-bound; authigenic CFA, biogenic apatite and $CaCO_3$-associated; organic; and detrital apatite P. This technique has been widely applied across numerous modern sites to gain an insight into P burial mechanisms in various marine settings (Slomp et al., 1996b; Eijsink et al., 1997; Anderson and Delaney, 2000; Van Der Zee et al., 2002; März et al., 2008; Goldhammer et al., 2010; Mort et al., 2010; Jilbert et al., 2011; Kraal et al., 2012; Jilbert and Slomp, 2013; Dijkstra et al., 2014; Poulton et al., 2015; Ni et al., 2015; Dijkstra et al., 2016; Kraal et al., 2017; Egger et al., 2015; Dijkstra et al., 2018). An updated method for ancient sediments has recently been developed by Thompson et al. (*in prep*), which incorporates magnetite-bound (P_{mag}) and hematite-bound P as measurable phases in the extraction, as well as those originally in the SEDEX method. This is an important development to the method as crystalline magnetite and hematite are primary constituents of ancient sedimentary rocks deposited under an anoxic ferruginous water column (Poulton et al., 2004b; Canfield et al., 2008). As investigated throughout this

discussion on the Proterozoic P cycle, P_{Fe} was an important drawdown mechanism under both oxic and ferruginous conditions. Compared to previous attempts solely looking at P bound to Fe oxides in BIF deposits (Bjerrum and Canfield, 2002; Konhauser et al., 2007; Planavsky et al., 2010; Jones et al., 2015), this technique incorporates all possible shuttles for P to reach the sediment-water interface, allowing an in-depth scrutiny of P burial mechanisms.

1.6 Isotope systematics

1.6.1 Carbon isotopes ($\delta^{13}C$)

The measurement of stable C isotopes involves the measurement of ^{13}C and ^{12}C ($^{13}C/^{12}C$; $\delta^{13}C$). Carbon is a useful proxy as it exists in a variety of redox states in nature: C(-IV) in organic (e.g. kerogen, fossil fuels) and methane phases; and C(+IV) in inorganic C pools (carbonate). In the global C cycle, the isotopes are fractionated as they are moved from one reservoir to another. The typical fractionations associated with each C reservoir are illustrated in Figure 1.8, and thus provide a signature of where and what processes have influenced their isotopic value. Carbon's ultimate sink is through burial either as organic C ($\delta^{13}C_{org}$) or as calcium carbonate ($\delta^{13}C_{carb}$). Once buried, tectonics move buried C until the rocks are exposed, weathered and eroded, releasing the previously stored C back into the hydrological cycle, a sink for CO_2 (Newton and Bottrell, 2007). Atmospheric CO_2 is exchanged with both the smaller terrestrial reservoirs as well as the larger ocean reservoir. This CO_2 kinetically exchanges with the ocean and is used during photosynthesis, one of the most important processes controlling the fractionation of organic C:

$$CO_2 + H_2O \rightarrow CH_2O + O_2$$

This process increases the amount of ^{12}C in organic C relative to the source of CO_2, and is termed a negative fractionation (Whiticar, 1999; Saltzman and Thomas, 2012). Kinetic effects of a heavier isotope are responsible for this behaviour, as the lighter molecule is preferentially diffused out of the system, leaving behind the heavier form (Sharp, 2017). The organic product of photosynthesis does not solely accumulate in sediments but is also recycled back to DIC through respiration:

$$CH_2O + O_2 \rightarrow CO_2 + H_2O$$

For this research only $\delta^{13}C_{org}$ will be examined. The $\delta^{13}C_{org}$ value can be further influenced by: input of marine vs. terrestrial sources of organic matter;

metabolic behaviour of the organic community; remineralization of DOC; and degradation of particulate organic C below the sediment-water interface (Hayes et al., 1999; Kump and Arthur, 1999; Guo et al., 2013). As shown in Figure 1.8, organic matter typically has a $\delta^{13}C_{org}$ value of -22‰ (Newton and Bottrell, 2007), though other work has shown that organic matter derived directly from autotrophic fixation of DIC has an isotopic fractionation between -28 to -30‰ (Kump and Arthur, 1999). Negative excursions from this value typically result from heterotrophic (secondary) and chemotrophic (sulfide-oxidizing) productivity, with values between -40 and -90‰ reflective of methanotrophic biomass (Hollander and Smith, 2001; Hayes et al., 1999). Terrestrial or detrital sources of organic C typically reflect those of source rocks rather than of the standing organic community, and usually record more positive values of $\delta^{13}C_{org}$ (Kennedy et al., 2006). Thermal alteration of C isotopic signals can also occur during post depositional processes (Derry, 2010), and have been invoked as a reason for the large scale negative excursions documented in Neoproterozoic rocks, as discussed in 1.1.2. Organic C isotopes are thus useful in tracking the dominant organic community in a water column, an essential task during the Proterozoic when important biological evolutionary pathways were forming.

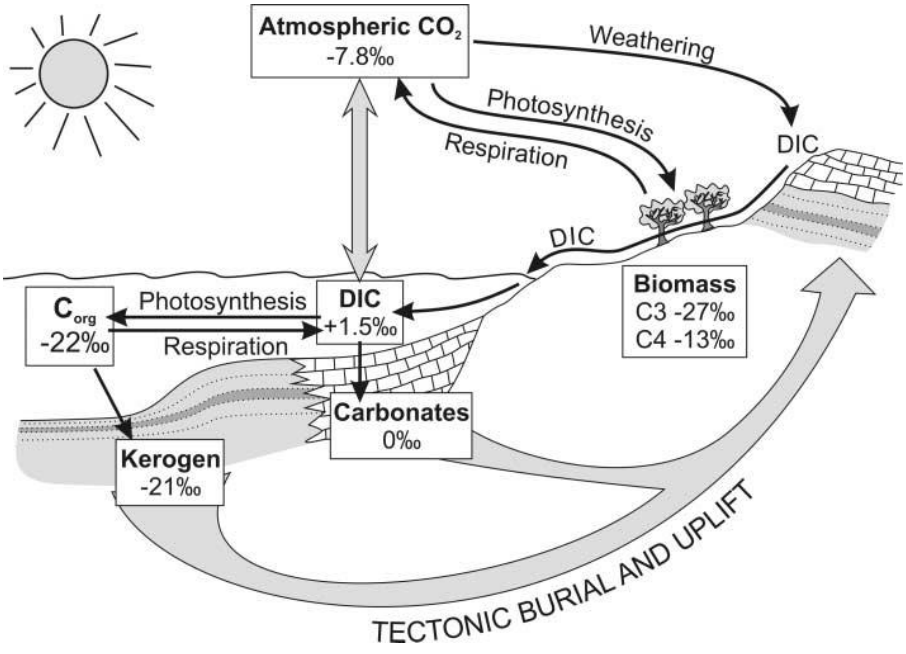

Figure 1.8 Schematic of the pre-industrial carbon cycle, taken from Newton and Bottrell (2007)

1.6.2 Sulfur isotopes ($\delta^{34}S$)

Similarly to C, the stable isotopes ($^{34}S/^{32}S$; $\delta^{34}S$) of S are fractionated as they are cycled through the different reservoirs of the global S cycle. All sinks and sources in the pre-industrial S cycle are illustrated in Figure 1.9.

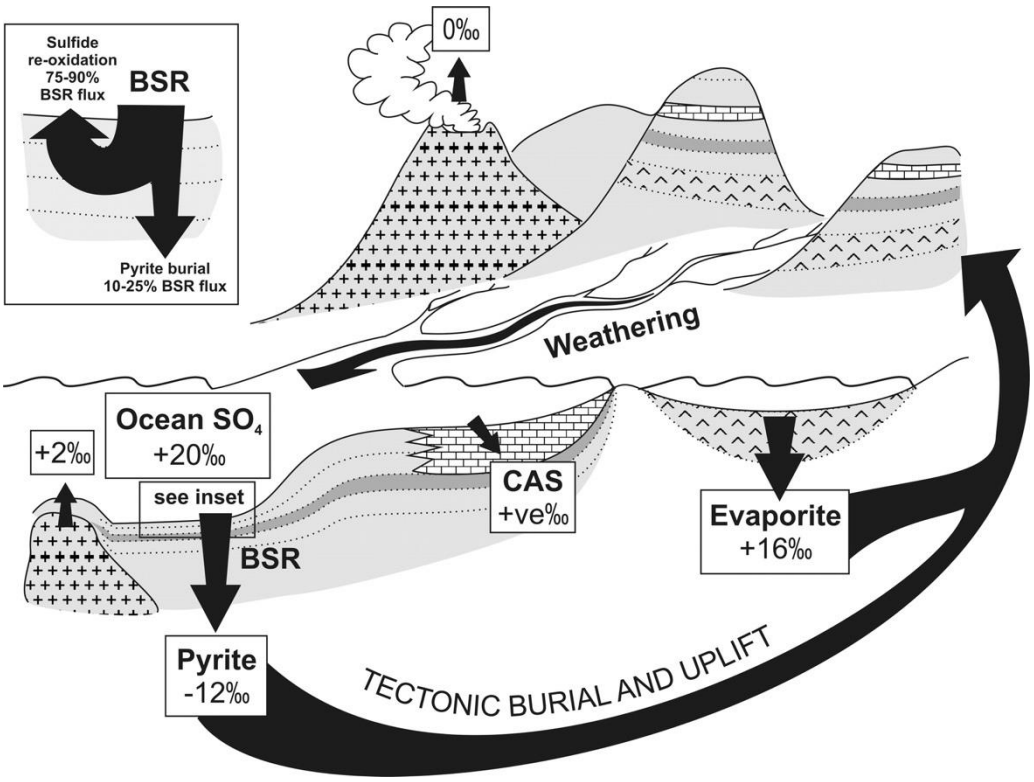

Figure 1.9 Schematic of the pre-industrial global S cycle. Figure taken from Newton and Bottrell (2007)

The three major reservoirs for S are: sulfate in ancient evaporate deposits; dissolved sulfate in the ocean; and sulfide, typically in the form of pyrite. Volcanic outgassing of SO_2 and H_2S, which rains out to the ocean, constantly changes these S reservoirs (Bottrell and Newton, 2006). Sulfur can exist in two redox states: -II (sulfide) and +VI (sulfate). There are two methods for analysing these isotopes: the measurement of $\delta^{34}S_{CAS}$ (CAS - carbonate associated sulfate) and $\delta^{34}S_{PY}$ (PY – pyrite). The measurement of $\delta^{34}S_{CAS}$ serves as a proxy for the sulfate content of the ocean as the fractionation between seawater and the oxidized form of S (sulfate) is negligible, as S is incorporated into the carbonate lattice during precipitation (Burdett et al., 1989; Bottrell and Newton, 2006; Theiling and Coleman, 2015). In this research, only $\delta^{34}S_{PY}$ will be investigated. Pyrite is the dominant sink for reduced S in the marine system, and forms through BSR (Froelich et al., 1979; Holland, 1973). During BSR, the sulfide product is depleted in ^{34}S relative to the reduced sulfate, as ^{32}S forms weaker bonds than the heavier isotope and results in a more rapid reduction

(Sharp, 2017). This results in a negative excursion in $\delta^{34}S_{PY}$ values and can also be used to track seawater sulfate concentrations. The presence of sulfate is a limiting factor in the formation of pyrite (Berner, 1982), and is supplied to the oceans from the oxidative weathering of terrestrial S-bearing minerals. Following the GOE, it is debated whether atmospheric oxygen levels remained steady or declined until the second rise in oxygen concentrations, the NOE (as discussed in section 1.1). If there was no enhanced flux of sulfate to the oceans during this prolonged period of time, the main control over sulfate concentrations in ocean would be drawdown with pyrite in euxinic settings. Thus, $\delta^{34}S_{PY}$ values play a crucial role in understanding oceanic chemistry during the Proterozoic. Sulfur isotopes have also been heavily used to investigate the history of atmospheric oxygenation, as discussed in section 1.1, through their MIF and MDF patterns.

1.7 This study

The current understanding of ocean redox throughout the Proterozoic Eon is based on an incomplete and patchy record. More studies are required to gain an understanding on how the ocean transitioned from a dominantly anoxic, ferruginous state with pockets of euxinia, to the almost completely oxygenated modern state. For the first time in Earth's history, environmental conditions were favourable for increasingly more complex life to evolve and occupy. The current understanding of the Proterozoic P cycle is either based on estimates for past seawater phosphate concentrations or simplified modelling approaches on total sedimentary P content. BIFs are not typical marine deposits and have a sparse geological record in the Neoproterozoic following their demise at approx. 1.85 Ga. A focus on the reactive P pool in marine shales is thus required to gain a better understanding of the P biogeochemical cycle during this period. This research seeks to address these gaps in the literature through the following aims and objectives:

1.7.1 Aims and Objectives

Apply the palaeoredox proxies of iron speciation and trace metal analyses to the sedimentary successions of the Bashkir Meganticlinorium in Russia, and the North China Craton to add to the current geochemical record of Proterozoic ocean redox

Evaluate if the water column chemistry within these successions matches other studies from this time period

Employ the newly adapted phosphorus speciation method to successions which document innovations in biological evolution, such as the emergence of macroscopic eukaryotes and metazoans

Resolve if the ultimate limiting nutrient, phosphorus, endured significant changes as a result of eukaryote and metazoan evolution, or whether changes in the Proterozoic P cycle reflect changes in ocean redox chemistry

Assess the importance of iron-bound P delivery to marine sediments under varying redox conditions

1.7.2 Thesis Outline

This project sets out to answer these aims using the methods outlined in Chapter 2. Chapter 3 focuses on examining the redox state of the Mesoproterozoic Bashkir Meganticlinorium from the South Urals in Russia, using iron speciation and trace metal palaeoredox proxies. This is the first record of water column chemistry spanning the entire Mesoproterozoic Era from this basin. In Chapter 4, continued attention on water column chemistry delves further back in time to the Late Palaeoproterozoic-Mesoproterozoic succession from the North China Craton. With previously found evidence for macroscopic eukaryotes in this basin, P burial mechanisms are investigated using the newly developed P speciation method for ancient sediments. Chapter 5 moves forward in time to the Ediacaran Period during the Late Neoproterozoic, where a compilation of previously published redox interpretations are used alongside new phosphorus speciation results in five different basins, to assess if the P cycle endured significant changes as a result of metazoan evolution and/or ocean oxygenation. Proposals are then suggested for future studies based on the outcomes of this research.

Chapter 2 Materials and Methodology

2.1 Sample Collection and Preparation

The samples used in this study were collected and supplied by other academics before this research commenced (Table 2.1). All samples and their lithologies can be found in Appendix A. The location of all samples' sedimentary successions is illustrated in Figure 2.1. For outcrop samples, extreme care was taken to ensure the freshest samples were collected by removing weathered surfaces in the field. Sampling was also conducted away from mineral veins or igneous intrusions that would potentially alter primary geochemical signals.

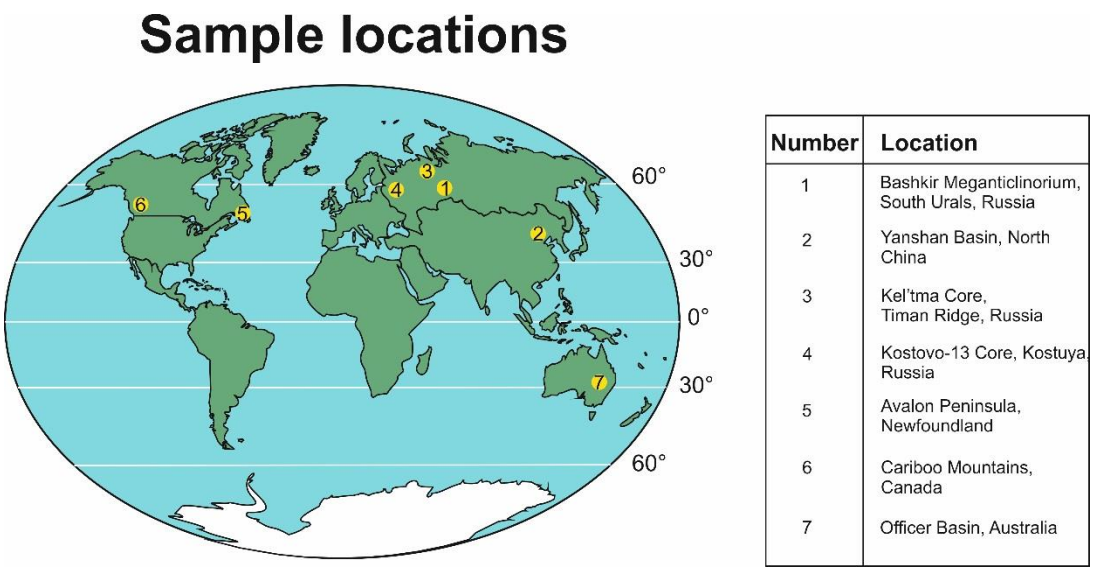

Number	Location
1	Bashkir Meganticlinorium, South Urals, Russia
2	Yanshan Basin, North China
3	Kel'tma Core, Timan Ridge, Russia
4	Kostovo-13 Core, Kostuya, Russia
5	Avalon Peninsula, Newfoundland
6	Cariboo Mountains, Canada
7	Officer Basin, Australia

Figure 2.1 Location of all sample used in this research

For all locations except the North China Craton, samples had already been crushed to a fine, homogenous powder. Shales and limestones from the China section were first cut using a saw with a water attachment to remove any fine-scale weathering surfaces. Samples were subsequently crushed using a disc mill to a size <63 µm and stored in plastic 50 ml centrifuge tubes. The compartments of the disc mill and mortar and pestle used to break up the samples were all cleaned with tap water and wiped with ethanol between each

individual sample. The workspace was also cleaned, with fresh paper put down on top to ensure no contamination between samples.

Table 2.1 Information regarding sample collection

Location	Source	Collected by	Crushed
North China Craton	Outcrop	Simon Poulton Graham Shields	No
Bashkirian Anticline, South Urals, Russia	Outcrop and core	Victor Podkovyrov	Yes
Kel'tma Core, Timan Ridge, North Russia	Core	Simon Poulton	Yes
Kostovo Core, St. Petersburg, Russia	Core	Romain Guilbaud	Yes
Avalon Peninsula, Newfoundland	Outcrop	Donald Canfield	Yes
Cariboo Mountains	Outcrop	Donald Canfield	Yes
Narana Formation, Officer Basin, Australia	Core (Munta-1)	Simon Poulton	Yes

2.2 Total Carbon, Total Organic Carbon and Total Inorganic Carbon

2.2.1 Total Carbon (TC)

TC was determined via combustion using a LECO C-S analyser. Approximately 0.3 g of dry sediment was weighed onto a ceramic boat and placed into the LECO C-S analyser. The LECO is kept at a constant 1350°C under a pure oxygen atmosphere. The instrument was first calibrated by six standards of known C content that are representative of the sediments being analysed. Replicate analyses of certified standards are shown in Table 2.2 for TC content.

Table 2.2 Statistics for certified standards used for TC analyses for North China and South Ural samples

Site	Reference Material	Certified Value (wt%)	Replicate	Recovery (%)	Average (wt%)	RDS (%)
North China	High C soil (502-814)	22.8 ± 0.3	10	95.3	21.7 ± 0.2	0.75
	$CaCO_3$ (501-034)	12	10	99.9	11.99 ± 0.09	0.76
South Urals	Low C soil (502-062)	1.99 ± 0.04	18	98	1.95 ± 0.07	3.39

2.2.2 Total Organic Carbon (TOC)

To measure the TOC fraction of sediments, the carbonate portion was first removed by acidifying the sediments (Ryba and Burgess, 2002). This was carried out by weighing approx. 0.5 g of sediment into a centrifuge tube, with the weight of each tube also recorded. Samples were subjected to two 10 ml 20% (v/v) HCl washes. For the first wash when the samples had ceased to effervesce, they were subsequently centrifuged and had the supernatant HCl decanted and put to waste. Another 10 ml of 20% HCl was added to the sediments, with the centrifuge tubes shaken to ensure sediment resuspension, and left on a shaker table at room temperature for 24 hours. After 24 hours, the samples were centrifuged and subjected to four Milli-Q washes to remove any remaining Cl, as it can interfere with the LECO machine. Four washes were necessary to remove traces of the acid and for the pH of the corresponding samples to be >4. The wet sediments in the centrifuge tubes were left to dry in an oven at 60°C. Once dry, the weight of the dry sediment and centrifuge tube was recorded. Approx. 0.3 g of the acid-washed sediment was measured on the LECO in the same method outlined in 2.2.1. To calculate the TOC wt% of each sample, the correction factor (CF) was first calculated by:

$$\mathrm{CF} = \frac{\text{Weight of sample after drying (g)}}{\text{Original weight of sample (g)}}$$

TOC wt% could then be calculated as:

$$\text{TOC wt\%} = \text{TC wt\%(from LECO)} \times \mathrm{CF}$$

Replicate analyses of the standard used for calibrations are shown in Table 2.3.

Table 2.3 Statistics for certified standards used for TOC analyses for North China and South Ural samples

Site	Reference Material	Certified Value (wt%)	Replicate	Recovery (%)	Average (wt%)	RDS (%)
North China	High C soil (502-814)	22.8 ± 0.3	17	98.9	22.5 ± 0.3	1.5
	$CaCO_3$ (501-034)	12	16	103.7	12.4 ± 0.2	1.5
South Urals	Low C soil (502-062)	1.99 ± 0.04	16	99.15	1.97 ± 0.03	1.27

2.2.3 Total Inorganic Carbon (TIC)

The TIC fraction of sediments can be used to categorize sedimentary rocks of unknown lithologies as carbonates or shales, based on their $CaCO_3$ content. This was carried out for the Bashkirian Anticline samples, as outcrop samples had already been crushed, thus not allowing identification through hand sample analysis. Samples with TIC > 6 wt% were classified as carbonates while those with TIC < 6 wt% were shales, as TC can reach a maximum of 12 wt% $CaCO_3$. TIC was calculated as the difference between the measured TC and TOC values.

2.3 Iron

2.3.1 Iron speciation

To quantitatively assess the palaeo-redox state of ancient sediments, iron speciation was the main proxy used in this research. This is a sequential extraction developed by Poulton and Canfield (2005) that targets biogeochemically reactive iron-bound phases within sediments. The targeted phases are: Fe_{CARB} e.g. siderite and ankerite; Fe_{OX} e.g. goethite, akaganeite, and hematite; Fe_{MAG}; and Fe_{PY}. Between 70 - 100 mg of sediment was first

weighed into a 15 ml centrifuge tube. A schematic of this extraction is illustrated in Figure 2.2.

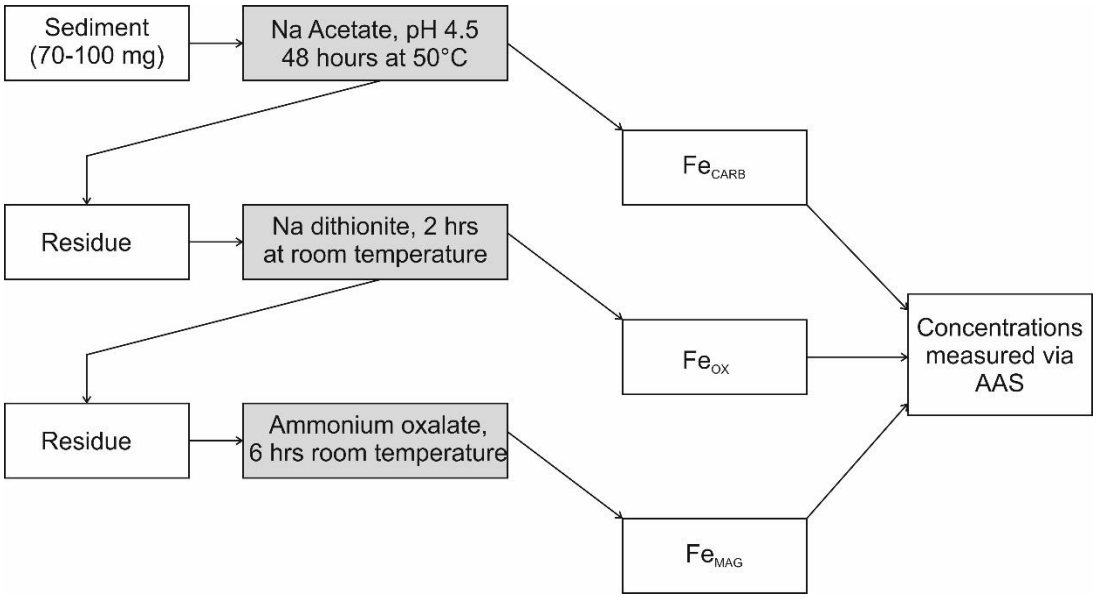

Figure 2.2 Flow chart illustrating the iron speciation method by Poulton and Canfield (2005). Reagents used during the extraction are highlighted in grey

For every step shown in Figure 2.2, 10 ml of the solution was pipetted into each sample tube. Regarding the Fe_{OX} stage, for each new batch of samples, fresh sodium dithionite solution was prepared, as its reactivity deteriorates in both aerobic and anaerobic environments once made (Housecroft and Sharpe, 2007).

During the extraction period, samples were kept agitated on a shaker table at 100 rpm. Once the extraction was complete, samples were centrifuged at 4000 rpm for four minutes to sufficiently separate the supernatant from the sediment. Of this solution, 8 ml was kept in a separate 15 ml tube for further analysis. The remaining solution was carefully decanted to waste without disturbing the sediment at the base of the centrifuge tube. All glassware used in this method had previously been acid washed (10% HCl) overnight and dried.

2.3.2 Analysis

All final concentrations of the iron speciation extractions were determined using an atomic absorption spectrometer (AAS) Analytik Jena, High Resolution Continuum Source Contr AA 700 Atomic unit. Solution concentrations were quantified spectroscopically, by aspirating a solution to an air-acetylene flame at 2300˚C. The gas was excited to an atomic absorption line of a known element i.e. iron, where the concentration of the known element was quantified by the difference in absorbance between the sample and a blank. The

instrument was calibrated at the beginning of each new solution by measuring standards of known concentration. For each solution analysed (sodium acetate, CDA, ammonium oxalate), the standards of the calibration line were 0, 1, 3, 5, 7 and 10 ppm Fe. A 0 ppm and 5 ppm Fe standard were measured after every 10 samples to ensure the machine did not drift in its precision of measurements. Each iron pool from iron speciation was run at a 20 x dilution. If the sample concentration was greater than 10 ppm, a further dilution of the sample was required. The wt% of each iron pool was calculated from the diluted concentration from the AAS as:

$$\mathrm{Fe\ (wt\%)} = \frac{\frac{[\text{Diluted conc (ppm)} \times \text{dilution factor}] \times \text{vol (L)}}{1000}}{\text{original sample weight (g)}} \times 100$$

RSD values for each step in the sequential extraction are given in Table 2.4 for samples from the South Urals and North China Craton.

Table 2.4 RSD values for new iron speciation data from the South Urals and North China Craton

Sample Locality	Sample Number	Fe phase	Replicates	Average (wt%)	RSD (%)
South Urals	746-13	Fe_{CARB}	5	0.31±0.004	1.4
		Fe_{OX}		0.24±0.004	1.7
		Fe_{MAG}		0.41±0.01	3.3
	746-12	Fe_{PY}	3	0.023±0.01	0.41
	746-13	Fe_{PRS}		3.09±0.25	8.1
		Fe_{T}	4	3.52±0.05	1.45
North China	ADS-37 (shale)	Fe_{CARB}	3	0.19±0.1	5.26
		Fe_{OX}		0.32±0.002	0.74
		Fe_{MAG}		0.05±0.002	3.47
		Fe_{PY}		0.02±0.001	5.68
		Fe_{PRS}		0.49±0.03	6.01
		Fe_{T}		1.98±0.02	0.86

2.3.3 Iron pyrite

2.3.4 Extraction

Though listed as an iron phase in the sequential extraction, Fe_{PY} is determined stoichiometrically by weight from an Ag_2S precipitate formed after a HCl and chromous chloride distillation (Canfield et al., 1986). Both pyrite (FeS_2) and acid volatile sulphides (AVS, FeS) are measured in this step. The required weight used depended on the lithology of the sample. Approx. 1 g of sediment was used for shales, while up to 7 g was used for carbonates. The sample was weighed into a reaction vessel and attached to the condensing column as illustrated in Figure 2.3.

Chromous chloride (533 g/L chromic chloride dissolved in 50% HCl) was the main reagent used. Before use in the extraction, the solution was added to a schott bottle containing a 2 – 3 cm layer of zinc shot pellets at the base. As shown in Figure 2.3B, a nitrogen (N_2) line was attached to the bottle and was purged through the solution for approx. 1 hour to ensure the solution was anoxic. A sufficient level of water was kept in the oxygen trap attached to the top of the schott bottle to allow bubbles of N_2 to escape without allowing oxygen into the system. If chromous chloride had been previously prepared and stored overnight in a fridge in 50 ml syringes, the chromous chloride was pumped back into the schott bottle through tap A and purged for 30 minutes.

The next step was setting up the sulfide trap (Figure 2.3A). This was prepared by pipetting 500 μL of silver nitrate ($AgNO_3$) into the required number of test tubes with two thirds of the test tube volume consisting of Milli-Q. A pasteur pipette submerged in the sulfide trap was used as a means of connecting the condensing column N_2 line to the test tube. Once all pasteur pipettes were connected to the N_2 line, a sufficient amount of gas was pumped through to ensure a steady stream of bubbles.

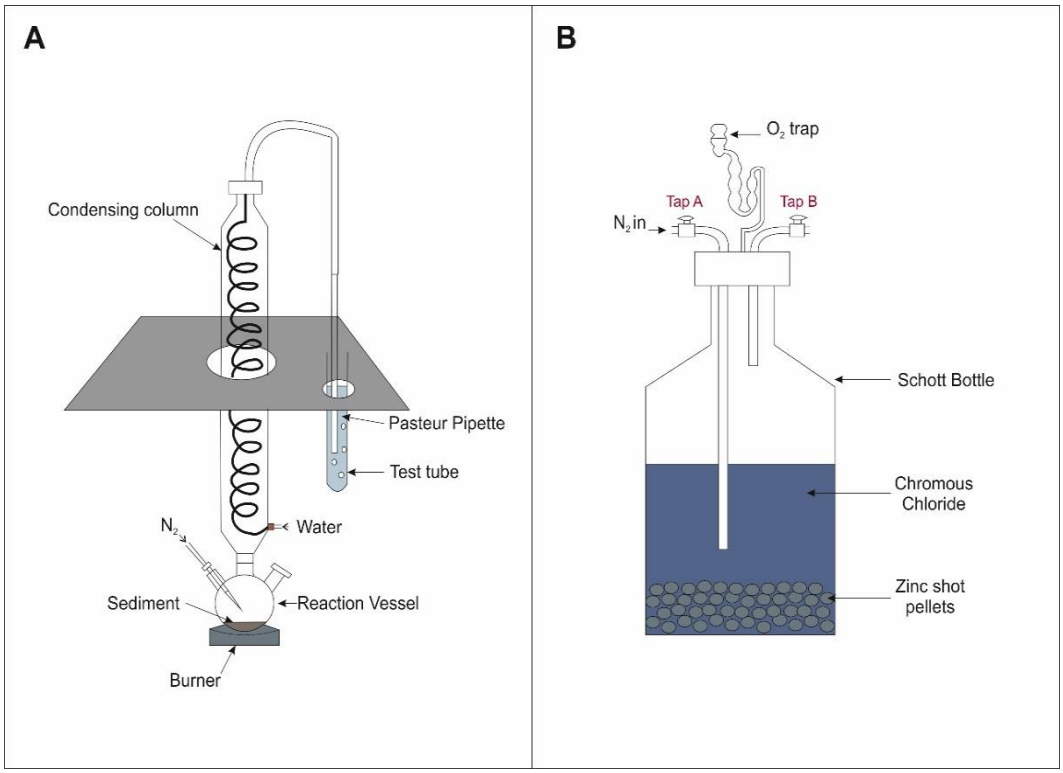

Figure 2.3 Schematic of the experimental setup for pyrite extractions

Each sample was first tested for AVS by adding 8 ml of 50% HCl (v/v) to the reaction vessel, with the stopper immediately put back into place. The solution was brought to the boil and then monitored to see whether any AVS was released and trapped as Ag_2S. The reaction time given for this step was 10 minutes. If the $AgNO_3$ solution turned brown with a black precipitate forming, the reaction was left for 45 minutes to collect AVS. A new trap was then created for pyrite collection. If the trap remained clear, ~16 ml of chromous chloride was added to each reaction vessel. Prior to this, the tap (Tap A; Figure 2.3B) between the nitrogen line and the chromous chloride was closed. A 50 ml syringe was connected to Tap A to extract the chromous chloride. On addition of the chromous chloride to the sediment, each vessel was swirled to ensure all sample was mixed into the acid, and the solution was brought to the boil. As the sulfide trap began to turn brown, 500 µl aliquots were added quickly until the trap became transparent. The traps were monitored closely to ensure they did not become saturated with the Ag_2S precipitate. The reaction was left for one hour in total. After one hour, the sulfide traps were collected and detached from the condensing columns.

2.3.4.1 Filtering

To measure the weight of the Ag_2S precipitate, the contents of the sulfide trap were filtered using a vacuum filtration kit (Figure 2.4). The boat and cellulose nitrate filters were first weighed before filtering. The pasteur pipette was rinsed with Milli-Q to ensure any precipitate caught in the pipette was removed. The remainder of the solution in the test tube was tipped into the filter funnel, and rinsed with Milli-Q. Once all the solution was drained from the funnel, the clamp was released, and the filter for each sample was carefully lifted off using a tweezers into its designated boat. The filter papers and boats were left to dry in an oven at 50˚C. Once dry they were reweighed, and the weight of the Ag_2S precipitate was calculated as the difference between the new and original weight of the boat and filter. The filter and precipitate was transferred to a glass vial and stored for later analysis. The following formula shows the calculation used for Fe_{PY} (wt%):

$$\mathrm{Fe_{PY}\ (wt\%)} = \mathrm{nFe} * \frac{\mathrm{Molecular\ Mass\ Fe}}{\mathrm{Original\ Sample\ Weight(g)}} * 100$$

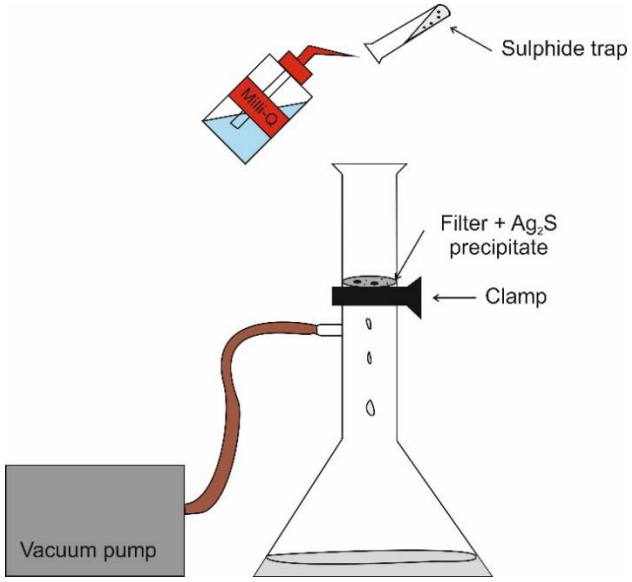

Figure 2.4 Filtering setup following pyrite extraction

2.3.5 Poorly reactive sheet silicate iron (Fe_{PRS})

A one minute boiling HCl extraction (Raiswell et al., 1994) was used to measure the concentration of Fe_{PRS} in sediments. A maximum of 60 mg of sediment was weighed into an acid washed test tube. Using a dispenser pipette, 5 ml of 12 M HCl was added to a single test tube. The sample was first brought to the boil over a Bunsen burner for 1 minute to remove the carbonate fraction of the sediment and prevent any loss of sample by effervescence. The sample was subsequently boiled vigorously for a further minute. Following

boiling, samples were immediately quenched with approximately 10 ml of Milli-Q before being transferred to 100 ml volumetric flasks, ensuring all sediment from the test tube was washed into the flask. The funnel used was rinsed with Milli-Q in between each sample. The flasks were made up to volume with Milli-Q and inverted slowly 12 times to ensure proper mixing. The sediment was left to settle to the bottom of the flask for ~3 hours. Next, 2 ml of the solution was pipetted from the top of the flask and transferred to a 15 ml centrifuge tube containing 8 ml of water. The samples were then measured on the AAS. RSD values for Fe_{PRS} are shown in Table 2.4, and are slightly higher than the RSD of the original method (5%; Raiswell et al., 1994). Errors from Fe_{PRS} also include those of Fe_{CARB}, Fe_{OX} and Fe_{MAG}, as this value is based on the accuracy of the iron sequential extraction as well as the boiling HCl method. The final solution at the end of this extraction represents the pool of Fe_{HCl}. Fe_{PRS} can thus be calculated as:

$$\mathrm{Fe_{PRS}} = \mathrm{Fe_{HCl}} - (\mathrm{Fe_{CARB}} + \mathrm{Fe_{OX}} + \mathrm{Fe_{MAG}})$$

with Fe_{CARB}, Fe_{OX} and Fe_{MAG} determined from iron speciation in 2.3.1.

2.4 Bulk Rock Digestion

2.4.1 Major elements (Fe, Al, Mn, P)

To determine the total wt% of the elements Fe, Al, Mn and P, a bulk rock digestion was performed. Prior to the digestion, ~50 – 80 mg of sediment was weighed into porcelain crucibles and ashed overnight at 550˚C. With every batch of 50 samples, one blank, one standard and a triplicate of one sample was also included. Once the crucibles were sufficiently cool, the ashed samples were transferred to acid washed teflon beakers by rinsing the crucible with 5 x 1 ml concentrated HNO_3 acid using a dispenser pipette, ensuring all sediment had been transferred. Next, 2 ml of concentrated (40%) hydrofluoric (HF) acid and 2 – 3 drops of concentrated $HClO_4$ acid were added to each beaker on a hotplate at 70˚C, and left to dry overnight. Once dry, the HF in the samples was neutralised using a 2 ml solution of a 50g/L boric acid (H_3BO_3), and again left to dry overnight on the hotplate at 70˚C.

Samples were brought back into solution through the addition of 5 x 1 ml 50% HCl using a dispenser pipette and placed on a low heat on a hotplate. Care was taken to wash down the sides of each of the teflon beakers to ensure all of the sample was brought back to solution. Once the samples had

dissolved, they were transferred to 100 ml volumetric flasks with Milli-Q. Each teflon pot was rinsed five times with Milli-Q to ensure complete transfer of the sample. The funnel was also rinsed in between each sample to prevent cross contamination between samples. Once the flasks were made up to volume, they were inverted and rotated 12 times to ensure sufficient mixing. For later analysis, ~15 ml of the solution was stored in a centrifuge tube.

Fe, Mn, P and Al concentrations were determined using a Thermo Fisher iCAP 7400 Radial Inductively Coupled Plasma Optical Emission Spectrometry (ICP-OES). The ICP-OES works on a similar method to that of the AAS. A flame of argon gas in this instance, excites atoms/ions aspirated from a solution to a known elemental wavelength, with the intensity of the emission resulting in the concentration of an element. Solutions were run with a Y internal standard to ensure the machine did not drift during the analysis. All RSD values and percentage recoveries for the reference materials used in these digests are shown in Table 2.5. Reference materials were chosen based on Fe and P content, and their relativity to the samples analysed in this research. The supply of reference material PACS-2 was exhausted during the early stages of this research, with manufacturing also discontinued. A high RSD of 21% from replicate analysis of the PACS-2 reference material resulted. However, replicate analysis of a sample chosen from the South Urals succession gave an RSD of 7.55%. Uranium recovery was also low from this material (67%), but in a similar manner, had a low RSD value from replicate analyses of a sediment sample. This potentially concludes that PACS-2 was an unsuitable reference material for Mo and U content. It was therefore only used for the samples first analysed. Two new reference materials (SBC-1 and SGR-1) were introduced based on their applicability to the sediments researched here, as they both contained appreciable levels of Fe and P. Replicate analyses of samples for each locality were also analysed during the digestions. Their associated RSD values are shown in Table 2.6. The limit of detection (LOD), limit of quantification (LOQ), and percentage uncertainty on each measurement is shown in Table 2.7. Errors given for the Cariboo Mountain samples also apply to those from the Narana Formation as they were all analysed within the same batch. As the recovery for these units were generally low, checks were conducted against other authors' data if available to ensure the values determined in this research were appropriate to use.

Table 2.5 RSD and recovery values of all elements using standard referencing materials

Locality	Element	Replicates	RSD (%)	Reference Material	Recovery (%)
North China Craton	Fe	3	0.86	SBC-1	90.4
	Al		0.7		102
	Mn		3.04		98.3
	P		2.26		104
	Mo		15.4		87
	V		18.4		93.4
	U		14		85.9
	Cr		16.4		92.2
South Urals	Fe	6	2.4	PACS-2	96
	Al		2.0		101.9
	Mn		1.4		96.4
	Mo	3	21		87.9
	V		4		93.1
	U		2		67.1
Kel'tma Core	Fe	6	4.3	SBC-1	99
	Al	6	6.6		93.7
	P	6	3.1		98.4
Avalon Peninsula	Fe	5	2.16	SGR-1	92.8
	Al	5	2.35		102
	P	5	2.95		87.5
Cariboo Mountains	Fe	6	1.88	SGR-1	84
	Al	6	1.62		82
	P	6	3.36		75
Narana Formation, Australia	Fe			SGR-1	85
	Al				83
	P				75.5

Table 2.6 RSD values for replicate analyses of all elements measured from sediment samples chosen from each locality

Locality	Element	Sample Number	Replicates	Average (wt%)	RSD (%)
North China Craton	Fe	ADS-37 (shale)	3	2.1±0.01	0.5
	Al			9.9±0.07	0.7
	Mn			0.006±0002	3.04
	P			0.03±0.0006	2.3
	Mo			<LOD	
	V			0.01±0.0004	3.7
	U			0.28±0.05	17.8
	Cr			0.009±0.0002	1.83
South Urals	Fe	746-13 (shale)	4	3.71±0.05	1.22
	Al			11.06±0.22	1.95
	Mn			0.01±0.0001	1.39
	Mo		3	1.8E-5±1.4E-6	7.55
	U			0.0002±4.2E-6	2.3
Kel'tma Core	Fe	K-1 (shale)	6	4.26±0.23	4.3
	Al		6	7.66±0.57	6.6
	P		6	0.08±0.002	3.1
Avalon Peninsula	Fe	DEC-05-103 (mudstone)	5	5.79±0.12	2.03
	Al		5	10.34±0.24	2.35
	P		5	0.034±0.001	2.95
Cariboo Mountains	Fe	DEC-04-56 (siltstone)	6	4.81±0.09	1.88
	Al		6	5.05±0.08	1.62
	P		6	0.01±0.0003	3.36

Table 2.7 LOD, LOQ and percentage uncertainty for major element analyses on the ICP-OES

	Fe ppb	**Al ppb**	**Mn ppb**	**P ppb**
LOD	82	86	2.13	15.1
LOQ	272	286	7.09	50.3
% uncertainty	0.83	2.81	0.691	1.22

2.4.2 Trace Metals (Mo, V, U, Cr)

The same method outlined in 2.4.1 was used for the extraction of trace metals from bulk rock samples. Mo, V, U and Cr concentrations were measured using a Thermo Fisher iCAPQc Inductively Coupled Plasa Mass Spectrometer (ICP-MS). This works by ionizing an aspirated solution and separating these ions based on their mass-to-charge ratio. The intensity of the ratio is then converted to a concentration signal. Samples analysed on the ICP-MS had a Rh internal standard added for internal calibrations. The RSD and recovery percentages for the trace metals from reference materials are given in Table 2.5, and from replicate analyses of sediment samples in Table 2.6.The limit of detection (LOD), limit of quantification (LOQ) and percentage uncertainty on each measurement is shown in Table 2.8.

Table 2.8 LOD, LOQ and percentage uncertainty on trace metal measurements on the ICP-MS

	Mo ppb	**V ppb**	**U ppb**	**Cr ppb**
LOD	0.242	0.424	0.033	0.559
LOQ	0.806	1.41	0.109	1.86
% uncertainty	0.516	0.711	0.347	0.591

2.4.3 Digestion Calculations

The concentration (ppm) of the total elements in each sample was calculated as:

$$\text{Concentration sample (ppm)} = \frac{\text{ICP Concentration (ppm)}}{\text{Sample weight (g)}} \times \text{Volume (ml)}$$

The ICP concentration is the number taken from ICP analysis. The volume is the total volume the digests were brought up to i.e. 100 ml in volumetric flasks. The final wt% of the sample was then determined as:

$$\text{Total (wt\%)} = \frac{\text{ICP conc. (ppm)} \times 10^{-6} \times \text{volume (ml)}}{\text{Sample weight (g)}} \times 100$$

2.5 Phosphorus Speciation

2.5.1 Method

The P speciation sequential extraction (SEDEX) was first developed by Ruttenberg (1992) to separately measure the five main sedimentary reservoirs of P in modern marine sediments: loosely sorbed P; ferric iron-bound P; authigenic carbonate fluorapatite (CFA), biogenic apatite and $CaCO_3$-associated P (P_{auth}); detrital P (P_{det}); and organic P (P_{org}). This technique has been successfully applied to a wide variety of modern sediments but has been found to be unsuitable for ancient studies due to the increased crystallinity of ancient sedimentary rocks affected by burial diagenesis (Shemesh, 1990), and not targeting “reactive phases” important in ancient rocks such as iron (oxyhydr)oxides e.g. hematite and magnetite (Canfield et al., 2008). A new technique (Thompson et al., *in prep*) incorporating iron speciation (Poulton and Canfield, 2005) with the original SEDEX method addresses these issues. The pH of the P_{auth} reagent is lowered to target the crystalline authigenic phases, and the introduction of steps from the iron speciation method now separates Fe-bound P (P_{Fe1}), crystalline Fe-bound P (P_{Fe2}), and magnetite-bound P (P_{mag}), allowing a better insight into Fe-P systematics in ancient environments.

The steps involved in the method undertaken are illustrated in Figure 2.5. Samples were first measured into 15 ml centrifuge tubes at weights of 0.15 – 0.19 g. All glassware used in the P speciation method was first acid-washed (10% HCl) for 24 hours and subsequently base-washed (1 M NaOH) overnight. The glassware was rinsed five times with deionised water in between each step and left to dry before use.

The reagents CDA and CDB involve the use of dithionite, and thus were always prepared on the day of use due to the oxidative behaviour of this solution (Housecroft and Sharpe, 2007). For each step, the appropriate volume of the solution was pipetted onto the sediment in the centrifuge tubes. Their lids

were replaced, and the tube was shaken vigorously to ensure sediment resuspension between each step. Samples were kept agitated on a shaker table at room temperature for the designated length of the extractions. Once complete, the samples were centrifuged at 4000 rpm for 4 minutes. Without disturbing the sediment at the base of the centrifuge tube, 8 ml of the supernatant was subsampled for later use with the remaining solution decanted to waste. Washes are conducted following the P_{Fe1}, $P_{auth,}$ P_{mag}, and P_{Fe2} stages to ensure all P targeted in that step is extracted and determined. A single $MgCl_2$ wash is performed following the P_{Fe1}, P_{mag}, and P_{Fe2} steps. After the P_{auth} stage, a $MgCl_2$ wash is conducted and if the absorbance of non-diluted samples on the spectrophotometer (discussed in 2.5.2) is higher than 0.1, another $MgCl_2$ wash followed by a Milli-Q wash is carried out.

The final P pool in the sequential extraction is P_{org}. Following the $MgCl_2$ wash after the CDA extraction, samples were transferred from the centrifuge tubes to porcelain crucibles using 4 – 6 ml of Milli-Q. The samples were dried in an oven at 100˚C, and subsequently ashed at 550˚C for 2 hours. Once cool, sample was gently scraped from the walls of each crucible with a spatula, to ensure all the sample could be transferred back to the centrifuge tubes. The spatula was cleaned with a new kimtech wipe between each sample. Any remaining sample was washed into the tube using 5 x 2 ml of 10% HCl solution. As this was a lengthy step, the time the first addition of the 10% HCl and the time when the samples were placed on a shaking table was noted. The middle point of these two times was taken as the beginning of the extraction time. Samples were shaken at 100 rpm for 16 hours at room temperature. Once complete, the samples were centrifuged and analysed in the same method as outlined for P_{det} in 2.5.2.1.

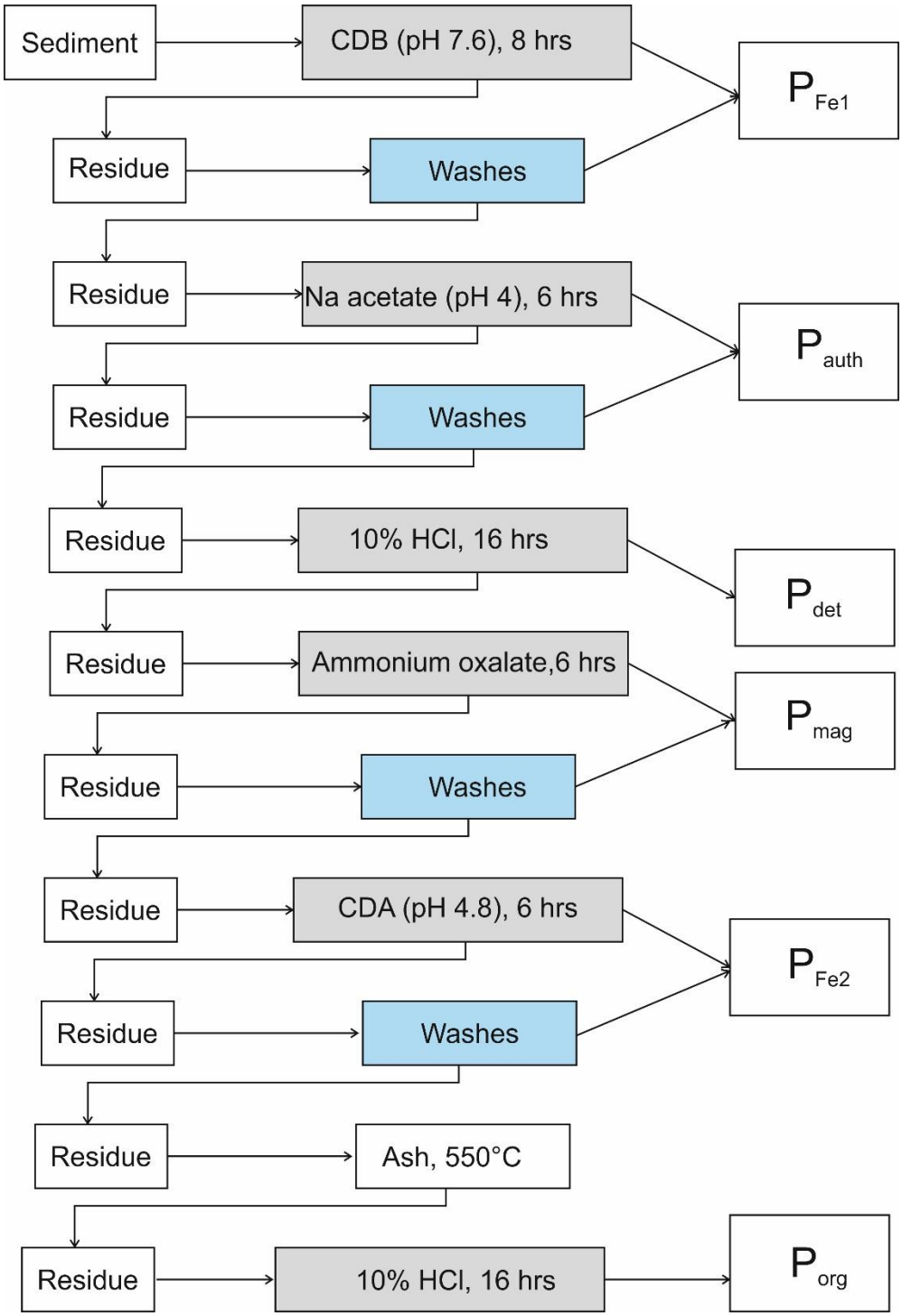

Figure 2.5 Flow chart depicting all steps involved in the modified P speciation sequential extraction by Thompson et al (*in prep*). Reagents used are highlighted in grey, while all washes ($MgCl_2$ or Milli-Q) are shown in blue

2.5.2 Analysis

2.5.2.1 Spectrophotometer

Stated in 2.5.1 are the several phases of the extraction measured on a spectrophotometer. The molybdate blue method (Strickland and Parsons,

1972; Ruttenberg, 1992) was used to measure both inorganic and organic-bound P in this research. The molybdate blue solution was prepared through the addition of 45 ml 10% H_2SO_4, 31 ml antimony potassium tartrate solution, and 62 ml ammonium molybdate tetrahydrate solution per 250 ml in a volumetric flask. The flask was made up to volume with Milli-Q. Molybdate blue was utilized as upon reduction in acidic conditions, it produces a blue coloured complex, phosphomolybdate, which can subsequently be measured at a known wavelength (880 nm) on the spectrophotometer. Problems have been encountered using molybdate blue to measure P, as molybdate reacts with other ions in the solution, such as silica or germanium, and can also form acid-labile organic compounds, that would both ultimately cause errors in the concentration of dissolved inorganic P (Benitez-Nelson, 2000). Modifications to the method through the introduction of new reagents and decreasing the contact period between the acids has been shown to overcome these issues (Benitez-Nelson, 2000). The $MgCl_2$ washes do not require such additions. Prior to measuring $P_{auth,}$ P_{det} and P_{org} absorbances, a range of aliquots of acid was tested on standards of known concentrations (0 ppm and 1 ppm) at 15 minutes and 30 minutes, to ensure the pH and absorbance of the sample remains stable over this time period. The aliquot volume which showed the least amount of change between these intervals was chosen. For these P phases, the acids and the potential range of volumes added to each sample are shown in Table 2.9. If the sample required a dilution i.e. the absorbance of the sample on the spectrophotometer > 0.8, the volume of acid added also changed.

To measure samples on the spectrophotometer, 1 ml of sample supernatant following an extraction was pipetted into a microtube. Sample volume was always 1 ml. Any further dilutions would also be at 1 ml e.g. five times dilution = 200 µl sample supernatant: 800 µl Milli-Q. The amount of molybdate blue reagent was also always kept at 200 µl, regardless of any further dilutions. On the addition of molybdate blue to the first sample, a timer was started. After 15 minutes, the blue colour complex had sufficiently formed for samples to be measured on the spectrophotometer. Each sample was transferred into a new 2 ml cuvette and checked for any bubbles that would interfere with measurements. A range of standards of known concentration, 0 – 1 ppm for a no dilution run, were first measured to generate a calibration line that would later be used to calculate sample concentration (ppm) from the absorbance given by the spectrophotometer. The calculation of the sample concentration is discussed later in 2.5.3. All calibration results are given in Table 2.10. The same calibration lines were used for the Kostovo core, Avalon Peninsula, Cariboo Mountain and Narana Formation units as all of these

samples were run as multiple batches at the same time. If further dilutions were needed for any samples, this procedure would be repeated until a value less than 0.8 on the spectrophotometer was given.

The relative errors and RSD values from the replicate analysis of sediment samples during P speciation are shown in Table 2.11. The errors from the Kostovo core also include those for the Avalon Peninsula, and those for the Cariboo Mountains similarly include the errors for the Narana Formation as they were run at the same time. Large errors are found for the Fe phases measured during the extraction. This is a result of the extremely low values of these respective phases, with slight deviations in the results generating large errors. The low RSD values for the larger pools (P_{auth}, P_{det}) gives confidence in the results generated during the sequential extraction. As this is a new method, no reference material could be used to ensure these results were accurate.

Table 2.9 List of acids added to molybdate blue method to keep pH constant during analysis

Phase	Acid added	Dilution Factor	Aliquot Range
P_{auth}	50% H_2SO_4	0	50 – 75 µl
		5	10 – 20 µl
P_{det}	5 M NaOH	0	210 – 250 µl
&		5	35 – 55 µl
P_{org}		20	10 – 20 µl

Table 2.10 Calibration values for all localities

Site	Reagent	Dilution	Gradient	R^2
North China Craton	$MgCl_2$	0	0.5479	0.992
	Milli-Q	0	0.6555	0.99
	Sodium Acetate	0	0.6035	0.992
	10% HCl	5	0.1183	0.992
Kel'tma Core	$MgCl_2$	0	0.5117	0.992
		5	0.1262	0.999
		20	0.0319	0.999
	Milli-Q	0	0.4508	0.99
	Sodium Acetate	0	0.6422	0.988
		5	0.1333	0.987
	1M HCl	0	0.4905	0.995
		5	0.1273	0.998
		20	0.035	0.986
Kostovo Core Avalon Peninsula Cariboo Mountains Narana Formation	$MgCl_2$	0	0.5117	0.994
	Milli-Q	0	0.4508	0.991
	Sodium Acetate	0	0.6422	0.988
	1 M HCl	0	0.4905	0.995
		5	0.1293	0.999
		20	0.035	0.986

Table 2.11 Relative errors and RSD values for replicate analysis of sediment samples from different locations

Site	Sample	P phase	Replicates	Average (wt%)	RSD (%)
North China	ADS-17 (shale)	P_{Fe1}	5	2.8E-5±5.8E-6	20.4
		P_{auth}		0.005±0.0002	3.5
		P_{det}		0.009±0.002	2.16
		P_{mag}		0.001±5.8E-5	6.3
		P_{Fe2}		1.25E-5±6E-6	47.6
		P_{org}		0.009±0.0007	7.46
Kel'tma Core	K-132 (marl)	P_{Fe1}	5	4.6E-5±6.1E-6	13.1
		P_{auth}		0.002±0.0002	7.8
		P_{det}		0.03±0.002	4.7
		P_{mag}		7.6E-5±1.3E-5	17.7
		P_{Fe2}		<LOD	
		P_{org}		0.005±0.001	26.2
Kostovo-13 Core	KS-96 (Siltstone)	P_{Fe1}	5	2.1E-5±1.4E-5	53.9
		P_{auth}		0.003±0.0002	6.2
		P_{det}		0.005±7.3E-5	1.38
		P_{mag}		0.0005±0.0004	72.5
		P_{Fe2}		8.3E-5±6.4E-5	77.3
		P_{org}		0.004±0.0001	3.1
Cariboo Mountains	DEC-04-163 (Siltstone)	P_{Fe1}	3	1.7E-5±6.5E-6	37.9
		P_{auth}		0.002±0.0001	4.3
		P_{det}		0.033±0.001	2.4
		P_{mag}		0.001±0.0001	11.6
		P_{Fe2}		6.2E-6±2.3E-6	37.3
		P_{org}		0.001±0.0002	34.3

2.5.2.2 ICP-OES

As discussed in 2.5.1, the newly introduced phases to the method, P_{Fe}, P_{mag} and P_{Fe2}, are measured using an ICP-OES. A Co internal standard (100 µl) is added to 4.9 ml of each sample for an internal calibration. During analysis on the ICP-OES, it was found that a residue can build up inside the nebulizer as a result of the acidic solutions used in the extraction. To counteract this, an argon humidifier was attached to the nebulizer. Before analysis, the best flow path of the sample through the nebulizer was determined using a 2 ppm zinc solution. The following calibration was performed before each new analysis: 0, 0.5 ppm, 1 ppm, 2 ppm, 5 ppm P. A quality check (QC) of 0 and 2 ppm P was run every 10 samples to ensure the machine was not drifting throughout the analysis. Standards used for the calibration were prepared using a different standard solution to the QC for a more accurate test of instrument drifting. The LOD, LOQ and percentage uncertainty on measurements are shown in Table 2.8.

2.5.3 Calculations

From the absorbance results using the spectrophotometer, the concentration (ppm) of P can be determined as:

$$\text{ppm} = \frac{\text{Absorbance}}{\text{Slope of calibration}} \times \text{Dilution factor}$$

The slope of the calibration line measured at the beginning of the analysis, and given in

Table 2.10, is used in the above equation. The weight (g) of P for each phase, determined from the concentration (ppm) from the spectrophotometer or ICP-OES, is calculated as:

$$\mathrm{P\ (g)} = \frac{\mathrm{Concentration\ (ppm)}}{1000} \times \mathrm{Volume\ (L)}$$

The volume in this equation is the amount of solution added to each extraction step. The wt% of each P phase can then be determined by:

$$\mathrm{P\ (wt\%)} = \frac{\mathrm{P\ (g)}}{\mathrm{Original\ sample\ weight\ (g)}} \times 100$$

The total weight (g) or wt% of each phase was finally calculated as the sum of the result from the extraction plus any following washes ($MgCl_2$/Milli-Q).

2.6 Sulfur Isotopes ($\delta^{34}S_{py}$)

Following the iron pyrite extraction outlined in 2.3.3, the Ag_2S precipitate was used to measure $\delta^{34}S_{py}$. Before samples were weighed, the workspace, microbalance and tools were cleaned with ethanol. All tools used were similarly cleaned in between weighing of each new sample. For each sample, 0.1 – 0.18 mg was weighed into 8 x 5 sized tin cups. Typically, each sample was run in duplicate, but if sufficient sample was available, four replicates were weighed out. If insufficient Ag_2S precipitate formed in order to directly weigh into the tin cups, the filter paper was cut up into a sufficient size to fit into the cups. Samples were then measured using a GV Isoprime mass spectrometer coupled to an Elementar Pyrocube. Combustion took place at 1150°C using pure oxygen (N5.0) injected into a stream of CP grade helium. Excess oxygen was removed by reaction with copper wires held at 850°C and water was removed using Sicapent reagent. SO_2 was separated from other gases via a temperature-controlled adsorption-desorption column. The $\delta^{34}S$ of the sample was derived from the integrated mass 64 and 66 signals when compared to an independently introduced pulse of SO_2 reference gas (N3.0). This value was calibrated to the international VCDT scale using the lab standard SWS-3A (BaSO4; assigned δ34S = +20.3‰) and the inter-lab standard CP-1 (chalcopyrite; assigned δ34S = -4.56‰). The assigned value for SWS-3A was produced by calibrating it against the following international standards (assigned values vs. VCDT in brackets): NBS-127 (+20.3‰), NBS-123 (+17.01‰), IAEA S-1 (-0.30‰) and IAEA S-3 (-32.06‰). Standards were

analysed in triplicate and samples in duplicate. Repeat analysis (n=28) of the standard $BaSO_4$ produced an average of 15 ± 0.53‰, with a recovery of 74%.

2.7 Organic Carbon Isotopes ($\delta^{13}C_{org}$)

Sample preparation for the measurement of $\delta^{13}C_{org}$ is the same acid washing procedure as outlined in 0. Once the samples were dry following acid washing, the sediment was ground up into a fine powder before measuring for this procedure. The required weight of C measured out for each sample was calculated so that 0.035 – 0.067 mg organic C was analysed. No more than 30 mg of sample was weighed out if the sample was particularly low in TOC due to instrumental limitations. At the beginning of each batch to calibrate the machine, triplicates of three international standards were weighed: Urea (0.15 – 0.4 mg; -46.83‰); T+L Sucrose (0.08 - 0.16 mg; -11.93‰); and Silverspoon Sucrose (0.08 – 0.16 mg; -26.19 ± 0.1‰). All sediment samples were run in duplicates, with each standard similarly run in duplicate for every eight samples. All utensils were cleaned with ethanol between measurements of each sample.

Samples were measured using a GV Isoprime mass spectrometer coupled to an Elementar Pyrocube, similarly to sulfur isotopes. In the presence of pure oxygen (N5.0) injected into a stream of helium (CP grade), samples were combusted to CO_2 at 1150˚C by passing the gases through tungstic oxide. Excess water was removed using a Sicapent trap, while oxygen was removed via reaction with hot copper wires at 850˚C. $\delta^{13}C_{org}$ values were determined from the integrated mass of 44, 45 and 46 signals from the sample CO_2 produced during combustion compared to that of a CO_2 reference gas (CP grade). The North China Craton sedimentary succession is the only location where $\delta^{13}C_{org}$ was measured. Replicate analyses (*n*=11) of the standard Silverspoon ($\delta^{13}C_{org}$ = -26.19 ± 0.1‰) gave an average of -26.51 ± 0.14‰, with an RSD of -0.53%.

2.8 Assessment of pyrite preservation with optical microscopy and SEM

Pyrite morphology was targeted in this study as a means to assess the degree of secondary weathering which can alter the primary geochemical signal of

sedimentary rocks. Pyrite was chosen for mineral analysis as its form is affected by levels of oxidation, whereby a coating of iron (oxyhydr)oxides can surround the pyrite grain or completely replace the mineral if sufficient levels of oxygen are encountered (Williamson and Rimstidt, 1994; Huminicki and Rimstidt, 2009; Gartman and Luther, 2014).

Prior to analysis, bulk rock samples were cut on a water lubricated saw perpendicular to bedding into blocks. Each block was set in epothin resin on a thin section glass slide at room temperature and left overnight to dry. Once the samples were set, one face of the block was ground down and polished to 30 µm thick before being sealed with another glass slide. Thin sections were carbon coated before viewing on the Scanning Electron Microscopy (SEM) to avoid charging the non-conductive rock samples. Samples were first mounted into the SEM (Tescan VEGA3 XM model), with analysis beginning once a vacuum had been created. The brightness and contrast of the SEM was set so only accessory and Fe-S bearing minerals were visible, allowing a scan to be conducted across the thin section using backscattered imaging and EDX elemental mapping (Aztec software). Where pyrite was identified, a backscattered image of the grain and EDX spectra were recorded. Only samples from the South Urals were analysed on the SEM due to availability of hand samples to produce thin sections. All SEM analysis was conducted at the Lemas facility at the University of Leeds

Chapter 3 Shallow water anoxia in the Mesoproterozoic ocean: Evidence from the Bashkir Meganticlinorium, Southern Urals

3.1 Introduction

The mid-Proterozoic (~1.8 – 1.0 Ga) is generally considered an interval of relative environmental and biological stasis. However this assertion may, at least in part, be a consequence of highly limited temporal and spatial geochemical records across this vast expanse of time. Canfield (1998) initiated a renewed focus on the evolution of mid-Proterozoic ocean chemistry by proposing that the disappearance of BIFs at ~1.85 Ga was due to the development of widespread sulfidic (euxinic) oceanic conditions, rather than the previously envisaged oxygenation of the deep ocean (e.g. Cloud, 1972; Holland, 1984). The increased potential for euxinia is linked to the first appreciable rise of atmospheric oxygen (the GOE) at ~2.43 – 2.06 Ga (Holland, 2002), as oxidative weathering of terrestrial sulfide-bearing minerals increased the flux of sulfate to the marine realm. Further investigations have revealed the limited spatial extent of euxinia, confining such conditions to productive continental margins and some intracratonic seas (Shen et al., 2002; 2003; Poulton et al., 2004; Gilleaudeau and Kah, 2013; Beghin et al., 2017), while deeper waters likely remained iron-rich (ferruginous) (Poulton et al., 2010; Poulton and Canfield, 2011; Reinhard et al., 2013; Guilbaud et al., 2015; Cox, Jarrett, et al., 2016) or possibly suboxic at certain times in some regions of the deep ocean (Slack et al., 2007; Slack and Cannon, 2009; Planavsky et al., 2018).

Several recent studies of geographically distinct regions of the ocean have, however, suggested that mid-Proterozoic deeper waters may have been oxic in certain areas at particular times (Sperling et al., 2014; Zhang et al., 2016; S. Yang et al., 2017). Specifically, Sperling et al. (2014) argued for oxic basinal waters based on geochemical data for the ~1.4 Ga Arlan Member of the Kaltasy Formation, Volga-Ural region, Russia, while Zhang et al. (2016) suggested that the ~1.4 Ga Xiamaling Formation of the North China Craton records deeper oxic waters beneath an anoxic ‘oxygen minimum zone’ on the shelf. Furthermore, Yang et al. (2017) proposed that less than 25% of ocean floor was anoxic at ~1.4 Ga based on U isotope data. These observations contrast with detailed studies of other mid-Proterozoic settings (Gilleaudeau

and Kah, 2015; Poulton et al., 2004, 2010, Shen et al., 2002, 2003) and, if correct, suggest significant spatial and/or temporal heterogeneity in the mid-Proterozoic ocean redox structure.

While there is significant debate over the temporal and spatial evolution of redox conditions in deeper waters, the shallow marine environment is generally considered to have remained oxic since the GOE (Poulton and Canfield, 2011; Li, Planavsky, Love, et al., 2015; Cox, Jarrett, et al., 2016; Kipp et al., 2017). However, the extent of shallow water oxygenation in the mid-Proterozoic is rather poorly constrained. Organic C isotopes in the ~1.65 – 1.3 Ga sediments from the North China Craton have been interpreted to indirectly reflect a very shallow chemocline (Luo et al., 2014), while rare earth element (REE) data from the same succession are posited to imply very low shallow water oxygen concentrations (~0.2 μM and below; Tang et al., 2016). These observations may be consistent with the suggestion of very low atmospheric oxygen concentrations through the mid-Proterozoic (Planavsky, Reinhard, et al., 2014). However, constraints on atmospheric oxygen across this time period vary widely, with recent suggestions of <0.1 to 10% PAL (Planavsky, Reinhard, et al., 2014; Cole et al., 2016; Zhang et al., 2016; Daines et al., 2017). In addition, while it is commonly tacitly assumed that atmospheric oxygen concentrations remained relatively constant through the mid-Proterozoic (Canfield, 2005; Lyons et al., 2014; Planavsky, Reinhard, et al., 2014), significant fluctuations in atmospheric oxygen remain a distinct possibility (Gilleaudeau et al., 2016; Zhang et al., 2016; Mukherjee and Large, 2016; S. Yang et al., 2017; Diamond et al., 2018). Given the close link between atmospheric oxygenation and ocean redox conditions, such fluctuations would naturally be expected to drive significant temporal and, potentially, spatial variability in ocean redox structure. Indeed, in a detailed study of the ~1.57 Ga Gaoyuzhuang Formation on the North China Craton, Zhang et al. (2018) found evidence for a significant oxygenation event that led to progressive deepening of the oxycline. However, current geochemical records are either too sparse, or too equivocal, to fully constrain the temporal and spatial evolution of mid-Proterozoic ocean redox chemistry. Clearly, there is a need for further studies on the evolution of ocean redox structure during this poorly understood interval of Earth's history.

Here, a multi-proxy geochemical approach is applied to assess water column redox conditions during deposition of marine sediments from the ~1.6 – 0.8 Ga Bashkir Meganticlinorium, Southern Urals. The succession comprises sediments from very shallow (near-coastal) settings to deeper marine environments (Maslov et al., 1997), allowing an evaluation of redox conditions

at different water depths across a prolonged period of Earth's history. Iron-sulfur-carbon systematics, major elements (Mn and Al) and trace metals (Mo and U) are utilized to gain a detailed understanding of the nature of water column redox conditions and controls on these conditions.

3.2 Geological setting

3.2.1 Regional geology

The Bashkir Meganticlinorium (BMA) in the South Urals of Russia is composed of a Mesoproterozoic to Neoproterozoic sedimentary and volcano-sedimentary succession unconformably overlying the Archean to Paleoproterozoic Taratash Complex. It consists of a series of tectonically stacked allochthonous sheets, thrusted to the west during the Late Palaeozoic Uralian orogeny (Puchkov, 1997; Maslov et al., 1997; Kuznetsov et al., 2017a). The BMA is located on the eastern margin of Baltica (Figure 3.1), a Precambrian craton assembled in the middle to late Paleoproterozoic and comprising three major segments: Fennoscandia, Sarmatia, and Volga-Uralia (Glasmacher et al., 2004; Lubnina et al., 2016). Though this region has endured several major orogenic events, the strata of the BMA only experienced deep burial diagenesis (Glasmacher et al., 2004) and were exclusively sampled in this study based on their applicability for the proxies used in this study. The eastern limb was subjected to eclogite-grade metamorphism and is separated from the rest of the BMA by the N-S trending Zuratkul Fault, a major metamorphic and structural boundary between the two limbs (Glasmacher et al., 2001; Giese et al., 1999). This complicated deformational history has further hindered estimates of the units' thicknesses, causing large ranges in the minimum and maximum thickness of each formation as shown in Figure 3.2.

The BMA consists of four first-order, unconformity-bounded sequences (Shatsky, 1945, 1960). The lower three sequences, each starting with mafic volcanic rocks and conglomerates, and fining upwards to shales and carbonates, define the stratotype section of the Riphean, a major Precambrian unit in the Russian stratigraphic nomenclature, lasting from 1750 to 640 Ma (Semikhatov et al., 2015). The thickness of the Riphean deposits of the BMA is estimated to be 12 – 15 km, deposited along the long-lived, passive continental margin of the Baltica craton since at least ~1380 Ma (Maslov, 2004; Puchkov et al., 2013; Romanyuk et al., 2013). This makes these sediments particularly amenable for determining open-marine redox conditions via geochemical

analysis. Furthermore, even older, Lower Riphean carbonates of the Satka and Bakal formations have Sr isotope values consistent with an open connection to the ocean (Kuznetsov et al., 2003, 2008; Semikhatov et al., 2009). An open marine setting, rather than isolation from the ocean, is supported by a combination of sedimentological and geochemical data: 1) the presence of glauconite in the Middle and Upper Riphean sequences, suggesting marine conditions (Keller and Chumakov, 1983); 2) facies changes and heavy-mineral textural and mineralogical maturity indicate deepening to the east towards the margin of Baltica; 3) paleocurrent directions indicate a westerly source (Akimova, 1967); 4) the large thickness (km-scale) of carbonates and mature composition of sandstones; and 5) Sr isotope values of the Riphean carbonates consistent with a seawater signal and indicating connection to the open ocean (Semikhatov et al., 2009). By contrast, the ~1.4 Ga Arlan Member of the Kaltasy Formation studied by Sperling et al. (2014) was deposited in the western part of the Kama-Belsk aulacogen of Volga-Ural region, more than 150 miles to the NW of the Baltica margin along which sequences in the BMA were deposited, and was hence likely more isolated from the open ocean.

The Riphean of the BMA is divided into three first-order, unconformity-bound sequences: the Burzyan Group of the Lower Riphean (1.75 – 1.35 Ga), the Yurmatau Group of the Middle Riphean (1.3 – 1.0 Ga), and the Karatau Group of the Upper Riphean (1.0 – 0.65 Ga) (Maslov et al., 1997). The stratigraphy of the Bashkir basin and the stratigraphic position of the sampled intervals are shown in Figure 3.2. Deposition of the Burzyan and Yurmatau Groups started with short periods of rifting, and was followed by the development of a broader sag basin in which subsidence continued over prolonged periods (Maslov, 2004). A large, shallow marine basin later developed during deposition of the Karatau Group, extending from the South to Middle Urals (Maslov et al., 2010). Basal unconformities separate the groups, with coarse siliciclastics marking the base, and marine carbonates occurring at the top of the groups. This upward-deepening cyclicity is a key feature of the Riphean depositional history, with all groups showing a progression from fluvial or near-shore conditions to shallow marine (above storm wave base), with the Lower Riphean expanding into settings below storm wave base (Maslov, 2004; Kuznetsov et al., 2017a). For simplicity, settings above storm wave base will be referred to as shallow marine, and those below the storm wave base as deeper marine. The two main depositional environments present in all three groups of the BMA can be grouped into inner (littoral and sublittoral) and outer (shallow marine) shelf (Maslov, 2002). Evidence for inner shelf deposits includes their predominantly red colour and sedimentary structures such as desiccation

cracks, small-scale cross-bedding, and wave and current ripple marks (Maslov et al., 1997). Outer shelf and shallow marine sediments show no evidence for subaerial exposure, and contain horizontal, small-scale cross- and planar bedding (Maslov et al., 1997), suggesting palaeo-water depths not greater than 120 m (Immenhauser, 2009). In addition, there is no evidence for turbidite deposition in the BMA succession (Maslov et al., 1997).

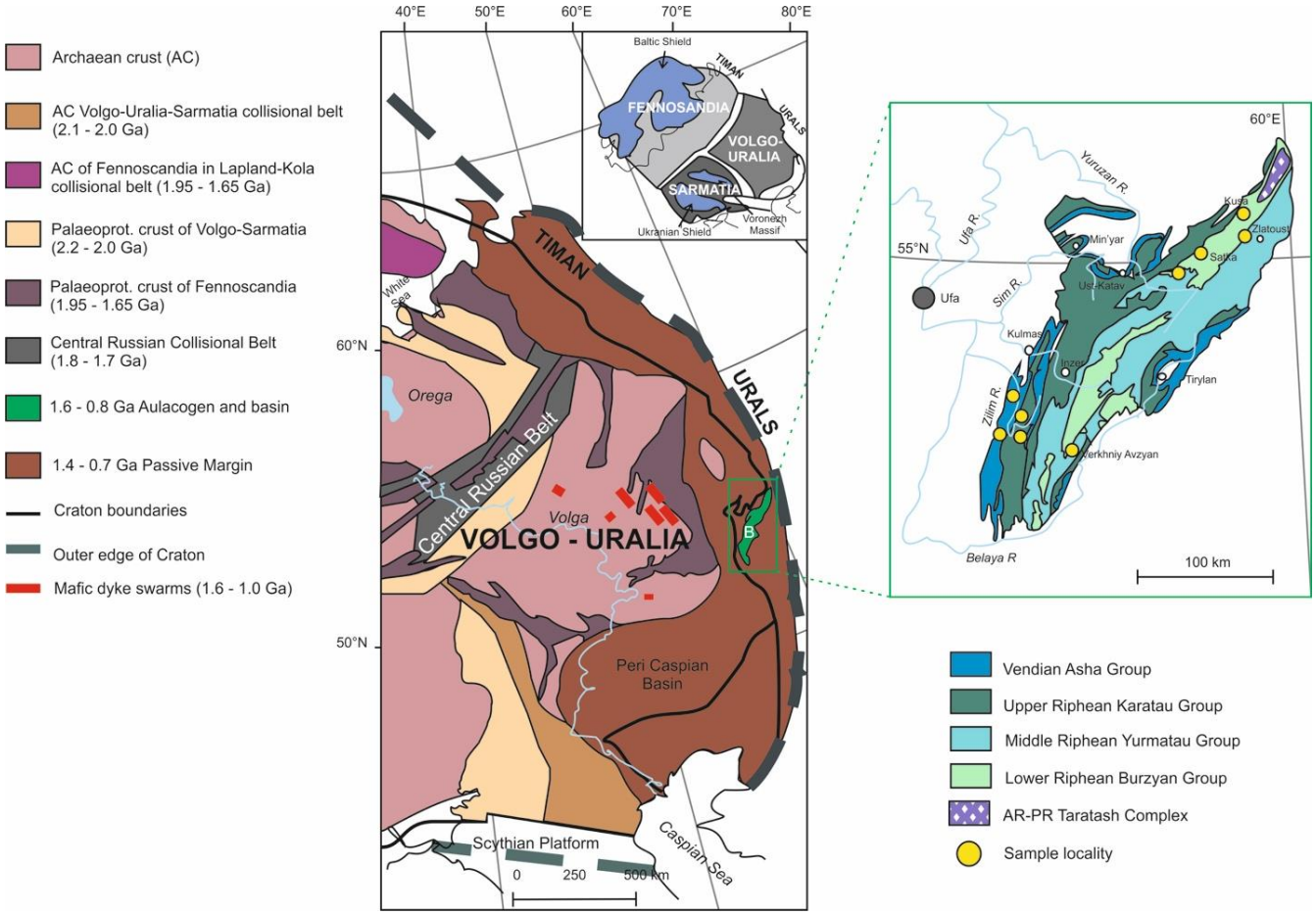

Figure 3.1 Geological map of the South Urals highlighting the position of the Bashkir Meganticlinorium (B), adapted from Puchkov et al. (2013). The inset illustrates the regional geology of the eastern margin of Baltica where the Urals Mountains developed. The geological map of the BMA is adapted from Kuznetsov et al. (2017a). Sample localities are highlighted by yellow circles

3.2.2 The Burzyan Group

The Lower Riphean (1.75 – 1.35 Ga) in the BMA comprises three formations: the Ai, Satka, and Bakal Formations (Figure 3.2). The lower member of the Ai Formation (not sampled in this study), is a terrestrial deposit of breccias, conglomerates, and sandstones with locally overlying trachybasalts, subalkaline basalts, and tuffs of the Navysh Complex (Krasnobaev et al., 2013; Gorozhanin et al., 2014). This terrestrial-alluvial environment transitioned to a moderately deep marine basin in the upper member, a thick deposit of black shales (Maslov, 2004) that was targeted for the present study. Trachybasalts in the basal part of the Ai Formation (Navysh Complex) gave a U-Pb age of 1752 ± 11 Ma (Krasnobaev et al., 2013). Considering that this alkaline, mafic magmatism occurred shortly after the amphibolite facies metamorphism and granitization of the underlying Archean basement (Krasnobaev et al., 2013), this age constraint might reflect orogen collapse, extension, and development of the successor basin. The overlying Satka Formation consists of five subformations: the Lower and Upper Kusa, Polovinka, and Lower and Upper Satka (Semikhatov et al., 2009). The formation consists predominantly of dolostone, but with minor interbedded shale and fine-grained siltstone (all sampled for the present study), highlighting changing depositional conditions. The shales and fine-grained siltstones were deposited below fair weather and storm wave base, with subsequent carbonate deposition occurring between storm wave base and fair weather wave base (Maslov, 2004; Kuznetsov et al., 2008). Conformably overlying the Satka Formation is the Bakal Formation, a shallow marine deposit of black shales (targeted for this study), siltstones, and fine-grained sandstones with minor amounts of limestone and dolostone (Maslov et al., 1997, 2012). The formation is subdivided into the Lower Bakal Subformation, an accumulation of grey-black shales deposited in a stagnant, shallow-marine basin (Maslov, 2004), and the Upper Bakal Subformation, a carbonate sequence containing diverse stromatolite forms (Semikhatov et al., 2009). A diabase dyke cutting the Bakal Formation yielded a U-Pb baddeleyite age of 1385 ± 1.4 Ma (Ernst et al., 2000), and nepheline syenites of the Berdyaush Massif that intrudes the underlying Satka Formation produced an ID-TIMS U-Pb age of 1368.4 ± 6.2 Ma (Ronkin et al., 2007).

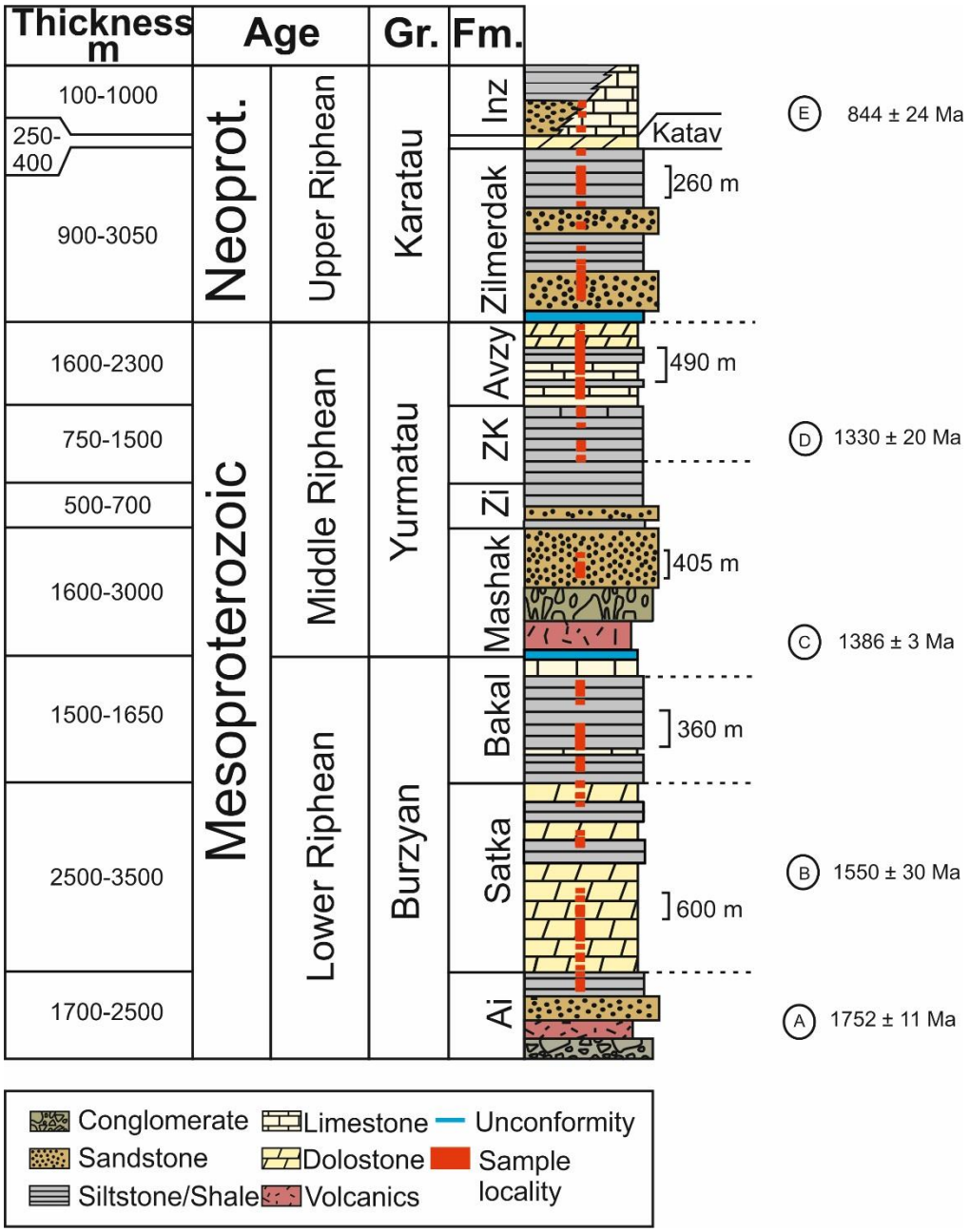

Figure 3.2 Stratigraphic column of the BMA sedimentary succession, adapted from Bartley et al. (2007). Sample positions are shown in red. Scale bars denote thickness used for corresponding samples. Zi – Zigalga Formation; ZK – Zigazino-Komarovo Formation; Avzy – Avzyan Formation; Inz – Inzer Formation. In between the Zilmerdak and Inzer Formations is the Katav Formation, which was too small to label in this figure. Dating: A – U-Pb zircon age (Krasnobaev et al., 2013); B – Pb-Pb carbonate age (Kuznetsov et al., 2008); C – U-Pb zircon age (Puchkov et al., 2013); D –Pb-Pb phosphorite age (Ovchinnikova et al., 2013); E – Pb-Pb carbonate age (Kuznetsov et al., 2017b)

3.2.3 The Yurmatau Group

The Middle Riphean Yurmatau Group overlies the Burzyan Group with an angular unconformity. It consists of four formations: the Mashak, Zigalga, Zigazino-Komarovo, and Avzyan formations. Rhyolites and dacites at the base

of the Mashak Formation gave a U-Pb zircon SHRIMP age of 1386 ± 3 Ma (Puchkov et al., 2013). The lower and middle parts of the Mashak Formation consist of conglomerates and siliciclastics deposited in a near-shore setting within the intracontinental rift basin (Maslov et al., 1997, 2012). The upper part of the Mashak Formation, where samples were collected, also consists of siliciclastics, but was deposited in a shallow marine setting. Similarly, the overlying Zigalga Formation, where two samples were taken, is also from a near-shore and shallow marine setting, comprising fine- and medium-grained quartzitic sandstones and siltstones. Siliciclastic deposition continued in the overlying Zigazino-Komarovo Formation with black shales and siltstones, which were sampled for the present study. The Zigazino-Komarovo Formation contains phosphorite nodules, which produced a Pb-Pb isochron age of 1330 ± 30 Ma (Ovchinnikova et al., 2013). Finally, the overlying Avzyan Formation consists of six members, the Kataskin, Malyi Inzer, Ushakov, Kutkur, Revet, and the locally developed Tyulmen members, of which five were sampled for the present study. The formation contains a spectrum of siliciclastic and carbonate rocks deposited under variable depositional conditions, from shallow marine to near-shore and lagoonal. Desiccation cracks, intraformational breccia, and conglomerate beds point towards a high-energy, shallow marine setting for the lower Kataskin Member (Bartley et al., 2007), which contains black shale at the base and micritic limestone in the upper part. Subtidal conditions developed during deposition of the middle Malyi Inzer Member, which is composed of thinly bedded shale, suggesting deposition in a low energy environment.

3.2.4 The Karatau Group

The Karatau Group includes five formations: the Zilmerdak, Katav, Inzer, Min'yar, and Uk formations, with only the Zilmerdak and Inzer Formations sampled for the present study. The Upper Riphean Karatau Group mainly consists of siliciclastics and carbonates, which are exposed on the western limb of the BMA (Kuznetsov et al., 2006, 2017a). An angular unconformity separates the Avzyan Formation from the overlying Zilmerdak Formation, marking the boundary between the Upper and Middle Riphean. The only age constraints for the Karatau Group are from the youngest U-Pb LA-ICP-MS age for detrital zircons of the Zilmerdak Formation (1817 ± 59 Ma; Romanyuk et al. (2013)) and Pb-Pb carbonate isochron ages of 844 ± 24 Ma and 820 ± 77 Ma for the Inzer and Min'yar Formations, respectively (Kuznetsov et al., 2017a). The Zilmerdak Formation is subdivided into four members (Maslov, 2002). The

lowermost unit, which was not sampled for this work, is the Bir'yan Member, consisting of red and light-coloured conglomerates, arkosic to subarkosic sandstones, and siltstones, deposited in a braided river system (Maslov et al., 1997). The overlying Nugush Member is an inner-shelf deposit of grey to dark-grey siltstones, shales and argillites, where eight samples were taken. The overlying Lemeza Member is a light-coloured sandstone unit with thin siltstone beds, also not sampled. The uppermost Bederysh Member of sandstones, siltstones and argillites, from which 21 samples were collected, was deposited in a littoral to sublittoral zone, similar to the Nugush Member (Maslov, 2004). Overlying the Zilmerdak Formation is the Katav Formation (not sampled), a shallow marine deposit of red and pink limestones and marls with carbonate flat-pebble breccias and red argillites at the base (Kuznetsov et al., 2017a). The uppermost formation sampled in this study (below the predominantly carbonate Min'yar and Uk Formations) is the Inzer Formation, a shallow marine siliciclastic (predominantly) and carbonate deposit containing glauconite at the boundary with the underlying Katav Formation (Maslov, 2004; Kuznetsov et al., 2006).

3.3 Materials and methods

All the techniques and relative errors on each method is detailed in Chapter 2. Table 3.1 lists the location of each of these procedures. In total, 193 samples from marine formations of the BMA were collected. Sampling locations are shown in Figure 3.1. Of these, 54 samples were carbonates and the remaining samples were shales. Excluding the Bakal Formation, which was sampled from a quarry, the remaining samples originated from fresh river cuttings or roadside outcrops. Care was taken to ensure that the freshest samples were collected, avoiding mineral veins and igneous intrusions that could potentially alter the primary geochemical signal, as well as areas with strong sediment reworking, such as in poorly sorted beds, areas with cross-bedding and fining upward layers.

Table 3.1. List and location of methods employed for the BMA sedimentary succession

Method	**Heading #**	**Page #**
Sample Preparation	2.1	41
Total Carbon (TC)	2.2.1	42

Total Organic Carbon (TOC)	2.2.2	43
Total Inorganic Carbon (TIC)	2.2.3	44
Iron Speciation	2.3	44
Bulk Digests	2.4	50
Sulfur Isotopes ($\delta^{34}S_{py}$)	2.6	63
Optical Mineralogy	2.8	64

3.4 Results

3.4.1 Evaluating the effect of secondary weathering

Although every effort was made to ensure that only pristine samples were analysed, it is important to evaluate the possibility for modification of geochemical redox data due to oxidative weathering of field samples. Thin sections for shale samples from the Zigazino-Komarovo Formation (*n*=6) and carbonate samples from the Inzer Formation (*n*=5) were examined to evaluate pyrite morphology. Pyrite was specifically targeted for mineral analysis to assess the degree of secondary weathering, as its morphology can be affected by oxidation. If a sufficient degree of oxidation has occurred, an iron oxyhydroxide coating is typically found surrounding the pyrite grains, if not completely replacing the mineral (Williamson and Rimstidt, 1994; Huminicki and Rimstidt, 2009; Gartman and Luther, 2014). Figure 3.3A shows a representative image of euhedral pyrite in a carbonate sample from the Inzer Formation, which shows no evidence for dissolution features or alteration products. Similar occurrences of euhedral pyrite grains were found in other thin sections, suggesting limiting conversion of pyrite to iron oxides. In one instance only, a single band of jarosite was found in a shale from the Zigazino-Komarovo Formation (Figure 3.3B), which may represent a secondary oxidation product of pyrite (cf. Raiswell and Canfield, 2012). Thus the SEM images give confidence that the Fe speciation data have not been compromised by significant oxidative weathering.

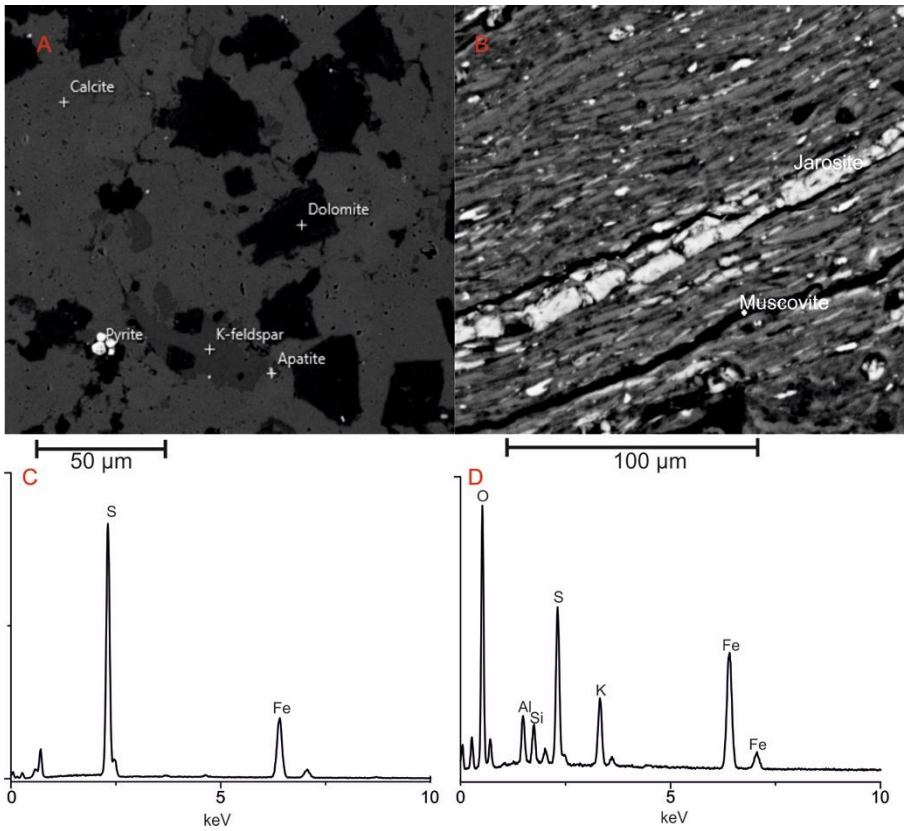

Figure 3.3 Representative SEM images. A: Backscatter image of euhedral pyrite in a carbonate sample from the Inzer Formation. B: Backscatter image showing a single occurrence of a jarosite (oxidized pyrite) band of ~10 µm thickness in a shale sample from the Zigazino-Komarovo Formation. C: EDX spectra of euhedral pyrite found in A. D: EDX spectra of jarosite found in B

3.4.2 Fe-S-C systematics

All geochemical data are reported in Appendix B. The major element and iron speciation data are shown in Figure 3.4, alongside a reconstruction of changes in depositional environment, where shallow water environments are considered to be above storm wave base, and deeper water sedimentation occurred below storm wave base (>120 m depth), based on published sedimentological evidence (Maslov et al., 1997; Maslov, 2002, 2004).

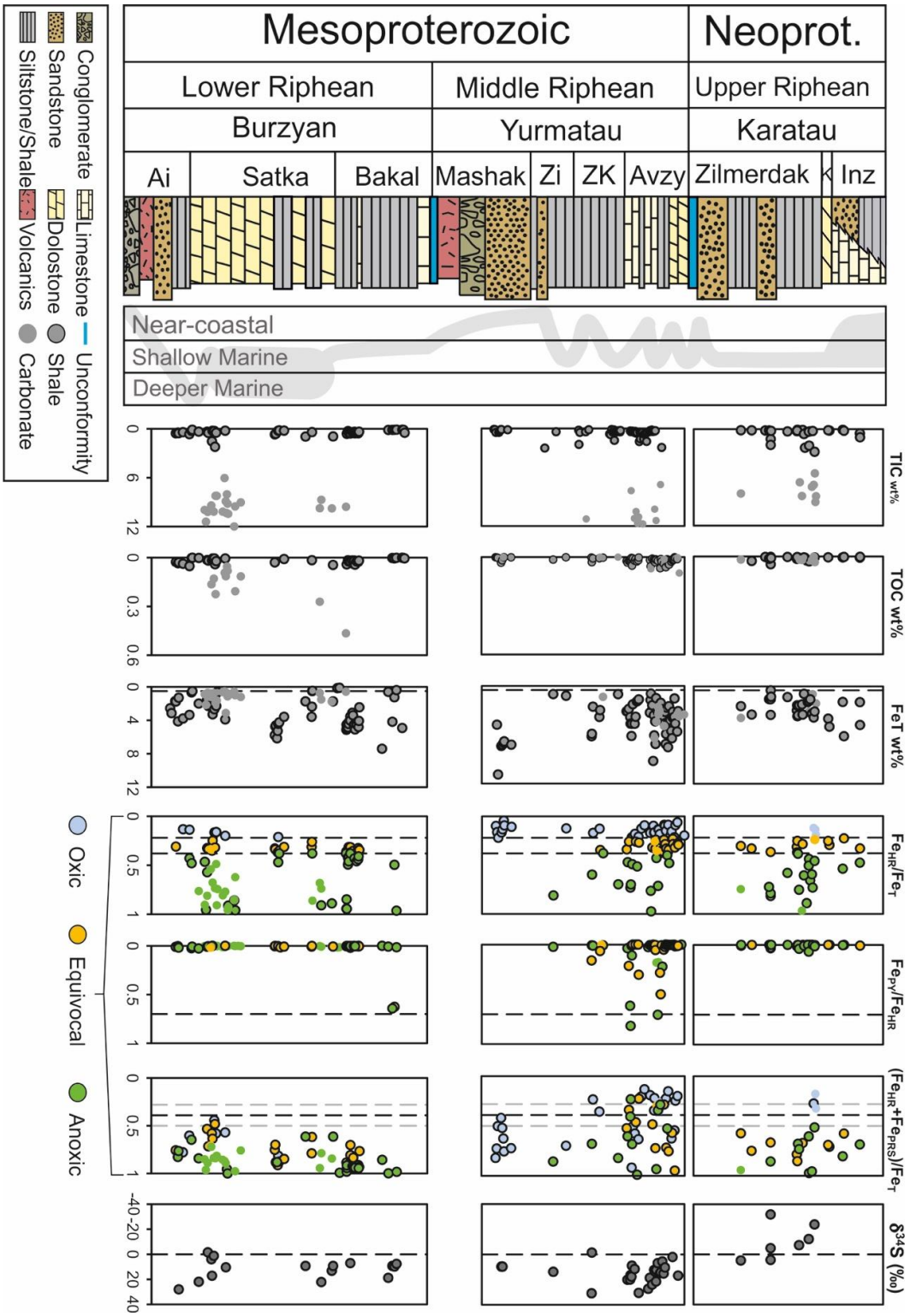
Mesoproterozoic
Neoprot.
Lower Riphean
Middle Riphean
Upper Riphean
Burzyan
Yurmatau
Karatau
Ai
Satka
Bakal
Mashak
Zi
ZK
Avzy
Zilmerdak
Inz
Near-coastal
Shallow Marine
Deeper Marine
Conglomerate
Sandstone
Siltstone/Shale
Limestone
Dolostone
Volcanics
Unconformity
Shale
Carbonate
Oxic
Equivocal
Anoxic
TIC wt%
TOC wt%
FeT wt%
FeHR/FeT
FePY/FeHR
(FeHR+FePRS)/FeT
δ34S (‰)

Figure 3.4 Chemostratigraphic section showing TIC, TOC, FeT, Fe_{HR}/Fe_T, Fe_{PY}/Fe_{HR}, $(Fe_{HR}+ Fe_{PRS})/Fe_T$, and $\delta^{34}S_{PY}$. Iron speciation data are colour-coded based on the identified redox state: blue for oxic, yellow for equivocal, and green for anoxic. Fe_{PY}/Fe_{HR} ratios are only shown for anoxic and equivocal samples as this ratio does not provide information on water column chemistry when samples are deposited under oxic water column conditions. The dashed line on the Fe_T plot is at 0.5 wt%, below which samples were not analysed for Fe speciation. Dashed lines on the Fe_{HR}/Fe_T plot distinguish oxic ($Fe_{HR}/Fe_T < 0.22$) from anoxic ($Fe_{HR}/Fe_T > 0.38$) depositional conditions. Dashed line on the Fe_{PY}/Fe_{HR} plot distinguishes ferruginous ($Fe_{PY}/Fe_{HR} < 0.7$) from euxinic ($Fe_{PY}/Fe_{HR} > 0.7$) water column conditions. Dashed lines on the $(Fe_{HR}+ Fe_{PRS})/Fe_T$ plot show the Palaeozoic range (average ± 1 σ) from Raiswell et al. (2008). The range of depositional environments for each formation is also shown and is adapted from Bartley et al. (2007), Maslov et al. (1997), and Maslov (2002, 2004)

As this sedimentary succession hosts deposits in a near-coastal and above SWB environment, it is important to check whether the delivery of Fe_{HR} was influenced by detrital material entering the marine system in these shallow depths, as a large fraction of particulate iron from riverine delivery is deposited in estuaries (Poulton and Raiswell, 2002). The relationship between Fe_{HR} and Al, a gauge for detrital content (Lyons and Severmann, 2006), is illustrated in Figure 3.5. A weak and negative correlation exists for both depositional environments, ruling out proximity to the coast as an influencer on the iron speciation results. Typically, the riverine supply of iron dominantly consists of Fe_{OX} phases (Poulton and Raiswell, 2002). To ensure the Fe_{OX} pool within the sediment samples were not influenced by proximity to the coast, Fe_{OX} versus Al content is also shown in Figure 3.5. Again no clear positive correlation exists across the depositional environments giving assurance in the iron speciation results presented here.

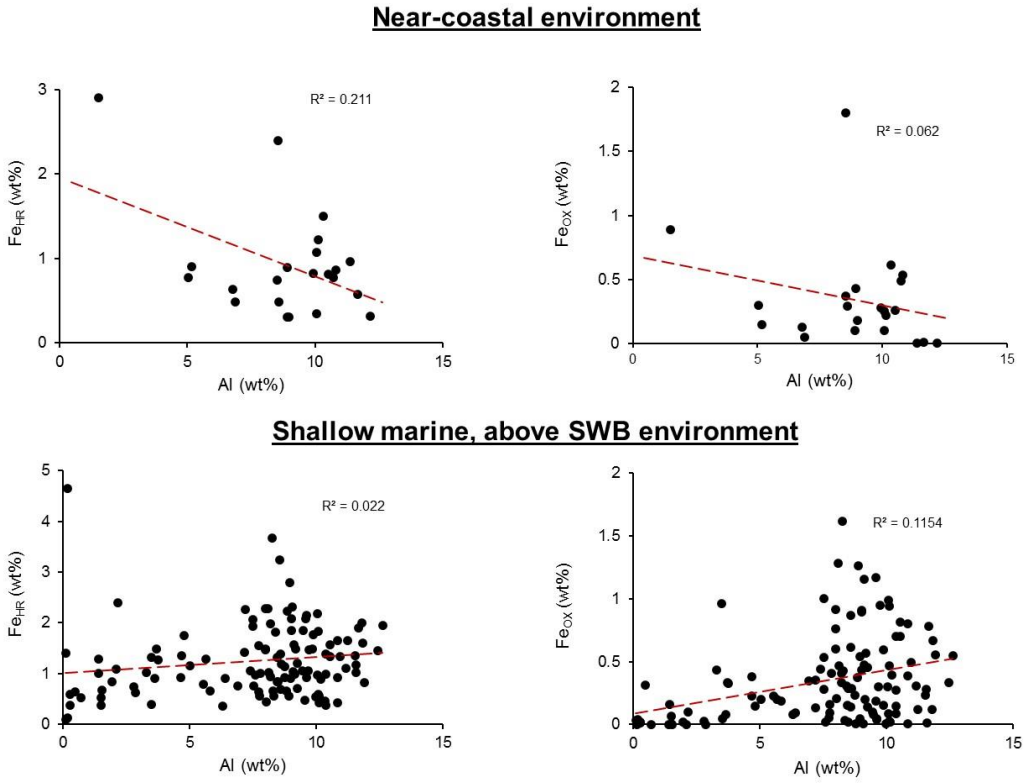

Figure 3.5 Plot of Fe_{HR} (wt%) versus Al (wt%) and Fe_{ox} (wt%) versus Al for samples from both near-coastal and shallow marine (above SWB) settings

A further check on whether Fe_{OX} phases dominate the Fe_{HR} pool within the near-coastal samples is shown in Figure 3.6. These histograms illustrate the percentage each highly reactive iron phase makes up of the total Fe_{HR} pool (Fe_{CARB}/Fe_{HR} (%); Fe_{OX}/Fe_{HR} (%); Fe_{MAG}/Fe_{HR} (%); Fe_{PY}/Fe_{HR} (%)) in all depositional environments. For the near-coastal samples, a minor percentage (30%) of samples have greater than 50% $Fe_{OX}/Fe_{HR,}$ implying the proximity to the coast did not significantly influence the delivery of Fe_{HR} to these sediments. The same result is given for samples deposited above storm wave base (30% samples), suggesting there is no discernible difference between samples deposited closer to the coastline in terms of Fe_{OX} content and those deposited at greater depths. Again, this gives confidence in the iron speciation results presented here.

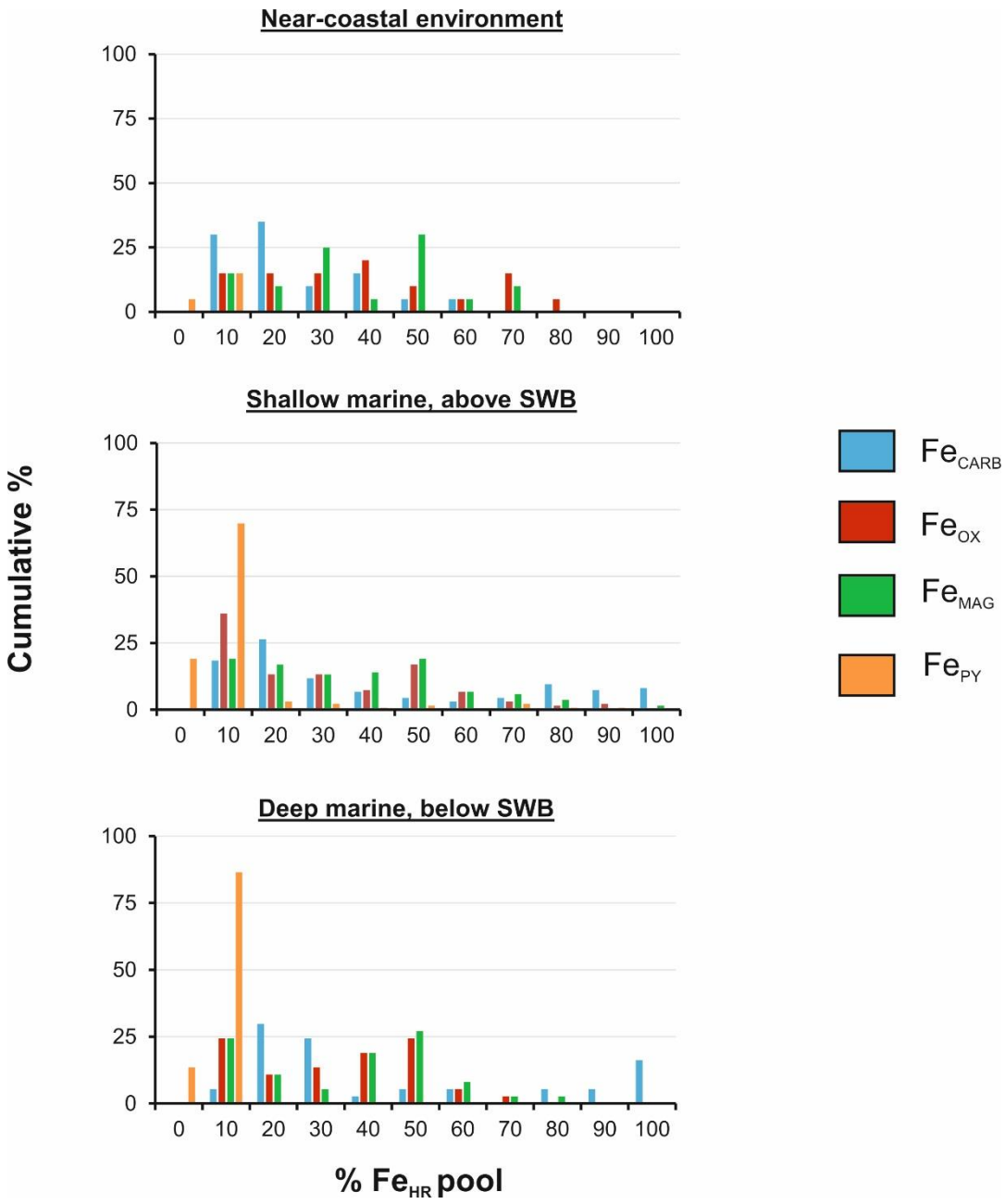

Figure 3.6 Histograms depicting the cumulative percentage of the different Fe_{HR} phases (Fe_{CARB}, Fe_{OX}, Fe_{MAG}, Fe_{PY}) in each depositional environment in the BA succession

Carbonate-rich sediments were analysed from four stratigraphic levels in the succession. In each case, interbedded shales were also analysed and gave consistent redox results. Organic C is low throughout the succession, with an average of 0.02 ± 0.01 wt% and no systematic variability up-section.

Most samples have appreciable Fe_T and are thus ideal for Fe speciation. The few samples with Fe_T <0.5 wt% were not analysed for Fe speciation

(Clarkson et al., 2014). A preliminary evaluation of water column redox is given by the Fe_{HR}/Fe_T profile, with the data colour coded to highlight oxic (Fe_{HR}/Fe_T <0.22), equivocal (Fe_{HR}/Fe_T 0.22 – 0.38), and anoxic (Fe_{HR}/Fe_T >0.38) samples. The sediments of the Lower Riphean show very little evidence for oxic depositional conditions, and instead the majority of shale and carbonate samples show persistent evidence for anoxia, with some samples falling in the equivocal zone. In all cases, Fe_{PY}/Fe_{HR} ratios are very low, suggesting ferruginous depositional conditions. This anoxia persists from the deeper upper member of the ~1.75 Ga Ai Formation, throughout the shallow marine Satka and Bakal Formations. For the unconformably overlying Middle Riphean Yurmatau Group, Fe_{HR}/Fe_T ratios suggest oxic water column conditions in the near-coastal Mashak Formation at ~1.38 Ga. These very shallow water sediments have some of the highest Fe_T values in the succession, up to 11 wt% with an average of 6.9 ± 1.9 wt%, demonstrating that their iron content predominantly consists of Fe_U or Fe_{PRS} phases as their Fe_{HR} content is relatively low. Such high Fe_T contents are potentially the result of weathering from an iron-rich continent, supplying abundant Fe_U or Fe_{PRS} phases to the sediments in shallow settings. Variable redox conditions developed during deposition of the Zigalga, Zigazino-Komarovo, and Avzyan formations, in concert with fluctuations in water depth. Where anoxic depositional conditions are indicated, almost all samples have Fe_{PY}/Fe_{HR} ratios consistent with ferruginous depositional conditions, although a few samples have higher Fe_{PY}/Fe_{HR}, which may reflect either intermittent euxinia or extensive pyritization of the Fe_{HR} pool during early diagenesis (Poulton and Canfield, 2011). Sediments from the shallow marine, upper Zilmerdak Formation show abundant evidence for anoxic, ferruginous depositional conditions. However, some samples from this formation, and most of the samples from the upper part of the Karatau Group, plot in the equivocal range. To evaluate the potential for transfer of unsulfidized Fe_{HR} to Fe_{PRS} in these low-sulfide sediments, $(Fe_{HR}+Fe_{PRS})/Fe_T$ ratios are plotted stratigraphically in Figure 3.4. This identifies samples that plot above the average Palaeozoic shale value (0.39 ± 0.11 wt%; Raiswell et al., 2008). In the Lower Riphean, the vast majority of equivocal samples plot above the upper limit of the Palaeozoic average, suggesting that they comprise significantly higher proportions of Fe_{PRS} than average Palaeozoic shale. In the Lower Satka Formation, oxic and equivocal samples are within the limits of average Palaeozoic shale. In the Middle Riphean succession, the near-coastal Mashak Formation contains several samples originally classified as oxic. Half of these plot within the average Palaeozoic shale range, while the other half plot above this range. The majority

of the remaining oxic samples in this group plot below the lower limit for average Palaeozoic shale. One anoxic and several equivocal Middle Riphean samples are also below this limit. Equivocal shallow water samples from the Upper Riphean also contain relatively high concentrations of Fe_{PRS}.

In general, $\delta^{34}S_{py}$ values are relatively heavy throughout much of the succession, with limited variability and no clear trend in relation to depositional setting (Figure 3.4). In the Lower Riphean, $\delta^{34}S_{py}$ averages 11.8 ± 8.0‰, which is similar to the average and the range of values for the Middle Riphean (14.7 ± 7.7‰). There is limited data for the Upper Riphean, but these data show more variability, with values as low as -31.8‰ and an average of -8.5 ± 13.5‰.

3.4.3 Trace metals

Normalized Mo, U, and Mn concentrations are shown in Figure 3.7, where dashed lines represent Post Archean Average Shale (PAAS) values from Taylor and McLennan (1995). Trace metals are normalized to Al to ensure the concentrations are not diluted or enriched as a result of detrital input (Lyons and Severmann, 2006). Moderate enrichments are evident for Mo, with the majority of shales from shallow and deep marine settings in the succession plotting above the PAAS average. However, a significant proportion of samples also plot below this average. The plot of U similarly depicts no overall enrichment, with a minor amount of samples in the Lower Riphean plotting slightly above the PAAS value. The plot of Mn illustrates muted levels for the majority of the samples compared to PAAS, with a few samples sporadically plotting above this value. A greater proportion in the Upper Riphean host Mn/Al values above the PAAS value in comparison to the remainder of the succession.

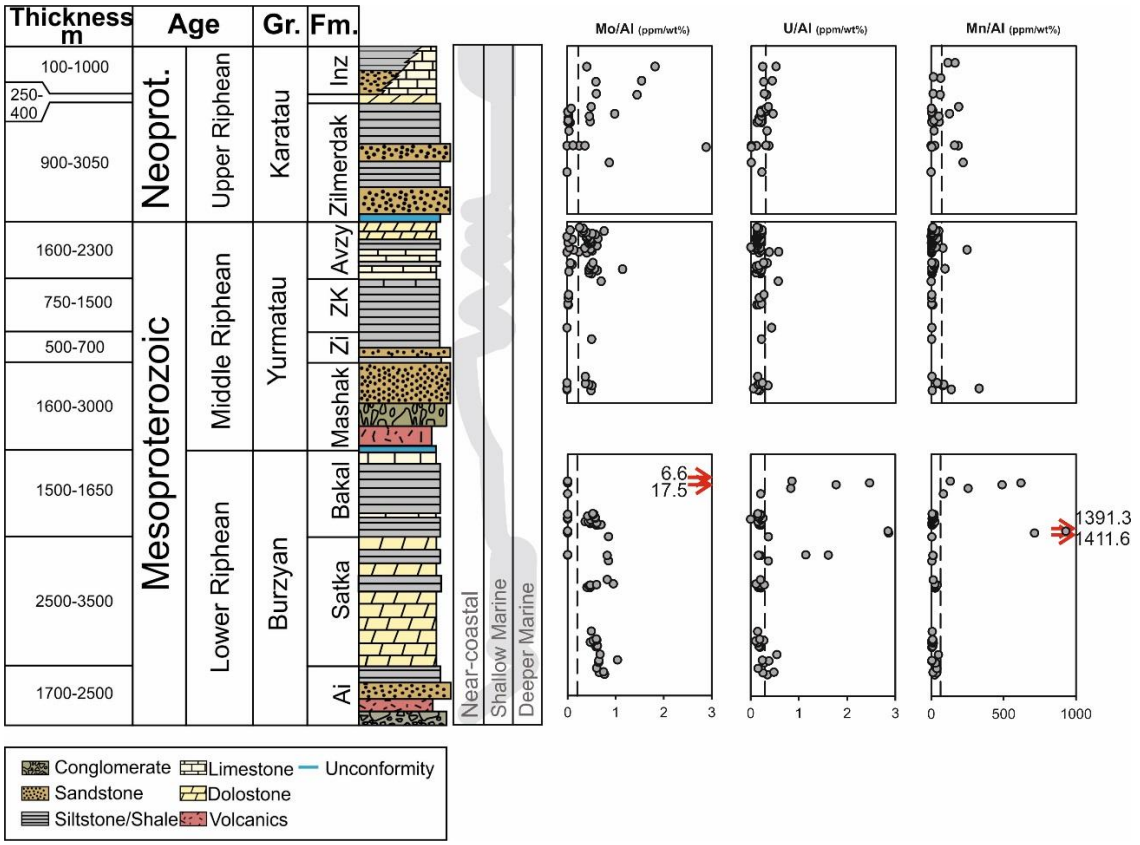

Figure 3.7 Normalized chemostratigraphic plot of Mo/Al, U/Al and Mn/Al. Dashed lines are representative of PAAS values from Taylor and McLennan (1995) and are as follows: Mo/Al – 0.2; U/Al – 0.35; and Mn/Al – 75. Only shales are included in this plot

3.5 Discussion

3.5.1 Ocean redox reconstruction from Fe speciation

In order to fully evaluate the dominant redox state of the water column through the extended period of time recorded by the BMA sediments, the potential for transfer of unsulfidized Fe_{HR} to Fe_{PRS} must first be considered. Where sulfide production is limited, either via low sulfate concentrations or low organic matter availability (as is clearly the case for the BMA), there is the possibility that dissolved Fe^{2+} sourced from Fe_{HR} during early diagenesis may be taken up in early diagenetic clay minerals, rather than precipitating as pyrite (Poulton et al., 2010; Cumming et al., 2013; Tosca et al., 2016). Figure 3.4 demonstrates that a significant number of 'equivocal' samples and some 'oxic' samples (based on a strict interpretation of Fe_{HR}/Fe_T ratios alone), have $(Fe_{HR}+Fe_{PRS})/Fe_T$ ratios that are well above the upper limit for the Palaeozoic average shale, suggesting a likely transformation of Fe_{HR} to Fe_{PRS}. This is evaluated quantitatively by

defining a conservative Fe_{HR}/Fe_T* ratio that incorporates potential transfer of Fe_{HR} to Fe_{PRS}:

Equation 1 FeHR/FeT* ratio

$$\frac{Fe_{HR}}{Fe_T} *= \frac{Fe_{HR}}{Fe_T}\text{meas} + (\frac{Fe_{PRS}}{Fe_T}\text{meas} - \frac{Fe_{PRS}}{Fe_T}\text{PAS})$$

where (Fe_{HR}/Fe_T)meas is the measured Fe_{HR}/Fe_T ratio, (Fe_{PRS}/Fe_T)meas is the measured Fe_{PRS}/Fe_T ratio, and (Fe_{PRS}/Fe_T)PAS is the upper limit for the Palaeozoic average shale (0.5 wt%) as quantified by Raiswell et al. (2008). Equation 1 was applied to all oxic and equivocal samples from the BMA to evaluate whether significant loss of Fe_{HR} to Fe_{PRS} may have altered the primary redox signal at the time of deposition. Anoxic samples do not need to be considered as, if Fe_{HR} has been lost to Fe_{PRS} phases, the redox signal would not change. This approach has an underlying assumption that the fine-grained sediments are not dominated by juvenile, unweathered materials. It must be stressed here, however, that while this refines redox interpretations and makes the observations more consistent throughout the succession, it does not lead to any significant change in the overall conclusions. Based on this approach, Figure 3.8 shows how water column redox conditions varied from near-coastal settings, through shallow marine environments (above storm wave base), and into the deeper basinal (below storm wave base) settings. A clear trend is found, whereby near-coastal settings were dominantly oxic, whereas shallow and deeper marine settings were dominantly anoxic, highlighting that oxic conditions were generally restricted to only the shallowest waters throughout the analysed succession. A small percentage (10%) of the shallowest samples plot as anoxic, and could signify shallowing of the chemocline, or the short-lived existence of a completely ferruginous water column.

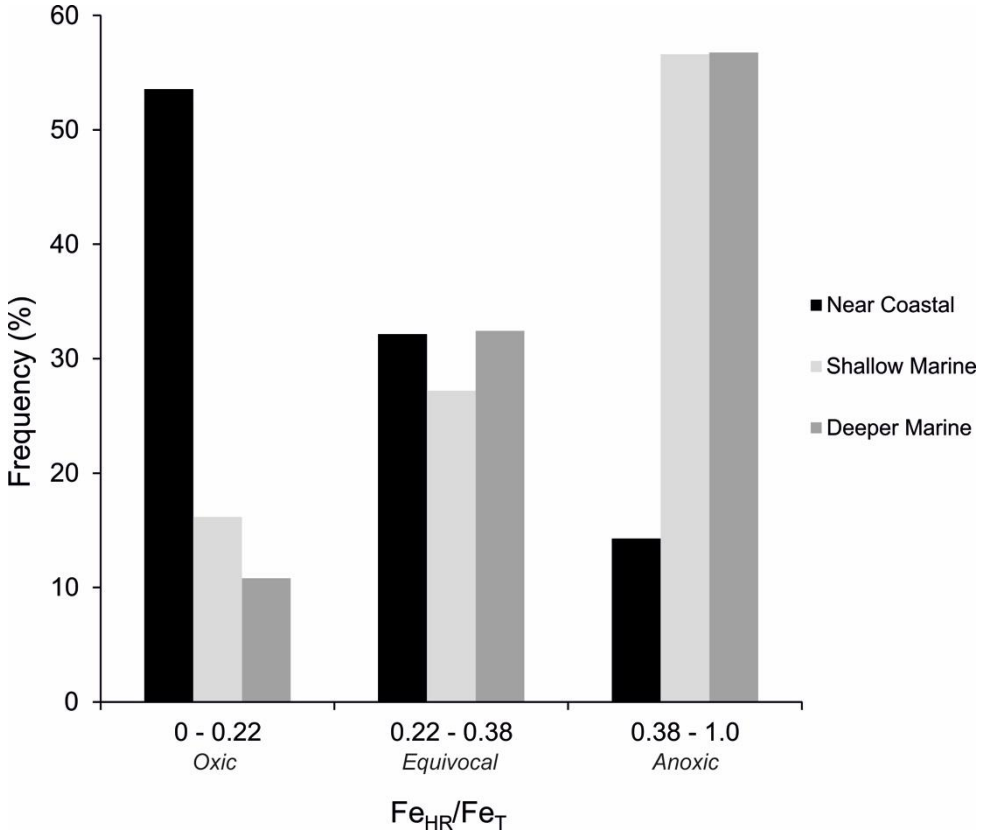

Figure 3.8 Frequency plot of FeHR/FeT ratios for near-shore, shallow marine, and deeper marine samples, binned in terms of oxic, equivocal, and anoxic depositional settings. FeHR/FeT* ratios were used for samples with FePRS/FeT values above the Palaeozoic average shale (for correction procedure see the main text)

3.5.2 Redox-sensitive metals

Redox-sensitive metals provide further insight and support for the evaluation of water column redox conditions. To assess the degree of enrichment or depletion relative to average shale, the data in Figure 3.7 is recast in terms of Enrichment Factors (EF) relative to PAAS (Brumsack, 2006; Algeo and Tribovillard, 2009; Tribovillard et al., 2012), where the EF for a given element (X) is calculated as:

Equation 2 Enrichment factor formula

$$X_{EF} = \frac{\frac{X}{Al}\text{sample}}{\frac{X}{Al}\text{AS}}$$

To calculate enrichment factors, PAAS values for Mo and U are taken from Taylor and McLennan (1995). Enrichment factors are plotted stratigraphically in Figure 3.9. Here, a value above 1 represents an enrichment and a value less than 1 denotes muted values, relative to PAAS. The data show considerable overlap in terms of the oxic, equivocal, and anoxic depositional conditions identified by Fe speciation. However, there are distinct differences between the

oxic and anoxic samples, with an average Mo_{EF} for oxic samples of 1.7, whereas anoxic samples have an elevated average Mo_{EF} of 5.2. This difference reflects the contrasting behaviour of Mo under different redox states. Mo initially enters the ocean as the molybdate anion (MoO_4^{2-}) derived from oxidative weathering of continental crust (Bertine and Turekian, 1973). In oxic settings, molybdate is largely unreactive and is only appreciably removed to the sediments through slow uptake by Fe-Mn (oxyhydr)oxide minerals (Bertine and Turekian, 1973). Thus, the average Mo_{EF} of 1.1 for shallow water samples is entirely consistent with the interpretation from Fe speciation of dominantly oxic water column conditions in the shallow ocean.

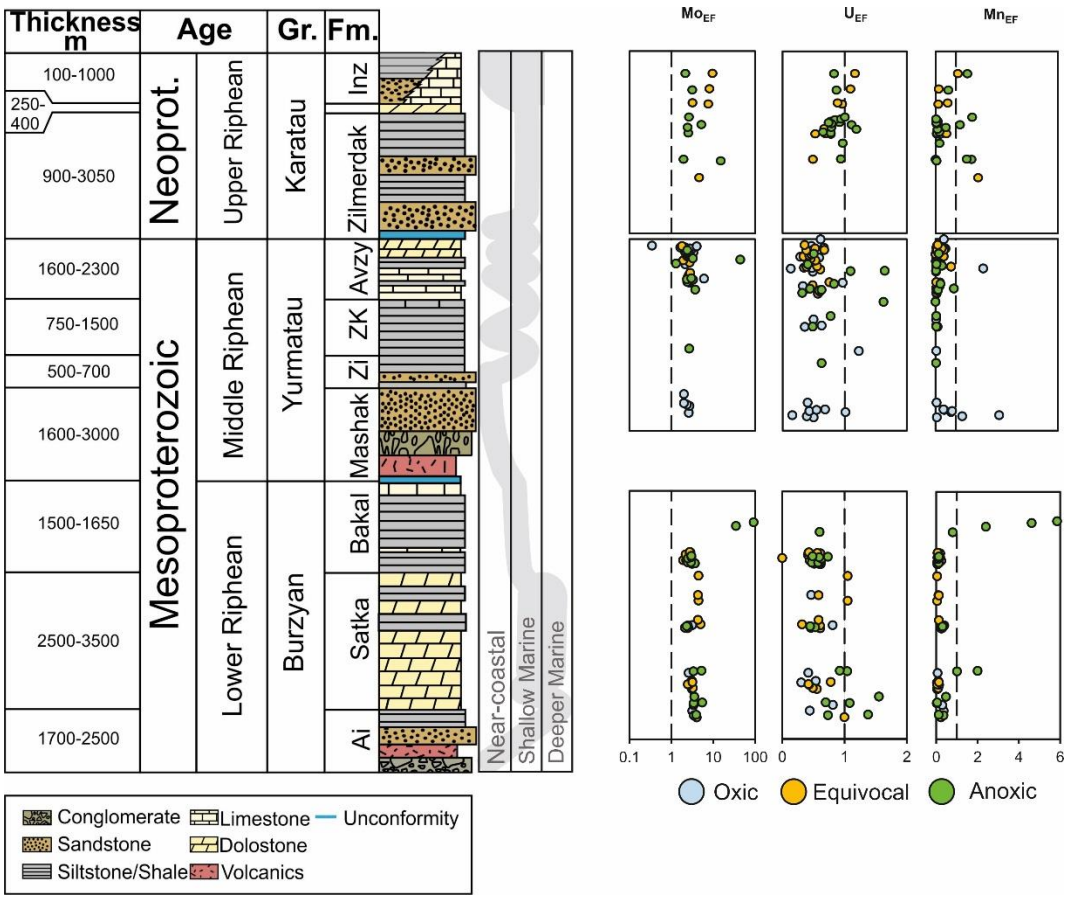

Figure 3.9 Chemostratigraphic log of Enrichment Factors for Mo, U, and Mn. Dashed lines at 1 represent the PAAS reference (Taylor and McLennan, 1995). Samples are colour coded according to the redox state indicated by iron speciation data; blue for oxic, yellow for equivocal, and green for anoxic. Fe_{HR}/Fe_T* ratios were used for the samples with elevated Fe_{PRS}/Fe_T ratios (for correction procedure see the main text)

By contrast, if a critical threshold of free H_2S is met under anoxic conditions, the molybdate anion is converted to particle-reactive thiomolybdate ($MoO_xS_{4-x}^{2-}, 1 < x < 4$,where x is from 0 to 3; Helz et al., 1996). Under such conditions in modern environments, Mo removal to the sediment is 200 to 5000 times more efficient than under oxic conditions (Scott et al., 2008), leading to significant Mo enrichments (Emerson and Huested, 1991; Helz et al., 1996; Erickson and Helz, 2000; Scholz et al., 2013). Sedimentary Mo enrichments generally scale with sulfide availability. The lower levels of enrichment tend to occur where H_2S is restricted to porewaters, whereas the more extreme enrichments are associated with high levels of water column sulfide (Scott et al., 2008). Authigenic Mo enrichments have also been shown to be sensitive to sedimentation rates in modern settings, with rates greater than 0.2 cm/yr capable of severely muting authigenic concentrations (Hardisty et al., 2018).

To further evaluate the potential mechanisms involved in Mo drawdown to the sediments under anoxic conditions in the Bashkir basin, the contrasting redox-dependent behaviour of U is taken into account. A large proportion of the

samples are relatively muted in U (Figure 3.9), although as with Mo, there is a clear difference between oxic, shallow water and anoxic, deeper water settings (average oxic U_{EF} = 0.51; average anoxic U_{EF} = 1.04). Unlike Mo, U is preferentially buried in sediments deposited beneath anoxic bottom waters regardless of whether euxinic or ferruginous conditions dominate, as U reduction primarily occurs in the sediments, not in the water column (Anderson et al., 1989; Klinkhammer and Palmer, 1991; Partin et al., 2013). This behaviour is evident as higher enrichments are found in anoxic samples in both deep and shallow environments, consistent with anoxic depositional conditions in the basin and, more broadly, low-oxygen conditions in the global ocean. It must also be taken into consideration the recovery values of U, as outlined in 2.4.2. The limited recovery of U in the reference material used (PACS-2) could be used to suggest there was also a partial recovery of the true U sedimentary content. However, replicate analyses (*n*=4) of a shale sample (746-13) from the Zilmerdak Formation (average 1.8 ± 0.04 ppm) gave a RSD value of 2.3%, giving confidence in the U results presented here.

A plot of Mo_{EF} as a function of U_{EF} (Figure 3.10) provides information on the mechanisms responsible for Mo and U enrichments. Particulate molybdate scavenging in the water column accelerates the accumulation of authigenic Mo relative to other trace metals, such as U, which are not so readily scavenged (Algeo and Tribovillard, 2009). Notwithstanding the possibility that the detrital sediments of the Bashkir basin may have contained relatively low U relative to PAAS, Figure 3.10 clearly demonstrates the preferential enrichment of Mo relative to U. The comparison of sedimentary Mo_{EF}:U_{EF} ratios from different contemporaneous redox settings with the modern seawater Mo:U [$(Mo:U)_{SW}$] ratio can help discriminate between different enrichment mechanisms. Only the Fe_{HR}/Fe_T ratio is used here to define between different redox states as no euxinic samples were recovered from the BMA. For example, sediments deposited beneath a suboxic water column in the modern-day tropical East Pacific are enriched in U relative to Mo, and thus feature a low Mo_{EF}:U_{EF} (~0.1 to 0.3) relative to $(Mo:U)_{SW}$ (Tribovillard et al., 2012). A progressive shift favouring Mo over U enrichment moves the sedimentary Mo_{EF}:U_{EF} ratio toward the seawater ratio, signalling a shift to more intense and stable anoxic water column conditions. Further Mo enrichment, resulting in Mo_{EF}:U_{EF} ratios greater than the equivalent seawater ratio, implies the operation of an Fe-Mn (oxyhydr)oxide particulate shuttle for Mo sequestration under anoxic (but not euxinic) water column conditions (Tribovillard et al., 2012). More pronounced Mo enrichment and higher Mo_{EF}:U_{EF} ratios are typically the product of euxinic

water column conditions, catalysed by the formation of particle-reactive thiomolybdate.

As the majority of samples from the BMA plot above the $(Mo:U)_{SW}$ ratio (Figure 3.10), and iron speciation data denotes ferruginous but not euxinic water column conditions (Figure 3.4), the data favour an Fe-Mn (oxyhydr)oxide particulate shuttle as a Mo enrichment mechanism rather than euxinic sedimentation. In Figure 3.10, the green ellipsoid highlights the field of the modern Cariaco basin sediments, where scavenging by Fe-Mn (oxyhydr)oxides promoted the accumulation of Mo in the sediments (Tribovillard et al., 2012). However, the original data for these Cariaco Basin samples do not solely plot in this field, but show a large degree of scatter, with the majority of values greater than the $(Mo:U)_{SW}$ (Algeo and Tribovillard, 2009). Only two samples from the BMA plot in this area, and these are from the Lower Riphean Bakal Formation. These samples have elevated Fe_{PY}/Fe_{HR} ratios (Figure 3.4), suggesting that increased sulfide availability rather than an intensified Fe-Mn (oxyhydr)oxide shuttle likely stimulated Mo accumulation in these isolated cases. Sulfide availability, however, was generally low throughout deposition of most of the succession, as testified by the low Fe_{PY}/Fe_{HR} ratios (Figure 3.4). Scott et al. (2008) highlighted that Mo concentrations in the mid-Proterozoic ocean were likely significantly lower than at present. Hence, Mo uptake by Fe-Mn (oxyhydr)oxides would be expected to result in lower Mo_{EF}:U_{EF} than in modern anoxic settings, as observed for our samples (Figure 3.10). There is also the potential that the seawater inventories of Mo and U were not as high in the past in comparison to modern studies. Molybdenum and U are mainly supplied to the oceans through fluvial input from the weathering of continental material (McLennan, 2001). During the Mesoproterozoic when atmospheric concentrations are considered to be between 0.1 – 1% PAL (Daines et al., 2017; Planavsky, Reinhard, et al., 2014; Zhang et al., 2016; Cole et al., 2016), the supply of TM to the marine system would have been lower due to weakened oxidative weathering in comparison to the modern. Lower seawater ratios would amend the plot presented in Figure 3.10, and thus the location of samples from the BMA and their corresponding position on the original figure by Tribovillard et al. (2012). Incorporating all of these factors together, Mo drawdown by an Fe-Mn (oxyhydr)oxide shuttle was likely the main mechanism for Mo sequestration beneath the ferruginous water column of the BMA.

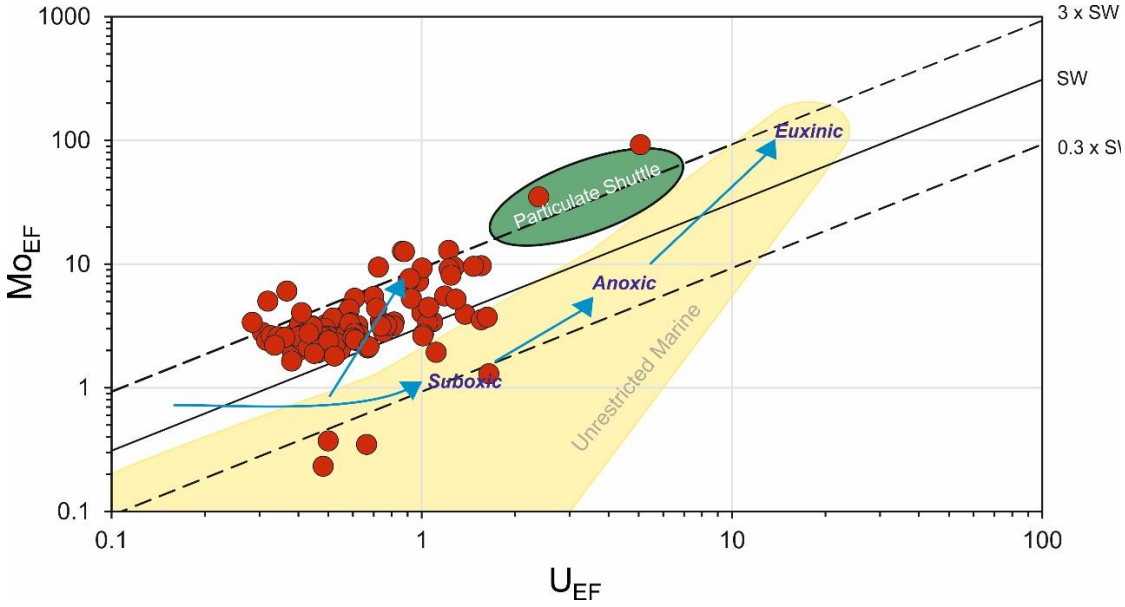

Figure 3.10 Plot of Mo_{EF} vs. U_{EF} for shales (red circles) from the BMA. The diagram is modified from Algeo and Tribovillard (2009) and Tribovillard et al. (2012) to accommodate for low levels of U (U_{EF}<1) by extending the axis values. The modern seawater molar Mo/U ratio (Mo/U)SW of 3.1 (Tribovillard et al., 2012) is represented by the solid black line. The dashed lines correspond to multiples of the (Mo/U)SW ratio. All redox labels were defined for modern environments in open-marine basins by Tribovillard et al. (2012). The arrow pointing to the particulate shuttle highlights how Mo_{EF} and U_{EF} would evolve as a result of drawdown via an Fe (oxyhydr)oxide particulate shuttle. The yellow field denotes the area established by Tribovillard et al. (2012) as unrestricted marine

3.5.3 Spatial and temporal variability in mid-Proterozoic ocean redox chemistry

The Fe-speciation and trace-metal data strongly suggest that below a very shallow chemocline, waters were dominantly anoxic and ferruginous. To further evaluate potential controls on the widespread development of ferruginous, rather than euxinic, water column conditions in the BMA, S isotope systematics are utilized. The isotopic composition of seawater sulfate is poorly constrained throughout the Mesoproterozoic and early Neoproterozoic, but low resolution estimates from carbonate-associated sulfate suggest a likely range of ~25 - 35‰ (Kah et al., 2004; Guilbaud et al., 2015; Turner and Bekker, 2016). Pyrite S isotope values average 11.8 ± 8.0‰ for the Lower Riphean and 14.7 ± 7.7‰ for the Middle Riphean (Figure 3.4), giving fractionations from seawater sulfate of around 15 - 25‰. Given the low pyrite content of these sediments, this suggests that the extent of S isotope fractionation imparted during bacterial sulfate reduction was subdued due to low seawater sulfate concentrations in this particular basin (Canfield, 2000; Habicht et al., 2002).

Following the GOE, the onset of oxidative continental weathering, and thus an increase in the flux of sulfate to the ocean, is supported by the disappearance of detrital pyrite from sediments (Holland, 2002; Bekker et al., 2004). As there is no evidence for a further rise in atmospheric oxygen until the Late Neoproterozoic that could have enhanced the flux of sulfate to the oceans, the primary control on low seawater sulfate concentrations would therefore be the expansive sulfate drawdown with pyrite in euxinic basins (Turner and Bekker, 2016). Indeed, there is abundant evidence for Mesoproterozoic euxinia in a variety of locations, including the 1.73 - 1.4 Ga McArthur basin, Australia (Shen et al., 2002, 2003; Brocks et al., 2005), the 1.45 Ga Belt basin (Lyons et al., 2000; Scott et al., 2008), the 1.1 Ga Vazante Group, Brazil (Geboy et al., 2013), and the 1.1 Ga Taoudeni Basin, Mauritania (Gilleaudeau and Kah, 2013; Beghin et al., 2017). The resultant low sulfate concentrations and concomitant low-oxygen content in the global ocean would allow for larger hydrothermal and diagenetic fluxes of Fe_{HR} to the ocean. Coupled with low TOC availability in the BMA sediments (Figure 3.4), these conditions likely poised the water column in the Bashkir basin at Fe reduction, rather than sulfate reduction, thus favouring the development of ferruginous, rather than euxinic conditions (Poulton and Canfield, 2011).

Pyrite sulfur isotope values show more variability in the middle Neoproterozoic Karatau Group sediments (Figure 3.4), potentially reflecting an increase in seawater sulfate content due to progressive oxygenation of the atmosphere-ocean system in the run-up to the Cryogenian glaciations (Thomson et al., 2015; Turner and Bekker, 2016). However, only a limited number of the Karatau samples provided enough sulfide for isotopic analysis and hence the data-set is too small to provide a firm interpretation. Nevertheless, in a global study of water column redox conditions, Guilbaud et al. (2015) suggest that open ocean seawater sulfate concentrations were relatively low in the early Neoproterozoic, with the oceanic influx of Fe_{HR} overwhelming the flux of sulfate. This led to a global expansion of ferruginous conditions, consistent with data from the BMA.

A particularly prominent feature of the data presented here is the general restriction of oxic water column conditions to the shallowest waters in the Bashkir basin, with minor occurrences of oxygenated conditions in deeper settings. This is consistent with some studies on the North China Craton through the Mesoproterozoic (Luo et al., 2014; Tang et al., 2016), but contrasts with recent evidence for progressive oxygenation and a deepening of the oxycline starting at ~1.57 Ga in the same area (Zhang, Xiangkun Zhu, et al., 2018). In addition, restriction of oxic conditions to very shallow waters contrasts

with suggestions of broadly contemporaneous deep water oxygenation at ~1.4 Ga elsewhere on the North China Craton (Zhang et al., 2016), in the McArthur basin of Northern Australia (S. Yang et al., 2017) and in the Kama-Belsk aulacogen of Volga-Ural region of Russia (Sperling et al., 2014). Interestingly, the records of atmosphere-ocean oxygenation in these latter basins are all associated with the ~1380 Ma large igneous province (LIP) linked to the breakup of the Columbia-Nuna supercontinent and the Mashak magmatic event in the BMA (Evans and Mitchell, 2011; Puchkov et al., 2013). It initially seems counterintuitive that atmosphere-ocean oxygenation followed the emplacement of LIPs, as the latter should have delivered reductants to the atmosphere and ocean. However, LIPs also supplied CO_2 and SO_2, which could have enhanced chemical weathering on the continents, providing more nutrients to the oceans. This, in turn, may have enhanced primary productivity and organic carbon burial, leading to oxygenation. It thus remains to be tested with higher resolution studies whether the spatial and temporal extent of shallow water oxygenation on the BMA was more variable and dynamic on timescales not encapsulated by the sampling strategy used here. This would agree with Figure 3.8, where occurrences of oxic conditions prevail, but are minor in comparison to anoxic waters, in deeper sections than near-coastal settings. Nevertheless, this data clearly highlight that in this particular basin, ferruginous conditions dominated all but the shallowest waters across a 900 m.y. time period.

It is additionally noted that there remains much uncertainty over the evolution of ocean redox chemistry and levels of atmospheric oxygen through the Mesoproterozoic (Planavsky et al., 2014a; Zhang et al., 2016; Daines et al., 2017). The study of Sperling et al. (2014) advocates for deep water oxygenation at ~1.4 Ga, largely based on a lack of enrichment in Fe_{HR} and redox-sensitive trace metals. In many ways this is a compelling argument, but there are alternative explanations for the data. For example, simple mass balance constraints denote that enrichments in Fe_{HR} are not possible across a global anoxic ocean. Thus, some areas of the anoxic ocean must constitute a source of Fe_{HR} to allow for enrichments elsewhere (Poulton and Canfield, 2011). In modern anoxic basins, a shallow to deeper basin Fe shuttle is commonly advocated (Anderson and Raiswell, 2004; Severmann et al., 2008). However, modern anoxic basins do not adequately reflect global ocean anoxia, as in ancient settings considerable water column Fe(II) was likely sourced from anoxic non-sulfidic porewaters in the deep ocean (Poulton and Canfield, 2011), as well as from submarine hydrothermal vents. This Fe(II) would upwell onto the continental shelves to a site where water column precipitation was promoted. Thus, under widespread anoxic conditions, deeper sediments should

not exhibit Fe_{HR} enrichments. In addition, as highlighted in the current study where there is very strong evidence for ferruginous conditions, trace metal enrichments in low-TOC, deep water ferruginous settings would not be expected in the absence of an Fe (oxyhydr)oxide shuttle to the sediments (i.e., if the sediments were a source rather than a sink of Fe_{HR}). Thus the evidence for deep water oxygenation in the Volga-Ural region remains rather equivocal. Furthermore, based on the Re-Os ages, sediments studied by Sperling et al. (2014) in the Kama-Belsk aulacogen of Volga-Ural region are correlative to the Middle Riphean Yurmatau Group of the BMA and are located inland from the continental margin by at least 150 miles, questioning their deep-basinal setting. Similarly, there is considerable debate over the evidence for deeper water oxygenation based on vanadium depletion in ~1.4 Ga North China Craton sediments (Planavsky et al., 2016; Zhang et al., 2016). However, recent investigations into the Xiamaling Formation from the North China Craton using multiple redox proxies has demonstrated variable bottom-water chemistry, ranging from oxic to both anoxic ferruginous and euxinic (X. Wang et al., 2017; Diamond et al., 2018). The contrasting observations and ongoing debate outlined above clearly emphasizes that further research is required to evaluate spatial and temporal variability in ocean redox conditions through the Mesoproterozoic Era, which would then ultimately inform the discussion on the evolution of atmospheric oxygen levels (Daines et al., 2017; Planavsky et al., 2014, 2016; Zhang et al., 2016) over this critical juncture in Earth history.

3.6 Conclusions

Iron speciation analyses provide strong evidence for anoxic water column conditions beneath a very shallow chemocline, throughout deposition of the ~1.75 - 0.8 Ga succession of the Bashkir Meganticlinorium of the South Urals. An integrated evaluation of Mo, U, and Mn concentrations provides robust support for this ocean redox reconstruction, and suggests that relatively minor sediment enrichments in Mo resulted from an Fe (oxyhydr)oxide particle shuttle that operated largely in the absence of dissolved sulfide. Sulfur isotope systematics suggest that ferruginous conditions in the basin likely arose due to low sulfate availability, which was exacerbated by low TOC in this relatively unproductive setting. These data add to a growing database highlighting major discrepancies and uncertainties in the spatial and temporal extent of ocean oxygenation through the Mesoproterozoic Era.

Chapter 4 Redox and nutrient cycling in the mid-Proterozoic: Evidence from the North China Craton

4.1 Introduction

The first appreciable rise in atmospheric oxygen concentrations had severe repercussions on the chemistry of the Earth's surface. The GOE saw oxygen levels rise to above 10^{-5} PAL at 2.3 – 2.2 Ga (Holland, 2002), initiating the onset of oxidative weathering of continental crust. However, the Earth's oceans lagged behind and remained predominantly anoxic for nearly two billion years until deep ocean oxygenation occurred in some areas during the Late Neoproterozoic (Canfield et al., 2007). As atmospheric levels of oxygen were still relatively low in comparison to PAL, only the surface mixed layer of the ocean became oxygenated, with deeper waters remaining anoxic (Poulton and Canfield, 2011). The advent of oxidative weathering of continental crust introduced new mineral species into the marine system via fluvial transport. Weathering of continental pyrite transported soluble sulfate into a widely anoxic ocean (Catling and Claire, 2005), and was hypothesized to have caused the development of widespread euxinic (sulfide-rich) conditions (Canfield, 1998). Further geochemical studies modified this theory by limiting the spatial extent of euxinia to productive continental margins (Poulton, Fralick, et al., 2004; Poulton et al., 2010; Scott et al., 2008; Partin et al., 2015; Kendall et al., 2011). It is now widely accepted that the Late Palaeoproterozoic to Mesoproterozoic oceans contained an oxic surface layer, overlying deeper ferruginous waters with a euxinic wedge on productive continental margins. However, substantial gaps still exist in this record and do not account for spatial and temporal redox variations that can occur in one location (Wang et al., 2017). This study aims to add to the record of ocean redox during this period with a multiproxy approach using iron speciation, major element (Mn, Al) and trace metal analyses (Mo, V, U, Cr) on sediments from the Late Palaeoproterozoic to Mesoproterozoic (1.8 – 1.4 Ga) Yanshan Basin in North China.

An increase in free oxygen concentrations not only had irreversible environmental impacts, but also shaped biological evolution during this period. The emergence of macroscopic eukaryotes in a prokaryote-dominated world is widely believed to be the result of increased oxygen availability in the oceans. Oxygen gives the largest amount of free energy compared to any other element

when it acts as a terminal oxidant in biological metabolism (Catling et al., 2005). The larger amount of energy required for oxygen consumption implies that organisms utilizing aerobic metabolism could grow to much larger body sizes than anaerobic metabolizers, thus placing oxygen at the forefront for the evolution of more complex organisms (Catling et al., 2005; Butterfield, 2009). The radiation of life is also restricted by limiting levels of nutrients. The three main limiting nutrients for life on the planet are P, N and C (Redfield, 1958). Phosphorus is generally considered the ultimate limiting nutrient over geological timescales (Tyrrell, 1999). Modelling studies propose that continued P burial in oxic settings limits primary production and as a result, less respiration occurs as organic matter settles through the water column, helping to maintain well oxygenated conditions that are required for complex life to evolve (Lenton et al., 2014). Until now there have been few detailed studies examining P burial mechanisms in ancient sediments, as discussed in Chapter 1. The intention of this study is to analyse the respective phases of sedimentary P in the 1.8 – 1.4 Ga Yanshan Basin sediments: P_{Fe}, P_{mag}, P_{det}, P_{org} and P_{auth}, to assess if the P cycle behaved differently during a period of Earth's history dominated by prokaryotic life. The Mesoproterozoic Gaoyuzhuang Formation in this sedimentary succession contains palaeontological evidence for the evolution of macroscopic eukaryotes (Zhu et al., 2016). The same subformation where these fossils are documented was sampled for this study, but the exact horizon where they were found was not. This research also focuses on examining the differences between the mean P content of sediments from the Gaoyuzhuang Formation, to the underlying Palaeoproterozoic horizons to assess if any significant changes occurred during this period linked to eukaryote evolution.

4.2 Geological Setting

4.2.1 North China Craton Formation

China can be divided into three separate Precambrian blocks, which later amalgamated during the Phanerozoic. They are the North China Craton (NCC), the South China Craton and the Tarim Craton (Figure 4.1; Zhao and Cawood, 2012). The NCC predominantly consists of Neoarchean igneous rocks that formed in two distinct phases at 2.8 – 2.7 Ga and 2.55 – 2.5 Ga, but it is also the oldest of the three cratons, with rocks dating back to 3.8 Ga (Kusky and Li, 2003; Zhao and Cawood, 2012). There are major divisions across the literature

surrounding the formation of the NCC. It is generally agreed that the craton represents an amalgamation of multiple micro-continental blocks, but the number of the blocks involved is strongly contested. The Eastern and Western Blocks were originally propose to have collided along the Central Orogenic Belt at ~2.5 Ga to form the Archaean basement of the NCC (Zhao, 2001; Kusky and Santosh, 2009). However, the basement has further been divided into five (Zhai et al., 2001) and seven separate blocks (Zhai and Santosh, 2011). Disagreements also exist concerning the formation date of the NCC. One theory suggests that the final amalgamation took place at 1.85 Ga in a continent-continent collision between the Eastern and Western Blocks, with evidence for this timing based on petrologic data and U-Pb isotopic dating in zircon grains (Zhao et al., 2005; Zhao et al., 2008; Zhao et al., 2012). Other authors argue for an earlier formation at ~2.5 Ga based on geochronological and field observations (Kusky and Li, 2003; Wang et al., 2017b; Kusky et al., 2001). Regardless of the ultimate formation date, there is a general agreement for the stabilization of the NCC occurring by 1.8 Ga. Continued extension of the NCC resulted in the emplacement of mafic dyke swarms (1.8 – 1.75 Ga) (Zhao and Cawood, 2012) in an intracontinental rift basin. The NCC remained in a stable tectonic setting during the Late Palaeoproterozoic to the Neoproterozoic, aiding the deposition and preservation of basin fills from this time period. The basal Changcheng Group was deposited in a basin undergoing extensional tectonics associated with early synrift subsidence (Meng et al., 2011). The post-rift stage involved the deposition of siliciclastics and carbonates on a shallow marine platform (Meng et al., 2011).

Also highly disputed throughout the literature is the palaeogeographic position of the NCC. During the Late Palaeoproterozoic, the Columbia/Nuna supercontinent accreted during the Luliang Orogeny (Rogers and Santosh, 2002; Zhao et al., 2002). Palaeomagnetic data indicate the supercontinent lasted from 1780 – 1400 Ma, coinciding with the Yanshan basin formation (Zhang et al., 2012). The long-lived nature of this supercontinent has been attributed to subduction-related growth at continental margins by the accretion of microcontinental blocks (Zhao et al., 2004). While the existence of the supercontinent is agreed upon, the locality of the NCC within the giant landmass is contested. Most authors suggest an intracontinental plate setting, far from the continental margin for the position of the NCC (Lu et al., 2008; Kusky and Santosh, 2009; Meng et al., 2011; Luo et al., 2014; Zhai et al., 2015), but several others hypothesize proximity to the supercontinent’s edge (Wan et al., 2015). Geological evidence of mafic dyke swarms, continental flood basalts, layered mafic intrusions and alkaline granites (Lu et al., 2008)

strongly agree with deposition in an intracontinental rift basin undergoing continental rifting and is favoured throughout the literature. An intracontinental setting for the NCC is considered in this study, with further geochemical evidence proposed here to support this position.

4.2.2 Stratigraphy

The sedimentary succession investigated in this research is located in the Yanshan basin, approx. 90 km east of Beijing in North China, as illustrated in Figure 4.1. This basin represents a failed arm, or aulacogen, of a triple junction involved in the formation of the NCC. The Yanshan aulacogen is a thick sequence of sedimentary strata (~9 km) deposited from the Late Palaeoproterozoic to Mesoproterozoic (~1.8 – 1.4 Ga). There is no record in the NCC of extensive metamorphism and magmatic activity associated with the assembly and subsequent breakup of the Neoproterozoic Rodinia supercontinent (Zhai et al., 2003; Zhai et al., 2015). This succession therefore escaped the global-scale Grenville collisional events, leaving the sediments essentially unmetamorphosed with no evidence for strong deformation (Zhai et al., 2015; Lu et al., 2008).

The stratigraphic log for the Yanshan sedimentary succession is illustrated in Figure 4.2, and documents the assembly and subsequent breakup of the supercontinent Columbia. The Changcheng Group sits unconformably on Archaean metamorphic basement established during the assembly of Columbia (Zhao et al., 2002). The unconformity between the Changcheng and Nankou Groups records the separation of the NCC from the Indian Craton at ~1.6 Ga, and the switch from an intracontinental setting to an epicontinental one (Meng et al., 2011).

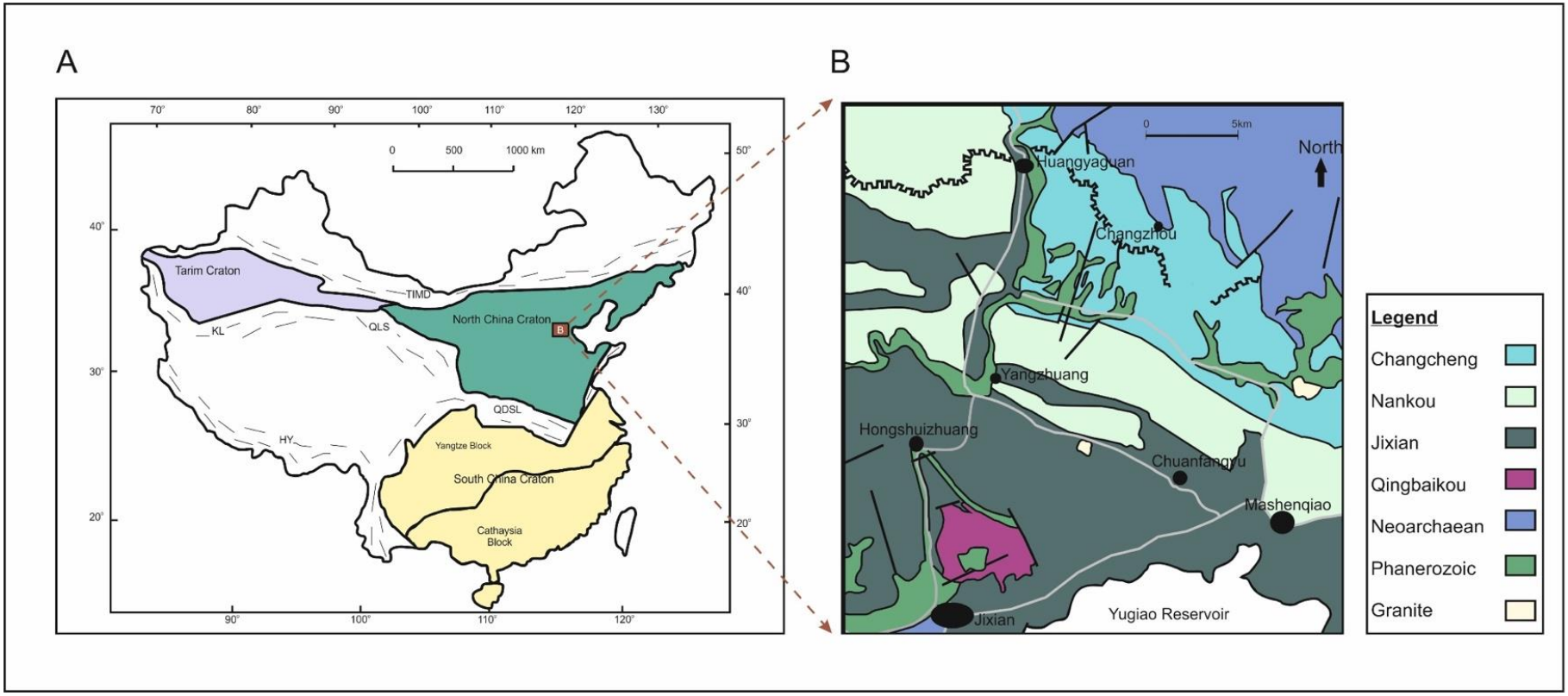

Figure 4.1 Tectonic map of China illustrating the three Precambrian cratons and Late Neoproterozoic and Palaeozoic fold belts. HY - Himalaya fold belt; KL - Kunlun fold belt; JSS- Jiangshan-Shaoxing suture; QDSL - Qinlin-Dabie-Su-Lu fold belt; QLS - Qilianshan fold belt; TIMD – Tianshan-Inner Mongolia-Daxinganling fold belt. Image taken and adapted from Zhao et al. (2001). B Geological map of Proterozoic sequences exposed in the north of Jixian County, Tianjin.

4.2.2.1 The Changcheng Group

The Changcheng Group (~1.8 – 1.6 Ga) consists of four formations: the Changzhougou, Chuanlinggou, Tuanshanzi and Dahongyu Formations. This group was deposited in narrow fault-bounded areas of an extensional basin (Li, Planavsky, Love, et al., 2015). The oldest of the formations, the Changzhougou Formation (854 m thick, 1.8 Ga; Wan et al. (2003)), is composed of coarse sandstones of alluvial facies with minor amounts of thick-bedded conglomerate and shale towards the base of the unit. The unit fines upwards into finer-grained sandstones of marine origin at the top of the formation, of which nine samples of mudstone were sampled for this study. Acritarch assemblages from this formation have been used to suggest that eukaryotic microbial life had evolved by this point (~1.8 Ga) (Zhu et al., 2000; Lamb et al., 2009). However, the affinity of acritarchs still remains unknown with a strong argument for their origin as remnants of unicellular protists rather than eukaryotic organisms (Butterfield, 2005a; Butterfield, 2005b).

The overlying Chuanlinggou Formation (1700 ± 50 Ma, Peng et al. (2009)) represents a transition to a subtidal low-energy environment. It is dominated by silty and illitic shales with some sandstone lenses. At the base where minor interbedded sandstone layers have been found, desiccation cracks and sand-veinlets are also present, signifying the occurrence of supratidal conditions and further suggesting episodic shallowing. More calcareous shales have been documented in the upper member of this formation, along with diagenetic carbonate nodules, lenses and laminae (Li, Planavsky, Love, et al., 2015). Acritarchs are also abundant in the microfossil assemblage of this unit (Peng et al., 2009). For this research, 27 shale samples were collected from a river cutting at the base of the Chuanlinggou Formation.

The next formation in the Changcheng Group, the Tuanshanzi Formation (518 m), was not sampled for this study. It is comprised of muddy dolostones at the base with a silty shale horizon in the upper portion of the unit. Here, ripple marks, desiccation cracks, flute and furrow casts, and cross bedding suggest a lagoonal or supratidal depositional environment (Zhu and Chen, 1995). An alkaline volcanic horizon also occurs at the top of the unit, consisting of ultrahigh-potassium basalts and trachybasalts (Lu et al., 2008). Dating (U-Pb) of zircon grains within this horizon gave a date of 1683 ± 67 Ma for this volcanic eruption event (Li et al., 1995). Potential further evidence for the emergence of multicellular organisms in the Tuanshanzi Formation has also been documented in this formation. Carbonaceous compressions of leaf-like megafossils are invoked as benthic, multicellular algal fossils (Zhu and Chen,

1995). Further geochemical work on the organic C isotopes ($\delta^{13}C_{org}$) and structural order of the organic matter C chains of these compressions similarly suggest these carbonaceous films are derived from phototrophic, eukaryotic algae (Qu et al., 2018).

The final member of the Changcheng Group is the Dahongyu Formation, also not used in this research. The lower part of this unit consists mainly of quartz sandstone with minor sandy dolostones. Overlying these siliciclastic units is a horizon consisting of volcanic breccia, and similar to the Tuanshanzi Formation, high potassium basalts. Radiometric dating of zircon grains from the basalts gave a U-Pb isochron age of 1625 ± 6 Ma (Lu and Li, 1991). The upper portion of the formation contains silty shale and dolomicrite, with abundant stromatolites. A peritidal environment is interpreted for the deposition of the Dahongyu Formation (Mei et al., 2007).

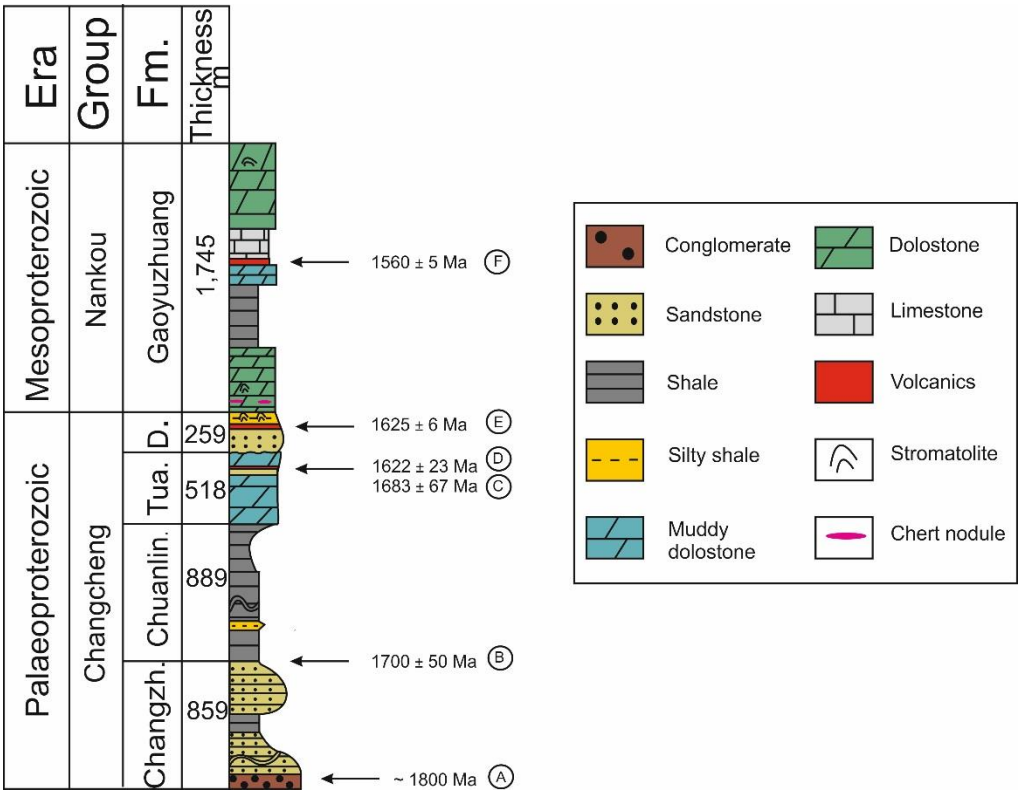

Figure 4.2 Stratigraphic log of the Proterozoic sedimentary succession on the northern margin of the NCC. Changzh - Changzhougou Fm; Chuanlin - Chuanlinggou Fm; Tua - Tuanshanzi Fm; D - Dahongyu Fm. Stratigraphic log adapted from Zhu et al. (2016) & Zhai et al. (2015). Relative age references are as follows: A - Wan et al. (2003); B - Peng et al. (2009); C - Li et al. (1995); D - Lu et al. (2008); E - Lu and Li (1991); F - Li et al. (2010)

4.2.2.2 The Nankou Group

As previously mentioned in 4.2.2, a transgressive unconformity separates the Nankou Group from the underlying Changcheng Group, representing a shift in the tectonic regime operating at this time. Rifting and normal faulting that reigned during the deposition of the Changcheng Group ceased and resulted in the development of a stable craton with an open shelf developing (Mei and Tucker, 2011). The Gaoyuzhuang Formation is the only formation in the Nankou Group but can be subdivided into four members: the Guandi, Sangshuan, Zhangjiayu and Huanxiusi Members. It is a 1000 m thick carbonate formation, thus validating the occurrence of long-lived shallow marine conditions (Mei, 2008). Carbonates are suitable for palaeoredox studies once certain criteria met. An Fe_T content greater than 0.5 wt% is used as the lower limit for carbonates, as it was found that Fe_T, rather than the proportion of carbonate in a sample, was a more suitable tool in identifying whether they are suitable for palaeoredox analyses. This limit will be taken into account when using these samples in this research.

The Guandi Member of the Gaoyuzhuang Formation predominantly consists of dolostone, with a thin bed of siltstone in the middle of the unit. Four muddy-dolostone samples were collected from here. The Sangshuan Member comprises manganiferous dolostone at the base, and transitions to thick-bedded dolostone at the top. No samples were taken from this unit. The third member, the Zhangjiayu Member, begins with a bed of muddy dolostone before transitioning to a siltstone and shale horizon in the middle, and a limestone unit at the top. A volcanic tuff at the boundary between the limestone and shale obtained a U-Pb LA-MC-ICP-MS age of 1560 ± 5 Ma and a U-Pb SHRIMP age of 1559 ± 12 Ma (H.K. Li et al., 2010). Six shales and 29 limestones were collected from the Zhangjiayu Member. The uppermost Huanxiusi Member is a thick bedded dolostone package, of which 15 muddy-dolostones were taken. The depositional environment for the Gaoyuzhuang Formation is evoked as an alternating assemblage of open shelf or outer ramp to peritidal, based on the carbonate cyclicity (Mei, 2008; Mei et al., 2009; Mei and Tucker, 2011).

The Gaoyuzhuang Formation has received substantial attention in the last decade due to the preservation of decimetre to centimetre scale eukaryote fossils in the Zhangjiayu Member. They are preserved as carbonaceous compressions, and provide compelling evidence that during the Mesoproterozoic Era, eukaryotes had evolved to more complex, macroscopic forms (Zhu et al., 2016). Macroscopic forms, such as colonies, of eukaryotes have been suggested to be more probable evidence for the transition from unicellular to multicellular life, as by arranging themselves into such structures, greater levels of gas exchange would be possible than in unicellular form (Butterfield, 2018).

4.3 Materials and Methods

All the techniques and relative errors on each method is detailed in Chapter 2. Table 3.1 lists the location of each of these procedures.

Table 4.1. List and location of methods employed for the North China sedimentary succession

Method	Heading #	Page #
Total Carbon (TC)	2.2.1	42
Total Organic Carbon (TOC)	2.2.2	43
Total Inorganic Carbon (TIC)	2.2.3	44
Iron Speciation	2.3	44
Bulk Digests	2.4	50
Phosphorus Speciation	2.5	56
Organic Carbon Isotopes ($\delta^{13}C_{org}$)	2.7	63

4.4 Results

All results for this chapter can be found in Appendix C.

4.4.1 TIC & TOC

The TIC and TOC results from the Yanshan basin are illustrated in Figure 4.3. All samples from the Changcheng Group have low TIC (0.085 wt% average), thereby classifying them as shales. The succession transitions into a more carbonate-dominated assemblage, as evidenced by high TIC values (7.19 wt% average) in the Gaoyuzhuang Formation.

TOC is consistently low in the Changzhougou Formation, with an average of 0.073 wt%. These limited values do not prevail in the overlying Chuanlinggou, with values reaching a maximum of 2.1 wt% in the middle of the sampled section. Following this rise, a decline to ~1 wt% TOC occurs for the remainder of the unit. The carbonate-dominated Gaoyuzhuang Formation similarly has muted TOC levels to the Changzhougou, with an average of 0.058 wt%.

4.4.2 Major Elements (Al, Mn, Fe)

Major elemental results are compared to Average Shale (AS) values to assess if their concentrations are enriched or depleted. Aluminium, Mn and Fe results are presented in Figure 4.3. In the Changzhougou Formation, Al and Fe parallel one another by rising to greater concentrations towards the top of the unit from lower values at the base. Aluminium reaches enriched levels in comparison to AS, while Fe does not reciprocate this trend and remains below. Manganese similarly exhibits depleted values in the Changzhougou. In the overlying Chuanlinggou Formation, enrichments in Al continue with an average of 10.6 wt% in the unit, 3.73 wt% Fe_T and Mn 0.032 wt% averages. Both Mn and Fe_T revert back to low values in the Gaoyuzhuang Formation, with the exception of high concentrations in carbonates at the base.

4.4.3 Iron Speciation

The proportions of each iron phase involved in the iron speciation extraction (Fe_{CARB}, Fe_{OX}, Fe_{MAG}, Fe_{PY}) and the boiling HCl extraction (Fe_{PRS}) in reference to Fe_T is shown in Figure 4.3. Iron oxides are the main highly reactive iron phase in the Changzhougou Formation, which also contains high proportions of $Fe_{PRS.}$ A more varied iron pool is evident in the Chuanlinggou, with a larger amount of Fe_{CARB}, Fe_{MAG} and small increases in Fe_{PY}. Where TOC is highest and Fe_T lowest, Fe_{PRS} dominates the total iron pool in comparison to reactive phases. A return to Fe_{OX} as the main iron phase occurs in the upper portion of the sampled Chuanlinggou and is accompanied by relatively high amounts of Fe_{PY}.

Another shift in Fe dynamics is evident in the Gaoyuzhuang Formation, where Fe_{CARB} is the main iron phase with a limited amount of Fe_{OX} and Fe_{PRS} in comparison to the Chuanlinggou Formation. Only samples with greater than 0.5 wt% Fe_T were sampled for iron speciation due to problems that can potentially arise in oxic carbonates with low iron values (Clarkson et al., 2014).

4.4.4 δ13Corg

The $\delta^{13}C_{org}$ results are presented in Figure 4.3. At the base of the succession, values consistently plot between -28‰ and -31‰. Transitioning into the black shales of the Chuanlinggou Formation, a gradual excursion to more negative values (~ -34‰) is seen. Though not every sample in the Gaoyuzhuang Formation returned a $\delta^{13}C_{org}$ result, those that did show a change from values at ~ -27‰ in the Guandi basal carbonates, to ~ -34‰ in both shales and carbonates in the Zhangjiayu Member.

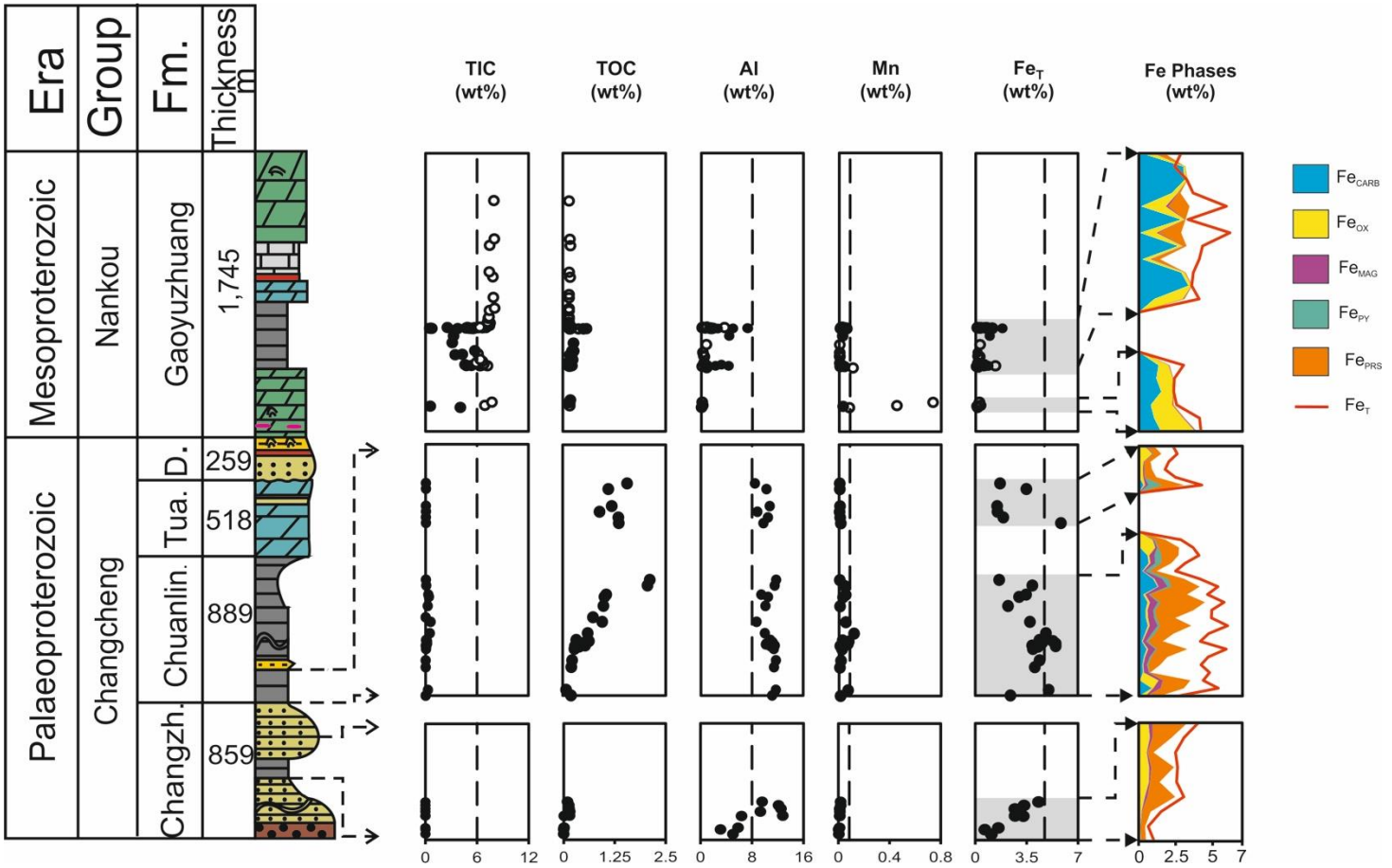

Figure 4.3 Chemostratigraphic log of TIC, TOC, $\delta^{13}C_{org}$, Al, Mn, Fe_T and each iron phase involved in iron speciation (Fe_{CARB}, Fe_{OX}, Fe_{MAG}, Fe_{PY}, Fe_{PRS}). Shales are represented by closed circles, while open circles are carbonates. Dashed lines represent average shale values for the respective elements, taken from Turekian et al. (1961): Al – 8 wt%; Mn – 0.085 wt%; Fe – 4.72 wt%

4.4.5 Trace Metals (Mo, V, U, Cr) and Mn

The normalized concentrations of Mo, V, U, and Cr are displayed in Figure 4.4. Trace metal (TM) concentrations are normalized to Al to filter out any potential dilutions to the TMs' signal, as high amount of detrital material can swamp the original concentration (Lyons and Severmann, 2006). No observable enrichments in reference to AS are found for all TM in the Changzhougou Formation. A similar muted signal continues into the Chuanlinggou Formation. Relatively small enrichments in comparison to AS are found for Mo and U in the shales from the Gaoyuzhuang Formation. Both V and Cr again exhibit depleted concentrations relative to AS. Though the sediments overall contain low levels of TM, the shape of the trends across all elements are very similar in both the Changzhougou and Chuanlinggou Formations, exhibiting similarly comparably located peaks and troughs.

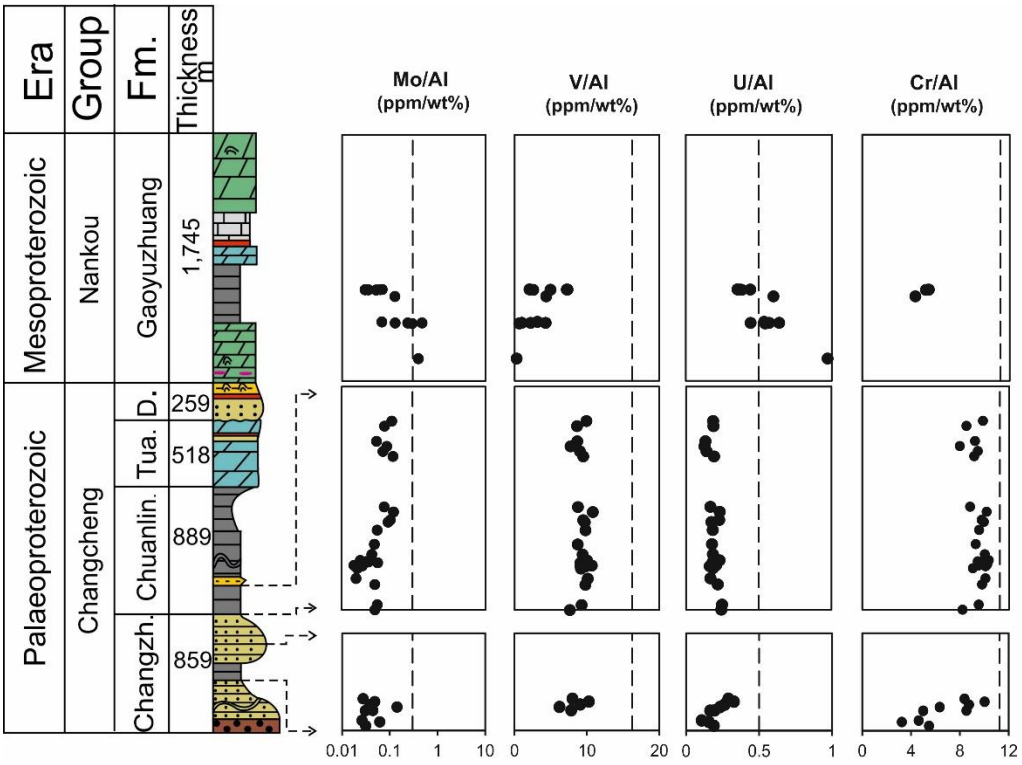

Figure 4.4 Chemostratigraphic log of normalized TM concentrations (ppm) to Al for Mo, V, U, and Cr. The dashed lines are indicative of the AS values determined by Turekian et al. (1961). They are: Mo/Al = 0.3; V/Al = 16.25; U/Al = 0.5; and Cr/Al = 11.25. Only shales are shown in this diagram

4.4.6 Phosphorus Speciation

Phosphorus recovered from the sequential extraction (P_{Sum}) versus P_{Tot} is illustrated in Figure 4.5. The majority of samples (81%) have an overall recovery of >70% P_{Tot} from the sequential extraction, with four samples in the

Changzhougou and two in the Chuanlinggou with a 50-70% recovery. Due to their low recovery, these samples will be removed from the discussion.

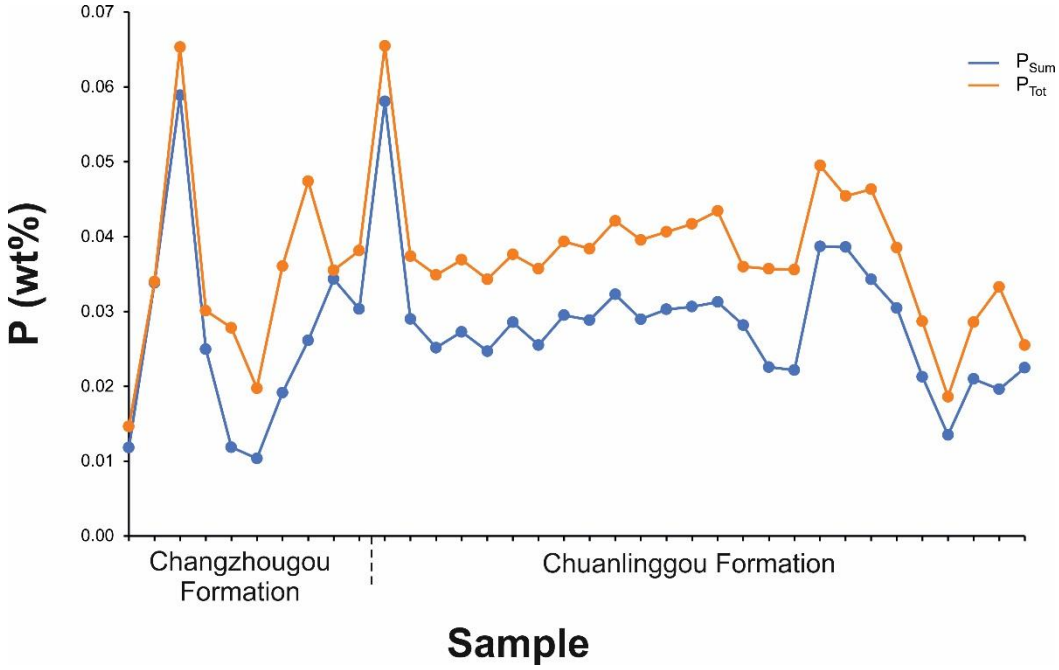

Figure 4.5 Graph of P_{Sum} vs. P_{Tot} for all samples used in the sequential extraction from the Yanshan basin

There are several explanations for low recovery of P: physical loss of sample while decanting of the supernatant solution during the extraction; and the incomplete extraction of P within highly refractory minerals (e.g. monazite), detrital apatite (März et al., 2014), highly refractory organic material (Ruttenberg and Goñi, 1997) or clay-bound P. Refractory organics and clay-bound P would most likely not be important constituents of ancient sediments due to their age or timescale these phases would persist at. To assess if detrital phases were not sufficiently extracted, the pool of remaining P (unextracted P; P_{unx}) was calculated as $P_{unx} = P_{Tot} – P_{Sum}$, and plotted against the Al content of the samples in Figure 4.6, and shows a positive but weak correlation ($R^2 = 0.508$). Due to the low recovery of some samples, it is possible that some P was lost during the extraction, as well as being associated with P_{unx}.

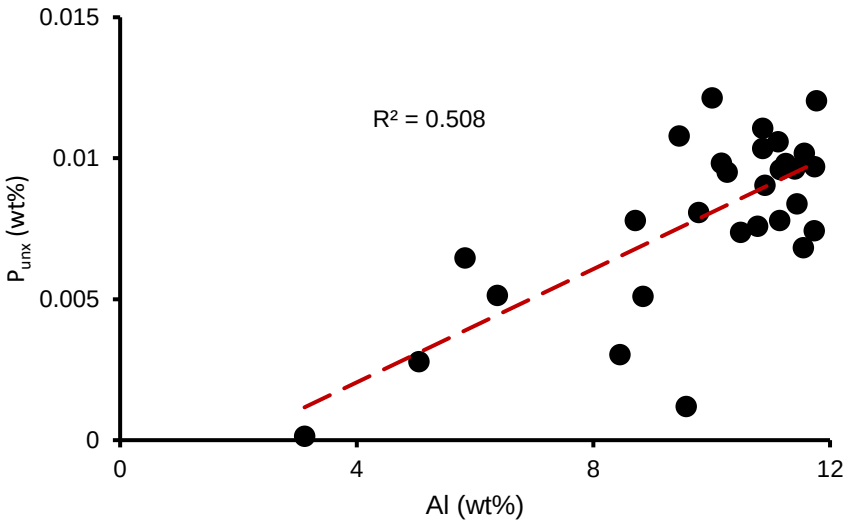

Figure 4.6 Plot of the remaining P at the end of the sequential extraction (P_{unx}) versus Al content (wt%) of the sample

A limitation of the sequential extraction which needs to be addressed is the potential removal of P_{auth} during the detrital stage. One of the major accomplishments of the original SEDEX technique by Ruttenberg (1992) was the ability to efficiently separate the reactive P pools (P_{Fe}, P_{auth}, P_{org}) from the non-authigenic, detrital fraction. Reactive P (P_{reac}) involves all phases available for biological uptake and are chemically reactive, capable of sink-switching during diagenesis (Ruttenberg, 1992; Ruttenberg and Berner, 1993). However, this technique was applicable for modern sediments and not ancient rocks. An added difficulty in using ancient sediments is the increased crystallinity of the minerals within the sediments, as a result of post-depositional alteration or its deformational history. This creates difficulty in efficiently separating the reactive phases from the detrital, and has also been shown to occur in some modern studies (Eijsink et al., 2000; Kraal et al., 2012). Such problems have been addressed by other authors (e.g. März et al., 2014) who used the relationships between P_{det} and P_{reac} to Al, to identify any correlation between the detrital fraction of the sediment (proportion of Al) to the sequential phases quantified during the extraction. In Figure 4.7A, P_{det} is plotted as a percentage of P_{Tot} against the Al content of the samples for the Changzhougou Formation. A strong negative correlation exists between these two pools (R^2=0.8045), suggesting higher amounts of P_{det} were associated with lower Al content. Such behaviour could potentially signify an issue previously encountered in sediments with high Al content, whereby overall recovery was lowest in those rich in Al (März et al., 2014). A very weak correlation between P_{reac} and Al (R^2=0.1014) in Figure 4.7B gives confirmation that the P extraction was successful in partitioning the detrital and reactive phases from one another, as

there is no correlation between the extracted P_{reac} and the detrital content of the sediment. More scattered relationships are evident for the Chuanlinggou Formation in Figure 4.7C and D, with no clear trends between P_{det} and P_{reac} against Al. This again could be a function of high Al content, resulting in an overall low percentage of P extracted during the procedure, and thus skewing any potential trends. In Figure 4.5, the difference between the P_{Sum} and P_{Tot} values for the Chuanlinggou Formation would corroborate with such reasons. Care must be taken in the interpretation of P speciation results as it cannot be ruled out by these trends alone that detrital phases were not removed during the authigenic stage of the procedure.

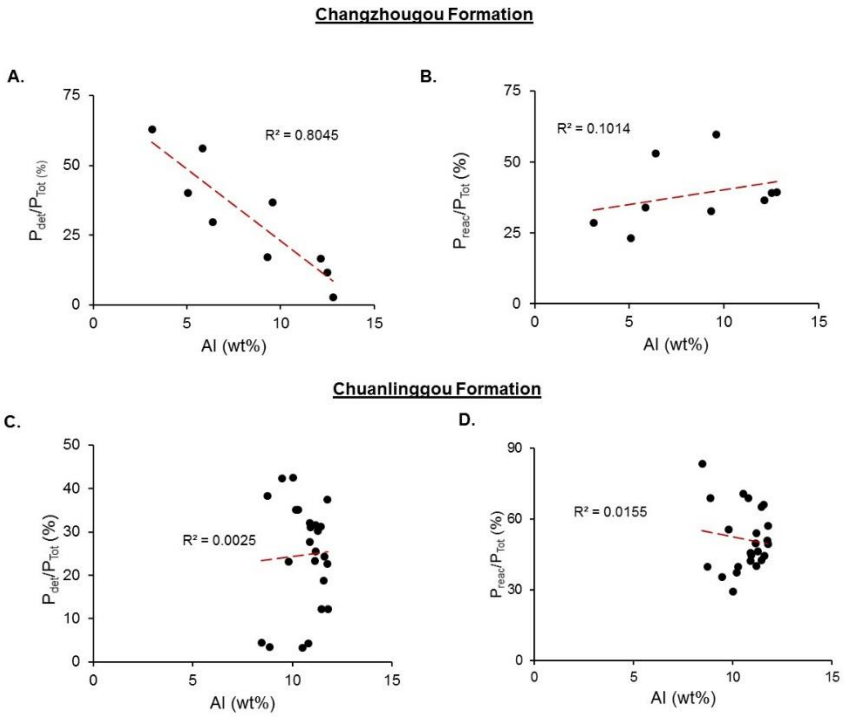

Figure 4.7 Assessment of trends between P_{det} and P_{reac} against Al for the Changzhougou and Chuanlinggou Formations. P_{det} and P_{reac} are reported as percentages of P_{Tot}.

The P_{Tot} and individual pools of P measured during the sequential extraction are shown in Figure 4.8. The Chuanlinggou Formation is subdivided into units A, B and C in Figure 4.8 for ease of explanation. Only shales and siliciclastics were analysed for P speciation as problems can arise in measuring the authigenic P fraction in carbonate-rich sediments. This occurs because apatite dissolution is promoted under low pH, but $CaCO_3$ has been found to buffer the acidity of the acetate solution used, thus preventing the complete

extraction of authigenic phases from the sediments (Kraal et al., 2009). Total P is generally low within the Changzhougou and Chuanlinggou Formations. Though not highlighted in Figure 4.8, the AS value of P in shales is 0.08 wt% (Turekian and Wedepohl, 1961). All samples from this succession plot below this, with an average of 0.035 wt% in the Changzhougou and a similar value of 0.038 wt% in the Chuanlinggou. The scatter in P_{Tot} at the base of the Changzhougou is far greater than the steady trend in the Chuanlinggou, even though their averages are comparable.

Though the samples across these two formations have remarkably similar P content, the proportions of individual P pools vary, as illustrated by their respective concentrations in Figure 4.8. At the base of the Changzhougou, P_{Fe} and P_{org} are not important phases, with the highest concentrations in P_{auth} (max. 191 ppm) and P_{det} (max. 367 ppm). A shift to higher concentrations in P_{Fe} and P_{auth} phases occurs at the top of the sampled unit, with P_{det} and P_{auth} phases at similarly low proportions before reverting back to levels found at the base.

Phosphorus burial mechanisms in the Chuanlinggou Formation remain relatively consistent in the bottom member (A). The presence of high concentrations of P_{Fe} (53 ppm) is accompanied by an increase in P_{org} (116 ppm) along with a decline in P_{det} and P_{auth} phases in A. Burial in both iron and magnetite phases becomes negligible in unit B, before P_{Fe} increases again to 130 ppm at the top in horizon C. Growth in P_{Fe} phases is accompanied by a rapid decline in P_{auth} and P_{det}, with organic phases remaining an important reservoir of P to these sediments. Both detrital and organic P pools display mirroring behaviour in the Changzhougou Formation, with higher P_{det} corresponding to lower P_{org} percentages, and vice versa. Within the Chuanlinggou Formation, P_{det} rises to 185 ppm at the A-B boundary before gradually declining to ≤ 16 ppm at the top of the sampled site in C. Organic P plots at 92 ± 38 ppm, until reaching a peak of 152 ppm at the top of horizon C.

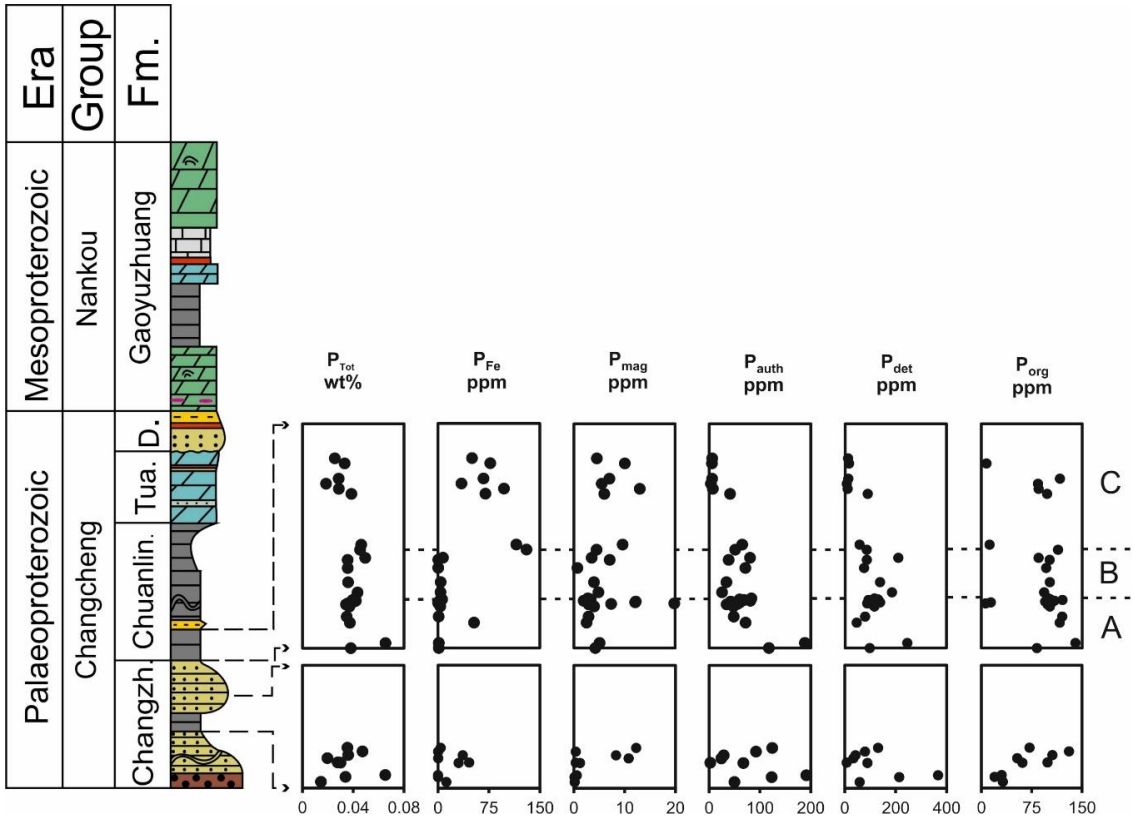

Figure 4.8 Phosphorus speciation results plotted stratigraphically for the Yanshan-Liaoxi Rift basin. P_{Tot} – Total P; P_{Fe} – Fe-bound P; P_{mag} – magnetite-bound P; P_{auth} – authigenic P; P_{det} – detrital P; P_{org} – organic-bound P. The Chuanlinggou is subdivided into units A, B and C.

4.5 Discussion

4.5.1 Fe-S-C systematics

The preliminary results presented in Figure 4.3 suggest the Yanshan basin experienced rapid fluctuations to its elemental sedimentary cycles. The coastal Changzhougou Formation exemplifies sediments dominated by a detrital input, with limited TOC and a high Al content. Aluminium is commonly used as an indicator for the detrital fraction in sediments (Lyons and Severmann, 2006), and with values greater than AS, this suggests an elevated input of Al-rich siliciclastic material. The dominant Fe phases within the Changzhougou sediments are Fe_{OX} and Fe_{PRS}. Another pool of sedimentary Fe that exists but was not individually measured during the speciation method is unreactive iron (Fe_U). Unreactive iron is iron which is unreactive towards dissolved sulfide (Canfield et al., 1992; Raiswell and Canfield, 1996; Anderson and Raiswell, 2004), and accounts for any gaps between the Fe_{HR} and Fe_{PRS} pools to Fe_T in Figure 4.3. The proportions of Fe_U and Fe_{PRS} are far greater than that of Fe_{HR} in these sediments, further corroborating with a terrestrial input as their main

source of iron. Reactive iron enrichments are typically sourced from a hydrothermal input (Poulton and Canfield, 2006), or from the intrabasinal mobilization of iron (Anderson and Raiswell, 2004). As the Changzhougou Formation was formed in a coastal depositional environment, far away from any potential hydrothermal input, and also at higher depths to shelf sediments where iron is diffusively released and mobilized to the deeper ocean, the incoming terrigenous input and proximal location to the riverine source resulted in iron silicates as the dominant phase here. The relationship between Fe_{HR} and Al for the Changzhougou Formation is shown in Figure 4.9. A positive correlation ($R^2 = 0.646$) between the Fe_{HR} pool and Al content of the sediments for the Changzhougou Formation exists, suggesting that proximity to the coast played a role in the delivery of reactive iron to this setting. No relationship is evident between Al and Fe_{HR} for the Chuanlinggou Formation, signifying detrital input did not play an important role in Fe delivery to these sediments.

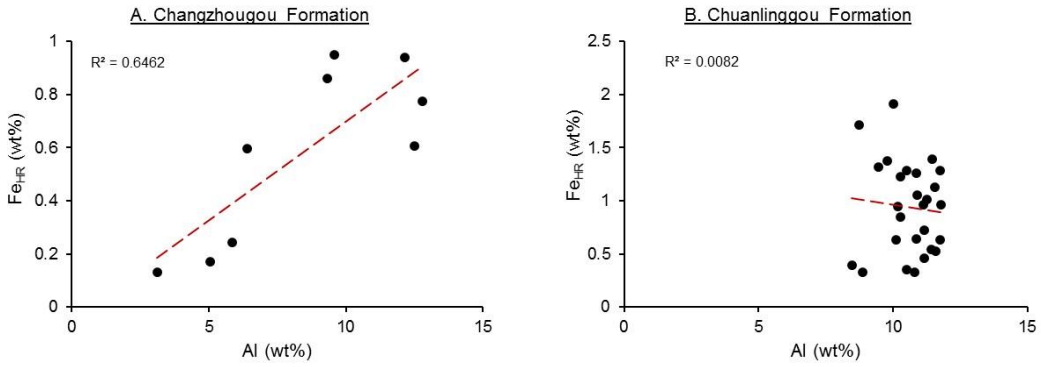

Figure 4.9 Relationship between the pool of Fe_{HR} and the detrital input (Al) for the Changzhougou (A) and Chuanlinggou (B) Formations

The individual pools of iron are subsequently used to identify the palaeoredox state of this basin through the Fe_{HR}/Fe_T ratio. The ratios from the Yanshan Basin are presented in Figure 4.11. Oxic to equivocal conditions are found in the Changzhougou Formation. While an equivocal result may represent oxic deposition, there are also two factors that might lead to these results under anoxic conditions: high sedimentation rates masking water column iron enrichments, or the diagenetic transformation of unsulfidized iron to Fe_{PRS} if insufficient free sulfide is available (Poulton and Canfield, 2011). As shown in Figure 4.3, there is a greater proportion of Fe_{PRS} to Fe_{HR} phases in

the Changzhougou Formation, suggesting the latter factor may be in operation here. A method to quantitatively assess if these equivocal values were initially deposited in an anoxic setting but subsequently transformed, involves the use of Fe_T/Al ratios. As previously mentioned, Al is a gauge for the detrital input to a sediment, and does not diffuse or travel during diagenesis (Lyons and Severmann, 2006). By normalizing Fe to Al, any detrital influence on the total elemental value is removed. The Fe_T/Al ratio is compared to the continental crust average (0.55 ± 0.11 wt%; Clarkson et al. (2014)), and if enriched is hypothesized to be indicative of an anoxic water column (Lyons and Severmann, 2006; Raiswell et al., 2008; Clarkson et al., 2014; Guilbaud et al., 2018). In Figure 4.11, it is evident that these equivocal samples are below the continental crust value for Fe_T/Al, suggesting these samples were oxic and are unlikely to be due to conversion of Fe_{HR} to Fe_{PRS} during early diagenesis. To rule out the transformation of reactive phases to Fe_{PRS} as a potential influence, the Fe_{HR}/Fe_T* ratio, as suggested in section 3.4.2, was applied to these samples to assess if the redox signal differed when taking Fe_{PRS} into account. The Fe_{HR}/Fe_T* ratio is defined as follows:

$$\frac{Fe_{HR}}{Fe_T}* = \frac{Fe_{HR}}{Fe_T}meas + \left(\frac{Fe_{PRS}}{Fe_T}meas - \frac{Fe_{PRS}}{Fe_T}PAS\right)$$

The new value (Fe_{HR}/Fe_T*) is incorporated into the data set when Fe_{HR}/Fe_T* is greater than the original Fe_{HR}/Fe_T ratio. Differences between the original and modified ratios are illustrated in Figure 4.10. Only one sample within the Changzhougou Formation depicts a change in redox, from an equivocal to anoxic state. It can thus be further advocated that the majority of the equivocal samples within this unit where not due to the loss of Fe_{HR} during diagenesis into the Fe_{PRS} pool.

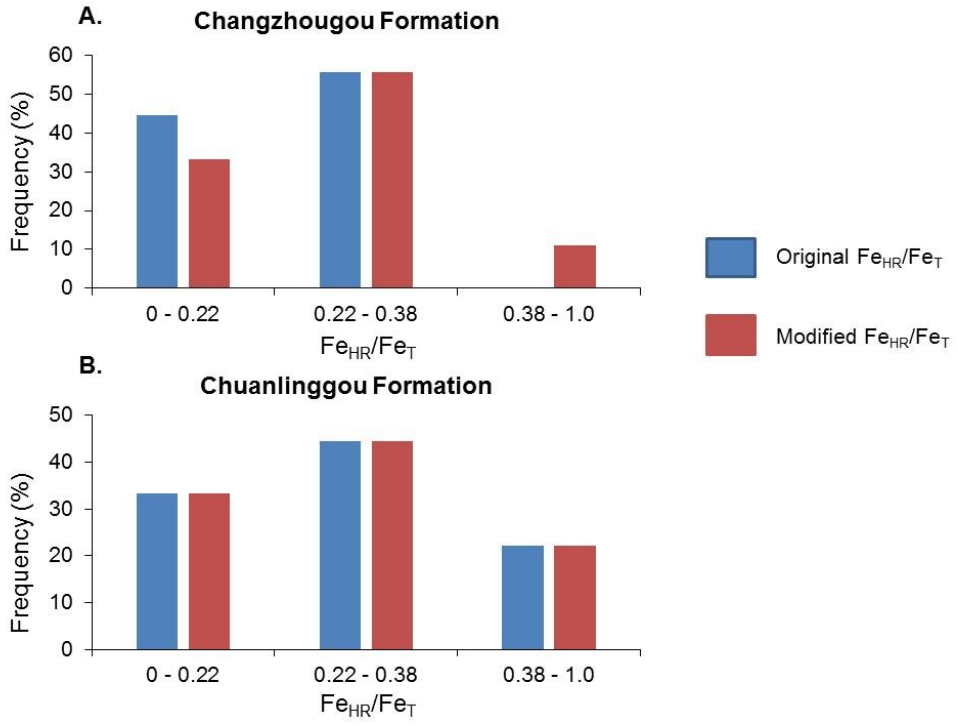

Figure 4.10 Bar chart illustrating the differences between the original Fe_{HR}/Fe_T ratio and the new Fe_{HR}/Fe_T* when incorporated into the data set

Further variations in redox occur throughout the subtidal Chuanlinggou Formation. Oxic and equivocal samples at the base in A, transition to anoxic at the A-B boundary before reverting back to dominantly oxic conditions at the top of the section in C. Equivocal samples all plot below 0.5 Fe_T/Al, and can consequently be considered as oxic, as Figure 4.10 shows there was no change to the identified redox state from the samples when using the Fe_{HR}/Fe_T* ratio. To assess whether this anoxic setting was ferruginous or euxinic, the ratio of Fe_{PY}/Fe_{HR} is utilized (Poulton and Canfield, 2011). The anoxic samples in B exhibit a gradual increase in Fe_{PY}/Fe_{HR} ratios, but do not reach a euxinic state (Fe_{PY}/Fe_{HR} >0.7), thus inferring this horizon as ferruginous. Iron carbonate and Fe_{MAG} are the dominant reactive iron phases within these sediments (Figure 4.3). The presence of these minerals in the Yanshan basin implies mixing of shallow oxic waters with deeper anoxic waters across a dynamic and shallow chemocline. Further evidence for this event can be seen in the depletion of Fe_T values in Figure 4.3, following the inferred location of the A-B boundary. This implies that a change in the position of the chemocline resulted in the drawdown of water column Fe. If Fe was removed from the seawater inventory, then little Fe_{HR} would remain to maintain ferruginous conditions. Such a scenario is witnessed in the low oxic-equivocal Fe_{HR}/Fe_T ratios in unit C of the

Chuanlinggou (Figure 4.11), suggesting deepening of the chemocline and oxygenated conditions pushing into deeper environments.

The gradual transition of the Chuanlinggou Formation to a ferruginous state is accompanied by a steady increase in TOC. Increased organic matter production led to the formation of pyrite through BSR, as evidenced by the increasing Fe_{PY}/Fe_{HR} ratios in unit B.

Dynamic redox conditions continue to prevail in the shallow marine Gaoyuzhuang Formation. A limited number of samples could be used for iron speciation as they contain <0.5 wt% Fe_T, which has been shown to potentially give inaccurate Fe_{HR}/Fe_T readings (Clarkson et al., 2014). The majority of carbonates and shales give an anoxic, ferruginous water column signal based on Fe_T/Al, Fe_{HR}/Fe_T and Fe_{PY}/Fe_{HR} ratios, perhaps with occasional development of oxic conditions. A rise in sea level deposited these sediments in a supratidal/intertidal environment (Luo et al., 2014), and prompted the chemocline to move to even shallower settings than in the Chuanlinggou, creating ferruginous shallow waters.

Other investigations into the chemistry of the NCC basin have utilized $\delta^{13}C_{org}$ values to suggest a shallow chemocline existed in a stratified water column (Luo et al., 2014). The $\delta^{13}C_{org}$ results from this study are illustrated in Figure 4.11 and closely match those from Luo et al. (2014). In the inter/supra-tidal Changzhougou Formation, fractionations range from -28 to -30‰, typical of organic matter produced via primary production (Hoefs, 2010). A negative excursion to more depleted values in the deeper Chuanlinggou (-31 to -34‰) similarly occurs across both studies. Lighter values in the organic C isotopic composition of sediments can be a function of: secondary production (heterotrophy/chemoautotrophy/methanotrophy; Jiang et al. (2012), Guo et al. (2013)); high productivity in anoxic waters fuelling organic matter generation (Froelich et al., 1982); increased preservation of organic matter in anoxic conditions (Canfield, 1994); or high sedimentation rates (Berner and Canfield, 1989). A combination of secondary production and prevailing anoxic waters potentially drove $\delta^{13}C_{org}$ isotopic values lighter. Evidence for secondary production stems from the divergence of the $\delta^{13}C_{org}$ away from typical values of primary production as hetero/chemo/methano-trophic bacteria assimilate C from depleted ^{13}C sources (Jiang et al., 2012). The role of redox can be identified by changes in the $\delta^{13}C_{org}$ value occurring across the A-B boundary. A switch from values typical of primary production in the oxic layer to lighter values in the ferruginous unit B and oxic unit C, suggests the deepening of the

chemocline lessoned oxygen demand in surface waters, and therefore primary production.

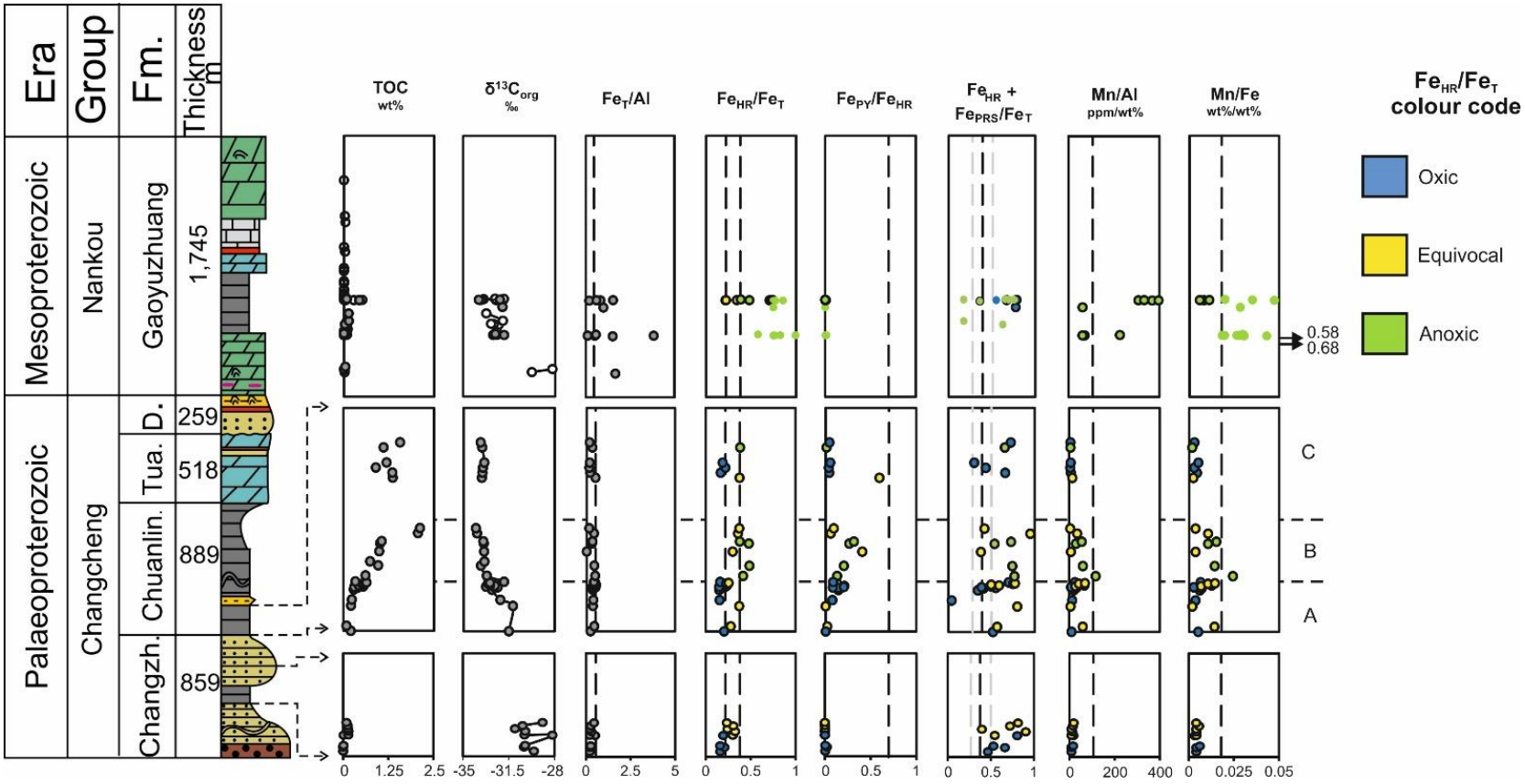

Figure 4.11 Log of TOC, $\delta^{13}C_{org}$, Fe_T/Al, Fe_{HR}/Fe_T, Fe_{PY}/Fe_{HR}, $(Fe_{HR}+Fe_{PRS})/Fe_T$; Mn/Al and Mn/Fe for the Yanshan basin. Samples are colour coded based on Fe_{HR}/Fe_T ratios: oxic – blue; equivocal – yellow; anoxic – green. Closed circles are shales while open circles signify carbonates. The dashed lines are as follows: 0.55 Fe_T/Al (Clarkson et al., 2014); 0.22 and 0.38 Fe_{HR}/Fe_T; 0.7 Fe_{PY}/Fe_{HR} (Poulton and Canfield, 2011); 106 Mn/Al, 11.25 Cr/Al, 0.018 Mn/Fe (Turekian et al., 1961)

4.5.2 Mn as a Palaeoredox Proxy

Classifying the redox state of a water column typically involves distinguishing a depositional environment as oxic or anoxic. These are two end members on a spectrum of a variety of redox states that can exist in nature. At a time in Earth's history when oceanic chemistry was evolving, it is possible suboxic conditions were an important redox state, as it is becoming commonly found across the literature (Cox, Jarrett, et al., 2016; Gilleaudeau and Kah, 2015; Kah and Bartley, 2011). Both Fe and Mn are sensitive to perturbations in redox, however Mn reduction always precedes that of Fe, making it much more sensitive to intermediate redox states (Sorensen and Jorgensen, 1987; Nealson and Saffarini, 1994; Tostevin et al., 2016). The ratio of Mn/Fe is commonly utilized as a proxy for the oxidation-reduction potential (Eh) of sediments during the time of deposition (Jackson, 2015). This tool is based on the sensitivity of Mn, as Mn oxides precipitate at higher O_2 concentrations and Eh than Fe (Jackson, 2015). In Figure 4.11 the Mn/Fe ratios for the Yanshan basin sediments are shown. All samples in the Changzhougou Formation plot below AS. As Mn (oxyhydr)oxides precipitate under oxic conditions, high Mn/Al values and thus larger Mn/Fe ratios would be expected. However, Mn/Al and Mn/Fe are relatively low within this horizon, potentially due to the high detrital input discovered in Figure 4.3. The Changzhougou may represent a period of pervasive oxygenation with naturally low Mn/Al in these sediments, thus pertaining to limited Mn/Fe ratios.

In the Chuanlinggou, a transition from an oxic interval at the base in unit A with low Mn/Fe, to horizon B with values greater than AS occurs before declining to depleted levels again in C. Ratios of Mn/Al as well as Mn/Fe are generally higher than the Changzhougou and exhibit larger fluctuations, consistent with episodic oxic-anoxic water column redox changes. Iron speciation results originally identified horizon B with high Mn/Fe as ferruginous. However, the high Mn/Fe ratio is indicative of a short-lived oxic event, potentially as a result of mixing between ferruginous deep waters upwelled from greater depths, precipitating Mn-Fe (oxyhydr)oxides at the chemocline. Evidence for this dynamic water column behaviour has previously been brought to attention by depleted Fe_T following this event (discussed in section 4.5.1). The demise of sedimentary structures such as cross bedding, and current generated structures (e.g. ripples, swash marks) moving stratigraphically up from the base of the Chuanlinggou provides evidence for the deepening of the section from supra-intertidal to subtidal in unit B and C, before experiencing further shallowing at the top of the formation (Li, Planavsky, Love, et al., 2015).

In the Gaoyuzhuang Formation, anoxic shales do not have high Mn/Fe ratios, solidifying their iron speciation results as ferruginous. Carbonates generally have a much higher Mn/Fe ratio (0.29) than shales (Mn/Fe = 0.018) (Turekian and Wedepohl, 1961). Calcite forms a nucleation site for Mn during carbonate precipitation, and when in an anoxic water column, is a major control on the removal of Mn (Mucci, 2004; Havig et al., 2015), forming manganese carbonates such as rhodochrosite ($MnCO_3$). Two samples in Figure 4.11 exhibit higher Mn/Fe ratios than the AS value. Iron speciation results identified these carbonates as ferruginous. Similar to the Chuanlinggou Formation, transient oxygenation events took place, resulting in ferruginous deep waters upwelling and mixing with surface oxic layers. These findings are consistent with a short-lived oxygenation event previously documented at the base of the Zhangjiayu Member of the Gaoyuzhuang Formation. Zhang et al. (2018) utilized iron speciation with Ce anomalies on carbonates from the Gaoyuzhuang Formation, and found evidence for weak oxygen events before persistent oxygenation in the deep marine (basin-slope) upper Zhangjiayu Member. This discovery has major implications due to the preservation of macroscopic eukaryotic fossils within this horizon (Zhu et al., 2016). The research presented here ties in with the findings of Zhang et al. (2018). Though water depths in the Chuanlinggou do not reach as deep as those in the upper portion of the Zhangjiayu Member, there is still evidence for the progression of oxygenated waters from supra-intertidal surface waters into the subtidal zone. Oxic waters are not found in the subtidal Sangshuan Member at the base of the Gaoyuzhuang Formation in this study or in Zhang et al. (2018), further implying that the base of the Chuanlinggou captures the first deepening of the chemocline, and thus deeper waters briefly becoming oxygenated before the chemocline returns to shallow depths. Again, it is important to note that these are still in shallow marine conditions, but these data add a dynamic history to the progression of deep ocean oxygenation within these mid-Proterozoic sediments.

4.5.3 Trace Metal (TM) Dynamics

Trace metal concentrations are widely used across the literature as palaeoredox proxies in ancient settings (Emerson and Huested, 1991; Tribovillard et al., 2006; Tribovillard et al., 2012; Algeo and Tribovillard, 2009; Algeo and Lyons, 2006; Crusius et al., 1996; Scott et al., 2008; Dahl et al., 2016; Gilleaudeau and Kah, 2013; Kendall et al., 2010; Parnell et al., 2015; Scott et al., 2012). The discovery of euxinic conditions in productive continental

margins from the Late Palaeoproterozoic to Neoproterozoic (Canfield, 1998; Shen et al., 2002; Poulton, Fralick, et al., 2004; Poulton et al., 2010; Poulton and Canfield, 2011; Meyer and Kump, 2008; Gilleaudeau and Kah, 2015; Cox, Jarrett, et al., 2016; Planavsky et al., 2018), prompted extensive investigations into the behaviour of Mo during this period (Arnold et al., 2004; Algeo and Lyons, 2006; Scott et al., 2008; Gilleaudeau and Kah, 2013; Kendall et al., 2011; Baldwin et al., 2013; Lyons et al., 2009; Dahl et al., 2016; Parnell et al., 2015). This is due to the strong coupling between sulfide availability and authigenic burial of Mo, as it is consistently observed that extensive enrichments in Mo accumulate under a euxinic water column. In ferruginous settings, Mo, V, U and Cr also accumulate to high levels in sediments, but display conservative behaviour in an oxygenated water column (Tribovillard et al., 2012). Pairing trace metal analyses with iron speciation results can give a better understanding of palaeoredox interpretations.

In Figure 4.4, no enrichments in Mo/Al or V/Al compared to AS occur in any of the sediments. This is unexpected for the anoxic samples, particularly for Mo, as elevated TOC typically operates as a shuttle for the drawdown of Mo in an anoxic water column if there is insufficient free sulfide (Algeo and Lyons, 2006). A weak but evident relationship between Mo and TOC ($R^2 = 0.44$) is shown in Figure 4.12A, compared to the scatter between Mo and Fe_{OX} ($R^2 = 0.2$, Plot B). In oxic settings, the slow deposition of Mo to sediments has largely been attributed to adsorption onto Fe and Mn (oxyhydr)oxide particulates and subsequent settling (Emerson and Huested, 1991; Tribovillard et al., 2006). A strong Fe and Mn particulate shuttle is also a mechanism for the drawdown of Mo in anoxic settings (Tribovillard et al., 2012), and it would therefore be expected to see a relationship in both oxic and anoxic settings between Mo and Fe_{OX}. However, it appears that the minor amount of Mo in these sediments was largely drawn down with TOC. Enhanced Mo drawdown with TOC is typically found in areas with sulfidic porewaters, where the sulfide is generated by higher TOC stimulating BSR. There is also no corresponding relationship between Mo drawdown with Fe_{PY} in Figure 4.12C. It must be stressed that very low levels of Mo (Figure 4.4) are found within these sediments, suggesting that sulfide availability was limited to porewaters, as seen in low Fe_{PY}/Fe_{HR} ratios, and not abundant in the water column. It is feasible that Mo was drawn down with organic matter at a much quicker rate than it could adsorb to Fe-Mn particulates in the water column, following the deposition of oxyhydroxides as a result of a deepening chemocline. Vanadium reduction occurs under mildly anoxic conditions (Emerson and Huested, 1991; Tribovillard et al., 2006), and

would thus be anticipated to accumulate under a suboxic or ferruginous water column. However, this is not the case with all values depleted compared to AS.

Uranium reduction does not take place in the water column, but in reducing sediments (Morford and Emerson, 1999). Enrichments in U are found in the Gaoyuzhuang Formation in Figure 4.4, which corresponds to a ferruginous horizon. These exact samples did not undergo the iron speciation procedure as they contain less than 0.5 wt% Fe_T, a limit of acceptable levels of iron for the extraction to work (Clarkson et al., 2014). The carbonate samples from this horizon (Figure 4.11) indicated that ferruginous conditions were prevalent in this setting. Increased concentrations of U have been documented where levels of HCO_3^- rose following the reductive dissolution of Fe-Mn (oxyhydr)oxides within the sediment, as the solubility of U increases during the formation of carbonate phases (Och et al., 2016). Such conditions could have prevailed as the depositional environment saw carbonate packages come to dominate the unit. This trend is not consistent in the Gaoyuzhuang Formation as U/Al declines to values below AS. The remainder of U values in the Chuanlinggou and Changzhougou Formations all plot below AS, again illustrating a depletion of the TM in the sediments. Limited U values gives further substantiation for oxygenated settings becoming more stable and driving the chemocline to further depths. Oxygen potentially penetrated to sufficient depths within these sediments to prevent the reduction of U, and thus any enrichments.

Chromium similarly depicts muted values throughout this entire succession, with all values below AS (Figure 4.4). Other studies focusing on Cr enrichments in the mid-Proterozoic, to gain insight on the spatial extent of anoxia in the ocean, similarly advocate for a lack of markedly high levels during this period (Reinhard et al., 2013).

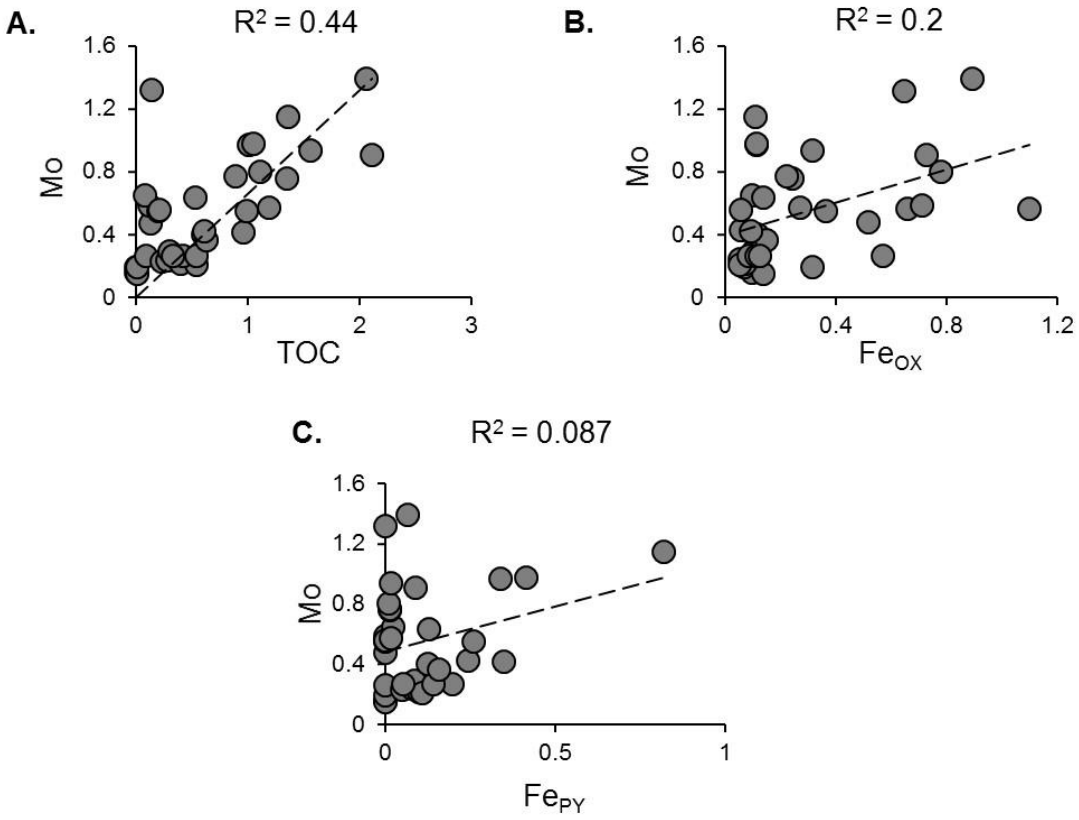

Figure 4.12 Relationship of Mo v TOC, Mo v Fe_{OX} and Mo v Fe_{PY}. Mo values are expressed in ppm, while TOC, Fe_{OX} and Fe_{PY} are in wt%. Samples are from the Changzhougou and Chuanlinggou Formations only.

There are numerous possibilities for the lack of TM drawdown in the anoxic samples of the Changcheng Group in the Yanshan basin and are: a depleted TM reservoir due to prevalent ferruginous conditions; and a restricted bathymetry of the basin restraining deep water circulation. Similar patterns of TM depletions have been observed during the Cenomanian-Turonian ocean anoxic event 2 (OAE 2, 93.5 Ma). The OAE observed in the Demerara Rise was hypothesized to have drained the oceanic TM inventory to the sediments, thus leaving diminished amounts available in the water column for further drawdown (Hetzel et al., 2009). As the Late Palaeoproterozoic to Mesoproterozoic Era's deep oceans are widely documented as ferruginous with pockets of euxinia (Scott et al., 2008; Poulton and Canfield, 2011; Sperling et al., 2015), these globally pervasive conditions could have depleted the oceanic reservoir of TM. Low TM values within the coastal to subtidal sediments of the Yanshan Basin would also suggest extensive anoxia below a shallow chemocline, whereby changes in TM behaviour are recording shifts in the depth of the chemocline. Deep water circulation is vital for replenishing the TM inventory in a basin. Restricted basins such as intracontinental settings or those topographically cut-off by sills, would be limited in their deep water

renewal. In the Demerara Rise and in the proto-North Atlantic during OAE-2, the restricted geometric position of these basins were postulated to have hampered deep water circulation, and thus be a factor in low TM values under anoxic waters (Goldberg et al., 2016; Hetzel et al., 2009). This influencing behaviour of basin position is also observed in a variety of modern localities (Algeo and Lyons, 2006) and other ancient sites during the Late Devonian (Algeo, 2004). The Yanshan basin is widely regarded as an intracontinental setting (discussed in 4.2.2), and thus would be an ideal candidate for a palaeogeographic barrier further depleting the TM inventory of the water column here. The identified ferruginous layer (unit B) in this study corresponds to peaks in TM concentrations in comparison to the oxic samples, but show no overall authigenic enrichments. This behaviour implies extrinsic factors were operating in this basin to prevent the typical levels of TM accumulating under anoxic waters.

4.5.4 Controls on the P cycle during the Late Palaeoproterozoic

From the iron speciation and TM palaeoredox indicators it is evident the Yanshan Basin experienced episodic shifts in redox, coupled with changes in chemocline depth. Marked variance in P burial mechanisms is therefore expected across this sedimentary succession, as the redox state of the overlying water column exerts a primary control on P sedimentary dynamics (Ingall et al., 1993). To aid the understanding of P cycling in this basin, the P speciation results are presented in Figure 4.13 alongside the Fe speciation and TOC, and colour-coded accordingly. For ease of explanation, the Changzhougou Formation will be discussed first before sections A, B and C of the Chuanlinggou Formation.

For a dominantly oxic setting, the Changzhougou Formation exhibits large fluctuations in P burial. However, this could potentially be a function of its coastal setting, with high sedimentation rates and variations in grain size of sediment from terrestrial runoff. Iron speciation results within this unit were shown to be influenced by the sediments' depositional environment, through the strong relationship between Al and Fe_{HR} content (Figure 4.9). The total amount of P becomes less varied moving up-section, progressing to similar values to that of the Chuanlinggou Formation. Phosphorus burial mechanisms within the Changzhougou Formation are illustrated in a simplified schematic in Figure 4.14. Detrital sources of P are the dominant phases in this setting, with minor amounts of P_{auth} and P_{Fe} phases. This behaviour is typical of sediments in an oxygenated setting. During organic matter degradation by heterotrophic

organisms, P is released from its labile sources (typically P_{org}) in the form of phosphate to pore waters (Berner, 1990). During early diagenesis, this P is either released back to the water column, or forms Ca-P minerals, typically carbonate fluorapatite (CFA) in oxic settings (Ruttenberg and Berner, 1993). Phosphorus adsorbed to Fe (oxyhydr)oxides entering this shallow environment from a riverine source was most probable in supplying the P_{Fe} fraction to these sediments. Iron (oxyhydr)oxides can form at a chemocline and subsequently sequester P from the water column, but as no change in redox was detected in this unit, P supplied directly to a coastal environment from riverine discharge seems more likely. An overall decline in P_{det} occurs with increasing stratigraphic height, as illustrated in both Figure 4.13 and Figure 4.14. This is potentially an outcome of the unit deepening, moving away from the direct input of coarse detrital material. Such trends coincide with an increasing amount of P in reactive phases, with P_{Fe} and P_{org} rising to 38% and 58% P_{sum} respectively, as the unit reaches greater water depths. It can thus be stated that as iron redox dynamics were controlled by the shallow depositional environment and detrital input to the Changzhougou Formation, P burial mechanisms were similarly influenced by the same parameters.

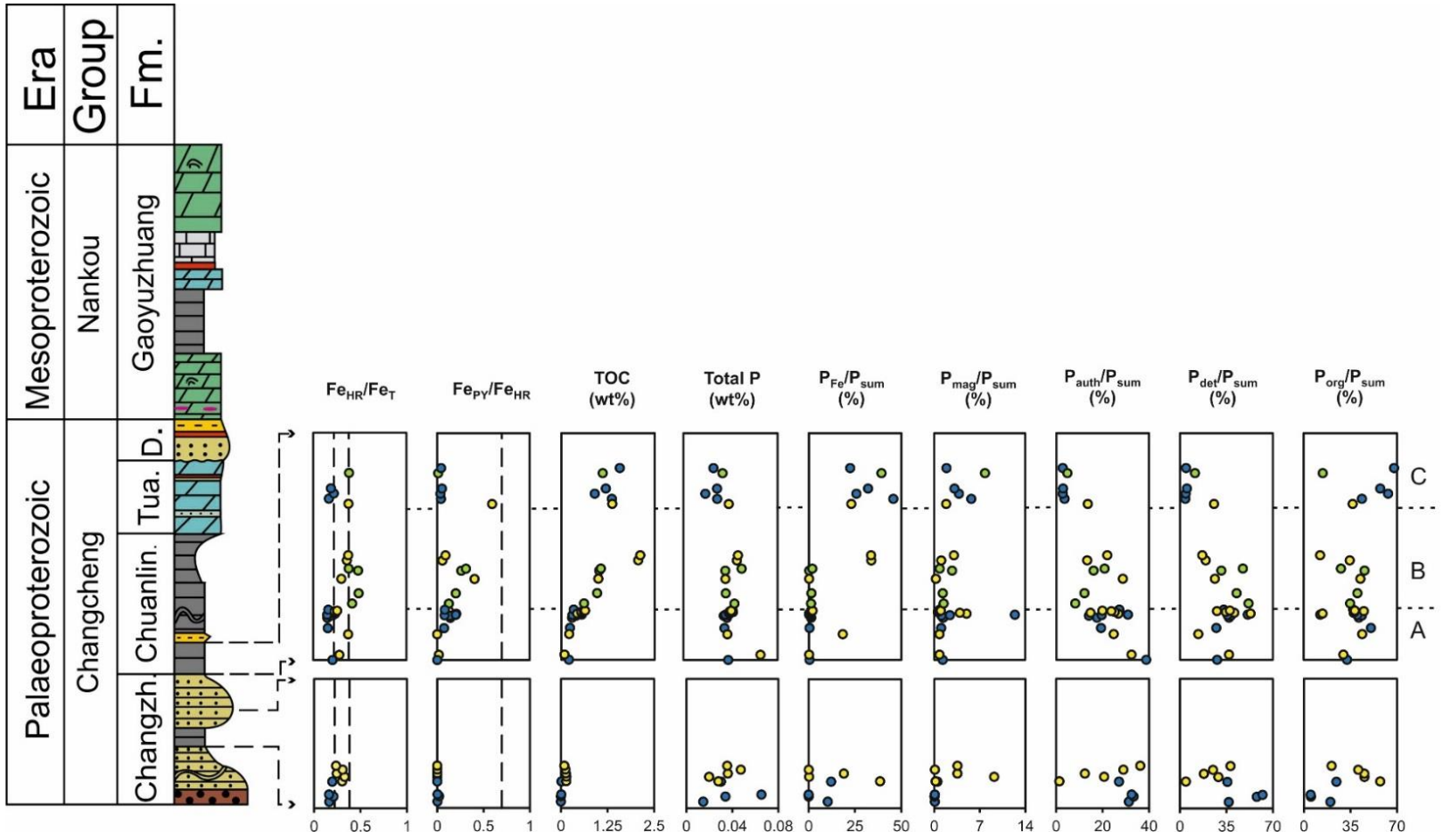

Figure 4.13 Colour coded iron specition, TOC and phosphorus speciation results. All P phases are reported as a percentage of the total amount of P extracted during the speciation method (P_{sum}). The colour code remains the same as Figure 4.11: oxic – blue; equivocal – yellow; anoxic – green. The section analyzed in the Chuanlinggou Formation is also subdivided into units A, B and C.

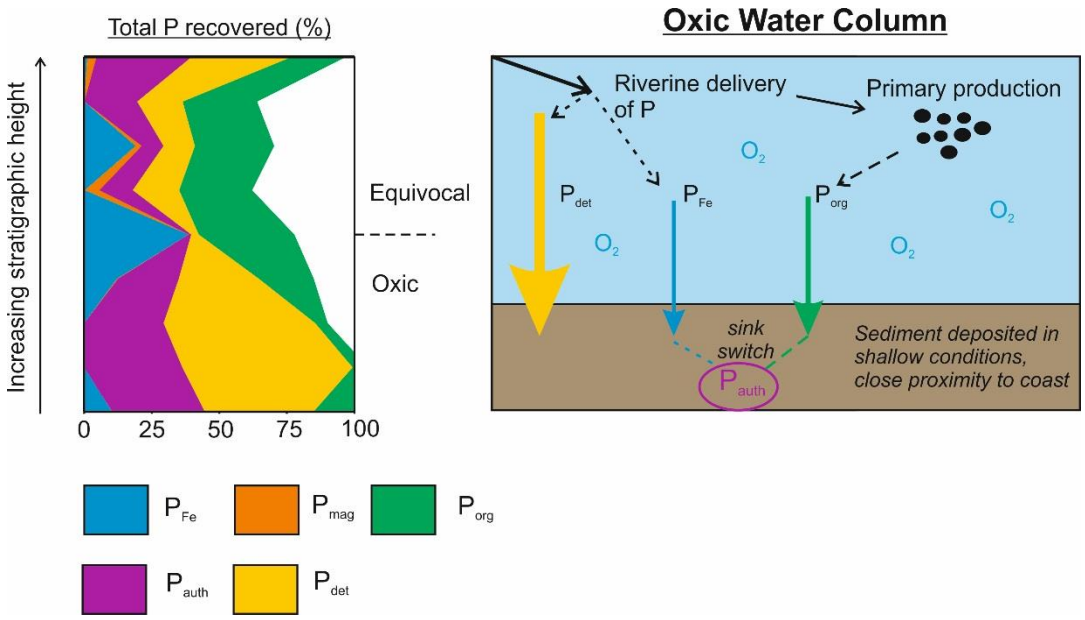

Figure 4.14 Simplified schematic of P burial mechanisms operating during deposition of the Changzhougou Formation. The proportions of P recovered during the extraction are illustrated next to the diagram to illustrate the dominant phases

Episodic changes to redox and P burial continue to occur throughout the subtidal Chuanlinggou Formation. In subsection A (samples ADS-10 to ADS-23), P burial mechanisms in this dominantly oxic setting exhibit differences to the underlying oxic Changzhougou. Total P content in Figure 4.13 remains consistently low at approximately 0.4 wt%, with the exception of one sample plotting at 0.065 wt%. To aid this interpretation, a schematic of redox and P systematics within this unit are illustrated in Figure 4.15. The importance of detrital P declines in comparison to that of the Changzhougou Formation, though still an important constituent of the overall amount of P. A decline in P_{det} could be related to the deepening environment from a coastal to subtidal setting, resulting in a lesser amount of detritus delivered to the sediment. Authigenic and organic P are the most abundant reactive phases within these samples. The increased generation of organic matter, as evidenced by rising TOC in Figure 4.13, brought down P_{org} to the sediment where during diagenesis, a fraction of this sink-switched to P_{auth}. As previously discussed, this is the common behaviour of P under an oxygenated water column. However, a substantial portion of the P_{org} has escaped diagenesis and remained in its original phase. Sedimentation rate also exerts a large control on P burial. Elevated sedimentation rates have been suggested as a method for organic matter to escape decomposition, and thus leave P_{org} preserved in the sediments (Ingall and Van Cappellen, 1990). Other proposed reasons for the preservation of P_{org} in ancient sediments include: the preferential preservation

of refractory organics such as phosphonates, as more labile fractions are broken down first during organic matter decomposition; or the presence of derivative compounds or bacterial biomass (Ingall and Van Cappellen, 1990; Ruttenberg, 2003). It must also be considered that though P_{org} represents the main phase within these samples, the overall P_{Tot} is primarily low, and thus does not represent an occasion of unusual amounts of $P_{org.}$ The decline of P_{auth} from the base of this unit, could represent the loss of reactive phases back to the water column, escaping sink switching to P_{auth}. This in turn would further enhance primary productivity, and generate more organic matter. A consistently increasing trend is seen in TOC across the A-B unit boundary, matching this hypothesis.

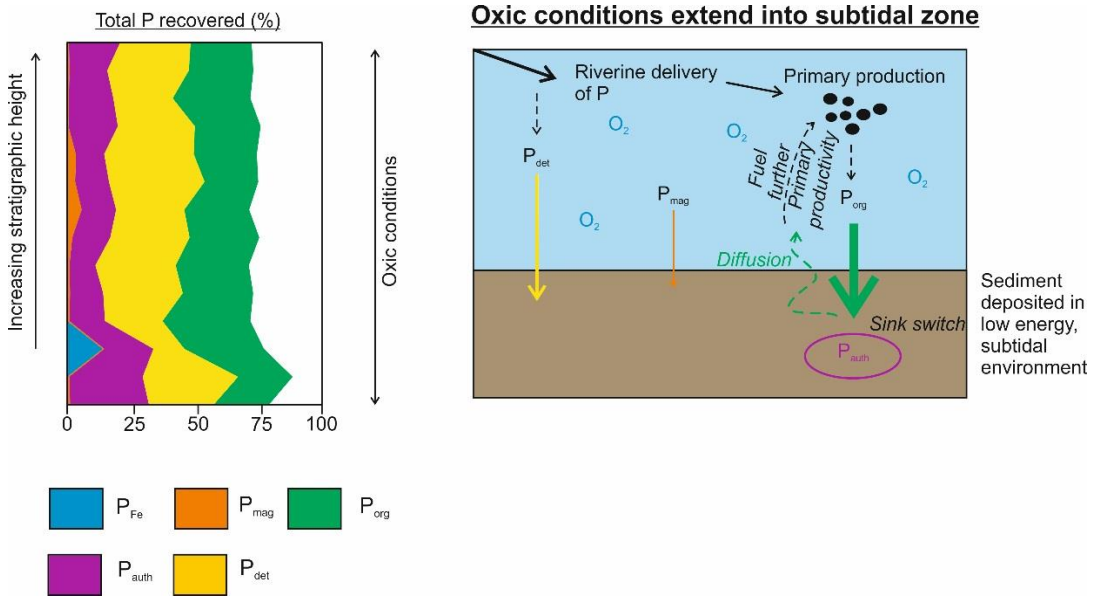

Figure 4.15 Schematic of redox and P burial mechanisms in subsection A (samples ADS-10 – ADS-23) of the Chuanlinggou Formation

A lowering in P_{auth} values could be indicative of P recycling back to the water column, as has been observed in anoxic settings (Ingall et al., 1993; Benitez-Nelson, 2000; Slomp et al., 2004; Mort et al., 2010; Poulton et al., 2015). To assess this, $(C:P)_{org}$ and $C_{org}:P_{reac}$ ratios are plotted in Figure 4.16 against the Redfield Ratio. The Redfield Ratio defines the relative proportions of C and P in settling organic matter and the amount of oxygen needed to respire it (C:P 106:1, Redfield, 1958). In Plot A of Figure 4.16, both oxic and ferruginous anoxic samples plot above the Redfield Ratio, thus signifying the preferential release of P over C from organic matter. Phosphorus recycling under ferruginous conditions typically only occurs when sulfide is present in

porewaters (März et al., 2008). Evidence for sulfidic porewaters can be seen in Figure 4.11 where Fe_{PY}/Fe_{HR} values rise in the ferruginous horizon B. In Plot B of Figure 4.16, when taking other reactive P phases into account i.e. P_{Fe}, P_{mag} and P_{auth}, it is seen that not all anoxic samples are indicative of P recycling as several plot on the Redfield line. This highlights the importance of other reactive phases storing P in sediments other than in organic-bound phases.

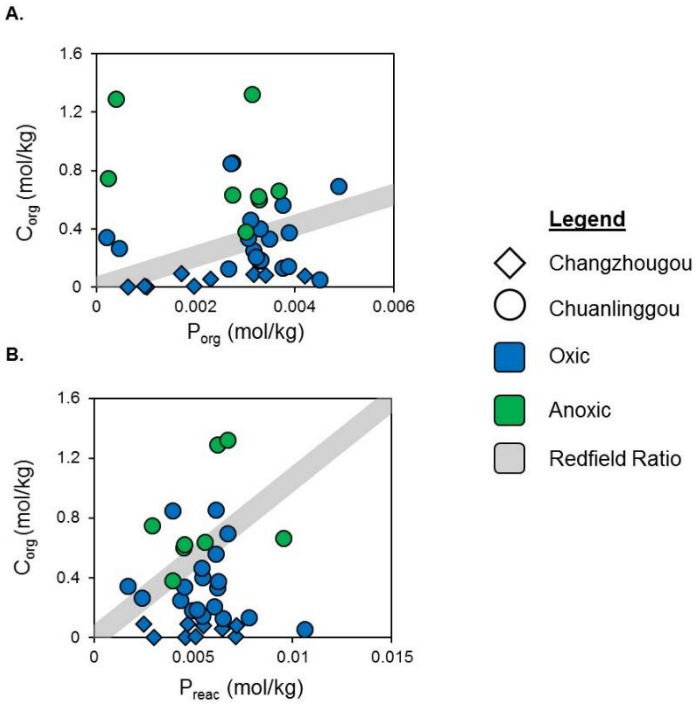

Figure 4.16. A: C_{org} v P_{org}. B –C_{org}:P_{reac} plots. Samples are colour coded based on redox: oxic – blue and anoxic – green. Formations are differentiated by diamonds for Changzhougou Fm and circles for Chuanlinggou Fm

Incorporating these findings into further interpretations, unit B, the ferruginous interval, has different trends in its P burial mechanisms in Figure 4.13. Total P content remains relatively steady, while as the unit deepens, P_{auth} phases accumulate to higher rates as P_{det} falls. The increased generation of authigenic phases under a ferruginous water column gives evidence against other authors who suggest P is only buried in sediments under oxic conditions (Ingall et al., 1993; Sundby et al., 1992; Calvert et al., 1996; Kraal et al., 2010, 2012; Mort et al., 2010; Slomp et al., 2004; Jilbert et al., 2011). Though P_{auth} is forming, from Figure 4.16, it is clear that a significant portion of P_{org} is returned to the water column, where it enters into a positive feedback with organic

matter production. Increased recycling of P_{org} from sediments fuels primary productivity, generating more organic matter and therefore, exporting more P_{org} to the sediments where it can be recycled again. In Figure 4.16B, samples from unit B plot below the Redfield ratio line, indicating other phases were important in the burial of P other than organic phases. Iron-bound phases show an abrupt increase to higher levels in Figure 4.13, signifying an important source of reactive P to the sediments. A simplified schematic of operations behind the P cycle in this unit are shown in Figure 4.17. A potential source of iron-bound P is from the production of Fe (oxyhydr)oxide particulates at the chemocline, as shallow oxic waters mixed across a dynamic chemocline with ferruginous deeper waters. A source of Fe_{ox} to these sediments can also be used to explain the increasing Fe_{PY}/Fe_{HR} ratio in unit B. In anoxic sediments, ferric (oxyhydr)oxides are reductively dissolved, returning Fe^{2+} to porewaters (Kraal et al., 2012). The ferrous iron reacts with sulfide produced by microbial sulfate reduction to form pyrite in the sediments (Raiswell and Canfield, 1998).

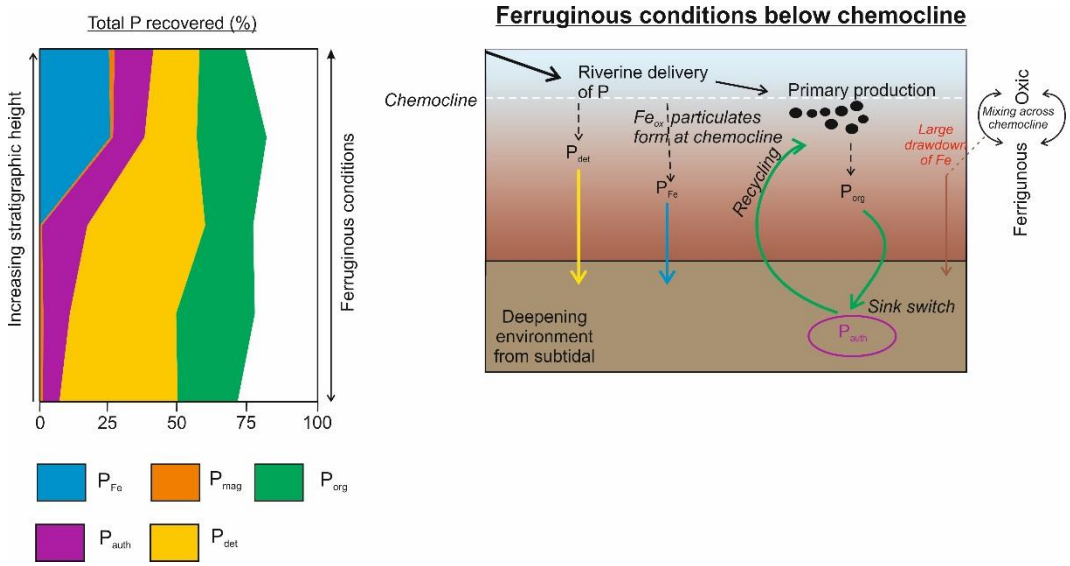

Figure 4.17 Schematic diagram of P burial mechanisms in unit B (ADS-24 – ADS-31) of the Chuanlinggou Formation. Proportions of each P pool removed during the extraction are illustrated. Iron speciation and Fe_T showed an oxic layer mixing with ferruginous deeper waters across a shallow and dynamic chemocline

In the upper Chuanlinggou (unit C), the redox state reverts back to dominantly oxic conditions. The large scale drawdown of iron in unit B impeded ferruginous conditions from prevailing. Coupled with the removal of the water column iron inventory, the intracontinental setting of this basin prohibited the replenishment of this inventory with further sources of Fe_{HR} and subsequently forced oxic waters to greater depths. A reorganization to P burial mechanisms

therefore occurs in this interval due to the change in redox, but contrasts to the underlying oxic setting in unit A. As there are no lithological changes to suggest shallowing, but rather deepening, the differing P burial may be the result of more stable oxic conditions, with the oxic-anoxic boundary in the sediments rather than the water column. This again demonstrates a deepening chemocline, with oxic waters moving to a greater depth. Iron and organic-bound P are the most important sources of P to these sediments, with P_{auth} and P_{det} both <5% P_{sum}, and P_{mag} <8.5%. Iron-bound P burial reaches a maximum of 45% in this stable oxic setting. In order for iron (oxyhydr)oxides to persist in their ferric (Fe^{3+}) state, redox conditions in the sediment must have been stably oxygenated (Berner, 1973). The iron speciation results revealed Fe_{OX} was the main source of iron (Figure 4.3), reflecting a change in Fe dynamics as well as P in the less pervasively oxygenated horizon below. Sources of P to the sediments in unit C are illustrated in Figure 4.18. Iron (oxyhydr)oxides can adsorb phosphate in both the water column and in the sediment porewaters. In ferruginous waters where there is low sulfate, the removal of phosphate by adsorption to iron oxides was particularly important during BIF deposition (Bjerrum and Canfield, 2002; Jones et al., 2015). Phosphorus can also be scavenged by Fe_{OX} produced in hydrothermal plumes (Wheat et al., 1996; Poulton and Canfield, 2006). Within sediment porewaters, phosphate released during organic matter degradation can be sequestered by Fe_{OX} in oxic regions. If this surface oxic layer is sufficiently thick, further diffusion of phosphate back to the water column is restricted (Slomp, Epping, et al., 1996), thus resulting in the overall retention of P. If these sediments are buried to anoxic depths, reductive dissolution of the ferric phases occurs, desorbing the phosphate to porewaters, and sink switching to CFA (Ruttenberg and Berner, 1993; Slomp, Epping, et al., 1996). As there is limited P_{auth} in the upper C horizon of the Chuanlinggou, Fe_{OX} acted as a substantial P trap for the limited amount being drawn down to the sediments. This finding greatly contrasts against other studies from this time period, which suggest P burial through adsorption to Fe_{OX} was negligible in the dominantly anoxic Palaeoproterozoic-Mesoproterozoic ocean (Planavsky et al., 2010; Reinhard, Planavsky, Gill, et al., 2016) as they do not account for local spatial and temporal variability in redox that can occur in one locality (e.g. Wang et al., 2017). Another possibility for the relatively high amounts of P_{Fe} within these sediments is through the formation of Fe(II) phosphates such as vivianite. Iron oxides deposited at the seafloor can escape surface redox processes if buried at sufficiently high rates on continental margins (Hensen et al., 2003; März et al., 2008). Diagenetic processes which operate deeper in the sediment profile, typically around the

sulfate-methane-transition zone, then become major controls on how these Fe_{OX} exist in the sediment. At this zone, anaerobic oxidation of methane reductively dissolves Fe_{OX}, where the adsorbed phosphate is released and can diffuse up or down the sediment profile (Sundby et al., 1992; Slomp, Van der Gaast, et al., 1996). The downwards diffusing phosphate can precipitate as an authigenic phase in the methanic zone that is not the typical CFA phase. High sedimentation rates are typically invoked as the cause for their formation (März et al., 2018), but as there are no sedimentological markers to suggest this in the Chuanlinggou Formation, the presence of Fe(II) phosphates can be ruled out. Other potential factors include depositional areas, such as on deep sea fans or depocenters off large rivers where a high sedimentation regime has switched to lower accumulation rates (März et al., 2008; März et al., 2018); lack of carbonate surfaces to act as a nucleation site for CFA formation; and low organic matter accumulation. As there is currently no extraction to separate Fe(II) phosphates, it cannot be declared for certain that this type of P phase was a significant portion of the sediments investigated in this study.

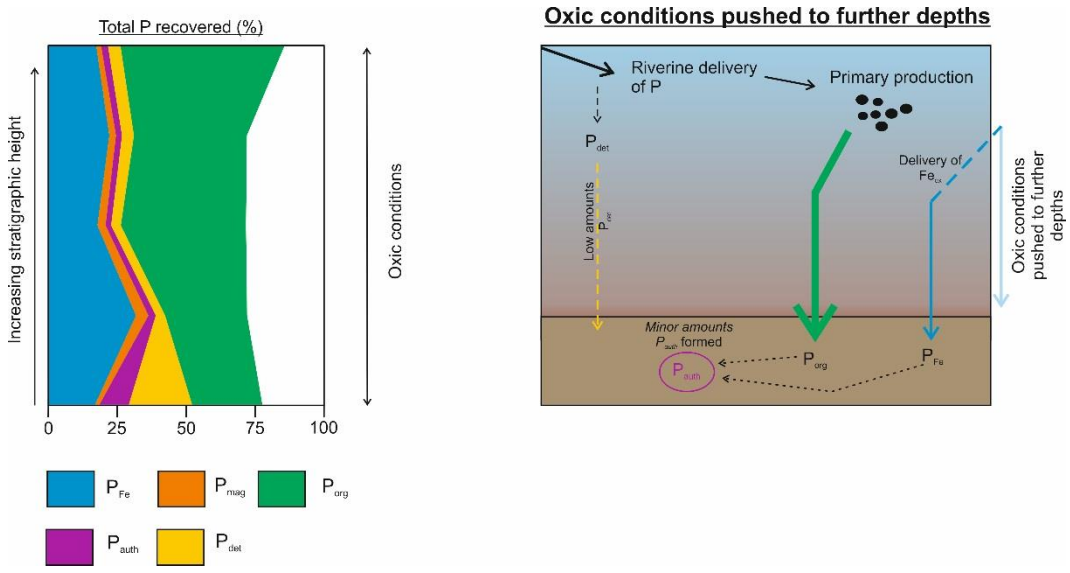

Figure 4.18 Schematic of redox and P burial mechanisms for unit C of the Chuanlinggou Formation. Following mixing of shallow oxic and deeper ferruginous waters, and the drawdown of Fe, oxic conditions push to deeper depths, modifying P burial mechanisms

The majority of P delivered to the sediment in the Yanshan Basin became buried. Limited total P content of the sediments could suggest this was an oligotrophic basin, with the continued burial of P further limiting primary production. However, as N was not measured in this study, it cannot be stated for certain this was a completely nutrient-limited basin, but rather a P-limited

one. Phosphorus limiting conditions potentially set up a positive feedback in terms of redox, as the continued burial of P would reduce primary productivity and thus oxygen demand in shallow waters, stabilizing an oxygenated water column. Modelling approaches (e.g. Lenton et al., 2014) have previously supported this, but it has never been geochemically observed in the Palaeoproterozoic before. The short lived recycling of P observed in the ferruginous samples (Figure 4.16) may have stimulated primary production, generating higher levels of organic matter reflected in the elevated TOC content (Figure 4.11). All oxic samples plot on or below the Redfield Ratio in Figure 4.16 for their $(C:P)_{org}$ and $C_{org}:P_{reac}$ ratios, further highlighting that the prevailing redox exerted a major control on authigenic apatite formation. It has previously been suggested that authigenic apatite could not form in a nutrient-limited Palaeoproterozoic-Mesoproterozoic basin due to high C:P ratios of organic matter at this time (Reinhard, Planavsky, Gill, et al., 2016). The research presented here disputes this hypothesis, as it is fluctuating redox that has hampered the development of P_{auth} in the Yanshan Basin, rather than high C:P ratios. Other basins from this time period similarly experiencing redox fluctuations would thus need to be analysed to quantitatively assess controls on authigenic apatite formation across this large expanse of time.

4.5.5 Nutrient Availability in the Yanshan basin

The P speciation technique allows detailed insight into how P is buried in sediments, and for this study, how the cycle of the ultimate limiting nutrient was potentially changing at the same time as eukaryotes were evolving. Eukaryotes are defined as complex multicellular organisms which have a 3D membrane and cytoskeletal system controlling their cellular patterns (Knoll, 2011). Prior to their evolution, microbial organisms were the dominant form of life on the planet. In the geological record, these are typically found in microbially induced sedimentary structures (MISS) or stromatolites. MISS are formed from the binding and trapping of sediment by microorganisms in shallow siliciclastic environments (Noffke and Awramik, 2011). If this continued layering of sediment through microbial activity occurs in a shallow marine carbonate environment, stromatolites form. Both MISS and stromatolites date back to the Early Archaean (Noffke and Awramik, 2011). However, stromatolites are much more abundant due to the preferential degradation of the more organic MISS. This makes the analysis of potential environments for simple microbial organisms in siliciclastic settings more difficult to investigate than in carbonate assemblages. However, MISS have been documented in the Chuanlinggou

Formation in the Yanshan Basin in the form of wrinkle structures and sand veins (H. Yang et al., 2017). The preservation of MISS ties in with the P-limited nature of this basin. Limited nutrient input, the restricted setting of the basin and fluctuating redox was not an environment conducive for eukaryotic evolution.

On entering the Mesoproterozoic Gaoyuzhuang Formation, substantial environmental, biological and geochemical changes occur. A change in basin configuration from a restricted to an open setting occurs (Meng et al., 2011). The Gaoyuzhuang Formation is widely regarded as the best preservation for Proterozoic filamentous and coccoidal microfossil assemblages, with evidence for stromatolites and MISS in differing members (Mei et al., 2009; Peng et al., 2016; Guo et al., 2018). What is most remarkable is the discovery of decimetre-scale macroscopic multicellular eukaryotic fossils in the Gaoyuzhuang. These fossils are preserved as carbonaceous compressions and thought to resemble benthic algae (Zhu et al., 2016). The emergence of large eukaryotes has long been attributed to the presence of oxygen in the ocean, as small and simple body plans are attributed to limited levels of oxygen (Mills and Canfield, 2014). The iron speciation results from the research presented here revealed a dominantly ferruginous water column in the Gaoyuzhuang Formation (Figure 4.11), however this is at a coarse resolution in a thick carbonate succession. A more detailed investigation coupling iron speciation and rare earth element patterns in the Gaoyuzhuang revealed an oxygenation event, coinciding with the appearance of these macroscopic eukaryotes, suggesting that an increase in oxygen levels in the shallow marine environment was a trigger for eukaryotic evolution (Zhang et al., 2018). Phosphorus speciation could not be conducted on the samples from this study due to their carbonate lithology and their low Fe_T content prohibiting iron speciation for redox identification, but comparisons can be made between P_{Tot} and P/Al ratios to the lower oligotrophic Changzhougou and Chuanlinggou Formations. Only shales are considered for P/Al ratios. Carbonates are not suitable for normalization by Al, as Al does not form part of their crystal structure in nature (Brumsack, 2006). Marked differences are evident in Figure 4.19 in both of these elemental trends. In Plot A, the majority of P_{Tot} values plot below the AS line for both carbonates and shales throughout all formations. However, in four of the shales from the Zhangjiayu member of the Gaoyuzhuang where the eukaryotic fossils are found, enrichments in P_{Tot} are found. Increased P burial has previously been hypothesized to have created an environment permissive to metazoan radiation as primary production became limited with lower P availability in the water column (Lenton et al., 2014). The stabilization of water column oxygenation

brought down P adsorbed to Fe and Mn (oxyhydr)oxides, and continued oxic waters would, most likely, have hampered the further recycling of P from marine sediments unless sulfide availability increased in porewaters. This research supports these model findings in that the increased burial of P, in terms of mean P content, in a stably oxygenated water column coincides with fossil evidence in the Zhangjiayu Member of the Gaoyuzhuang Formation.

Other studies have suggested detrital-bound P as the main source of P to pre-Cryogenian sediments (Reinhard, Planavsky, Gill, et al., 2016). Normalizing P to Al in shales takes into account this detrital dilution, and is presented in Plot B of Figure 4.19, to ensure the increase in P_{Tot} is the result of a rise in reactive phases. Again, there is a significant difference in the behaviour of mean P/Al content between the Palaeoproterozoic and Mesoproterozoic basins. A sharp rise in P/Al at the base of the Gaoyuzhuang occurs, but is short-lived. All shales from the Zhangjiayu Member however plot above AS, highlighting that a P_{reac} enrichment occurred in the same horizon where the eukaryote fossils are found. If prolonged oxic settings were accompanied by increased P burial, these factors could have intrinsically interworked to provide an ideal setting for the evolution of eukaryotes by limiting primary production and hence respiration. Such a set up would have lessened oxygen demand and helped maintain stable oxygenated conditions.

A.

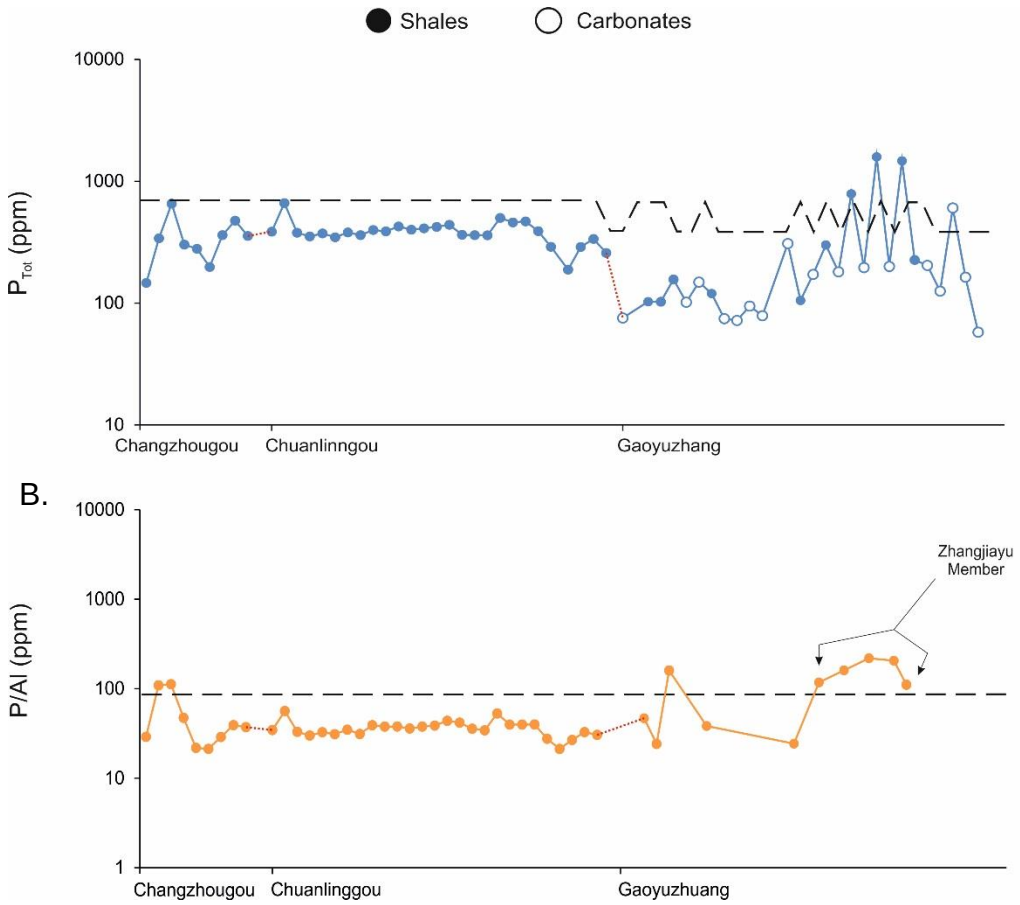

Figure 4.19 A - Evolution of Total P in the sampled units of the Yanshan Basin. The black dashed line represents the AS value at 700 ppm for shales and 400 ppm for carbonates. B – P/Al for samples from the Yanshan Basin. Dashed line is 87.5 ppm. All AS values taken from Turekian et al. (1961). The red dashed lines represent gaps between the formations.

4.6 Conclusions

Through the combined use of iron speciation and trace metal analyses as palaeoproxies, a basin which experienced fluctuations in its redox state was identified in the NCC during the Late Palaeoproterozoic. A dynamic chemocline resulted in the mixing of deep ferruginous water with the oxygenated surface layer of the water column. An elevated drawdown of Fe following mixing, caused the expansion of oxic conditions into subtidal waters for the first time in this succession. Due to the restricted nature of the basin during a period of Earth's history where ocean anoxia was widespread, trace metal proxies did not function as they typically do in ferruginous settings. A depleted oceanic inventory of trace metals is thus proposed to explain this behaviour, as a function of restricted deep water renewal in an intracratonic basin.

A P-limited basin was distinguished from the low total P content of the Yanshan basin sediments. The continued burial of P under an oxic water column generated a positive feedback by reducing primary productivity but promoting the development of more stable oxic conditions in subtidal waters. The main source of P to the sediments was largely dependent on both redox and the position of the chemocline. High amounts of P_{org} and P_{Fe} were preserved where organic matter escaped degradation in oxic settings, and resulted in minor amounts of authigenic apatite forming. On deepening of the chemocline, a larger amount of authigenic apatite was capable of accumulating to higher levels, potentially as a result of the large deposition of Fe (oxyhydr)oxides, a known source for P to the sediments. The Palaeoproterozoic P cycle thus behaved in a similar manner to the modern P cycle, as it is drawn down in its reactive phases and through post-depositional internal recycling of P, that forms its typical authigenic phases.

In a comparison between the mean P content of sediments in the oligotrophic Changcheng Group to the Mesoproterozoic Gaoyuzhuang Formation, the locality of macroscopic eukaryotic fossils, an increase in both total and reactive sedimentary P content occurred in the younger horizon. This has major implications for the role P played as the ultimate limiting nutrient in conjunction with oxygen availability for the evolution of more complex organisms. The increased burial of reactive P in an oxygenated setting potentially created an ideal habitat for eukaryotes to evolve in.

Chapter 5 Redox controls on the Ediacaran phosphorus cycle

5.1 Introduction

The Ediacaran Period (635 – 541 Ma) marks the termination of the Neoproterozoic Era (1 – 0.54 Ga), and is arguably the most important time in Earth's history for environmental and biological innovations. Sitting at the Precambrian-Cambrian boundary, it records the very first appearance of soft-bodied metazoans, the *Ediacaran Biota* (Hoyal Cuthill and Han, 2018). Several intertwining theories have been put forward as possible mechanisms for the evolution of metazoans. They include: increasing atmospheric oxygen concentrations; perturbations to the C cycle; and the termination of Snowball Earth events. The other major environmental change during this period, and most frequently used to explain the emergence of animals, is deep ocean oxygenation. Geochemical evidence from the deep marine (>1 km) Mistaken Point Formation on the Avalon Peninsula gives support for a sufficiently oxygenated water column, which potentially drove the evolution of soft-bodied metazoans (Canfield et al., 2007). Alternatively, it has also been proposed that the expansion of oxic conditions into the deep ocean was the result (rather than the driver) of animal evolution. The emergence of larger and more complex organisms would have resulted in a flux of bigger, eukaryotic particles to the sediment, which would have sank at a faster rate than those produced by more primitive organisms, reducing oxygen consumption in shallow environments and allowing oxygenated conditions to reach greater depths (Butterfield, 2009; Lenton et al., 2014). Before metazoan development, the biological pump was dominated by eukaryotic algae in the early Neoproterozoic, with evidence from biomarkers (Brocks et al., 2017) and microfossil assemblages (Moore et al., 2017; Nagy et al., 2009; Porter et al., 2003). The switch to a pump dominated by motile animals, combined with the advent of filter feeding in these animals, is hypothesized to have moved oxygen demand to greater depths, due to the fossil evidence of the *Ediacaran biota* at the oxic, deep marine Mistaken Point unit. However, as more studies emerge, ocean redox structure during the Ediacaran has become increasingly heterogeneous (Johnston et al., 2012b; Lang et al., 2016; Li et al., 2010, 2015a; Wood et al., 2015; Xiao et al., 2012). Detailed studies have shown that ocean oxygenation was likely an initial driver of animal expansion (e.g., Wood et al., 2015), but that the radiation of animals subsequently helped to stabilise oxic conditions.

The evolution of motile metazoans, as well as deep ocean oxygenation would have profoundly impacted nutrient cycling during the Ediacaran. Phosphorus is generally considered the ultimate limiting nutrient for life over geological timescales (Tyrrell, 1999). This is based on the residence time of P in the oceans and the proportion of P in organic matter to the other limiting nutrients, N and C. This proportional relationship between limiting nutrients is termed the Redfield Ratio (Redfield, 1958) and is commonly used to assess whether P is preferentially buried or recycled from sediments (Anderson et al., 2001; Algeo and Ingall, 2007). The cycling of nutrients exerts an overall control on primary production rates in surface waters and is also greatly influenced by the prevailing redox of the water column. Organic matter is generally the main source of potentially reactive P to sediments (Delaney, 1998) under oxic and euxinic conditions, and is discussed in detail in Chapter 1. Under ferruginous conditions, Fe oxides can be a major source of P to the sediments, and can also act as a more minor supply of P under oxic conditions. If P is recycled back to the water column and not retained within the sediments, this P may be reused in primary production, generating more organic matter. The burial or recycling of P has also been attributed to redox, with an enhanced preservation of P typically occurring in oxic and anoxic, iron-rich (ferruginous) conditions (März et al., 2008) and recycling in anoxic, sulfide-rich (euxinic) settings (Slomp et al., 2004). Trapping P under oxic and ferruginous conditions is dependent upon the availability of sulfide in pore waters at the sediment-water interface, as if present, can result in the escape of P back to the water column.

At a time when redox was shifting and the dominant producers in the biological pump were evolving to larger sizes, it is hypothesized that significant changes to P burial mechanisms occurred. Previous attempts to examine this have mainly used modelling approaches, and propose an increase in the total P content of shallow marine sediments occurred after the Tonian Period (1 – 0.72 Ga) as a result of oxygenation in shallow waters, and a switch from P buried in detrital to authigenic phases (Reinhard et al., 2016a). Metazoans capable of movement was also a major biological innovation that developed during the Ediacaran. Bioturbation is defined as the mixing of sediments due to animal activity, and has been attributed to promoting organic matter remineralization and causing fluctuating redox (Aller, 1994). Bioturbation has also been regarded as an influence on P burial mechanisms, resulting in the increased exposure of sediments to oxygen in the overlying water column, and subsequently developing a substantial organic P sink through rising levels of microbial polyphosphate sequestration (Boyle et al., 2014). At the onset of bioturbation, it was also proposed that the burial of P in iron-bound phases was

important (Boyle et al., 2014). However, the earliest motile metazoans in the Ediacaran are believed to have moved across the sea floor, rather than burrowing significantly into the sediment, and it is currently unclear whether this significantly affected the P cycle.

There are currently no detailed empirical attempts to asses P burial mechanisms in the Ediacaran. Modern P studies are abundant and have been driven by the development of the SEDEX method (Ruttenberg, 1992), a sequential extraction that measures both reactive and detrital phases of P within marine sediments, which allows an in-depth scrutiny of P burial mechanisms. This method, as well as modelling studies, have been applied to a host of modern localities, and are the main source for understanding how P behaves in different redox settings (Calvert et al., 1996; Delaney, 1998; Dijkstra et al., 2014, 2016, 2018; Goldhammer et al., 2010; Ingall et al., 1993; März et al., 2008; Mort et al., 2010; Reed et al., 2011; Schenau and De Lange, 2001; Slomp et al., 2004; Van Cappellen and Ingall, 1996). Other Proterozoic P studies have been focused on estimating past phosphate concentrations using BIFs (Bjerrum and Canfield, 2002; Konhauser et al., 2007; Jones et al., 2015), or have used simple modelling approaches to track bioavailable P through time (Reinhard et al., 2016a) and assess the effect of bioturbation on P burial mechanisms (Boyle et al., 2014). The limitations of each of these studies is discussed in detail in Chapter 1. In this study, an adapted SEDEX technique (Thompson et al., *in prep*) has been applied to five different Ediacaran localities, of which their palaeoredox has previously been evaluated. By determining the redox conditions under which P is buried in multiple sedimentary successions, the theories put forward by models can be addressed. These theories are: a shift in ocean redox, from ferruginous to oxygenated, resulted in the main sedimentary P phase changing from detrital to authigenic (Reinhard et al., 2016); there was a rapid increase in total P concentrations following the Cryogenian period (Reinhard et al., 2016); with the advent of metazoans, the ocean oxygen reservoir declined due to the continued burial of P_{org} (Boyle et al., 2014); and primary production became limited as P burial was sustained under an oxygenated water column, potentially allowing the evolution of metazoans (Lenton et al., 2014). This research gives the first geochemical evidence for P burial mechanisms during the Ediacaran Period as well as a comprehensive insight into the relationship between redox and P cycling in different marine depositional environments.

5.2 Geological Setting

The location of all investigated sites are illustrated in Figure 5.1.

5.2.1 Kel'tma-1 Drill core, Russia

The Kel'tma-1 drill core was taken from the Vychegda trough of the Timan Ridge in northern Russia. This trough was part of the Mezen shallow-water foreland basin (Podkovyrov et al., 2011), a palaeobasin situated on the north-eastern side of the East European Platform (EEP), which later filled with a thick succession of Upper Vendian siliciclastics (Maslov et al., 2008). It is widely recorded that the EEP formed in a shallow-water epicontinental basin as a result of a postglacial transgression (Nikishin et al., 1996). Though its Phanerozoic structural history remains debated, it is suggested that the Upper Vendian sediments were deposited in the distal zone of the foreland basin, and were not subject to later deformation (Maslov et al., 2008). For this study, depths from 1370 – 4901 m are investigated, representing 780 ± 85 Ma to ~542 Ma (Johnston et al., 2012a).

At the base of the succession is the Yskemess Formation, a 959 m thick unit of microcrystalline dolostones and clayey dolostones interbedded with thin beds of siltstones and shales (Maslov et al., 2008; Vorob'eva et al., 2006). Overlying the Yskemess Formation is the Vapol' Formation, a 1033 m deposit of dolomitized limestones interlayered with calcareous shales and siltstones (Maslov et al., 2008; Veis et al., 2006). Stromatolites are found in the Vapol Formation, typical of the Upper Riphean assemblages of this region (Golubkova et al., 2015). The Vychegda Formation is a 600 m siliciclastic succession above the Vapol Formation. At the base is a deposit of coarse clastics such as conglomerates and gravelstones to siltstones. This fines upwards into shales and siltstones, highlighting a change from nearshore environments to mid-shelf deposits (Vorob'eva et al., 2009a). Separating the Vychegda Formation from the remaining Upper Vendian sequence is an unconformity thought to be the result of thrust-loading of the craton margin causing flooding in the area (Maslov et al., 2008), or a postglacial transgression (Vorob'eva et al., 2009a).

The upper Neoproterozoic of this drill core includes the Redkino and Kotlin shale horizons found throughout the EEP. These horizons have been correlated to other boreholes and outcrops in the Mezen basin using lithogeochemistry (Podkovyrov et al., 2011) and palaeontology (Veis et al., 2006; Golubkova et al., 2015; Vorob'eva et al., 2009a). The most famous correlative site for the Kel'tma core is the White Sea, where abundant

Ediacaran fauna are preserved in alluvial and fluvial deposits (Grazhdankin, 2003). The boundary between the two units is marked by a weathering horizon and typically denudation of the Redkino beds (Mens and Pirrus, 1986).

The Redkino horizon is defined by the preservation of *Ediacaran biota* macrofossils (*Kimberella, Charnia, Dickinsonia, Hiemalora;* Martin (2000)), trace fossils and a diverse assemblage of algae (Fedonkin et al., 2007; McCall, 2006; Grazhdankin, 2004; Pirrus, 1992; Crimes, 1992). The characteristic microfossils consist of a variety of acritarchs and filamentous forms (Sokolov and Iwanowski, 1985). Lithologically, the Redkino consists mainly of grey-green shales with some minor sandstones and siltstones. The later Kotlin horizon is classified by its microfossil assemblages, typically more primitive than that of the Redkino (Pirrus, 1992; Chumakov, 2010). Preservation of soft-bodied animals is not common in the Kotlin stage, but there are a limited number of trace fossils to suggest animal activity (Crimes, 1992). The microfossil assemblage within these two horizons differ from other Ediacaran successions due to the absence of acanthomorphic acritarchs (Vorob'eva et al., 2009a; Vorob'eva et al., 2009b).

Siltstones and shales are the main lithologies of the Kotlin horizon. There has been some debate across the literature on whether the Kotlin unit is of a freshwater or marine origin. Arguments for a freshwater deposit stem from the presence of siderite and its lack of glauconite, phosphatic or pyritic nodules (Felitsyn, 2004; Mens and Pirrus, 1986; Pirrus, 1992, 1993). However, evidence for the diagenetic modification of kaolinite has been found to help explain the absence of such minerals, and subsequent marine origin of the unit (Gorokhov et al., 1994). The contention that the Kotlin horizon represents an offshore marine deposit stems from its expansive lateral extent, lithostratigraphy and geochemical signatures (Grazhdankin, 2003; Podkovyrov et al., 2017; Bessanova et al., 1987).

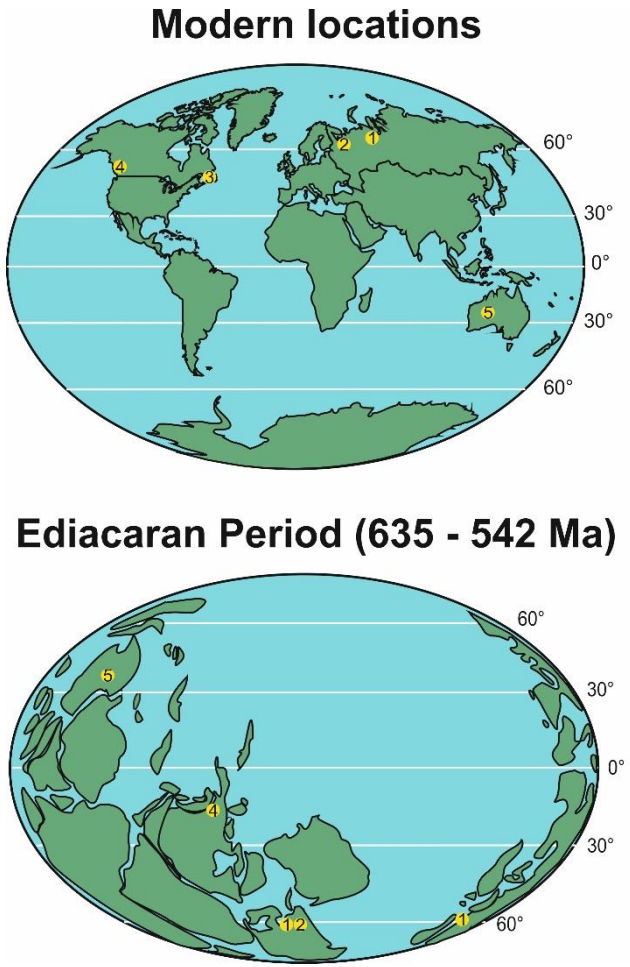

#	Locality	Depositional Environment
1	Kel'tma Core - correlated to the White Sea	Mid shelf deposit >150 m
2	Kostovo-13 Core - correlated to the White Sea	Mid shelf deposit >150 m Potential shallow deposits
3	Avalon Peninsula Newfoundland	Deep Marine >1 km
4	Cariboo Mountains, Western Canada	Basin floor - slope deposit Deep marine >500 m
5	Ungoolya Group, Officer Basin, Australia	Outer shelf deposit >storm wave base

Figure 5.1 Map of localities for each sample site. Ediacaran palaeogeographic map is adapted from Shen et al. (2008)

- 146 -

5.2.2 Kostovo-13 Drill core, Russia

The Kostovo-13 borehole was drilled outside St Petersburg near the village of Kostuya (Gorokhov et al., 1994). Similar to the Kel'tma core, it contains the Redkino and Kotlin stages, and can thus be correlated to other regions of the EEP, including the White Sea. The upper Neoproterozoic strata in this study range from 125 – 445 m in depth. Also found in this core is the Gdov Formation, which lies in between the Redkino and Kotlin horizons. This interlying member is defined geochemically by anomalies in Eu/Eu^{*} ratios (Maslov and Isherskaya, 2006), but also lithologically by coarser sandy-silty rocks (Podkovyrov et al., 2017), but is not synchronous across the EEP. These three horizons together represent the Valdai Group, a more common term given to the Redkino and Kotlin horizons (Podkovyrov et al., 2011, 2017). The succession at the White Sea is a vast deltaic and alluvial system (Fedonkin et al., 2007) making it unsuitable for marine sedimentary geochemistry analysis. By using cores correlated to this region but deposited at greater depths in the palaeobasin, an understanding of the ocean chemistry operating during this dynamic interval can be achieved.

5.2.3 Avalon Peninsula, Newfoundland

The Avalon Peninsula in Newfoundland hosts 7.5 km of Neoproterozoic turbidite and volcaniclastic strata (Myrow, 1995). The upper Mistaken Point Formation (565 – 575 Ma) from the Conception Group was sampled for this study. Mistaken Point is a siliceous sandstone and red shale unit and has long been considered evidence for the oldest benthic animal community (Clapham et al., 2003). A water depth of greater than 1 km is estimated for the depositional environment of Mistaken Point (Liu et al., 2010). This is based on the lack of wave-generated structures and palaeoflow directions in the turbidite deposits (Wood et al., 2003). The Mistaken Point Formation has a coarse tuff layer at the top of the unit which accounts for the remarkable preservation of the *Ediacaran biota* (Conception-style), and has received a lot of research interest over the years (Narbonne, 2004; Gehling et al., 2000; Retallack, 2016).

Overlying the Mistaken Point Formation is the St. Johns Group. At the base, the Trepassey Formation is a silty shale slope deposit. Based on the abundance of slump structures of the sedimentary strata, the Trepassey Formation is hypothesized to have accumulated along mid-slope, while the underlying Mistaken Point is regarded as a deposit from the toe of a slope (Wood et al., 2003). A coarsening upwards sequence results in the overlying

Fermeuse Formation. The lower member consists predominantly of pyritic shales with soft sediment deformation features (Gehling et al., 2000). The prominent slumps and deformation in the Fermeuse represent an evolving basin to more shallow depths (Liu et al., 2010). The progradation of the basin continues with the development of coarser grained and thicker beds of sandstone with interbedded shale (Gehling et al., 2000). These packages are also noted for their preservation of trace fossils and holdfasts for certain types of *Ediacaran biota* e.g. *Aspidella* (Narbonne, 2005).

5.2.4 Cariboo Mountains, Western Canada

The Kaza Group and overlying Isaac Formation of the Windermere Supergroup in the Cariboo Mountains were sampled for this study. The Neoproterozoic Windermere Supergroup is an extensive (> 6 km thick) deep-marine meta-sedimentary deposit found in the southern Canadian Cordillera (Smith et al., 2011). Deposition initially took place in grabens as a result of early continental rifting along the western margin of Laurentia (Schwarz and Arnott, 2007; Arnott, 2007). The Kaza Group and Isaac Formation represent post-rift deposition on a prograding passive margin, below the continental slope of an open ocean basin (Ross et al., 1995; Schwarz and Arnott, 2007).

The upper Kaza Group is a sand-rich turbidite from a terminal fan deposit on the basin floor (Terlaky et al., 2016). The overlying Isaac Formation sits conformably over the Kaza Group and is a mud-rich slope deposit (Ross et al., 1995). The Cariboo Mountains underwent lower greenschist facies metamorphism during the Mid-Jurassic (Ross et al., 1995).

5.2.5 Narana Formation, Upper Ungoolya Group, Officer Basin, Australia

The Upper Ungoolya Group, or Narana Formation, was uncovered in the Munta-1 drill core of the Officer Basin in South Australia. Not many drillcores exhume the Upper Ungoolya Group, leading to a bias in the study of the lower Ungoolya Group throughout the literature (Gostin et al., 2010; Arouri et al., 2000; Logan et al., 1997; Grey et al., 2003; Jenkins et al., 1992). The Narana Fm can be subdivided into three members. The lowermost member (depth 997 – 1152 m) consists of dark grey to green silty shales, deposited on an outer shelf below sub-wave base (Arouri et al., 2000). The overlying unit contains thin beds of limestone in a calcareous mudstone, from depths 943 – 1152 m. The

upper unit exhibits shallowing to a marine shelf and is a package of grey limestone (Arouri et al., 2000).

Deposition occurred in a foreland basin at approx. 565 – 550 Ma during the second compressional event associated with the breakup of the Centralian Superbasin (Arouri et al., 2000). This event, known as the Petermann Ranges Orogeny, was a local event causing intense metamorphism of the nearby Amadeus Basin, but did not significantly alter the sediments of the Officer Basin (Calver and Lindsay, 1998).

5.3 Methods

5.3.1 Organic Carbon

Different techniques for TOC measurement were used in this study due to data from some of the locations being previously published. For the Kel'tma core, TOC was measured using a Carlo Erba EA interfaced with a Thermo-finnigan Delta V configured in continuous flow mode following decalcification using a 10% HCl treatment (Johnston et al., 2012a). The Kostovo-13 core and Narana Formation TOC measurements were conducted using the technique outlined in section 2.2.1. TOC values for the Avalon Peninsula have also been published (Canfield et al., 2007). Sediments similarly endured a 10% HCl wash for 24 hours before being measured on a Carlo Erba 1106 Elemental Analyser via combustion. Samples for the Cariboo Mountains, though not published, were determined in the same manner as those from the Avalon Peninsula.

5.3.2 Palaeoredox proxy

Iron speciation was the main palaeoredox tool applied to the sediments from each basin. The methodology of this technique is discussed in detail in section 2.3. The data sets were not produced during this research but were collected from other authors. The source of each data set and corresponding locality is shown in Table 5.1, with the publication or individual who collected the data specified.

Table 5.1 List of sources for iron speciation data used in this project

Locality	Author/Publication
Kel'tma Core	Johnston et al. (2012a)
Kostovo-13 Core	Romain Guilbaud (unpublished)
Avalon Peninsula	Canfield et al. (2007)
Cariboo Mountains	Canfield et al. (2008)
Narana Formation, Officer Basin	Rachel Beaumont (unpublished)

5.3.3 Phosphorus Speciation

To assess how P burial mechanisms potentially changed during the Ediacaran Period, an adapted version of the P speciation SEDEX method by Thompson et al. (*in prep*), was performed on a selection of samples from each basin. The methodology for this extraction is reviewed in section 2.5.

5.4 Results

All results for this chapter can be found in Appendix D. Lithologies for all samples can also be found in Appendix A.

5.4.1 White Sea

For comparative purposes, the Kel'tma and Kostovo-13 cores are further referred under the White Sea, due to their common stratigraphic and palaeontological correlations with this locality as discussed in sections 5.2.1 and 5.2.2 respectively.

5.4.1.1 Kel'tma Core

Before examining the P speciation results, the amount of P recovered from the extraction (P_{Sum}) needs to be addressed. For the Kel'tma core, P_{Sum} is plotted against P_{Tot} in Figure 5.2A. There is an overall low recovery for the Kel'tma core, with an average of 66 ± 6.2% P_{Tot} recovered. A potential cause for this low recovery is the existence of crystalline or refractory detrital phases (e.g. detrital apatite, monazite, xenotime) that are not removed during the sequential

extraction (März et al., 2014). To assess if the remaining fraction of P following the extraction (P_{unx}) is related to the detrital portion of the sediment (Al content), P_{unx} is plotted against Al in Figure 5.3A. No clear relationship is evident between these two phases, suggesting P was either lost during the method through the multiple decanting or transferring stages, or P exists in other refractory phases not targeted by the extraction. To address the low recovery, a bulk rock digestion was performed on the remaining sediment following P speciation. More P was recovered through the digestion method, increasing the average percentage recovery to 73 ± 5.9%. The additional recovery implies these sediments hosted P phases not targeted by the extraction. Further discussions on the detrital P fraction of these samples can be found in section 5.4.5. Care will be taken in interpreting these results due to the overall low recovery using the P speciation method.

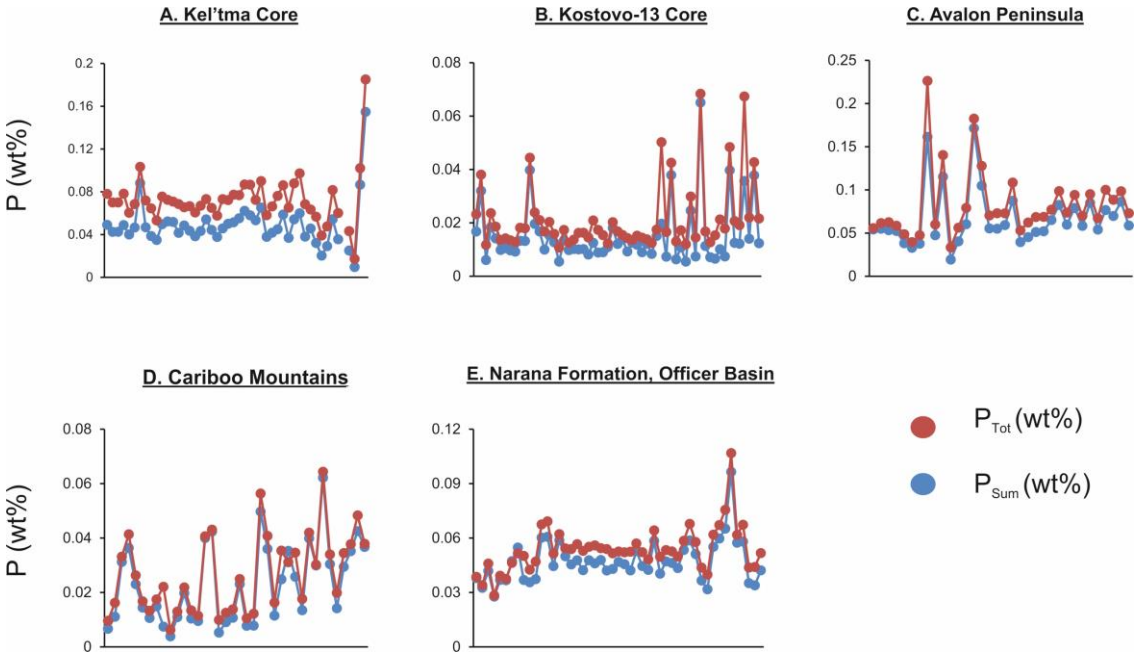

Figure 5.2 P_{Sum} vs P_{Tot} for all localities to illustrate P recovery from the sequential extraction. A – Kel'tma Core; B – Kostovo-13 core; C- Avalon Peninsula; D- Cariboo Mountains; E- Narana Formation, Officer Basin

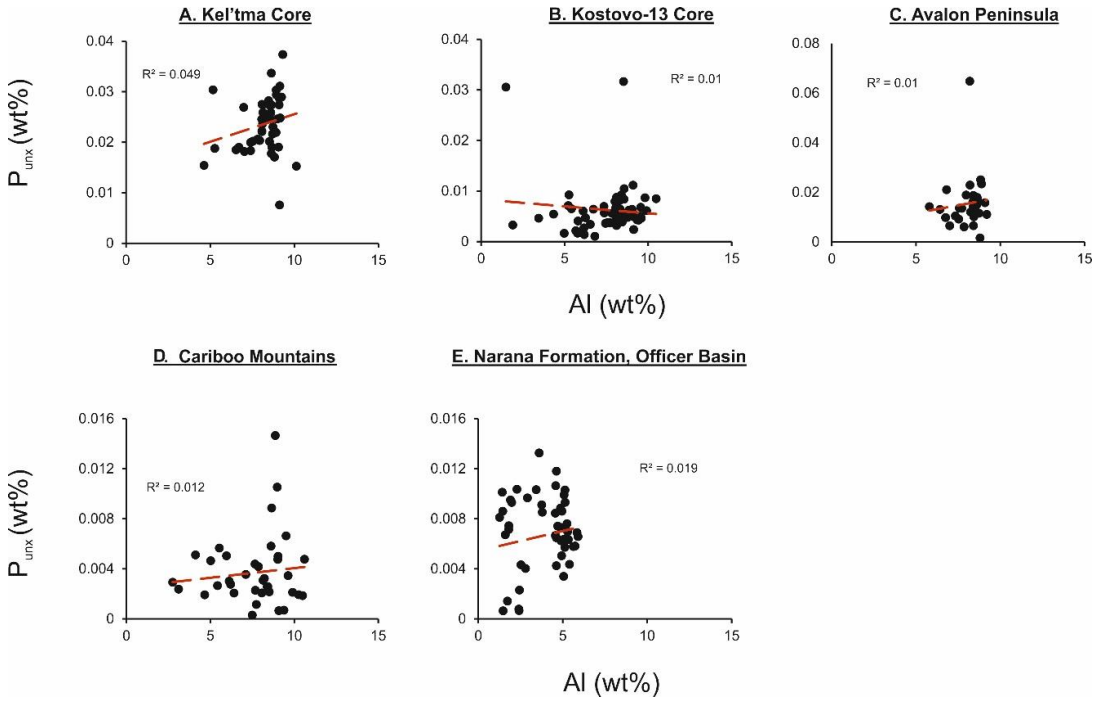

Figure 5.3 Relationship between P_{unx} and Al content for all sample localities

Total elemental (Fe, Al, P), TOC and Fe and P speciation results are shown in Figure 5.4. Phosphorus speciation results are the only new data presented here as all other elements were previously published in Johnston et al. (2012a). At the base in a mixed lithology package of Cryogenian age (approx. 780 – 635 Ma) (Ovchinnikova et al., 2000; Sergeev and Seong-Joo, 2006) Fe_T, Al and P exhibit fluctuations in their range of values throughout the Yskemess Formation. Only shales are included for P speciation, as problems have been found using carbonate-rich sediments due to the $CaCO_3$ buffering the acidity of the sodium acetate solution used to extract P_{auth} (Kraal et al., 2009)$_{\sim 9.4}$ Where there are relative increases in any of the total elements, corresponding rises in the others occur. Total organic C reaches a maximum of 0.38 wt% in the Yskemess Formation before declining to values < 0.04 wt%. This high value coincides with the highest Fe_T in the Cryogenian section at approximately 5 wt%. Total Fe is less than 2 wt% for the majority of these samples. Aluminium also exhibits fluctuations, with the lowest at the top of the section, similar to Fe, and the highest in the middle interval. The Fe_{HR}/Fe_T ratio signifies a dominantly anoxic water column in the Cryogenian unit. The ratio Fe_{PY}/Fe_{HR} indicates this anoxic water column was ferruginous, with the ratios all below 0.7. A small incursion in sulfide production is seen towards the top of the section, but not enough for the water column to become euxinic. Total P plots well above the average shale value (0.08 wt%; Turekian et al., 1961) at the base of the Yskemess Formation, and matches a similar increase in Al.

Overall the P_{Tot} values are relatively low, with a cyclic pattern to higher values in the middle and upper members of this formation, mirroring that of Fe and Al. The majority of P at the base of this unit is in the form of P_{det}, matching the high concentrations of Al, as Al is commonly used as an indicator for detrital material (Lyons and Severmann, 2006). Authigenic P burial is negligible in these samples, with P_{det} and P_{org} the most dominant phases. A decline in P_{det} to <50% P_{Sum} is accompanied by a minor increase in P_{auth}.

Moving stratigraphically upwards into the Ediacaran sediments (558 – 542 Ma), apparent shifts are evident in the behaviour of the analysed elements compared to their Cryogenian trends. Total organic C is consistently low throughout the Redkino and Kotlin horizons at an average of 0.09 wt%, with an overall decrease occurring in the Kotlin horizon. Total Fe plots relatively consistent through both horizons, with a decline in values at the Redkino-Kotlin boundary which recovers to initial values towards the top of the succession. Aluminium firstly declines at the base of the Redkino before steadily plotting in the range of 8 – 9 wt% for the remainder of the section. The previously published Fe_{HR}/Fe_T and Fe_{PY}/Fe_{HR} ratios are indicative of an oxic water column, and do not show variability between the Redkino and Kotlin horizons. However, P burial mechanisms fluctuate between the two members. At the base of the Redkino, an immediate increase in P stored in iron and magnetite phases occurs, though at a relatively small percentage. A declining trend occurs in both P_{auth} and P_{org} with a corresponding rise in the P_{det} content. Magnetite-P burial in the overlying Kotlin horizon is maintained throughout the section, but P_{Fe} falls to near zero values in the middle of the unit as Fe_T increases again. The Redkino-Kotlin boundary depicts the beginning of a switch to P_{auth} accumulation, where values reach 50% at the highest sampled level. Coinciding with this is a decrease in the proportion of P in detrital phases, falling from >50% in the Redkino to 33%. Organic P remains consistently low throughout the Kotlin horizon.

Kel'tma Core, Russia

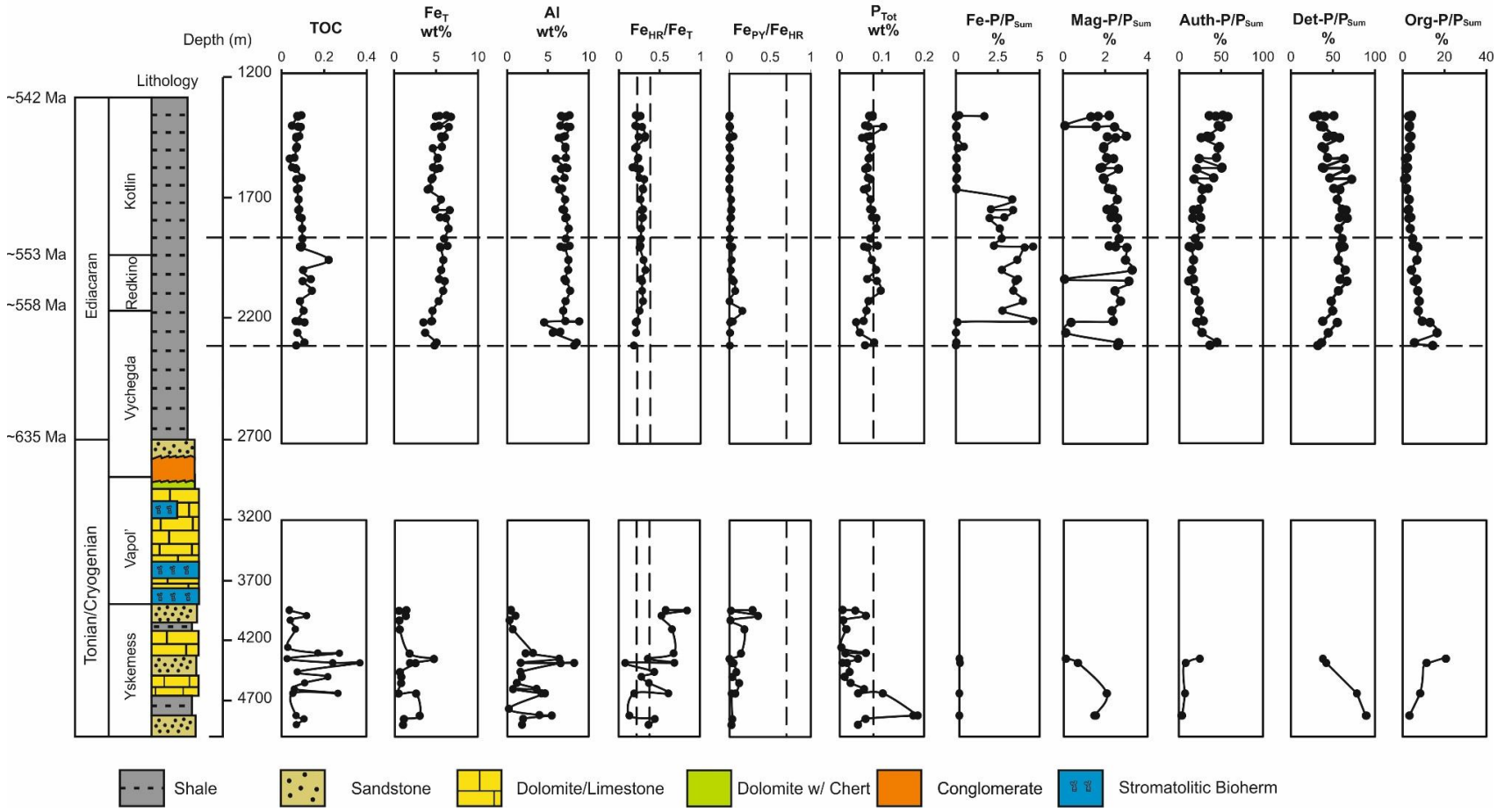

Figure 5.4 Log of TOC, Fe_T, Al, Fe_{HR}/Fe_T, Fe_{PY}/Fe_{HR}, P_{Tot}, and P speciation results for the Kel'tma Core. All P pools are reported as a percentage of the total amount of P extracted during the method (P_{Sum}). Fe_{HR}/Fe_T dashed lines are: oxic 0-0.22; equivocal 0.22-0.38; and anoxic 0.38-1. Fe_{PY}/Fe_{HR} dashed line at 0.7 is the boundary between ferruginous conditions (<0.7) and euxinic conditions (>0.8). The average shale value for P_{Tot} is 0.08 wt% (Turekian et al., 1961). The sedimentary log for this succession is taken from Johnston et al. (2012a)

5.4.1.2 Kostovo-13 Core

The results for the Kostovo-13 Core are shown in Figure 5.5. An average recovery of 70 ± 14.6% from the extraction (Figure 5.2B) is given. All values with P_{Sum} less than 70% are further removed from the discussion as they will not give accurate representations of P burial mechanisms in this basin. As the majority of samples gave an acceptable level of recovery, as outlined in the original Ruttenberg (1992) method, no further digests were performed on these samples. The relationship between P_{unx} and Al content of the sediment is shown in (Figure 5.3B). No correlation exists between these two phases (R^2 = 0.01), suggesting the sediments did not consist of a detrital pool that was not extracted during the method. At the base of this section in the Redkino and Gdov horizons, TOC and Fe_T display consistent trends. Levels of Al increase at the Redkino-Gdov boundary to 10.7 wt%, but subsequently fall to similar levels of the Redkino (~8 wt%). Both the Redkino and Gdov Formations are identified as anoxic, ferruginous by their Fe_{HR}/Fe_T values >0.38, and Fe_{PY}/Fe_{HR} values <0.7. One sample in the Gdov plots in the equivocal range, but the remaining samples are all in the anoxic realm. With Fe, Al and TOC largely consistent between the two horizons, P shows much more diversity in comparison. Total P values are low in comparison to the average shale value, with an average of 0.024 wt%. An increase to 0.067 wt% occurs in the Redkino corresponding to a rise in P_{Fe}, but is short-lived before returning to lower values typical of the succession.

At the Kotlin boundary, dynamic changes occur to the iron cycling within these sediments. The Fe_T contents reach up to 49 wt%, making these sediments incredibly iron-rich and further classified as ironstones. Pyrite nodules have been found at the boundary between Kotlin-1 and Kotlin-2 (Figure 5.5), and also correspond to the location of an ironstone.

Oxic intervals repeatedly occur following ironstone deposition in ferruginous conditions. A short-lived increase in P_{Tot} corresponds to a rise P_{Fe} up to 70% P_{Sum} but is accompanied by a decline to low levels in all other P pools. Iron-

bound P remains the dominant mechanism for P burial until the middle portion of the Kotlin horizon where organic sheets first appear. At this level, an immediate rise in P_{mag} and P_{org} occurs alongside a decline in P_{Fe}, P_{auth} and P_{det}. Towards the upper portion of the Kotlin horizon (315 m depth), redox stabilizes and reverts back to an anoxic, ferruginous state. Total P also steadies, with P_{auth} accumulation rising to 70% P_{Sum}, and coincides with a decline in P_{org} from 50% at the beginning of this unit, to 15% at the top of the section. Detrital P phases remain relatively consistent for the remaining samples with an average of 38%.

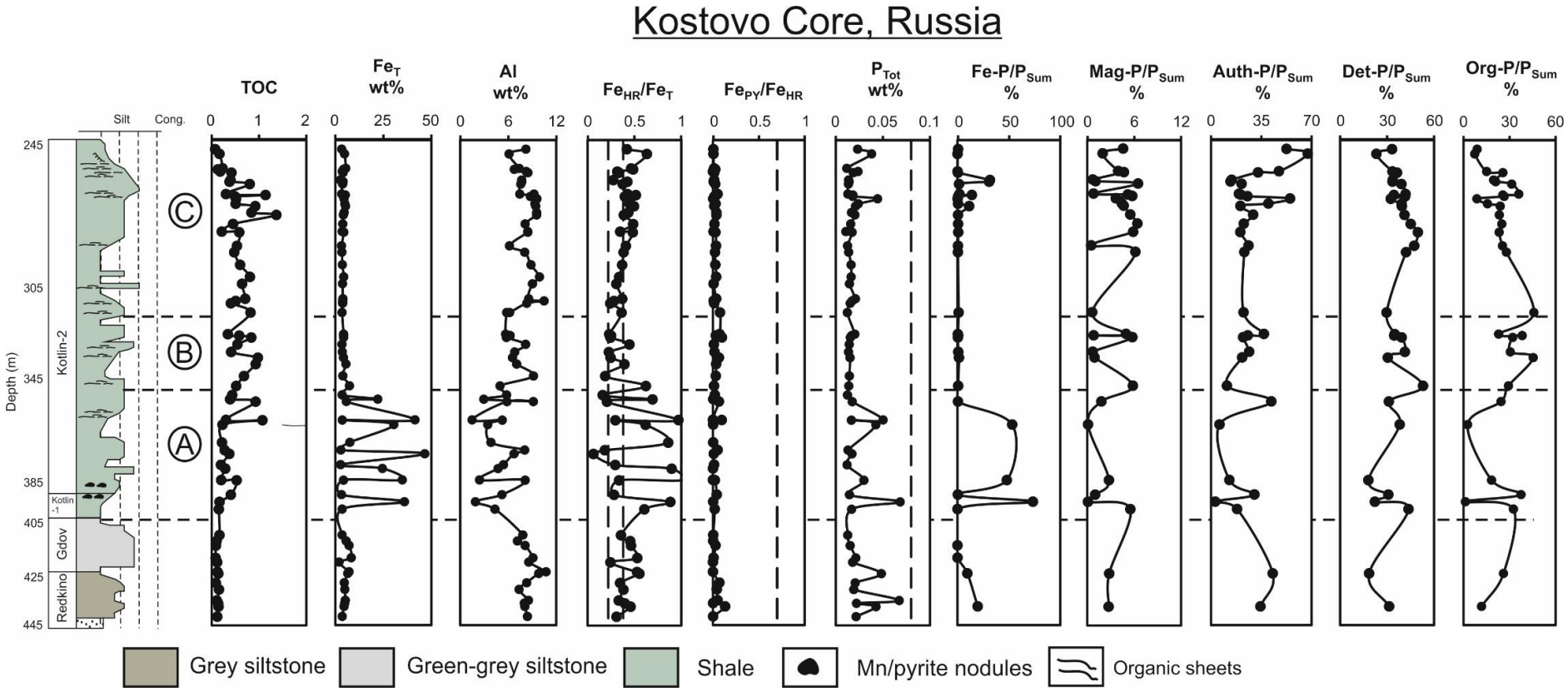

Figure 5.5 Chemostratigraphic log of TOC, Fe_T, Al, Fe_{HR}/Fe_T, Fe_{PY}/Fe_{HR}, P_{Tot}, and P speciation results for the Kostovo-13 Core. P speciation results are reported as a percentage of the total amount of P extracted during the method (P_{Sum}). The Kotlin-2 horizon is subdivided into units A, B, and C based on varying redox intervals

5.4.2 Avalon Peninsula

The Fe-S-C-P results for the deep marine Avalon Peninsula section are presented in Figure 5.6. An average recovery of 81 ± 7.2% resulted for the samples from this section, illustrated in Figure 5.2C. All samples had a recovery greater than 70% P_{Tot} and are thus included for further discussion. Similarly to the other locations, no correlation exists between P_{unx} and Al content ($R^2 = 0.01$).

Iron speciation and TOC analyses were previously published for the Avalon Peninsula (Canfield et al., 2007, 2008). At the boundary between the Mistaken Point Formation and the lower Trepassey Formation, TOC is close to zero and remains so throughout the Mid to Upper Trepassey. At the base of each member of the Fermeuse Formation, an increase in TOC to an average of 0.12 wt% occurs before declining to levels below detection. Total Fe and Al exhibit similar behaviour throughout the succession, plotting relatively consistently at averages of 4.4 wt% and 8.1 wt% respectively. Three excursions to lower values from these average values are seen in both elements at the top of the upper Trepassey, the base of the Mid Fermeuse and top of the Upper Fermeuse. The redox state given by Fe_{HR}/Fe_T highlights a dominantly oxic water column, with some values in the Upper Trepassey plotting in the equivocal range. One sample has a Fe_{HR}/Fe_T ratio greater than 0.38, suggesting a possible anoxic state. Variations in the Fe_{PY}/Fe_{HR} ratio occur throughout the succession, but all plot below 0.5.

Though the concentrations of Fe and Al remain moderately steady in the Avalon unit, the same cannot be said for that of P. Total P values show marked increases in the Upper Trepassey and the Lower Fermeuse with the remaining samples plotting close to or at the average shale value. These rises in P_{Tot} do not all result in the same relative increase in P burial mechanisms. In the Upper Trepassey, the greater than average shale value of P_{Tot} coincides to high P_{det} values. The same occurs for the base of the Lower Fermeuse. However, the remainder of this unit sees an increase in the proportion of P buried as P_{auth}. A return to low levels of P_{auth} formation (<15%) is shown for the remainder of the unit. Iron-bound P exhibits some changes in behaviour. At the base of Mid Fermeuse, P_{Fe} shifts from levels below 4% to 9.5%. Magnetite-bound P values are all below 3% for the entire section. These sediments contain little P_{org} with all except one sample from Mistaken Point, with a value below 0.1%.

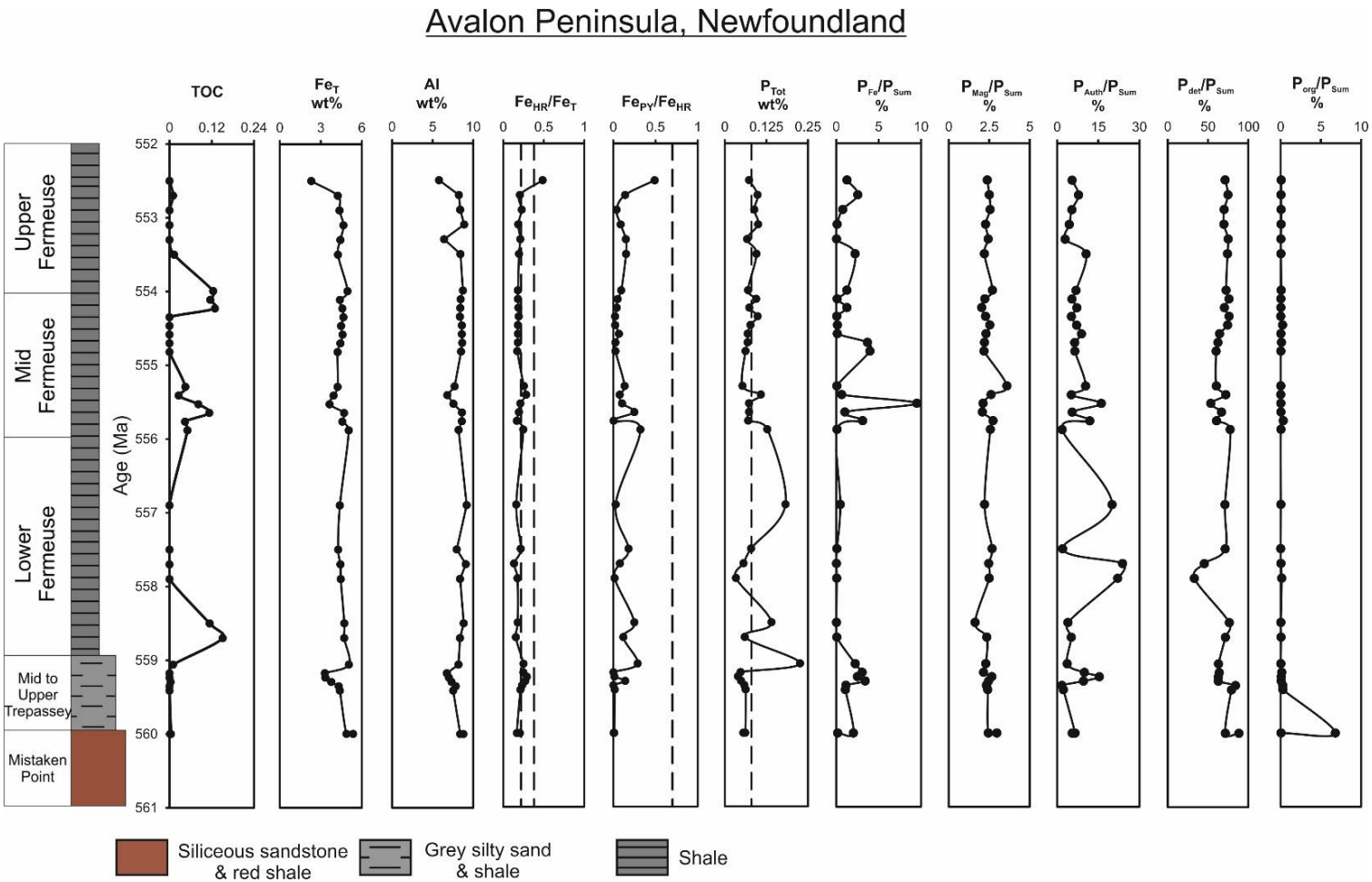

Figure 5.6 Chemostratigraphic log of TOC, Fe_T, Al, Fe_{HR}/Fe_T, Fe_{PY}/Fe_{HR}, P_{Tot}, and P speciation results for the Avalon Peninsula sedimentary succession. Sedimentary log adapted from McCall (2006). P speciation results are reported as a percentage of the total amount of P extracted during the method (P_{Sum})

5.4.3 Cariboo Mountains

Recovery from the P speciation method for samples from the Cariboo Mountains stands at an average of 81 ± 15.8% P_{Tot} (Figure 5.2D). Samples with less than 70% or greater than 100% P_{Tot} are further removed from the results. Assessment of the relationship between P_{unx} and Al showed no observable correlation (R^2 = 0.012) between the pair, implying the remaining P phases were not related to the detrital content.

The results for the Cariboo Mountain sedimentary succession are shown in Figure 5.7. At the base, the Kaza Group (approx. 595 – 590 Ma) exhibits consistently low TOC with values below 0.1 wt%. Total Fe and Al show a generally decreasing trend until the boundary with the overlying Lower Isaac Formation, where they subsequently increase. At the top of the Lower Isaac, Fe_T rises to an average of 4.6 wt%, which coincides with a decline in Al. An oxic redox state is identified in both the Kaza and Lower Isaac Formations based on the Fe_{HR}/Fe_T ratio. Strong variations in the Fe_{PY}/Fe_{HR} occur throughout the succession, with one sample marking as euxinic in the Kaza. Total P exhibits some variation between the two formations but is overall low with an average of 0.027 wt%. Detrital P is the main P phase for these sediments and typically exceeds 70% of the P_{Sum}. Iron-bound P and P_{mag} remain at low values (~2%). P_{auth} burial falls in the Kaza and base of the Lower Isaac. Small increases to values of 10% occurs towards the top of the unit. This rise in P_{auth} also correlates to a rise in P_{org} to 15%, with the underlying samples typically falling below 5%.

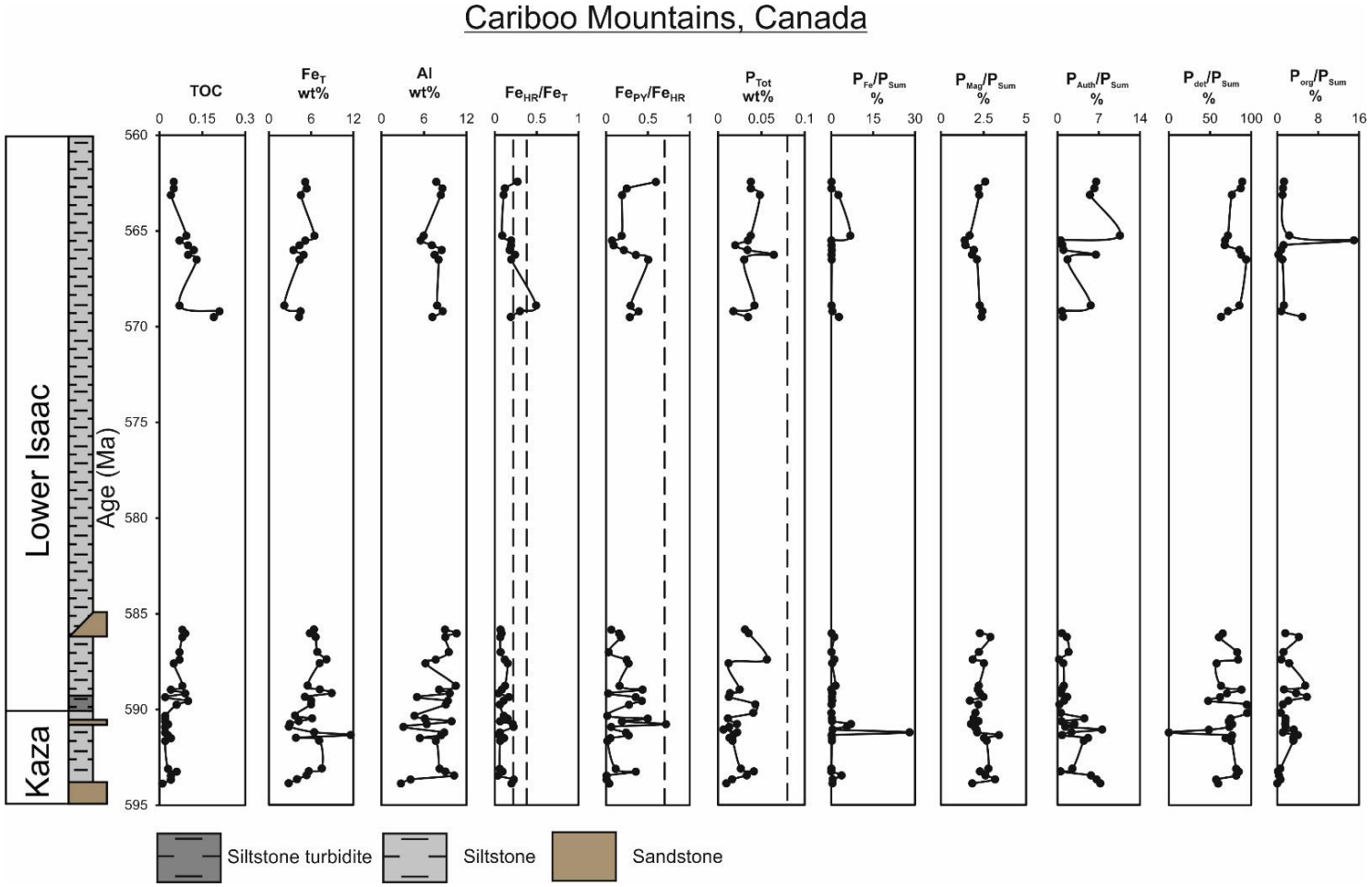

Figure 5.7 Chemostratigraphic log of TOC, Fe_T, Al, Fe_{HR}/Fe_T, Fe_{PY}/Fe_{HR}, P_{Tot}, and P speciation results for the Cariboo Mountains unit, Canada. The sedimentary log is drawn based on the lithologies recorded during sample collection. P speciation results are reported as a percentage of the total amount of P extracted during the method (P_{Sum})

5.4.4 Narana Formation, Upper Ungoolya Group

An average recovery of 88 ± 6.5% P_{Tot} (Figure 5.2E) resulted for samples from the Narana Formation following the sequential extraction. Comparably to all other investigated sites, no correlation exists between P_{unx} and Al (R^2 = 0.019). The geochemical results for the Upper Ungoolya Group of the Officer Basin are displayed in Figure 5.8. Total organic C values are consistent until the calcareous mudstone interval where it fluctuates to higher levels (>0.3 wt%) in the middle and top of the section. At the base of the green silty member, increasing trends are seen across Fe_T and Al but are relatively low in comparison to the other sections. Following the initial increase, values remain steady before beginning to decline in the calcareous mudstone, to their lowest values in the limestone member. Fluctuating redox conditions also occur across this unit. Anoxic conditions at the base correspond to a rise in total elements. Anoxia is initially ferruginous, with Fe_{PY}/Fe_{HR} ratios low but show a gradual increase to a possible short-lived euxinic event. Above this horizon, oxic conditions prevail in the shale member before changing to anoxic, ferruginous, and equivocal values in the upper two members of the unit.

Total P mirrors the trends of Fe_T and Al. High values at the base of the succession plot above the average shale value and coincide with anoxic settings and the highest P_{Tot} values before the interval containing high Fe_{PY}/Fe_{HR} ratios. Thus differences in P burial mechanisms are prevalent between the base of the shale member and the remainder of the succession. The base is the only location where burial in P_{Fe} phases occurs, but still remains at low levels (<2%). Coincidentally this is where the lowest amount of P_{mag} is, along with P_{det} and P_{org}. The most consistent burial in P_{auth} is also found here, with an average value of 27.3%. The rest of the shale member exhibits negligible burial in P_{Fe} and P_{auth}, with the dominant source of P in detrital phases. At the boundary to the calcareous mudstone, a shift to higher levels of P_{auth} occurs, along with an immediate rise in $P_{org,}$ but at a small level (2%). P_{det} levels similarly decline and remain at approx. 70% throughout the succession. P_{auth} levels decline but remain a significant proportion of the buried P in the limestone member with values at ~25%. As Fe_{HR}/Fe_T values increase, so does P_{org} burial but at minute levels.

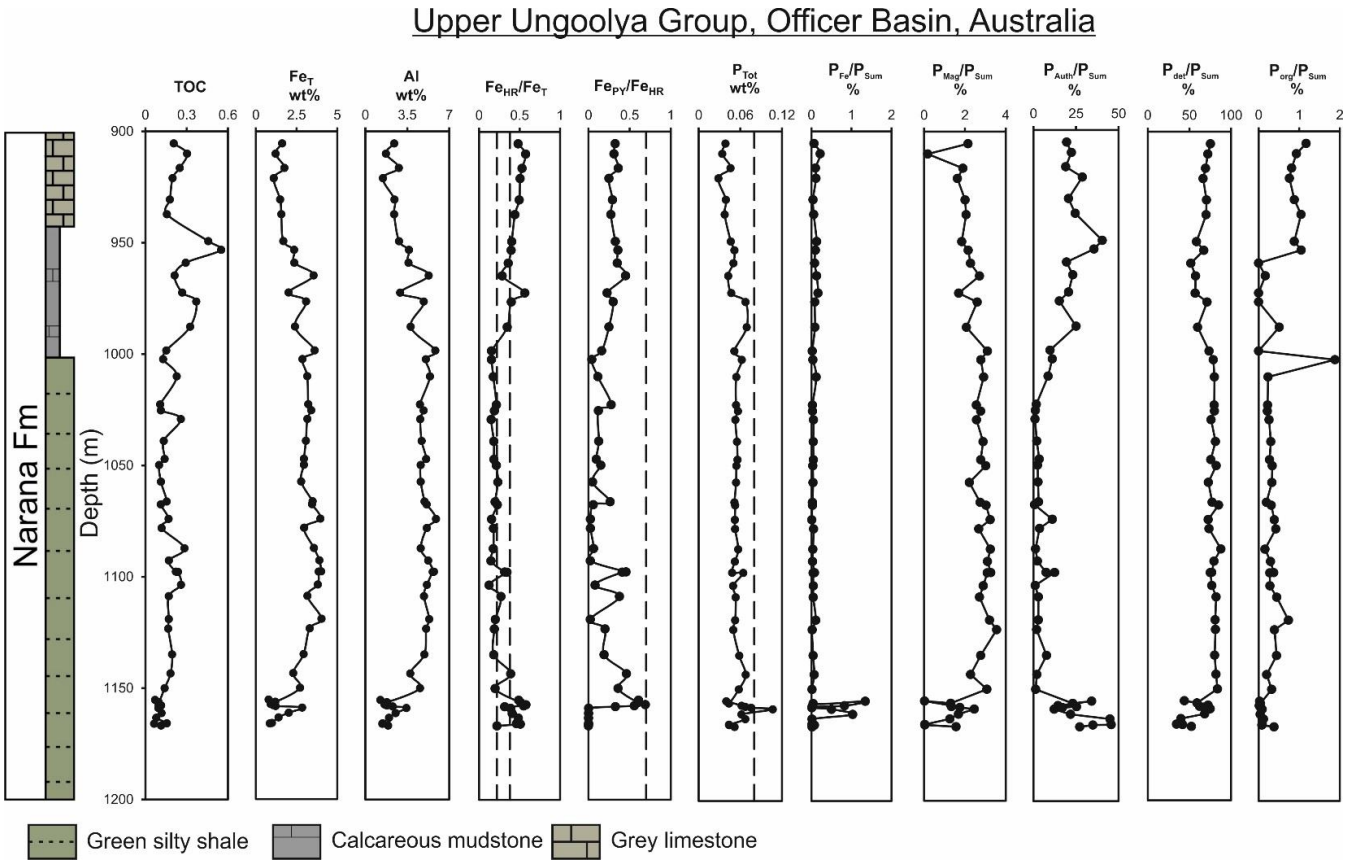

Figure 5.8 Chemostratigraphic log of TOC, Fe_T, Al, Fe_{HR}/Fe_T, Fe_{PY}/Fe_{HR}, P_{Tot}, and P speciation results for the Narana Formation, Upper Ungoolya Group, Australia. The sedimentary log is drawn based on the lithological divisions of the Munta-1 drill core presented in Arouri et al. (2000). P speciation results are reported as a percentage of the total amount of P extracted during the method (P_{Sum})

5.4.5 Detrital P

A limitation of the new P speciation method is the potential extraction of P_{auth} phases during the P_{det} stage of the method. This is because authigenic and detrital phases of P exist along one continuous spectrum of potential forms of P minerals, from francolite to detrital apatite, with the boundary between them poorly defined. Apatite is an abundant accessory mineral in both igneous and metamorphic rocks, and typically exists in the detrital form of fluorapatite in sedimentary rocks. Authigenic phases typically consist of CFA, a carbonate-rich variety of fluorapatite. Their mineralogical similarities creates complications in operationally defining these two pools. This is particularly more difficult in ancient sediments, as during burial diagenesis P_{auth} can transform to P_{det} as a result of increased crystallinity, rendering the Na acetate step of the sequential extraction ineffective at measuring the original pool of P_{auth}. However, this issue has also been observed in more modern sediments (e.g. Eijsink et al., 2000; Kraal et al., 2012; März et al., 2014; Faul et al., 2005). An overestimation of the detrital pool can further complicate interpretations of P burial mechanisms in sediments, as detrital P is not bioavailable and thus not an important factor in ancient nutrient studies. Other authors have assessed the relationship between P_{det} and P_{reac} to Al to understand the detrital fraction of their investigated sediments. A positive correlation would be expected to result between P_{det} and Al if the extraction is successful at separating detrital phases from other reactive phases, as Al is widely used as a tracer for detrital content (Lyons and Severmann, 2006). For the localities researched here, these relationships are shown in Figure 5.9. For all sites, no strong positive correlation results. To further ensure P_{reac} is not related to the detrital content of the sediment, P_{reac} is also plotted against Al in Figure 5.9. A positive but weak relationship is shown for the Kel'tma core ($R^2 = 0.3702$), tying into the previous concerns raised surrounding P speciation results in 5.4.1.1. No definitive conclusions can thus be stated based on these relationships concerning the success of the extraction at separating detrital and authigenic phases. Proposed here is a new potential method to assess this issue by analysing the correlation between P_{det} and P_{Tot}. If a depositional area, such as a continental margin, would expected to be a large sink of reactive P, as typically seen in modern environments (Ruttenberg, 2003), these areas should not show a strong correlation between P_{det} and P_{Tot} if there is no link between P_{det} and Al, as reactive phases should constitute the bulk proportion of P. Redox and sedimentation rate would be the major controls on the type of P within these sediments, rather than the settling of detrital material. The reverse could then be suggested for deep sea

environments (e.g. basin floor, continental slope), whereby they would be expected to be dominated by detrital material. Biomineralization of skeletons would not have evolved during the investigated time period, implying skeletal debris would not be a source of reactive P to deep sea sediments that is observed in modern studies (Faul et al., 2005; Schenau and De Lange, 2001). A weak but positive relationship results for the Kel'tma core (R^2 = 0.471). This gives confidence in the P speciation results from this succession which had overall low recovery values. The Kosotovo-13 core however shows a much stronger relationship (R^2 = 0.741) between P_{det} and P_{Tot}, potentially implying detrital phases were incorrectly extracted. It must also be noted the extremely low values of P within this site's samples, with the majority P_{Tot} less than 0.02 wt%. This creates a larger room for error when dealing with such low values. Both the Avalon Peninsula (R^2 = 0.946) and Cariboo Mountains (R^2 = 0.919) exhibit strong positive relationships between P_{det} and P_{Tot}, matching their depositional environment of basin floor and continental slope respectively. A strong, positive correlation also results for the Narana Formation (R^2 = 0.696), a continental slope deposit, again giving assurance to the P speciation method. This is a qualitative method of assessing the detrital pool within these sediments, and for the majority of locations, gives confidence in the results presented here. Care will be taken in investigating the Kostovo-13 core, due to their low values as well as positive correlation between P_{det} and P_{Tot}.

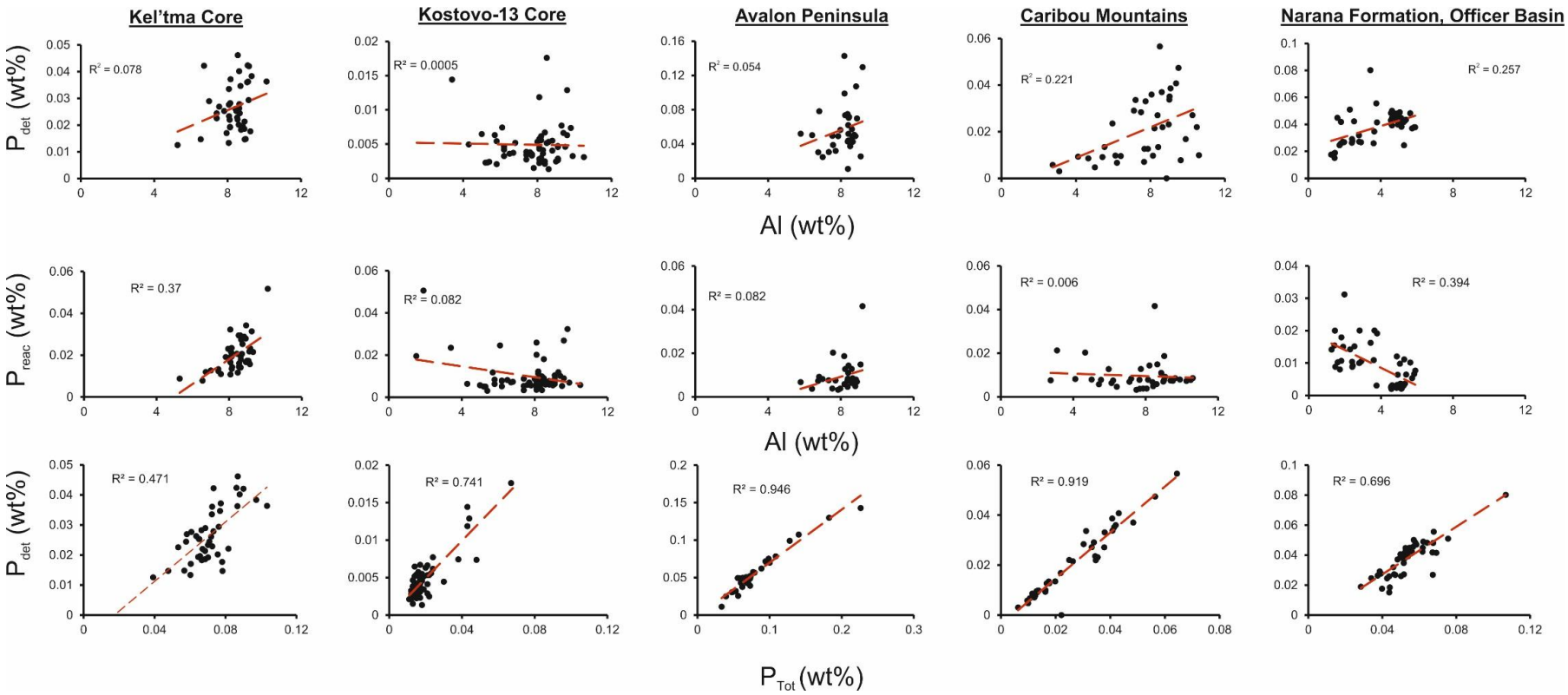

Figure 5.9 Assessment of relationship between P_{det} and P_{reac} to Al content from all localities investigated in this study. P_{det} versus P_{Tot} is also shown for each locality.

5.5 Discussion

The Fe and P speciation results will first be discussed by location before being pieced together in a global context to gain a detailed insight into P burial mechanisms during the Ediacaran Period.

5.5.1 White Sea

As both the Kel'tma and Kostovo-13 cores contain the same horizons and are correlated to the White Sea, comparisons can made between their Fe-C-P cycling patterns in Figure 5.4 and Figure 5.5. Across the two cores, TOC, Fe_T and Al are markedly similar in both horizons, but their redox state, P_{Tot} and P cycling all vary. In the Kel'tma core, the Redkino Formation was previously classified as an oxic water column (Johnston et al., 2012a). This is not mirrored in the Redkino Formation in the Kostovo-13 core, as ferruginous conditions are identified by Fe_{HR}/Fe_T ratios greater than 0.38. There is no difference in the average Fe_T of these sediments, only the proportion of reactive iron driving the Kostovo-13 basin anoxic (Anderson and Raiswell, 2004; Poulton and Raiswell, 2002). The Kel'tma Kotlin horizon persists in its oxic redox state, but episodic changes to the water column redox state transpire in the Kostovo-13. Based on the varying redox intervals, the Kostovo-13 Kotlin horizon is divided into the following members (Figure 5.6).

Member	**Redox**	**Depth (m)**
A	Ferruginous	348 – 437
B	Oxic	307.5 – 344.2
C	Ferruginous	244.5 – 301.2

As previously mentioned in 5.4.1, ironstones are present in member A, indicating a large flux of iron during these intervals. To ensure the large enrichments in iron within these sediments are the result of authigenic processes and not from an influx of detrital material, the relationship between Fe_{HR}, Fe_{OX}, and Fe_T are illustrated in Figure 5.10.

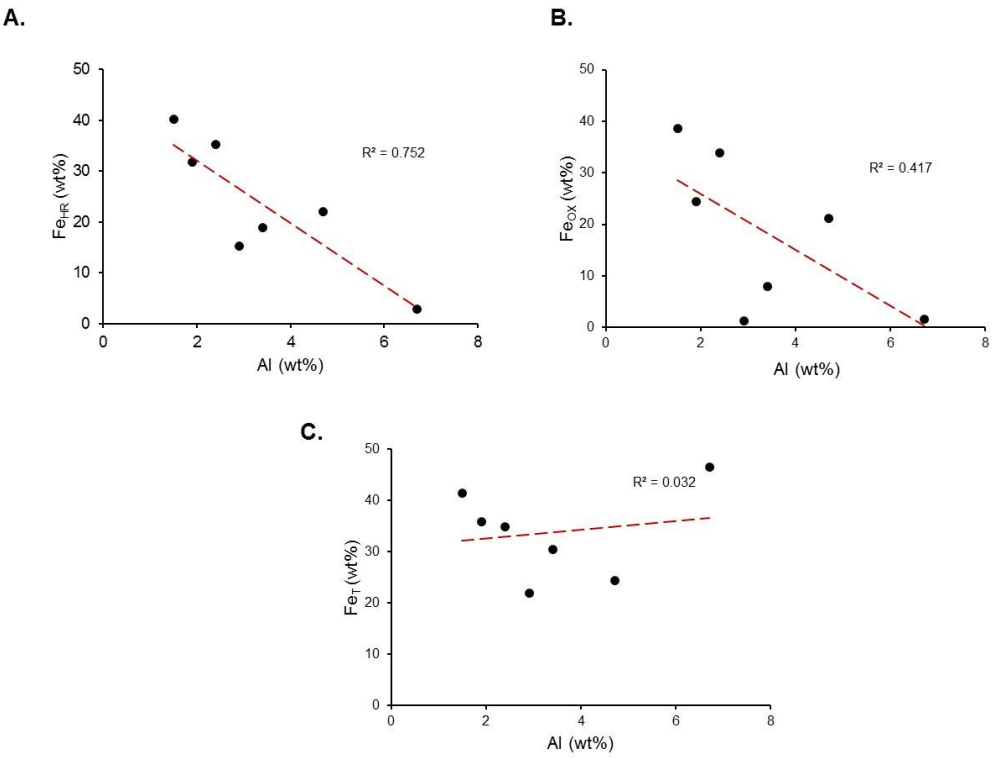

Figure 5.10 Assessment of relationship between detrital content of ironstone samples, represented by Al, versus Fe_{HR} (A), Fe_{OX} (B), and Fe_T (C) for the Kostovo-13 core

There is no positive correlation between any of these iron phases with Al to suggest detrital content influenced the sedimentary iron fractions. Large volumes of dissolved iron typically accumulate in sediments as a result of two processes: hydrothermal activity and anoxic diagenesis (Poulton and Raiswell, 2002; Poulton and Canfield, 2011). Under anoxic settings, particulates can also act as a substantial source of iron to sediments during their transport and deposition. Water column formation of unsulfidized iron minerals further supply an additional sedimentary iron enrichment mechanism under ferruginous settings. As this unit is generally considered a shallow marine deposit, hydrothermal activity is unlikely to have acted as a source of iron to this unit. Several of the ironstones consist of almost equal parts Fe_{CARB}, Fe_{OX} and Fe_{MAG}, suggesting water column precipitation of these iron minerals formed the basis behind their enrichment mechanism. Certain criteria need to be met for sedimentary Fe enrichments to prevail, such as during upwelling on continental slopes and shelves (Poulton and Canfield, 2011) . This suggests a ferruginous water column with further Fe(II) supplied from upwelling played a role in ironstone formation. Other ironstones in this unit consist predominantly of Fe_{OX}. Substantial amounts of Fe_{OX} have been known to accumulate as a result of anoxygenic phototrophs, which use dissolved Fe(II) as an oxidation substrate

and result in the precipitation of poorly crystalline Fe(III) hydroxides such as ferrihydrite, which quickly age (over weeks) to crystalline phases e.g. lepidocrocite or goethite P (Kappler and Newman, 2004). As these iron-enriched sediments contain different proportions of Fe_{HR} phases, this has influenced P burial mechanisms. Only two of the ironstones could be included in the P results due to their low recovery in unit A, but from Figure 5.6Figure 5.6, these are not the only layers to accumulate high levels of P_{Fe}, as other finely bedded, shale samples (KS-63, KS-65, KS-119, KS-138) record P_{Fe} values greater than 20% P_{Sum}. All of these samples correspond to ferruginous Fe_{HR}/Fe_T ratios (>0.38) in units A and C, thus implying P was potentially scavenged from the water column as unsulfidized iron minerals formed and precipitated. The highest peak in P_{Tot} corresponds to the highest $P_{Fe,}$ suggesting a large amount of P was sequestered in the sediments, potentially depleting the seawater inventory and resulting in the overall low P_{Tot} for the remainder of the succession. Thus the dynamic behaviour of redox and iron mineral formation played an intrinsic role in P burial. Iron-bound P typically acts as a source of P to form authigenic minerals. However, in the Kostovo-13 core, high levels of P_{Fe} are preserved and do not depict that P_{Fe} sink-switched to P_{auth}. A potential reason for this is the existence of Fe(II) phosphates e.g. vivianite, authigenic P minerals which are not targeted in the P_{auth} stage of the extraction. The formation of these minerals usually occurs below the sulfate-methane transition zone in the sediment, when phosphate released from Fe_{OX} during reductive dissolution diffuses downwards and precipitates in an authigenic form within the methanic zone (März et al., 2018). A more detailed outline of this process is discussed in 1.5.2.2.2. If these Fe(II) phosphates existed they would be removed during the P_{Fe} stage of the sequential extraction, however there is no definitive way of assessing their existence within these sediments. Iron phosphate minerals have been documented to form in freshwater settings (Fagel et al., 2005) but also in marine areas with high organic matter loading (Berner, 1990); and shallow anoxic sediments in the Baltic Sea and Black Sea (Jilbert and Slomp, 2013; Dijkstra et al., 2014, 2016, 2018). Total organic C values for the Kostovo-13 core are generally high in comparison to the other localities, and are also in shallow anoxic environments, potentially compatible for Fe(II) phosphate formation, if the Fe_{OX} escaped surface redox processes and were buried to the SMT zone. Excluding the ironstones from the analysis of the Kostovo-13 Kotlin, the average Fe_T for the Kotlin is 7.9 wt%, higher than the 5.4 wt% average in the Kel'tma core. A rise in TOC also occurs in member B to an average of 0.33 wt% before returning to similarly low values as recorded in the Redkino horizon. Total

organic C is generally higher in the Kostovo-13 core than in the Kel'tma, implying increased organic matter loading in comparison to the Kel'tma. Such differences will be tied into the discussion concerning P burial mechanisms in these two localities. The differing redox and elemental trends contributes to the emerging evidence that the Ediacaran Period experienced local heterogeneities in ocean redox (Bowyer et al., 2017; Canfield et al., 2008; Sperling et al., 2015; Wood et al., 2015; Li et al., 2015a; McFadden et al., 2008; Li et al., 2010), with two basins in relatively close proximity to one another experiencing dynamic changes to their redox states.

The burial and recycling of P in marine sediments is largely controlled by the redox state of the overlying water column (Ingall et al., 1993; Calvert et al., 1996; Benitez-Nelson, 2000; Anderson et al., 2001; Algeo and Ingall, 2007; März et al., 2008). As a result, P cycling between the oxic Kel'tma and dominantly ferruginous Kostovo-13 core would foreseeably be different. Increased burial of P under oxic conditions and promoted P recycling in anoxic conditions has long been observed in modern marine sediments (Krom and Berner, 1981; Berner, 1973; Ingall et al., 1993; Van Cappellen and Ingall, 1996; Slomp et al., 1996a; Delaney, 1998; Anschutz et al., 1998; Bjerrum and Canfield, 2002). However, the division of anoxia into iron-rich, ferruginous or sulfide-rich, euxinic conditions has a profound effect on whether P is buried or recycled. Recycling of P is promoted in euxinic settings, while burial can occur more readily under a ferruginous water column (März et al., 2008). However, this latter case will also depend on the redox state of porewaters close to the sediment-water interface. Significant recycling of P back to the water column might also be expected beneath ferruginous bottom waters if interstitial porewaters are sulfidic. This corroborates with the P burial mechanisms found in both cores. In the Kel'tma core, P_{auth} increases at the Redkino-Kotlin boundary to a maximum of 52% at the top of the Kotlin when P_{Fe} and P_{org} are exhausted. The lack of significant P_{org} and P_{Fe} suggests near-complete 'sink-switching', with release of P from organic matter and Fe oxides during diagenesis and subsequent formation of CFA. A similar trend occurs in the ferruginous Kotlin of the Kostovo-13 core. The initially high values of P_{org} and P_{Fe} all deplete towards the top of the unit, where P_{auth} reaches a maximum of 67%. This demonstrates that in these settings, P was extensively buried as authigenic phases under ferruginous conditions as well as oxic. Trapping of P in the sediments under ferruginous conditions in the Kostovo-13 core is consistent with the very low pyrite contents of ferruginous intervals (Figure 5.5), suggesting that porewaters close to the sediment-water interface were not sulfidic. It also gives further evidence for the Kotlin horizon as a marine deposit,

as high rates of CFA formation at the expense of P_{org} and P_{Fe} are typical of oceanic sediments (Delaney, 1998).

To further validate P burial under different redox conditions, $(C:P)_{org}$ and $C_{org}:P_{reac}$ ratios are compared to the Redfield ratio (molar C:P, 106:1) (Anderson et al., 2001; Kraal et al., 2010). In Figure 5.11A, molar $(C:P)_{org}$ values for the Kel'tma core all, with the exception of one anoxic sample from the Yskemess Formation (Cryogenian), plot below or at the Redfield ratio, demonstrating that P_{org} has not been preferentially recycled from organic matter during microbial remineralization. This is consistent with a lack of free sulfide in the porewaters under the low C_{org} contents evident for this core. However, most of the oxic samples plot below the Redfield Ratio when $C_{org}:P_{reac}$ ratios are considered (Figure 5.11B), which suggests that any P which was released during organic matter remineralization was largely retained in the sediment. In addition, Fe (oxyhydr)oxides were likely a flux of P to the sediments, and also largely retained as P_{auth}. Anoxic samples show some scatter in $C_{org}:P_{reac}$ ratios (Figure 5.11B). However, these samples often plot at higher ratios than oxic samples, which suggests that under anoxic ferruginous conditions, although P was not extensively recycled from organic matter (Figure 5.11A), some P was likely recycled back to the water column from the reductive dissolution of Fe (oxyhydr)oxide minerals (probably as a result of dissimilatory Fe reduction).

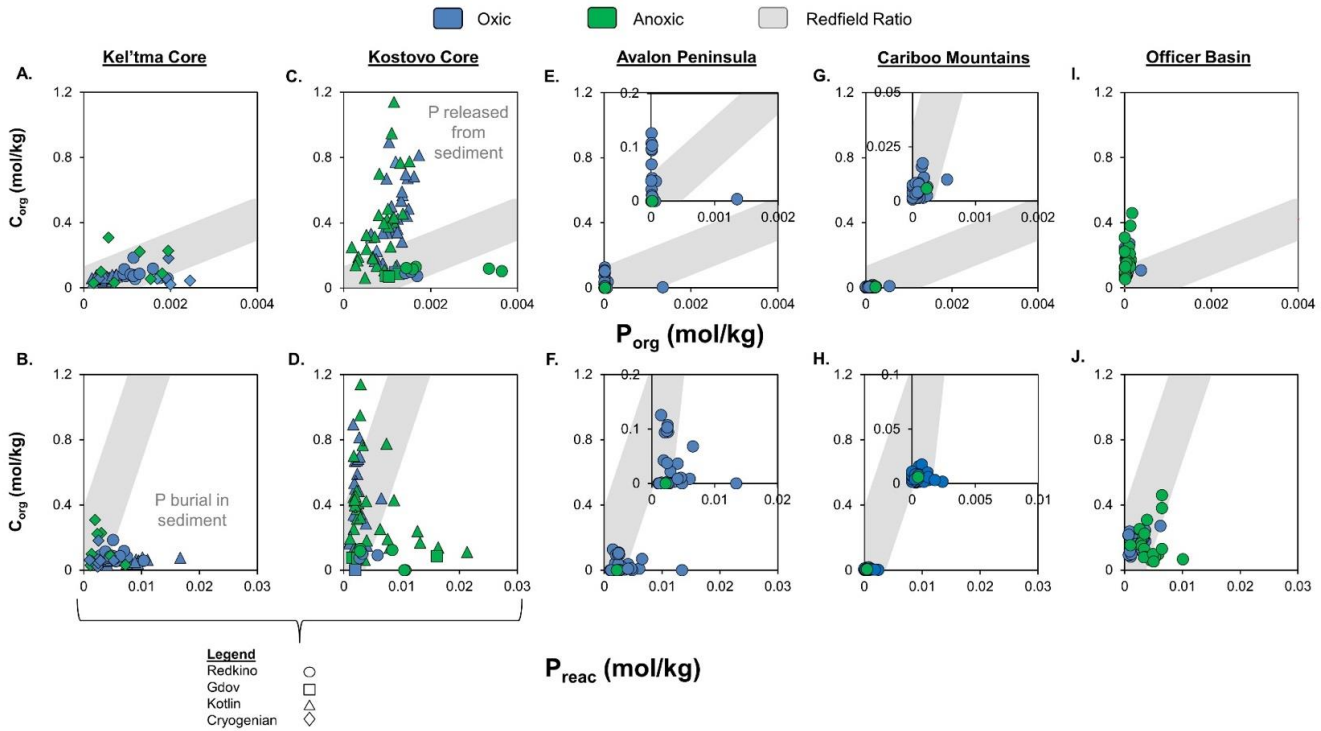

Figure 5.11 $(C:P)_{org}$ and $C_{org}:P_{reac}$ plots for each locality. Each sample is colour-coded based on redox, with oxic samples in blue ($Fe_{HR}/Fe_T < 0.38$) and anoxic samples in green ($Fe_{HR}/Fe_T > 0.38$). Equivocal samples are not individually categorized due to potential complications when interpreting these scatter plots. Insets in the Avalon Peninsula and Cariboo Mountains show these trends at smaller scales than depicted by the other sites. The Redfield Ratio is indicated by the grey band on each chart. The size of this line is to account for the low values of C_{org}, P_{org} and P_{reac} in these basins, as they are typically much higher in modern settings

For the Kostovo-13 core (Figure 5.11C), C_{org}:P_{org} ratios display marked variance based on the horizon examined. Samples from the Gdov and Redkino horizons tend to mirror the behaviour of Kel'tma samples. C_{org}:P_{org} ratios for these formations generally plot close to the Redfield Ratio, suggesting a limited, preferential release of P_{org} from organic matter, with the exception of two samples. C_{org}:P_{reac} ratios also tend to be mostly, very close to the Redfield Ratio, implying there was not a significant source of P_{Fe} to these sediments, and most of the P was retained in the sediment. Phosphorus trapping and limited recycling is entirely agreeable with the low TOC content of these units (Figure 5.5). The majority of samples from the Kotlin, however, have C_{org}:P_{org} ratios which plot above the Redfield ratio (Figure 5.11C), consistent with preferential release of P_{org} compared to C_{org}. Furthermore, both oxic and anoxic samples often have C_{org}:P_{reac} ratios higher than the Redfield ratio. This implies that there was extensive recycling of P back to the water column under both ferruginous and oxic conditions. In modern sediments, recycling has been observed in anoxic and hypoxic settings (Algeo and Ingall, 2007; Mort et al., 2010; Jilbert et al., 2011), where the dissolution of Fe_{ox}-bound P promoted the release of P from the sediment, as the redox states changed between these two forms. A larger proportion of oxic samples have C_{org}:P_{reac} ratios higher than the Redfield ratio in comparison to their respective C_{org}:P_{org} ratios. This suggests that other phases, such as P_{Fe}, than P_{org} were recycled to the water column, during these oxic-anoxic intervals. There is no current evidence to suggest hypoxic conditions were encountered during these intervals, as no hypoxic settings have been recorded during this period. Rather, rapid switching of the water column between oxic and ferruginous conditions could potentially have promoted the dissolution of Fe_{ox} in surface sediments, removing the Fe_{ox} barrier which can retain phosphate in the sediments (Slomp et al., 1996a), and thus recycling P back to the water column. The re-establishment of anoxic water column conditions, in addition to the much higher TOC loading evident for the Kotlin Formation in this core (Figure 5.5), resulted in the further release of P from organic matter and Fe_{ox} for sediments that were initially deposited under both oxic and ferruginous conditions. A positive productivity feedback was likely reinforced, leading to the enhanced deposition of TOC in this unit. Additionally, the anoxic Kotlin samples that do plot below the Redfield Ratio (Figure 5.11D), are all from member A of the Kotlin, with either extremely high Fe_T (>20 wt%) or very high burial in iron phases compared to the rest of the section. This suggests that Fe oxides were a major source of P in these samples, and while some of this original P_{Fe} was likely recycled back to the water column, a proportion was also retained in the sediment. It is also worth

noting that the apparent role of TOC concentrations in these sediments is similar to that observed in modern environments. For open ocean sediments in the central Pacific with TOC < 0.4 wt%, values of $(C:P)_{org}$ were lower than the Redfield Ratio, while samples with TOC > 0.4 wt% where greater than the Redfield ratio (Ni et al., 2015). This behaviour has been attributed to the remineralization of organic matter (Anderson et al., 2001). Though P is being recycled from these sediments in both the anoxic (iron-rich) and oxic intervals, P_{auth} still continues to form and shows no noticeable difference in overall percentages between the different redox intervals.

The final major difference between the two basins is sedimentary P_{Tot} values. In the Redkino horizon, an average of 0.042 wt% occurs in Kel'tma and 0.024 wt% in Kostovo-13. Both exhibit increasing trends towards the boundary with the overlying Kotlin horizon, rising to an average of 0.07 wt% in the Kel'tma, but remaining relatively unchanged in the Kostovo-13. The steady low values of P_{Tot} in the Kostovo-13 core contrasts to the theory that a shift in the mean P content of shales occurred following the termination of large scale glaciations in the Cryogenian (Reinhard et al., 2016a). Why P_{Tot} values between the two cores are different could be a function of the ultimate source of P to the ocean, riverine input (Ruttenberg, 2003). The depositional area of the Vendian sediments is hypothesized to have been a thin belt squeezed between two continental shields enduring uplift, the Fennoscandian and Ukranian-Sarmation shields (Pirrus, 1993). It is possible that the Kel'tma core was formed in a basin that was subjected to a greater influx of terrigenous material from the uplifting areas, and thus had a larger amount of P deposited in its sediments. The overall total amount could also be a function of water column redox, and the stability of such conditions. It has been shown in both cores that the ultimate burial of P in the form of P_{auth} undoubtedly occurs in oxic and ferruginous settings. However, $(C:P)_{org}$ and C_{org}:P_{reac} ratios confirmed recycling of P_{org} and P_{Fe} in the Kotlin horizon as a potential outcome of rapidly changing redox. Less stable conditions may have thus promoted a lower P_{Tot} content within these sediments in comparison to those in the Kel'tma core under long-standing oxygenated waters.

5.5.2 Avalon Peninsula

The Avalon Peninsula sedimentary succession is considered to be one of the first sources of evidence for deep ocean oxygenation in the late Neoproterozoic, with ferruginous conditions prior to and during the Gaskiers glaciation, and oxygenation immediately after (Canfield et al., 2007). This unit

also postdates the heavily documented Mistaken Point assemblages by about 5 m.y., where organisms were preserved in-situ by ash (Clapham et al., 2003; Narbonne and Gehling, 2003; Narbonne, 2004; Antcliffe et al., 2015). Geochemical analysis of these sediments allow an in-depth investigation into P burial mechanisms in an oxic deep marine setting, with abundant evidence for the emergence of animal life.

In Figure 5.6, an oxic water column with relatively consistent total elemental values (Fe, Al, P) is documented. Total P values plot along the average shale value with the exception of higher values in the Upper Trepassey and Lower Fermeuse Formations. It is clear that in the Avalon Peninsula, P_{det} phases are the dominant source of P to these sediments. Small amounts of P_{auth} do accumulate (< 30%), but do not reach the same levels as those seen in the White Sea. Organic matter has long been considered the principal source of reactive P phases to the sediment (Benitez-Nelson, 2000), but in a deep Ediacaran ocean where organic matter is predominantly produced by eukaryotic algae, this organic matter may not have persisted to great enough depths in this section to be buried. In Figure 5.11E, $(C:P)_{org}$ ratios predominantly plot along the Redfield ratio, and are consistent with very limited remobilisation of P from organic matter during diagenesis in these low TOC, sulfide poor sediments. C_{org}:P_{reac} values (Figure 5.11F) all plot below the Redfield Ratio, suggesting that there was likely an Fe (oxyhydr)oxide source of P to the sediment. However, the reactive P contents are very low, suggesting that this source was very minor, fitting with the lack of a significant Fe oxide shuttle in these non-ferruginous sediments. This P_{Fe} would have then sink-switched to authigenic P, which we see in small proportions throughout the Avalon succession.

Although there is potential for some transfer of P_{auth} to P_{det} during recrystallization, Figure 5.6 shows that detrital P is high throughout the profile – the average mean P content of the Avalon unit is 0.082 wt%, with 68.5% of this sourced from detrital P (Figure 5.9C). A high detrital input of P would be entirely as expected in this oxic deep sea setting, where the flux of organic and Fe (oxyhydr)oxide-bound P were likely very low.

5.5.3 Cariboo Mountains, Canada

The age of the sedimentary succession at the Cariboo Mountains allows an insight into P burial mechanisms prior to and after the Gaskiers glaciation. The upper member of the Kaza Formation, dated from 595 – 590 Ma (Canfield et

al., 2008) was deposited from an oxic water column based on the iron speciation results presented in Figure 5.7. Within this member, TOC values remain relatively low, all below 0.05 wt%. P_{Tot} is similarly at low levels compared to the average shale value. The Cariboo succession is suggested to formed in a deep marine setting (approx. 500 m), but both the water depth and P_{Tot} are less than those of the Avalon Peninsula. However, similar to the Avalon Peninsula, detrital phases are the main source of P to these sediments. As detrital is the main source of P, authigenic and organic P phases are overall low in comparison (<10%). A small increase in P_{auth} occurs where P_{Fe} is similarly at higher values.

In the upper Lower Isaac, the water column was also dominantly oxic, with the possibility of short-lived ferruginous conditions. Fe_{PY}/Fe_{HR} ratios tend to be higher than in some of the other sections, suggesting that porewaters were dominantly sulfidic beneath the oxic water column. These higher levels are not accompanied by high levels of TOC that are typically associated together, as sulfide production is limited by organic matter availability (Berner, 1970), but there is a relatively small depletion of highly reactive iron that has also been coupled to the accumulation of sulfide in sediments (Canfield et al., 1992; Meyers, 2007). P_{Tot} values remain below the average shale value and do not show a significant increase. P_{det} still endures as the main source of P. The accumulation of P_{auth} reaches a maximum of 10.6% in this unit before declining to a steady 7%. In the sample prior to the authigenic maximum, P_{org} also hits its highest level in the Cariboo unit at 16%.

Using the iron speciation results to categorize the samples by redox, the relationship between $(C:P)_{org}$ and $C_{org}:P_{reac}$ are shown in plots G and H of Figure 5.11 respectively. These data are generally consistent with those seen for the similarly oxic, deep water Avalon Peninsula, in that $C_{org}:P_{org}$ ratios show little evidence for preferential release of P from organic matter. However, $C_{org}:P_{reac}$ ratios are essentially also at the Redfield Ratio suggesting very little drawdown of P in association with Fe oxides, although there is some Fe-bound P in this section (Figure 5.7).

The Cariboo Mountain sedimentary succession illustrates small changes to P burial occurred across this time period. This basin was dominantly oxic and similar in depositional environment to the Avalon Peninsula as a deep marine setting, but P burial mechanisms here, again do not mirror those of the oxic Kel'tma shelf. Small amounts of P_{auth} occur in the siltstone members of both formations, but ultimately P_{det} is the main source to these sediments. From examining two deep water environments, it appears that the P cycle operating

on continental shelves was significantly different from that operating under oxic deeper water conditions.

5.5.4 Narana Formation, Upper Ungoolya Group

A palaeobasin with changing redox conditions is presented in Figure 5.8 for the Narana Formation. An anoxic water column, dominantly ferruginous but with the possible sporadic development of euxinic conditions at the base of the unit, transitions into a prolonged oxic interval, and reverts back to a ferruginous state at the top. This resembles the Kostovo-13 Core in terms of redox dynamics, but not in terms of P burial mechanisms. P_{Tot} greater than the average shale value coincides with a gradual increase in Fe_T and Al content, but not TOC. P_{auth} exhibits unusual behaviour in comparison to the other analysed sections. A decline at the base of the green silty shale corresponds with an increase in Fe_{HR}/Fe_T and Fe_{PY}/Fe_{HR}, potentially signifying the initiation of P recycling. This is a short-lived interval as Fe_{HR}/Fe_T ratios plummet to low oxic values until the calcareous mudstone, where a further rise to anoxic ferruginous values occurs. As this sedimentary unit is experiencing shallowing from the base upwards, this gives more evidence of a deep (below storm wave base) oxic ocean situated beneath ferruginous conditions in shallower waters. As was seen in the Kel'tma and Kostovo-13 core, oxic and ferruginous conditions typically result in the accumulation of authigenic P, but not in this basin, as limited CFA formation occurs in the oxic horizon. In modern environments, apatite formation has been found to accumulate at higher rates under anoxic conditions than oxic in the Benguela upwelling system of Namibia. This is not a function of organic matter mineralization, but due to bacterial sequestration of inorganic P in sediments with high concentrations of hydrogen sulfide (Goldhammer et al., 2010). Iron speciation results (Fe_{PY}/Fe_{HR}) show high concentrations of sulfide are found at the base of the Narana Formation (Figure 5.8). This could potentially signify that microbial activity played a major role in P_{auth} accumulation under ferruginous conditions in this basin. Similar amounts of P_{auth} are found in the upper limestone member of this unit. However, Fe_{PY}/Fe_{HR} ratios do not classify as euxinic, but do show higher levels compared to the other basins in this study, potentially eluding to the return of microbial apatite formation.

Of all the basins analysed in this study, this section has the lowest Fe_T and Al contents. A small incursion to lower values at the base of the succession correlates to anoxic ferruginous conditions as well as low values in P_{Tot} and P_{det}. In the oxic interval, detrital phases are the main source of P to the sediments, as also seen in the deep oxic settings of the Avalon Peninsula and

Cariboo Mountains. On entering into the ferruginous conditions of the calcareous mudstone, a decline in Fe_T and Al concurs with the rise in P_{reac} phases again. This suggests that it is not the total amount of iron within sediments that may exert a control on P burial, but whether the iron is predominantly of a highly reactive nature or unreactive. To support this statement, the ratios of $(C:P)_{org}$ and $C_{org}:P_{reac}$ are shown in Plots I and J in Figure 5.11 respectively. Both oxic and anoxic samples exhibit the preferential release of P_{org} to C_{org} in Plot I, with a number of samples also plotting on the Redfield Ratio. It should be noted that P_{org} values are particularly low in this basin. However, when taking the other reactive P phases into consideration in Plot J, a different relationship transpires. Oxic samples dominantly plot close to the Redfield Ratio, consistent with P_{org} being the dominant supplier of P to the sediments. By contrast, under anoxic ferruginous conditions, $C_{org}:P_{reac}$ ratios are dominantly below the Redfield Ratio, consistent with an enhanced P_{Fe} flux in association with Fe minerals under ferruginous conditions.

5.5.5 The Ediacaran marine P cycle

Across the five basins examined in this study, it is clear P burial mechanisms were not globally consistent, and were heavily dependent on both water column redox conditions and the organic matter loading of the sediment. From the results presented here, P_{det} is an important constituent of the P_{Tot} pool and needs to be considered when discussing the Proterozoic P cycle. This contrasts to modern studies where detrital phases are not extensively investigated. Schematics for the Kel'tma and Kostovo-13 cores correlated to the White Sea are shown in Figure 5.12 and Figure 5.13 respectively. The exact locations of these depositional sites in regard to basin bathymetry cannot be included as they have not been researched in great detail. The relative proportions of each P phase accompanies the schematics, further aiding in the understanding of how P burial mechanisms prevailed.

There is little difference between the Redkino and Kotlin horizons of the Kel'tma core in terms of P burial mechanisms. The main finding is the continued generation of P_{auth} at the expense of P_{Fe} and P_{org} phases as oxic conditions prevailed, with an overall increase in younger sediments as shown in Figure 5.14. This has further implications for the emergence of metazoans. It was previously hypothesized by Lenton et al. (2014) that the continued burial of P under oxic conditions resulted in a negative feedback on primary production, limiting productivity but potentially creating suitable conditions for more complex organisms to evolve. As shown in Figure 5.14, there is a steady

increase in the amount of authigenic phases forming in sediments approaching the Precambrian-Cambrian boundary. It must also be taken into consideration the low recovery of P during the sequential extraction for the Kel'tma core samples. Though these results give an insight into P burial mechanisms, a significant portion of the P pool was lost during the extraction and is thus missing from the story.

In Figure 5.13, modifications to the P cycle in the Kostovo-13 core are visible. During the Redkino stage, when metazoans and a diverse algal assemblage dominated the biological pump, the shelf was in a ferruginous redox state. P_{org} was the main source of reactive P to sediments with also a significant amount in iron phases compared to the Kel'tma core. At the Kotlin boundary, ironstone deposition suggests an intensely ferruginous water column. Authigenic P accumulates to 50% of the P_{Tot} content, similarly to the Kel'tma core. However P recycling is kick-started in the Kotlin horizon, potentially fuelling primary productivity and generating more organic matter. This recycling may have promoted primary production in surface waters, generating more organic matter and ultimately more P to the sediments, allowing P_{auth} to form even though P_{Tot} was much lower. The White Sea has been regarded as the most diverse assemblage of Ediacaran biota in the world (Muscente et al., 2018). By examining sediments at a greater depth to their habitat, it is clear that the redox state of the shelves in the respective basins exerted an overall control on P burial mechanisms in the Kel'tma and Kostovo-13 cores, placing water column redox as the most important parameter on the P cycle, that could be further influenced by sedimentation rate or biological development. The preservation of high P_{org} and P_{Fe} values under iron-rich anoxia and subsequent transformation to P_{auth} gives evidence that P burial also occurs under anoxic, ferruginous conditions. Though both basins exhibit dynamically evolving P cycles, they reveal P_{auth} was forming under both oxic and ferruginous conditions on the EEP.

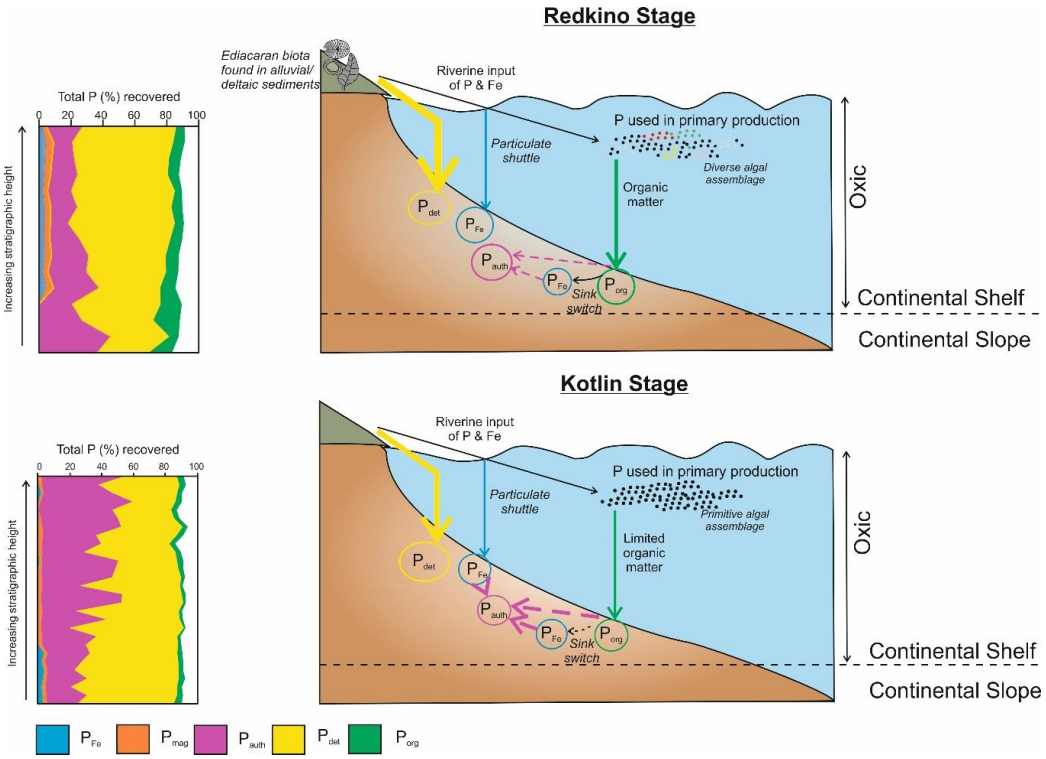

Figure 5.12 Schematic of the P cycle operating in the Kel'tma core basin. The relative proportions of each P phase is shown next to both the Redkino and Kotlin horizons

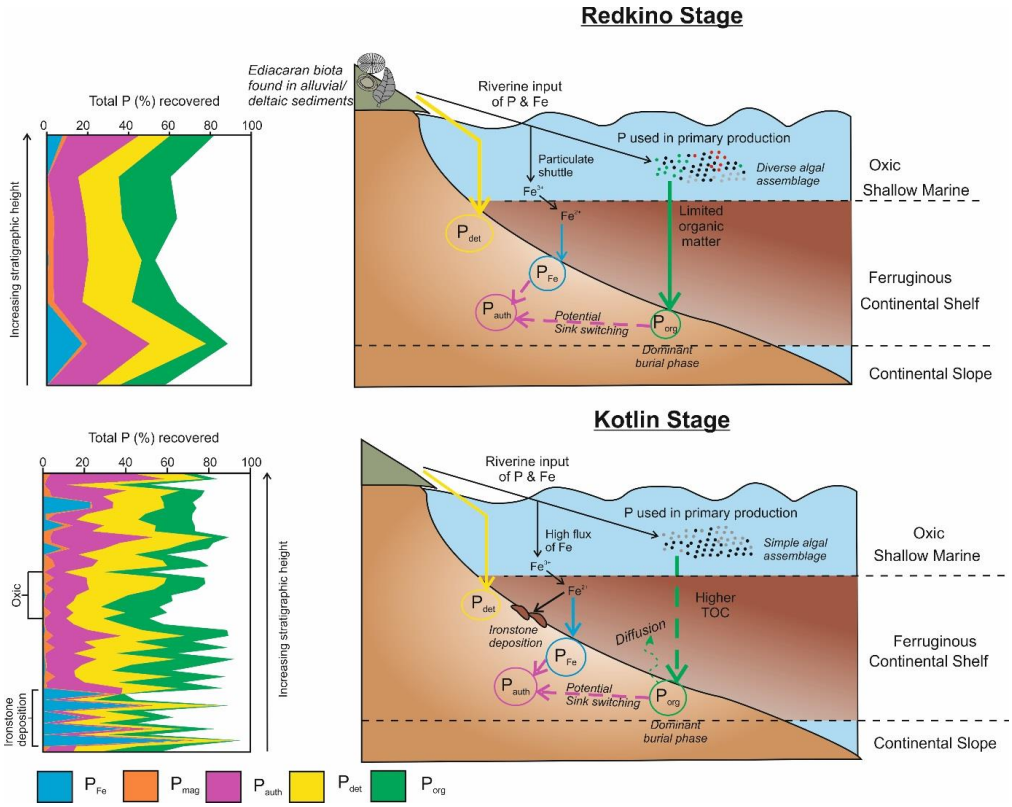

Figure 5.13 Schematic of the redox state and P burial mechanisms in the Kostovo-13 core basin. Relative proportions of each P phase measured in the extraction are shown beside each stage.

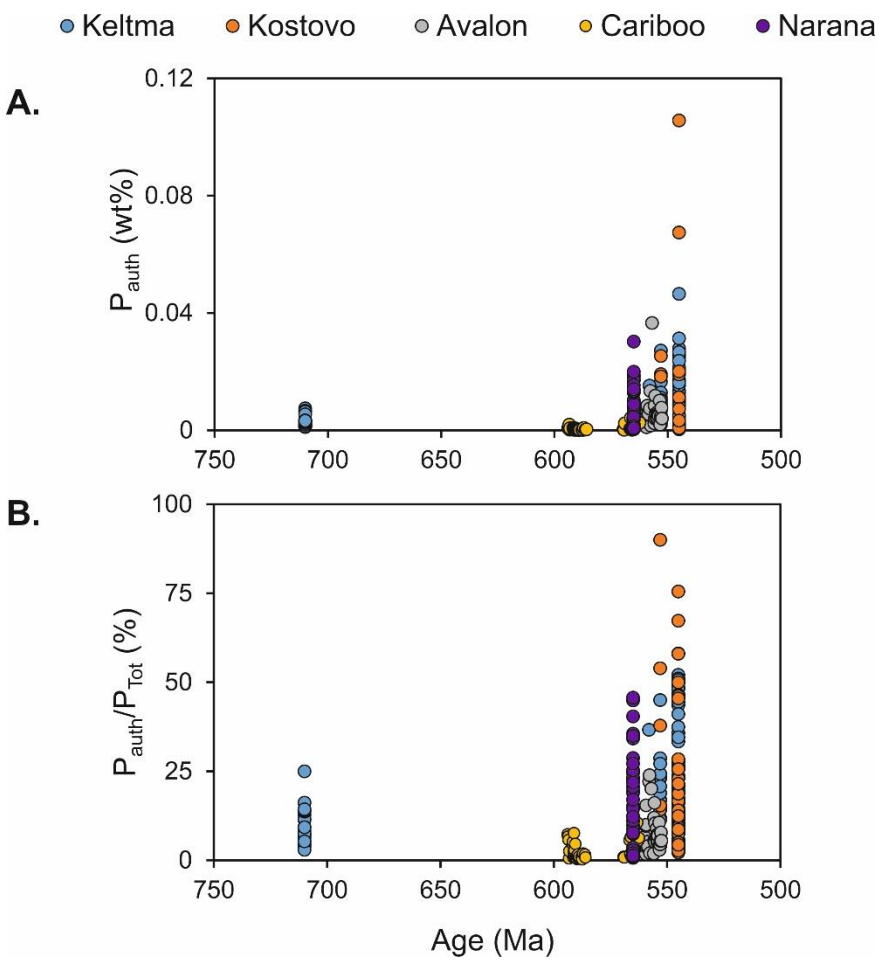

Figure 5.14 A – P_{auth} (wt%) for all samples measured in this study B – P_{auth}/P_{Tot} (%) for each Ediacaran locality

The Avalon Peninsula and Cariboo Mountains support deep open ocean oxygenation during the Ediacaran Period (Canfield et al., 2007), as well as the existence of benthic metazoan communities living on the basin floor in the Avalon Peninsula succession (Clapham et al., 2003; Narbonne, 2005). Though oxygenated environments were found in both continental shelf settings, as evidenced by the Kel'tma core, as well as deep basin and slope environments, there are fundamental differences in P burial mechanisms between shallow and deep waters. In Figure 5.15, a schematic for the two deep water sedimentary units is illustrated. Similarly to the Kel'tma and Kostovo-13 cores, exact bathymetric locations of these sites cannot be included in the schematic. From their respective percentage plots of the different pools of P, P_{det} is clearly the largest phase in the Avalon and Cariboo settings and is thus important to include when discussing the Ediacaran P cycle. This is not typical of modern deep ocean sediments, as they have been shown to accumulate P_{auth} in deep environments (Ni et al., 2015). The dominance of P_{det} in both these deep sites could be a function of three factors: a weaker biological pump as it was dominated by eukaryotic algae in the lead up to the Ediacaran; the absence of

biogenic fish debris (biogenic P) as a source of reactive P to deep sediments; and variable redox conditions on Ediacaran shelves. As free-swimming animals had not evolved during this time, the biological pump would have been dominated by eukaryotic algae rendering it slower and producing smaller sized organic matter (Lenton et al., 2014). A slower pump generating less organic matter would imply a more limited amount reaching great depths before mineralization, and thus the main source of P, as P adsorbed to organic matter is typically considered the main mechanism for P reaching the sediment-water interface (Ingall and Van Cappellen, 1990). As the evolution of skeletons had not transpired yet and only soft bodied metazoans existed, there was no source of biogenic P to these sediments that is routinely seen in modern settings (Faul et al., 2005). It is also important to note that in modern oceans, the majority of P burial occurs on continental shelves (Ruttenberg, 1993). If most of the reactive P is trapped within mid-shelf settings, than the main source of P to deeper sediments would be in passively settling detrital phases. In comparison to modern studies, processes important for the distribution of P_{det} are poorly constrained during this time period, such as: sedimentation rates; water depth; depositional energy; and proximity of the localities to terrestrial sedimentation areas. Though it is clear these environments were dominated by P_{det}, certain controls on why this is cannot be addressed.

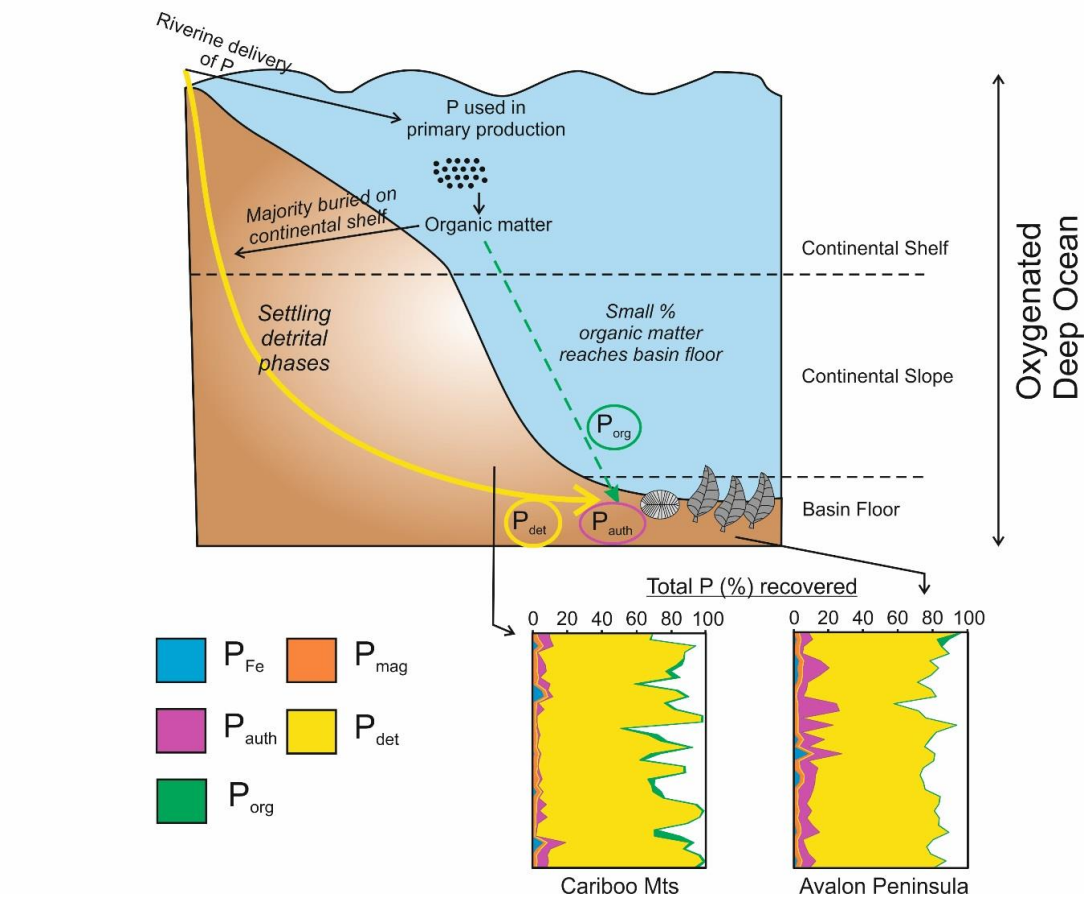

Figure 5.15 Schematic for the redox mechanisms in the Avalon Peninsula and Cariboo Mountain sedimentary units. Potential P burial mechanisms for each of these sections is also illustrated, with the percentages of each P phase designated next to their appropriate depositional environment

Regardless of the redox state of the water column, the previously mentioned factors could potentially explain why Ediacaran deep sediments were starved of a source of P_{reac}. However, unlike the modern world, local redox heterogeneities are well documented across the Ediacaran (Bowyer et al., 2017; Tostevin et al., 2016; Wood et al., 2015). In this study, it is continental shelf settings that exhibit the most variation. Both the Narana Formation and the Kostovo-13 Core show intermittent oxic conditions bracketed by ferruginous settings. If a ferruginous wedge on the continental shelf overlay an oxic slope/basin, this would further impact P burial mechanisms at depth. Organic C would be preferentially stored over P_{org}, as is shown for the Narana Formation and the Kostovo-13 core in Figure 5.11. An even smaller flux of organic matter would therefore reach abyssal depths as the majority is buried on the shelf. Iron (oxyhydr)oxides supplied from the iron shuttle would also not persist through the wedge as a source of P before being reduced, and the adsorbed P would

subsequently be released. A schematic for the Narana Formation is presented in Figure 5.16. Similar proportions of P_{det} in the Narana Formation are evident in the oxic member compared to those of the Avalon and Cariboo Mountain deeper marine settings. This has implications for the importance of redox on P mechanisms across a shelf. The Kel'tma and Kostovo-13 cores from mid-shelf settings revealed the accumulation of P_{auth} to high levels under both an oxic and ferruginous water column, though care should be taken with these findings due to their lower recovery rates. In the outer shelf Narana Formation, the waxing and waning of a ferruginous wedge promoted P burial, but not under oxic conditions. The high amounts of P_{det} in the oxic samples suggest outer shelf settings would also have been starved of organic matter, with only the preferential retention of C_{org} under anoxic conditions fuelling CFA formation. If organic matter was not the main source of P to these sediments, then P_{Fe} phases would have engaged as the main P source and would be more prevalent under ferruginous settings than oxic. These dynamic shelves stimulate the growing findings that the Ediacaran Period was a dynamic time for both redox and nutrient cycling.

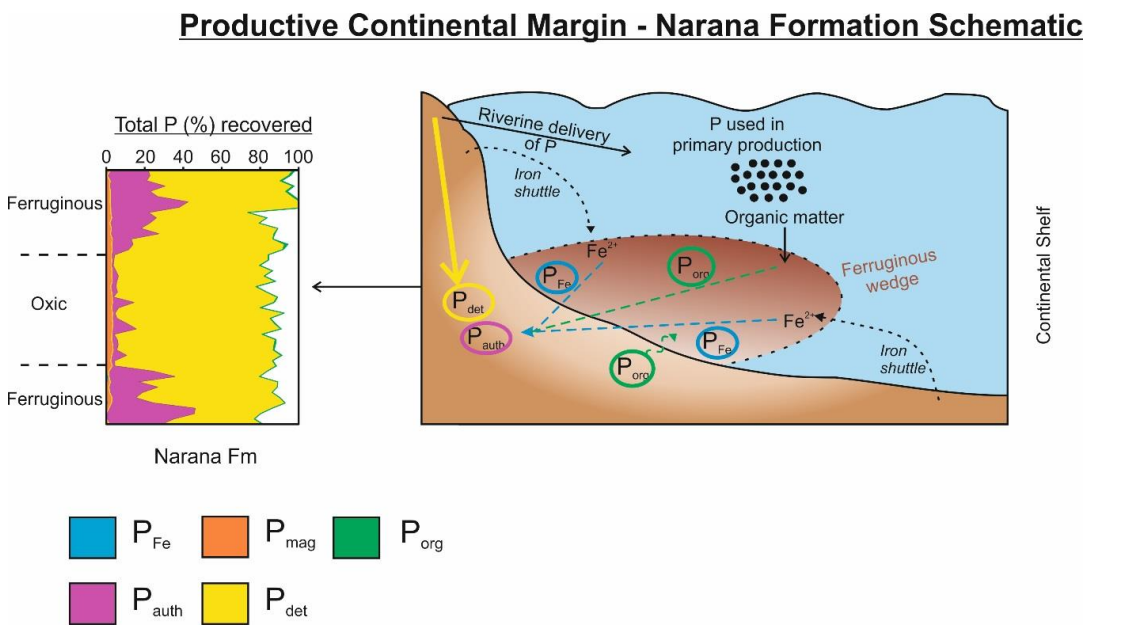

Figure 5.16 Simplified schematic for water column redox and P burial mechanisms for the Narana Formation

5.5.6 Evolution of the total P content in Neoproterozoic sediments

Recent modelling studies have focussed on analysing the total P content of shales across the Proterozoic in a bid to understand the ancient P cycle. A

large and comprehensive dataset (sample *n*>7000) by Reinhard et al. (2016) documented an apparent large increase in total P content of marine sediments deposited after the Tonian Period. A shift in ocean redox was proposed as the cause behind this change as oceans transitioned from a dominantly ferruginous state to more oxygenated settings. The authors suggest that such a change would have led to the removal of the water column Fe oxide sink. However, a major assumption made by this study is that the total P content of sediments tracks bioavailable P through time. This is incorrect as only P_{reac} phases are bioavailable, and as P_{det} comprised a significant portion of the total P pool during this time, inaccuracies in how the P cycle evolved are evident. Also discounted from their model is the importance of P recycling. Phosphorus burial occurs under ferruginous conditions, but with euxinic conditions becoming increasingly more common following the GOE, sulfide availability in sedimentary porewaters would have promoted P recycling back to the water column (März et al., 2008). In Figure 5.17, the data from this modelling study is included along with the P_{Tot} values determined here and referenced against the average shale value for P (0.08 wt%; Turekian et al., 1961). Prior to the Sturtian SE, a range in P_{Tot} predominantly to lower values agrees with their theory. Following the Marinoan SE, samples from their study surge to 15 wt% P, and is the basis for their conclusion that this period documents an upheaval to the global P cycle. These trends to higher values are not recorded in the new results presented here. A potential reason for this, and what is not taken into account in the modelling study, is the depositional history of these outliers. The vast majority of these high plotting samples are from the Doushantuo Formation in the Yangtze Platform of South China, a well-documented locality due to the exceptional preservation of animal embryos in phosphorites (Xiao et al., 1998; Xiao and Knoll, 2000). This basin endured both euxinic and ferruginous settings in deeper environments, with oxygenated waters confined to the surface layer (McFadden et al., 2008; Ader et al., 2009; Wang et al., 2012; Xiao et al., 2012; Sahoo et al., 2012; Lang et al., 2016). Other samples in Figure 5.17 which demonstrate high P_{Tot} contents are from the Rapitan Group of the Windemere Supergroup and the Fulu Formation on the Yangtze Platform. These basins also record the presence of phosphorites, but in association with interglacial BIF deposition. The formation of phosphorites has been linked to: a high input of organic matter; deposition of previously reworked continental shelf material; low sedimentation rates (Schenau et al., 2000); and upwelling of P-rich bottom waters due to the retreat of ice sheets (Donnelly et al., 1990). Each of these reasons is a possible contributing factor to the post-Marinoan P-rich sediments in the Doushantuo Formation, with the demise of

glacial conditions the most probable contributing factor for the Rapitan Group and Fulu Formation. However, this trend in high P_{Tot} values is not a global signal, as evidenced from Figure 5.17. A large proportion of the sediments from all five basins are below the average shale value, suggesting there was not a global surge in P_{Tot} contents to marine sediments.

The Cariboo Mountain and Avalon Peninsula sections are localities with evidence for the Gaskiers glaciation, either through correlation to diamictites, such as in the Windermere Supergroup for the Cariboo Mountains (Narbonne et al., 1994), or containing the Gaskiers horizon, as seen in the Avalon Peninsula (Gardiner and Hiscott, 1988; Myrow, 1995; Retallack, 2016). The Cariboo Mountain P_{Tot} content declines towards the Gaskiers glaciation, and subsequently rises to average shale values after (Figure 5.17). A similar trend occurs in the Avalon unit, with values rising to ~0.2 wt%. This suggests glacial activity did play an important role in the release of nutrients to the ocean, as has been previously suggested (Planavsky et al., 2010). However, the P speciation results of these sections have shown to predominantly consist of detrital phases, and thus would not tie into the theory that elevated P contents stimulated biological evolution as the bulk of this sedimentary P is not bioavailable.

From this study, it can thus be stated that examining total P contents of sediments is not a robust indicator for the marine P cycle during this dynamic time. Total P values have been shown to vary globally across all the basins examined, with no similarities as a function of redox or depositional environment. The range of mean P content of the sediments examined here do not synchronously show an increase across the Ediacaran, as each basin is subjected to differing sedimentation rates, bathymetry and redox. To accurately assess ancient P cycles, the burial of P in its various reactive phases are the key to understanding how the ultimate limiting nutrient cycled. The research presented here offers a more detailed view of the Ediacaran P cycle in comparison to Reinhard et al. (2016), but is still a qualitative outlook on a complicated cycle.

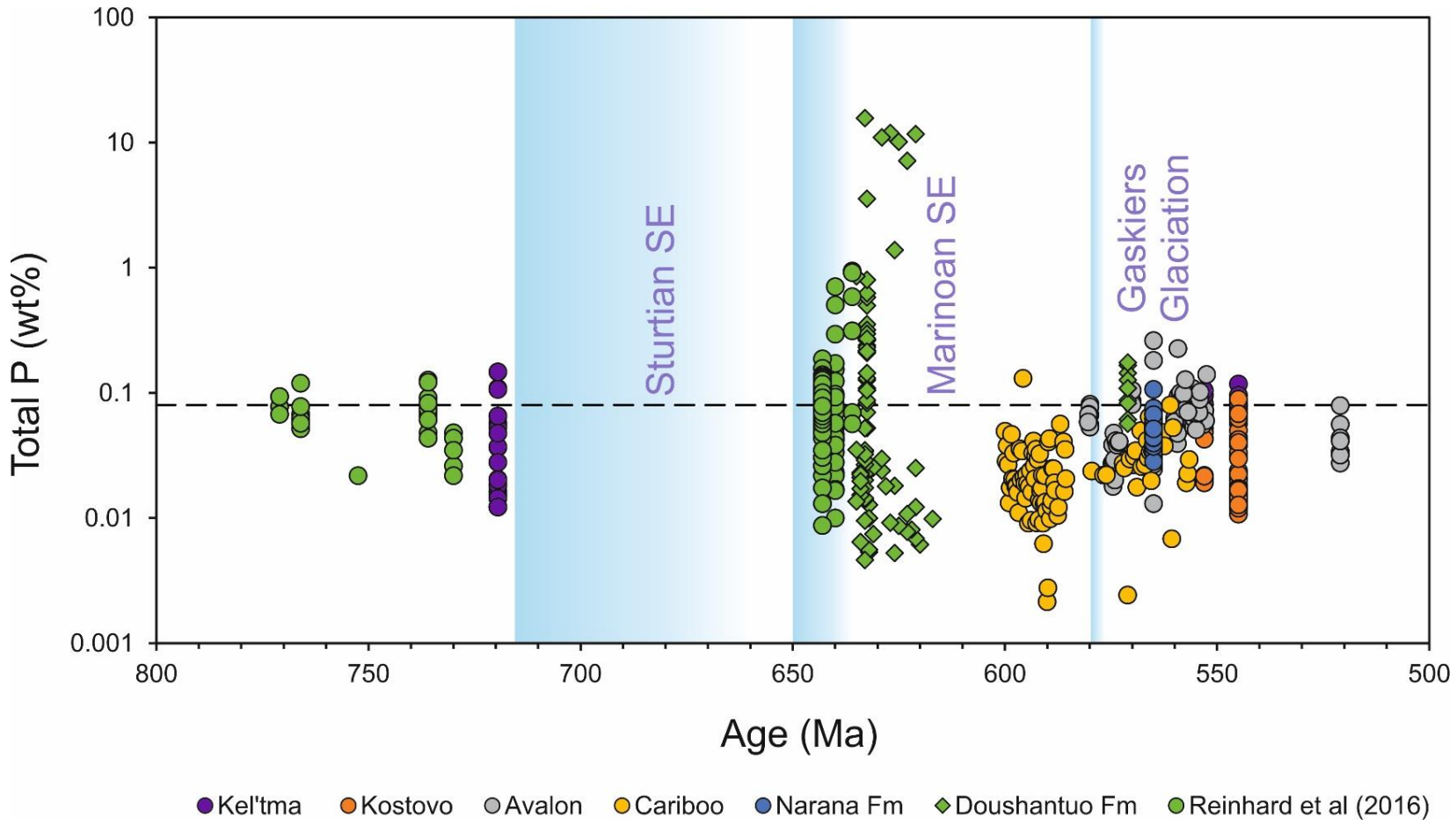

Figure 5.17 Plot of the total P content of sediments throughout the Neoproterozoic. Samples in green are taken from Reinhard et al. (2016). Snowball earth ages are taken from Rooney et al. (2015). The black dashed line is representative of the average shale value for phosphorus (0.08 wt%) from Turekian et al. (1961)

5.6 Conclusions

Through the analysis of palaeoredox proxies and the individual phases of reactive and unreactive P across five different basins, it is clear that P burial mechanisms endured significant changes as a function of redox and depositional environment during the Ediacaran. On continental shelves, variations in local redox influenced the main source of P to the sediments as well as their potential for P recycling. Ferruginous conditions were found to promote the accumulation of P_{auth} through an increased organic matter and iron-bound P flux to the sediments. Microbial sequestration of inorganic P in anoxic settings with high levels of sulfide were also uncovered as sites for CFA formation. Even though P recycling occurred under ferruginous settings, a greater proportion was ultimately buried in the sediments.

Oxic shelves and oxygenated slope/basin environments display very different P burial mechanisms, whether or not there was evidence for animal activity. Oxic conditions at mid-shelf depths were sites for steady CFA formation, while oxic outer shelves and slopes or basins predominantly consist of detrital P. Detrital P phases dominate deep Ediacaran sediments. This is potentially due to a weaker organic matter flux from a eukaryote-dominated biological pump, or overlying anoxic conditions starving the deep ocean of organic matter and reactive P phases. The geochemical evidence presented here both supports and contradicts previous modelling studies. Iron-bound P and P_{org} burial are important phases in P burial during the Ediacaran, especially on ferruginous shelves, agreeing with the potential effect bioturbated sediments had on the P cycle. A global shift to higher P_{Tot} content in sediments is not witnessed across these basins. The largest values pertain to locations initially covered by ice during the Gaskiers Glaciation, with their subsequent retreat possibly fuelling an increased nutrient supply. This behaviour is not mirrored in other basins, and reflects the dynamic behaviour of P during the Ediacaran as a function of redox and depositional environment.

Chapter 6 Conclusions

6.1 Summary

6.1.1 The chemical evolution of Proterozoic redox

Through the application of multiple palaeoredox proxies (iron speciation and trace metal analyses) on the Mesoproterozoic Bashkir Meganticlinorium (BMA) succession in Russia, and on the Late Palaeoproterozoic-Mesoproterozoic Yanshan Basin sedimentary unit in China, this research has added to the current geochemical record of the evolution of Proterozoic ocean chemistry. Strong evidence for prevalent ferruginous conditions under a shallow chemocline was uncovered in the Mesoproterozoic BMA, with oxic waters confined to only the shallowest environments. Assessment of the relationship between sedimentary Mo and U content within these samples suggests a strong Fe-Mn (oxyhydr)oxide shuttle was operating in this basin, allowing Mo enrichments to accumulate under a ferruginous water column. The finding of a dominantly anoxic water column is in stark contrast to other studies from this time period that advocate deeper water oxygenation, and strongly highlights the spatial and temporal variability in ocean redox conditions across basins.

The existence of a shallow chemocline was also uncovered in the mid-Proterozoic Yanshan Basin sedimentary succession using palaeoredox proxies. Redox dynamics operated differently in this basin due to its dynamically fluctuating chemocline and intracontinental setting. Evidence for the mixing of deep ferruginous waters with an oxic surface layer was discovered as the basin deepened, resulting in the large-scale drawdown of iron, depleting the water column of reactive phases and advancing oxic conditions to greater depths for the first time in this sedimentary succession. Anoxic conditions return in the overlying Mesoproterozoic Gaoyuzhuang Formation before becoming stably oxygenated. Trace metal proxies used in this study highlight how pervasive globally anoxic conditions resulted in a depleted water column inventory within this confined basin, as respective enrichments were not uncovered under ferruginous conditions in the Yanshan Basin.

Both of the units' redox records add to the history of Proterozoic ocean redox by highlighting how dynamic this interval in Earth's history was. Local factors such as basin configuration and the position of the chemocline, as well

as global conditions (e.g. levels of atmospheric oxygen and dominant ocean redox), need to be taken into consideration when attempting to unravel the evolution of the Proterozoic ocean. Each researched unit stands out for their importance as a record of the evolution of ocean chemistry, but also for their significance in highlighting the discrepancies and uncertainties that still exist in our understanding of this time period.

6.1.2 Proterozoic P dynamics

A newly adapted version of a P speciation scheme was applied to Late Palaeoproterozoic sediments from the Yanshan Basin in North China and to five separate basins formed during the Ediacaran. By examining each reactive P phase within marine sediments, the role of the probable ultimate limiting nutrient, and what factors governed the P cycle prior to macroscopic eukaryote and metazoan evolution, was determined. An oligotrophic, nutrient-limited basin existed during deposition of the Yanshan Basin sediments. Both water column redox and the position of the chemocline exerted an overall control on P burial mechanisms. As oxygenated waters spread to deeper depths, the mixing of ferruginous deep waters with an oxic layer resulted in the drawdown of iron-bound P, as well as P adsorbed to organic matter. This significant sink for P, initially triggered by a change in redox and chemocline depth, fuelled the formation of authigenic P phases during early diagenesis. Modelling approaches have previously suggested that authigenic P was unlikely to be significant in such ancient environments, in contrast to the results presented here. The Late Palaeoproterozoic P cycle behaved in a similar manner to that of the modern, coupled with an important role for Fe-bound phases.

Though P speciation could not be performed on sediments from the Zhangjiayu Member in the Gaoyuzhuang Formation, examination of their total P and P/Al contents demonstrates that an increase in reactive P burial occurred during macroscopic eukaryote evolution. Elevated P burial in stably oxygenated environments could have created an ideal habitat for the radiation of increasingly complex life by limiting primary production and oxygen demand in surface waters.

The analysis of both Fe and P speciation on multiple Ediacaran basins gives a critical assessment of P cycle dynamics during a time of significant biological and environmental change. Again it was the role of redox, coupled with depositional environment that exerted an overall control on P burial mechanisms. Oxygenated continental shelves display very different modes of P

burial compared to oxic basin/slope environments. The deeper water settings were found to be dominated by detrital material, potentially as a result of shallower ferruginous waters starving the deep ocean of organic matter and other reactive P phases. Another possible reason for this behaviour is a biological pump dominated by eukaryotes, resulting in a weaker organic matter flux to the basin floor. In continental shelf settings, authigenic phases were found to accumulate under both oxic and ferruginous conditions, with the dominant source of P in both organic and iron-bound phases. Evidence for recycling of P was discovered in certain ferruginous intervals, but the overall accumulation of authigenic P outpaced recycling rates, therefore leading to the ultimate burial of P. In an effort to highlight the importance of reactive P burial rather than solely the mean P content, a compilation of all total P values gathered in this research, as well as from other literature sources, emphasized that no global increase in total sedimentary P content occurred across the Late Neoproterozoic as a result of ocean oxygenation. Local increases were found to occur in basins with evidence for ice cover during the Gaskiers glaciation, suggesting that the melting of ice induced an elevated nutrient flux into the marine system.

The research presented here is an important addition to our understanding of the Proterozoic P cycle. It is the first geochemical record to document P burial mechanisms in shales during the Proterozoic, as previous experimental attempts have focused on BIFs or total P concentrations in shales. The data also show that redox as well as depositional environments, similarly to the present day, exerted an overall control on P cycling in the oceans during this dynamic time. During a time of variable redox, as documented not only in the Yanshan basin and Ediacaran localities, but also the BMA sedimentary unit, the importance of iron as a source of P to the sediments has been uncovered and is often subsequently a source for authigenic P phases, similar to organic bound P. The role of P as the ultimate limiting nutrient has become increasingly clear in potentially driving biological evolution from this research.

6.2 Future work

6.2.1 Palaeoredox studies

The palaeoredox records uncovered in the basins researched here do not typically match those of other studies. In Chapter 3, the sampling strategy used

was at a coarse resolution to document the evolution of redox within the BMA basin over a substantial period of time. For future work, a field campaign should return to this area to sample the BMA sedimentary succession at a much higher resolution to identify if redox conditions remain dominantly ferruginous, or to investigate if there was substantially more variability in water column redox chemistry.

Evidence for progressive, but short-lived, oxygenation into deeper waters was uncovered at the base in the Chuanlinggou Formation. Approximately 150 Ma exists between this and stable oxygenated conditions in the Gaoyuzhuang Formation. To better understand the dynamics involved in this transition, palaeoredox studies need to be applied to the horizons between these events to piece together a complete picture of ocean oxygenation in the Mesoproterozoic. A variety of proxies need to be utilized, both applicable to shales and carbonates with low iron content, to avoid bias towards lithologies.

It is commonly mentioned throughout Proterozoic redox studies that a globally ferruginous ocean cannot be sustained without an enhanced hydrothermal flux, as seen during the Archean (Poulton and Canfield, 2011), due to simple mass balance constraints. The reason behind this statement is that other sediments need to be depleted in reactive iron in order for enrichments to be sustained elsewhere. This has not been extensively investigated and it remains unknown if this is correct. Future work could set out to model the Proterozoic ocean in terms of reactive iron enrichments and assess if the global ocean can be sustained in a ferruginous state without elevated hydrothermal emissions. Such a study could quantify how much reactive iron needs to enter the oceans via riverine supply or is diffusively released and mobilised from deeper sediments, to maintain a ferruginous state.

An issue with ancient redox studies is in the identification of the bathymetric localities of samples sites. If applicable and where possible, sequence stratigraphy methods could be performed on the sample sites investigated in this research. This would greatly aid in constraining the evolution of ocean redox during the Proterozoic, as the community currently separates the ocean into shallow and deeper waters. However, modern studies show ocean redox can significantly vary across a single continental shelf, and thus would greatly help in constructing the record of how the oceans evolved from an anoxic to oxic state.

6.2.2 Proterozoic P studies

As the adapted P speciation technique is new, the method has not been applied to many sections in the Proterozoic with the exception of this research. Particularly in the lead up to the emergence of eukaryotes, the wide application of the new technique would significantly contribute to our understanding of the role of nutrients in biological evolution. In Chapter 5, many of the sections are *correlated* to fossil localities for *Ediacara Biota* rather than documenting the P cycle *within* the fossil sites themselves. By applying the new method to these sites, this may answer, or even help in answering, whether the emergence of motile animals had a profound impact on nutrient cycling through shallow sediment mixing.

Fossil localities such as the Nama Group first document the emergence of *Ediacaran Biota*, followed by the later radiation of skeletal organisms towards the Precambrian-Cambrian boundary at ~550 Ma. It would be an incredibly interesting study to see whether changes to the marine P cycle played a role in the incorporation of P minerals e.g. apatite into their bodies. Along with the P speciation method, petrological and palaeontological analyses of such successions would also need to be examined in-depth to answer such a question.

It is consistently observed across the sections analysed that sediments deposited during the Proterozoic Eon have limited P_{Tot} content. Future work on the Proterozoic P cycle could potentially address the supply of P to the oceans from continental weathering. This could be investigated by analysing Li isotopes to assess whether an arid landscape during this period, due to the absence of vegetation and the presence of LIPs, was the reason behind the limited amount of P reaching the oceans. Such a study would greatly add to the current understanding of the Proterozoic P cycle and address the debate concerning when sedimentary P_{Tot} began to rise to average shale values.

Future work on the P speciation extraction method would also be imperative to gain a full understanding of ancient P burial mechanisms. SEM analyses of sediment samples may give a further understanding on the type of detrital P phases within the samples. A method of determining the proportion of typical detrital phases to reactive phases using an SEM could be used to compare against the sequential extraction results, and subsequently assess if the extraction was successful in partitioning these two phases. This would also aid interpretations in P speciation results where there was a low recovery of P_{Tot} from the sequential extraction, as the occurrence of crystalline or refractory detrital phases (monazite, xenotime) is typically attributed to low recovery values.

Bibliography

Adelson, J.M., Helz, G.R. and Miller, C. V. 2001. Reconstructing the rise of recent coastal anoxia; molybdenum in Chesapeake Bay sediments. *Geochimica et Cosmochimica Acta*. **65**(2),pp.237–252.

Ader, M., Macouin, M., Trindade, R.I.F., Hadrien, M.H., Yang, Z., Sun, Z. and Besse, J. 2009. A multilayered water column in the Ediacaran Yangtze platform? Insights from carbonate and organic matter paired δ13C. *Earth and Planetary Science Letters*. **288**(1–2),pp.213–227.

Ader, M., Sansjofre, P., Halverson, G.P., Busigny, V., Trindade, R.I.F., Kunzmann, M. and Nogueira, A.C.R. 2014. Ocean redox structure across the Late Neoproterozoic Oxygenation Event: a nitrogen isotope perspective. *Earth and Planetary Science Letters*. **396**,pp.1–13.

Akimova, G.N. 1967. Cross-bedding in Zil'merdak Formation Rocks in the Southern Urals *In*: *Materialy po stratigrafii i tektonike Urala (Materials on the Stratigraphy and Tectonics of the Urals*. Leningrad: Vses. Geol. Inst., pp. 36–65.

Albani, A. El, Bengtson, S., Canfield, D.E., Bekker, A., MacChiarelli, R., Mazurier, A., Hammarlund, E.U., Boulvais, P., Dupuy, J.J., Fontaine, C., Fürsich, F.T., Gauthier-Lafaye, F., Janvier, P., Javaux, E., Ossa, F.O., Pierson-Wickmann, A.C., Riboulleau, A., Sardini, P., Vachard, D., Whitehouse, M. and Meunier, A. 2010. Large colonial organisms with coordinated growth in oxygenated environments 2.1 Gyr ago. *Nature*. **466**(7302),pp.100–104.

Algeo, T.J. 2004. Can marine anoxic events draw down the trace element inventory of seawater? *Geology*. **32**(12),pp.1057–1060.

Algeo, T.J. and Ingall, E. 2007. Sedimentary Corg:P ratios, paleocean ventilation, and Phanerozoic atmospheric pO2. *Palaeogeography, Palaeoclimatology, Palaeoecology*. **256**(3–4),pp.130–155.

Algeo, T.J. and Lyons, T.W. 2006. Mo-total organic carbon covariation in modern anoxic marine environments: Implications for analysis of paleoredox and paleohydrographic conditions. *Paleoceanography*. **21**(1),pp.1–23.

Algeo, T.J. and Maynard, J.B. 2004. Trace-element behavior and redox facies in core shales of Upper Pennsylvanian Kansas-type cyclothems. *Chemical Geology*. **206**(3–4),pp.289–318.

Algeo, T.J. and Maynard, J.B. 2008. Trace-metal covariation as a guide to water-mass conditions in ancient anoxic marine environments. *Geosphere*. **4**(5),p.872.

Algeo, T.J. and Rowe, H. 2012. Paleoceanographic applications of trace-metal concentration data. *Chemical Geology*. **324**–**325**,pp.6–18.

Algeo, T.J. and Tribovillard, N. 2009. Environmental analysis of paleoceanographic systems based on molybdenum-uranium covariation.

Chemical Geology. **268**(3–4),pp.211–225.

Aller, R.C. 1994. Bioturbation and remineralization of sedimentary organic matter: effects of redox oscillation. *Chemical Geology*. **114**(3–4),pp.331–345.

Anbar, A.D., Duan, Y., Lyons, T.W., Arnold, G.L., Kendall, B., Creaser, R.A., Kaufman, A.J., Gordon, G.W., Scott, C., Garvin, J. and Buick, R. 2007. A whiff of oxygen before the great oxidation event? *Science*. **317**(5846),pp.1903–1906.

Anderson, L.D. and Delaney, M.L. 2000. Sequential extraction and analysis of phosphorus in marine sediments: Streamlining of the SEDEX procedure. *Limnology and Oceanography*. **45**(2),pp.509–515.

Anderson, L.D., Delaney, M.L. and Faul, K.L. 2001. Carbon to phosphorous ratios in sediments: Implications for nutrient cycling. *Global Biogeochemical Cycling*. **15**(1),pp.65–79.

Anderson, R.F., Fleisher, M.Q. and LeHuray, A.P. 1989. Concentration, oxidation state, and particulate flux of uranium in the Black Sea. *Geochimica et Cosmochimica Acta*. **53**(9),pp.2215–2224.

Anderson, T.F. and Raiswell, R. 2004. Sources and mechanisms for the enrichment of highly reactive iron in euxinic Black Sea sediments. *American Journal of Science*. **304**(3),pp.203–233.

Anschutz, P., Zhong, S., Sundby, B., Mucci, A. and Gobeil, C. 1998. Burial efficiency of phosphorus and the geochemistry of iron in continental margin sediments. *Limnology and Oceanography*. **43**(1),pp.53–64.

Antcliffe, J.B., Hancy, A.D. and Brasier, M.D. 2015. A new ecological model for the ~565Ma Ediacaran biota of Mistaken Point, Newfoundland. *Precambrian Research*. **268**,pp.227–242.

Arnold, G.L., Anbar, A.D., Barling, J. and Lyons, T.W. 2004. Molybdenum isotope evidence for widespread anoxia in mid-Proterozoic oceans. *Science (New York, N.Y.)*. **304**(5667),pp.87–90.

Arnott, R.W.C. 2007. Stratal architecture and origin of lateral accretion deposits (LADs) and conterminuous inner-bank levee deposits in a base-of-slope sinuous channel, lower Isaac Formation (Neoproterozoic), East-Central British Columbia, Canada. *Marine and Petroleum Geology*. **24**(6–9),pp.515–528.

Arouri, K., Conaghan, P.J., Walter, M.R., Bischoff, G.C.O. and Grey, K. 2000. Reconnaissance sedimentology and hydrocarbon biomarkers of Ediacarian microbial mats and acritarchs, lower Ungoolya Group, Officer Basin. *Precambrian Research*. **100**(1–3),pp.235–280.

Asael, D., Tissot, F.L.H., Reinhard, C.T., Rouxel, O., Dauphas, N., Lyons, T.W., Ponzevera, E., Liorzou, C. and Chéron, S. 2013. Coupled molybdenum, iron and uranium stable isotopes as oceanic paleoredox proxies during the Paleoproterozoic Shunga Event. *Chemical Geology*. **362**,pp.193–210.

Baldwin, G.J., Nagler, T.F., Greber, N.D., Turner, E.C. and Kamber, B.S. 2013. Mo isotopic composition of the mid-Neoproterozoic ocean: An iron formation perspective. *Precambrian Research*. **230**,pp.168–178.

Bartley, J., Kah, L., Mcwilliams, J. and Stagner, A. 2007. Carbon isotope chemostratigraphy of the Middle Riphean type section (Avzyan Formation, Southern Urals, Russia): Signal recovery in a fold-and-thrust belt. *Chemical Geology*. **237**(1–2),pp.211–232.

Beck, M., Dellwig, O., Schnetger, B. and Brumsack, H.J. 2008. Cycling of trace metals (Mn, Fe, Mo, U, V, Cr) in deep pore waters of intertidal flat sediments. *Geochimica et Cosmochimica Acta*. **72**(12),pp.2822–2840.

Beghin, J., Storme, J.Y., Blanpied, C., Gueneli, N., Brocks, J.J., Poulton, S.W. and Javaux, E.J. 2017. Microfossils from the late Mesoproterozoic – early Neoproterozoic Atar/El Mreïti Group, Taoudeni Basin, Mauritania, northwestern Africa. *Precambrian Research*. **291**(January),pp.63–82.

Bekker, A., Holland, H.D., Wang, P.-L., Rumble, D., Stein, H.J., Hannah, J.L., Coetzee, L.L. and Beukes, N.J. 2004. Dating the rise of atmospheric oxygen. *Nature*. **427**(6970),pp.117–120.

Benitez-Nelson, C.R. 2000. The biogeochemical cycling of phosphorus in marine systems. *Earth-Science Reviews*. **51**(1–4),pp.109–135.

Berner, R.A. 1964. An idealized model of dissolved sulfate distribution in recent sediments. *Geochimica et Cosmochimica Acta*. **28**(9),pp.1497–1503.

Berner, R.A. 1982. Burial of organic carbon and pyrite sulfur in the modern ocean: Its geochemical and environmental significance. *American Journal of Science*. **282**(4),pp.451–473.

Berner, R.A. 1990. Diagenesis of phosphorus in sediments from non-upwelling areas *In*: *Phosphate Deposits of the World: Volume 3, Neogene to Modern Phosphorites*., pp. 27–30.

Berner, R.A. 1973. Phosphate removal from sea water by adsorption on volcanogenic ferric oxides. *Earth and Planetary Science Letters*. **18**(1),pp.77–86.

Berner, R.A. 1970. Sedimentary pyrite formation. *American Journal of Science*. **268**,pp.1–23.

Berner, R.A. and Canfield, D.E. 1989. A new model for atmospheric oxygen over Phanerozoic time. *American Journal of Science*. **289**(4),pp.333–361.

Bertine, K.K. and Turekian, K.K. 1973. Molybdenum in marine deposits. *Geochimica et Cosmochimica Acta*. **37**(6),pp.1415–1434.

Bessanova, V.Y., Velikanov, V.A., Keller, B.M. and Kirsanov, V.V. 1987. *PALAEOGEOGRAPHV AND LITHOLOGY OF THE VENDIAN AND CAMBRIAN OF THE WESTERN EAST-EUROPEAN PLATFORM*.

Betts, J.N. and Holland, H.D. 1991. The oxygen content of ocean bottom waters, the burial efficiency of organic carbon, and the regulation of atmospheric oxygen. *Palaeogeography, Palaeoclimatology, Palaeoecology*. **97**(1–2),pp.5–18.

Bjerrum, C.J. and Canfield, D.E. 2002. Ocean productivity before about 1.9 Gyr ago limited by phosphorus adsorption onto iron oxides. *Nature*. **417**(6885),pp.159–162.

Bjerrum, C.J. and Canfield, D.E. 2011. Towards a quantitative understanding of the late Neoproterozoic carbon cycle. *Proceedings of the National*

Academy of Sciences. **108**(14),pp.5542–5547.

Bottrell, S.H. and Newton, R.J. 2006. Reconstruction of changes in global sulfur cycling from marine sulfate isotopes. *Earth-Science Reviews*. **75**(1–4),pp.59–83.

Bowyer, F., Wood, R.A. and Poulton, S.W. 2017. Controls on the evolution of Ediacaran metazoan ecosystems: A redox perspective. *Geobiology*. **15**(4),pp.516–551.

Boye, M., Nishioka, J., Croot, P., Laan, P., Timmermans, K.R., Strass, V.H., Takeda, S. and de Baar, H.J.W. 2010. Significant portion of dissolved organic Fe complexes in fact is Fe colloids. *Marine Chemistry*. **122**(1–4),pp.20–27.

Boyle, R. A, Clark, J.R., Poulton, S.W., Shields-Zhou, G., Canfield, D.E. and Lenton, T.M. 2013. Nitrogen cycle feedbacks as a control on euxinia in the mid-Proterozoic ocean. *Nature communications*. **4**(1533),pp.1–10.

Boyle, R.A., Dahl, T.W., Bjerrum, C.J. and Canfield, D.E. 2018. Bioturbation and directionality in Earth's carbon isotope record across the Neoproterozoic-Cambrian transition. *Geobiology*. (January),pp.1–27.

Boyle, R.A., Dahl, T.W., Dale, A.W., Shields-Zhou, G.A., Zhu, M., Brasier, M.D., Canfield, D.E. and Lenton, T.M. 2014. Stabilization of the coupled oxygen and phosphorus cycles by the evolution of bioturbation. *Nature Geoscience*. **7**(9),pp.671–676.

Brasier, M.D., McIlroy, D., Liu, A.G., Antcliffe, J.B. and Menon, L.R. 2013. The oldest evidence of bioturbation on Earth. *Geology*. **41**(5),p.289.

Brocks, J.J., Jarrett, A.J.M., Sirantoine, M., Hallmann, C., Hoshino, Y. and Liyanage, T. 2017. The rise of algae in Cryogenian oceans and the emergence of animals. *Nature*. **548**,pp.578–581.

Brocks, J.J., Logan, G.A., Buick, R., Summons, R.E., Brocks, J.J., Logan, G.A., Buick, R. and Summons, R.E. 1999. Archean Molecular Fossils and the Early Rise of Eukaryotes. *Science*. **285**(5430),pp.1033–1036.

Brocks, J.J., Love, G.D., Summons, R.E., Knoll, A.H., Logan, G.A. and Bowden, S.A. 2005. Biomarker evidence for green and purple sulphur bacteria in a stratified Palaeoproterozoic sea. *Nature*. **437**(7060),pp.866–870.

Brounce, M., Stolper, E. and Eiler, J. 2017. Redox variations in Mauna Kea lavas, the oxygen fugacity of the Hawaiian plume, and the role of volcanic gases in Earth's oxygenation. *Proceedings of the National Academy of Sciences*. **114**(34),pp.8997–9002.

Brumsack, H.J. 2006. The trace metal content of recent organic carbon-rich sediments: Implications for Cretaceous black shale formation. *Palaeogeography, Palaeoclimatology, Palaeoecology*. **232**(2–4),pp.344–361.

Buick, R. 1992. The antiquity of oxygenic photosynthesis: evidence from stromatolites in sulphate-deficient Archaean lakes. *Science (New York, N.Y.)*. **255**(5040),pp.74–7.

Buick, R. 2008. When did oxygenic photosynthesis evolve? *Philosophical*

transactions of the Royal Society of London. Series B, Biological sciences. **363**(May),pp.2731–2743.

Burdett, J.W., Arthur, M.A. and Richardson, M. 1989. A Neogene seawater sulfur isotope age curve from calcareous pelagic microfossils. *Earth and Planetary Science Letters*. **94**(3–4),pp.189–198.

Burdige, D.J. 1993. The biogeochemistry of manganese and iron reduction in marine sediments. *Earth Science Reviews*. **35**(3),pp.249–284.

Burns, S.J. and Matter, A. 1993. Carbon isotopic record of the latest Proterozoic from Oman. *Eclogae Geologicae Helvetiae*. **86**(2),pp.595–607.

Butterfield, N.J. 2000. Bangiomorpha pubescens n. gen., n. sp.: implications for the evolution of sex, multicellularity, and the Mesoproterozoic/Neoproterozoic radiation of eukaryotes. *Paleobiology*. **26**(3),pp.386–404.

Butterfield, N.J. 2018. Oxygen, animals and aquatic bioturbation: An updated account. *Geobiology*. **16**(1),pp.3–16.

Butterfield, N.J. 2009. Oxygen, animals and oceanic ventilation: an alternative view. *Geobiology*. **7**(1),pp.1–7.

Butterfield, N.J. 2005a. Probable Proterozoic fungi. *Paleobiology*. **31**(1),pp.165–182.

Butterfield, N.J. 2005b. Reconstructing a complex early Neoproterozoic eukaryote, Wynniatt Formation, arctic Canada. *Lethaia*. **38**(2),pp.155–169.

Cairns-Smith, A.G. 1978. Precambrian solution photochemistry, inverse segregation and banded iron formations. *Nature*. **276**(5690),pp.807–808.

Calver, C.R. and Lindsay, J.F. 1998. Ediacarian sequence and isotope stratigraphy of the Officer Basin, South Australia. *Australian Journal of Earth Sciences*. **45**(4),pp.513–532.

Calvert, S.E., Bustin, R.M. and Ingall, E.D. 1996. Influence of water column anoxia and sediment supply on the burial and preservation of organic carbon in marine shales. *Geochimica et Cosmochimica Acta*. **60**,pp.1577–1593.

Calvert, S.E. and Pedersen, T.F. 1993. Geochemistry of Recent oxic and anoxic marine sediments: Implications for the geological record. *Marine Geology*. **113**(1–2),pp.67–88.

Calvert, S.E. and Pedersen, T.F. 1996. Sedimentary geochemistry of manganese: Implications for the environment of formation of manganiferous black shales. *Economic Geology*. **91**(1),pp.36–47.

Canfield, D.E. 1998. A new model for Proterozoic ocean chemistry. *Nature*. **396**,pp.450–453.

Canfield, D.E. 1994. Factors influencing organic carbon preservation in marine sediments. *Chemical geology*. **114**(93),pp.315–329.

Canfield, D.E. 1989. Reactive iron in marine sediments. *Geochimica et Cosmochimica Acta*. **53**(3),pp.619–632.

Canfield, D.E. 2000. The Archean Sulfur Cycle and the Early History of Atmospheric Oxygen. *Science*. **288**(5466),pp.658–661.

Canfield, D.E. 2005. The Early History of Atmospheric Oxygen: Homage to Robert M. Garrels. *Annual Review of Earth and Planetary Sciences*. **33**(1),pp.1–36.

Canfield, D.E. and Farquhar, J. 2009. Animal evolution, bioturbation, and the sulfate concentration of the oceans. *Proceedings of the National Academy of Sciences of the United States of America*. **106**(20),pp.8123–8127.

Canfield, D.E., Lyons, T.W. and Raiswell, R. 1996. A model for iron deposition to euxinic Black Sea sediments. *American Journal of Science*. **296**(7),pp.818–834.

Canfield, D.E., Poulton, S.W., Knoll, A.H., Narbonne, G.M., Ross, G., Goldberg, T. and Strauss, H. 2008. Ferruginous Conditions Dominated Later Neoproterozoic Deep-Water Chemistry. *Science*. **321**(5891),pp.949–952.

Canfield, D.E., Poulton, S.W. and Narbonne, G.M. 2007. Late-Neoproterozoic deep-ocean oxygenation and the rise of animal life. *Science*. **315**(5808),pp.92–5.

Canfield, D.E. and Raiswell, R. 1999. The evolution of the sulfur cycle. *American Journal of Science*. **299**(7–9),pp.697–723.

Canfield, D.E., Raiswell, R. and Bottrell, S.H. 1992. The reactivity of sedimentary iron minerals toward sulfide. *American Journal of Science*. **292**(November),pp.659–683.

Canfield, D.E., Raiswell, R., Westrich, J.T., Reaves, C.M. and Berner, R.A. 1986. The use of chromium reduction in the analysis of reduced inorganic sulfur in sediments and shales. *Chemical Geology*. **54**,pp.149–155.

Van Cappellen, P. and Ingall, E.D. 1996. Redox stabilization of the atmosphere and oceans by phosphorus-limited marine productivity. *Science (New York, N.Y.)*. **271**(5248),pp.493–496.

Catling, D.C. and Claire, M.W. 2005. How Earth's atmosphere evolved to an oxic state: A status report. *Earth and Planetary Science Letters*. **237**(1–2),pp.1–20.

Catling, D.C., Glein, C.R., Zahnle, K.J. and Mckay, C.P. 2005. Why O2 Is Required by Complex Life on Habitable Planets and the Concept of Planetary "Oxygenation Time". *Astrobiology*. **5**(3),pp.415–438.

Chernikova, D., Motamedi, S., Csürös, M., Koonin, E. V and Rogozin, I.B. 2011. A late origin of the extant eukaryotic diversity: divergence time estimates using rare genomic changes. *Biology Direct*. **6**(1),p.26.

Chumakov, N.M. 2010. Precambrian glaciations and associated biospheric events. *Stratigraphy and Geological Correlation*. **18**(5),pp.467–479.

Claire, M.W., Kasting, J.F., Domagal-Goldman, S.D., Stüeken, E.E., Buick, R. and Meadows, V.S. 2014. Modeling the signature of sulfur mass-independent fractionation produced in the Archean atmosphere. *Geochimica et Cosmochimica Acta*. **141**,pp.365–380.

Clapham, M.E., Narbonne, G.M. and Gehling, J.G. 2003. Paleoecology of the oldest known animal communities: Ediacaran assemblages at Mistaken Point, Newfoundland. *Paleobiology*. **29**(4),pp.527–544.

Clarkson, M.O., Poulton, S.W., Guilbaud, R. and Wood, R. a. 2014. Assessing

the utility of Fe/Al and Fe-speciation to record water column redox conditions in carbonate-rich sediments. *Chemical Geology*. **382**,pp.111–122.

Cloud, P. 1972. A working model of the primitive Earth. *American Journal of Science*. **272**(6),pp.537–548.

Cloud, P.E. 1968. Atmospheric and Hydrospheric Evolution on the Primitive Earth. *Science*. **160**(3829),pp.729–736.

Cole, D.B., Reinhard, C.T., Wang, X., Gueguen, B., Halverson, G.P., Gibson, T., Hodgskiss, M.S.W., Mckenzie, N.R., Lyons, T.W. and Planavsky, N.J. 2016. A shale-hosted Cr isotope record of low atmospheric oxygen during the Proterozoic. *Geology*. (7),pp.1–4.

Colman, A.S. and Holland, H.D. 2000. The Global Diagenetic Flux of Phosphorus from Marine Sediments to the Oceans: Redox sensitivity and the control of atmospheric oxygen levels *In*: *Marine Authigenesis: From global to microbial*., pp. 53–77.

Cox, G.M., Halverson, G.P., Stevenson, R.K., Vokaty, M., Poirier, A., Kunzmann, M., Li, Z.-X., Denyszyn, S.W., Strauss, J. V. and Macdonald, F.A. 2016b. Continental flood basalt weathering as a trigger for Neoproterozoic Snowball Earth. *Earth and Planetary Science Letters*. **446**,pp.89–99.

Cox, G.M., Jarrett, A., Edwards, D., Crockford, P.W., Halverson, G.P., Collins, A.S., Poirier, A. and Li, Z.-X. 2016a. Basin redox and primary productivity within the Mesoproterozoic Roper Seaway. *Chemical Geology*. **440**,pp.101–114.

Cox, G.M., Lyons, T.W., Mitchell, R.N., Hasterok, D. and Gard, M. 2018. Linking the rise of atmospheric oxygen to growth in the continental phosphorus inventory. *Earth and Planetary Science Letters*. **489**,pp.28–36.

Crimes, P.T. and Fedonkin, M.A. 1994. Evolution and Dispersal of Deepsea Traces. *SEPM*. **9**(1),pp.74–83.

Crimes, T.P. 1992. Changes in the trace fossil biotal across the Proterozoic-Phanerozoic boundary. *Journal of the Geological Society of London*. **149**,pp.637–646.

Crowe, S.A., Døssing, L.N., Beukes, N.J., Bau, M., Kruger, S.J., Frei, R. and Canfield, D.E. 2013. Atmospheric oxygenation three billion years ago. *Nature*. **501**(7468),pp.535–8.

Crowe, S.A., Jones, C., Katsev, S., Magen, C., O'Neill, A.H., Sturm, A., Canfield, D.E., Haffner, G.D., Mucci, A., Sundby, B. and Fowle, D.A. 2008. Photoferrotrophs thrive in an Archean Ocean analogue. *Proceedings of the National Academy of Sciences*. **105**(41),pp.15938–15943.

Crusius, J., Calvert, S., Pedersen, T. and Sage, D. 1996. Rhenium and molybdenum enrichments in sediments as indicators of oxic, suboxic and sulfidic conditions of deposition. *Earth and Planetary Science Letters*. **145**(96),pp.65–78.

Cui, H., Kaufman, A.J., Xiao, S., Zhou, C. and Liu, X.-M. 2017. Was the Ediacaran Shuram Excursion a globally synchronized early diagenetic event? Insights from methane-derived authigenic carbonates in the

uppermost Doushantuo Formation, South China. *Chemical Geology*. **450**,pp.59–80.

Cumming, V.M., Poulton, S.W., Rooney, A.D. and Selby, D. 2013. Anoxia in the terrestrial environment during the late Mesoproterozoic. *Geology*. **41**,pp.583–586.

Dahl, T.W., Canfield, D.E., Rosing, M.T., Frei, R.E., Gordon, G.W., Knoll, A.H. and Anbar, A.D. 2011. Molybdenum evidence for expansive sulfidic water masses in ~750Ma oceans. *Earth and Planetary Science Letters*. **311**(3–4),pp.264–274.

Dahl, T.W., Chappaz, A., Hoek, J., McKenzie, C.J., Svane, S. and Canfield, D.E. 2016. Evidence of molybdenum association with particulate organic matter under sulfidic conditions. *Geobiology*. **15**,pp.311–323.

Daines, S.J., Mills, B.J.W. and Lenton, T.M. 2017. Atmospheric oxygen regulation at low Proterozoic levels by incomplete oxidative weathering of sedimentary organic carbon. *Nature Communications*. **8**(Level 7),p.14379.

Delaney, M.L. 1998. Phosphorus accumulation in marine sediments and the oceanic phosphorus cycle. *Global Biogeochemical Cycles*. **12**(4),p.563.

Dellwig, O., Leipe, T., Marz, C., Glockzin, M., Pollehne, F., Schnetger, B., Yakushev, E. V., Bottcher, M.E. and Brumsack, H.J. 2010. A new particulate Mn-Fe-P-shuttle at the redoxcline of anoxic basins. *Geochimica et Cosmochimica Acta*. **74**(24),pp.7100–7115.

Derry, L.A. 2010. A burial diagenesis origin for the Ediacaran Shuram-Wonoka carbon isotope anomaly. *Earth and Planetary Science Letters*. **294**(1–2),pp.152–162.

Dhuime, B., Wuestefeld, A. and Hawkesworth, C.J. 2015. Emergence of modern continental crust about 3 billion years ago. *Nature Geoscience*. **8**(7),pp.552–555.

Diamond, C.W., Planavsky, N.J., Wang, C. and Lyons, T.W. 2018. What the ~1.4 Ga Xiamaling Formation can and cannot tell us about the mid-Proterozoic ocean. *Geobiology*. (October 2017),pp.1–18.

Dijkstra, N., Kraal, P., Kuypers, M.M.M., Schnetger, B. and Slomp, C.P. 2014. Are iron-phosphate minerals a sink for phosphorus in anoxic black sea sediments? *PLoS ONE*. **9**(7),pp.1–12.

Dijkstra, N., Kraal, P., Séguret, M.J.M., Flores, M.R., Gonzalez, S., Rijkenberg, M.J.A. and Slomp, C.P. 2018. Phosphorus dynamics in and below the redoxcline in the Black Sea and implications for phosphorus burial. *Geochimica et Cosmochimica Acta*. **222**,pp.685–703.

Dijkstra, N., Slomp, C.P. and Behrends, T. 2016. Vivianite is a key sink for phosphorus in sediments of the Landsort Deep, an intermittently anoxic deep basin in the Baltic Sea. *Chemical Geology*. **438**,pp.58–72.

Donnelly, T.H., Shergold, J.H., Southgate, P.N. and Barnes, C.J. 1990. Events leading to global phosphogenesis around the Proterozoic/Cambrian boundary. *Phosphorite Research and Development*. **52**(52),pp.273–287.

Douzery, E.J.P., Snell, E.A., Bapteste, E., Delsuc, F. and Philippe, H. 2004. The timing of eukaryotic evolution: Does a relaxed molecular clock

reconcile proteins and fossils? *Proceedings of the National Academy of Sciences*. **101**(43),pp.15386–15391.

Duan, Y., Anbar, A.D., Arnold, G.L., Lyons, T.W., Gordon, G.W. and Kendall, B. 2010. Molybdenum isotope evidence for mild environmental oxygenation before the Great Oxidation Event. *Geochimica et Cosmochimica Acta*. **74**(23),pp.6655–6668.

Duce, R.A., Liss, P.S., Merrill, J.T., Atlas, E.L., Buat-Menard, P., Hicks, B.B., Miller, J.M., Prospero, J.M., Arimoto, R., Church, T.M., Ellis, W., Galloway, J.N., Hansen, L., Jickells, T.D., Knap, A.H., Reinhardt, K.H., Schneider, B., Soudine, A., Tokos, J.J., Tsunogai, S., Wollast, R. and Zhou, M. 1991. The atmospheric input of trace species to the world ocean. *Global Biogeochemical Cycles*. **5**(3),pp.193–259.

Dunk, R.M., Mills, R.A. and Jenkins, W.J. 2002. A reevaluation of the oceanic uranium budget for the Holocene. *Chemical Geology*. **190**(1–4),pp.45–67.

Egger, M., Jilbert, T., Behrends, T., Rivard, C. and Slomp, C.P. 2015. Vivianite is a major sink for phosphorus in methanogenic coastal surface sediments. *Geochimica et Cosmochimica Acta*. **169**,pp.217–235.

Eickmann, B., Hofmann, A., Wille, M., Bui, T.H., Wing, B.A. and Schoenberg, R. 2018. Isotopic evidence for oxygenated Mesoarchaean shallow oceans. *Nature Geoscience*.

Eijsink, L.M., Krom, M.D. and Herut, B. 2000. Speciation and burial flux of phosphorus in the surface sediments of the Eastern Mediterranean. *American Journal of Science*. **300**(6),pp.483–503.

Eijsink, L.M., Krom, M.D. and De Lange, G.J. 1997. The use of sequential extraction techniques for sedimentary phosphorus in eastern Mediterranean sediments. *Marine Geology*. **139**(1–4),pp.147–155.

Eme, L., Sharpe, S.C., Brown, M.W. and Roger, A.J. 2014. On the Age of Eukaryotes: Evaluating Evidence from Fossils and Molecular Clocks. *Cold Spring Harbor Perspectives in Biology*. **6**(8).

Emerson, S.R. and Huested, S.S. 1991. Ocean anoxia and the concentrations of molybdenum and vanadium in seawater. *Marine Chemistry*. **34**,pp.177–196.

Erickson, B.E. and Helz, G.R. 2000. Molybdenum(VI) speciation in sulfidic waters: Stability and lability of thiomolybdates. *Geochimica et Cosmochimica Acta*. **64**(7),pp.1149–1158.

Ernst, R.E., Pease, V., Puchkov, V.N., Kozlov, V.I., Sergeeva, N.D., Hamilton, M. and Ernst, R.E., Pease, V., Puchkov, V.N., Kozlov, V.I., Sergeeva, N.D., Hamilton, M. 2000. Geochemical Characterization of Precambrian Magmatic Suites of the Southeastern Margin of the East European Craton , Southern Urals , Russia. *Geological collection*. **5**,pp.119–161.

Erwin, D.H., Laflamme, M., Tweedt, S.M., Sperling, E.A., Pisani, D. and Peterson, K.J. 2011. The Cambrian conundrum: early divergence and later ecological success in the early history of animals. *Science (New York, N.Y.)*. **334**(6059),pp.1091–7.

Evans, D.A.D. and Mitchell, R.N. 2011. Assembly and breakup of the core of Paleoproterozoic-Mesoproterozoic supercontinent Nuna. *Geology*.

39(5),pp.443–446.

Fagel, N., Alleman, L.Y., Granina, L., Hatert, F., Thamo-Bozso, E., Cloots, R. and André, L. 2005. Vivianite formation and distribution in Lake Baikal sediments. *Global and Planetary Change*. **46**(1–4 SPEC. ISS.),pp.315–336.

Farquhar, J., Bao, H. and Thiemens, M. 2000. Atmospheric Influence of Earth's Earliest Sulfur Cycle. *Science*. **289**(August),pp.757–758.

Farquhar, J., Bao, H. and Thiemens, M. 1997. Atmospheric Influence of Earth ' s Earliest Sulfur Cycle. *Science*. **031**(2),pp.10–13.

Farquhar, J., Cliff, J., Zerkle, A.L., Kamyshny, A., Poulton, S.W., Claire, M., Adams, D. and Harms, B. 2013. Pathways for Neoarchean pyrite formation constrained by mass-independent sulfur isotopes. *Proceedings of the National Academy of Sciences*. **110**(44),pp.17638–17643.

Farquhar, J. and Wing, B. a. 2003. Multiple sulfur isotopes and the evolution of the atmosphere. *Earth and Planetary Science Letters*. **213**,pp.1–13.

Farquhar, J., Zerkle, A.L. and Bekker, A. 2011. Geological constraints on the origin of oxygenic photosynthesis. *Photosynthesis Research*. **107**(1),pp.11–36.

Faul, K.L., Paytan, A. and Delaney, M.L. 2005. Phosphorus distribution in sinking oceanic particulate matter. *Marine Chemistry*. **97**(3–4),pp.307–333.

Fedonkin, M.A. 2003. The origin of the Metazoa in the light of the Proterozoic fossil record. *Paleontological Research*. **7**(1),pp.9–41.

Fedonkin, M.A., Simonetta, A. and Ivantsov, A.Y. 2007. New data on Kimberella, the Vendian mollusc-like organism (White Sea region, Russia): palaeoecological and evolutionary implications. *Geological Society, London, Special Publications*. **286**(1),pp.157–179.

Fedonkin, M.A. and Waggoner, B.M. 1997. The Late Precambrian fossil Kimberella is a mollusc-like bilaterian organism. *Nature*. **388**(6645),pp.868–871.

Felitsyn, S.B. 2004. Vendian volcanism, weathering, and phosphorus cycle variation in the East European platform. *Lithology and Mineral Resources*. **39**(4),pp.322–332.

Fike, D.A., Grotzinger, J.P., Pratt, L.M. and Summons, R.E. 2006. Oxidation of the Ediacaran Ocean. *Nature*. **444**(7120),pp.744–747.

Filippelli, G.M. 1997. Controls on phosphorus concentration and accumulation in oceanic sediments. *Marine Geology*. **139**(1–4),pp.231–240.

Filippelli, G.M. 2011. Phosphate rock formation and marine phosphorus geochemistry: The deep time perspective. *Chemosphere*. **84**(6),pp.759–766.

Filippelli, G.M. and Delaney, M.L. 1996. Phosphorus geochemistry of equatorial Pacific sediments. *Geochimica et Cosmochimica Acta*. **60**(9),pp.1479–1495.

Fischer, W.W., Hemp, J. and Johnson, J.E. 2016. Evolution of Oxygenic Photosynthesis. *Annual Review of Earth and Planetary Sciences*. **44**(1),pp.647–683.

François, L.M. 1986. Extensive deposition of banded iron formations was possible without photosynthesis. *Nature*. **320**(6060),pp.352–354.

Frei, R., Gaucher, C., Poulton, S.W. and Canfield, D.E. 2009. Fluctuations in Precambrian atmospheric oxygenation recorded by chromium isotopes. *Nature*. **461**(7261),pp.250–253.

French, K.L., Hallmann, C., Hope, J.M., Schoon, P.L., Zumberge, J.A. and Hoshino, Y. 2015. Reappraisal of hydrocarbon biomarkers in Archean rocks. *Proceedings of the National Academy of Sciences*. **112**(19).

Froelich, P.N., Bender, M.L., Luedtke, N.A., Heath, G.R. and DeVries, T. 1982. The marine phosphorous cycle. *American Journal of Science*. **282**,pp.474–511.

Froelich, P.N., Klinkhammer, G.P., Bender, M.L., Luedtke, N.A., Heath, G.R., Cullen, D., Dauphin, P., Hammond, D., Hartman, B. and Maynard, V. 1979. Early oxidation of organic matter in pelagic sediments of the eastern equatorial Atlantic: suboxic diagenesis. *Geochimica et Cosmochimica Acta*. **43**(7),pp.1075–1090.

Gaillard, F., Scaillet, B. and Arndt, N.T. 2011. Atmospheric oxygenation caused by a change in volcanic degassing pressure. *Nature*. **478**(7368),pp.229–232.

Gardiner, S. and Hiscott, R.N. 1988. Deep-water facies and depositional setting of the lower Conception Group (Hadrynian), southern Avalon Peninsula, Newfoundland. *Canadian Journal of Earth Sciences*. **25**(10),pp.1579–1594.

Gartman, A. and Luther, G.W. 2014. Oxidation of synthesized sub-micron pyrite (FeS2) in seawater. *Geochimica et Cosmochimica Acta*. **144**,pp.96–108.

Geboy, N.J., Kaufman, A.J., Walker, R.J., Misi, A., de Oliviera, T.F., Miller, K.E., Azmy, K., Kendall, B. and Poulton, S.W. 2013. Re-Os age constraints and new observations of Proterozoic glacial deposits in the Vazante Group, Brazil. *Precambrian Research*. **238**,pp.199–213.

Gehling, J.G. and Droser, M.L. 2009. Textured organic surfaces associated with the Ediacara biota in South Australia. *Earth-Science Reviews*. **96**(3),pp.196–206.

Gehling, J.G., Narbonne, G.M. and Anderson, M.M. 2000. The first named Ediacaran body fossil, Aspidella terranovica. *Palaeontology*. **43**(3),pp.427–456.

Gehling, J.G. and Rigby, J.K. 1996. Long Expected Sponges from the Neoproterozoic Ediacara Fauna of South Australia. *Journal of Paleontology*. **70**(2),pp.185–195.

Geider, R. and La Roche, J. 2002. Redfield revisited: variability of C:N:P in marine microalgae and its biochemical basis Redfield revisited: variability of C:N:P in marine microalgae and its biochemical basis. *European Journal of Phycology*. **37**(September 2012),pp.37–41.

German, C.R., Holliday, B.P. and Elderfield, H. 1991. Redox cycling of rare earth elements in the suboxic zone of the Black Sea. *Geochimica et Cosmochimica Acta*. **55**(12),pp.3553–3558.

Giese, U., Glasmacher, U., Kozlov, V.I., Matenaar, I., Puchkov, V.N., Stroink, L., Bauer, W., Ladage, S. and Walter, R. 1999. Structural framework of the Bashkirian anticlinorium, SW Urals. *Geologische Rundschau*. **87**(4),pp.526–544.

Gilleaudeau, G.J. and Kah, L.C. 2015. Heterogeneous redox conditions and a shallow chemocline in the Mesoproterozoic ocean: Evidence from carbon-sulfur-iron relationships. *Precambrian Research*. **257**,pp.94–108.

Gilleaudeau, G.J. and Kah, L.C. 2013. Oceanic molybdenum drawdown by epeiric sea expansion in the Mesoproterozoic. *Chemical Geology*. **356**,pp.21–37.

Gilleaudeau, G.J.J., Frei, R., Kaufman, A.J.J., Kah, L.C.C., Azmy, K., Bartley, J.K.K., Chernyavskiy, P. and Knoll, A.H.H. 2016. Oxygenation of the mid-Proterozoic atmosphere: clues from chromium isotopes in carbonates. *Geochemical Perspectives Letters*. **2**(2),pp.178–187.

Glasmacher, U.A., Bauer, W., Clauer, N. and Puchkov, V.N. 2004. Neoproterozoic metamorphism and deformation at the southeastern margin of the East European Craton, Uralides, Russia. *International Journal of Earth Sciences*. **93**(5),pp.921–944.

Glasmacher, U.A., Bauer, W., Giese, U., Reynolds, P., Kober, B., Puchkov, V., Stroink, L., Alekseyev, A. and Willner, A.P. 2001. The metamorphic complex of Beloretzk, SW Urals, Russia - A terrane with a polyphase Meso- to Neoproterozoic thermo-dynamic evolution. *Precambrian Research*. **110**(1–4),pp.185–213.

Goldberg, T., Poulton, S.W., Wagner, T., Kolonic, S.F. and Rehkämper, M. 2016. Molybdenum drawdown during Cretaceous Oceanic Anoxic Event 2. *Earth and Planetary Science Letters*. **440**,pp.81–91.

Goldblatt, C., Lenton, T.M. and Watson, A.J. 2006. Bistability of atmospheric oxygen and the Great Oxidation. *Nature*. **443**(7112),pp.683–686.

Goldhammer, T., Brüchert, V., Ferdelman, T.G. and Zabel, M. 2010. Microbial sequestration of phosphorus in anoxic upwelling sediments. *Nature Geoscience*. **3**(8),pp.557–561.

Golubkova, E.Y., Zaitseva, T.S., Kuznetsov, A.B., Dovzhikova, E.G. and Maslov, A. V. 2015. Microfossils and Rb-Sr age of glauconite in the key section of the Upper Proterozoic of the northeastern part of the Russian plate (Keltmen-1 borehole). *Doklady Earth Sciences*. **462**(2),pp.547–551.

Gorokhov, I.M., Clauer, N., Turchenko, T.N., Melnikov, N.N., Kutyavin, E.P., Pirrus, E. and Baskakov, A.V. 1994. Rb-Sr systematics of Vendian-Cambrian claystones from the east European Platform: implications for a multi-stage illite evolution. *Chemical Geology*. **112**(1–2),pp.71–89.

Gorozhanin, V.M., Puchkov, V.N., Gorozhanina, E.N., Sergeeva, N.D., Romanyuk, T.V. and Kuznetsov, N.B. 2014. The Navysh graben-rift of the South Urals as a fragment of the Early Proterozoic aulacogen. *Doklady Earth Sciences*. **458**(1),pp.1052–1057.

Gostin, V.A., McKirdy, D.M., Webster, L.J. and Williams, G.E. 2010. Ediacaran ice-rafting and coeval asteroid impact, South Australia: Insights into the terminal proterozoic environment. *Australian Journal of Earth Sciences*.

57(7),pp.859–869.

Grazhdankin, D.V. 2004. Patterns of Distribution in the Ediacaran Biotas: Facies versus Biogeography and Evolution. *Paleontological Society*. **30**(2),pp.203–221.

Grazhdankin, D.V. 2003. Structure and depositional environment of the Vendian Complex in the southeastern White Sea area. *Stratigraphy and Geological Correlation*. **11**(4),pp.313–331.

Grey, K., Walter, M.R. and Calver, C.R. 2003. Neoproterozoic biotic diversification: Snowball Earth or aftermath of the Acraman impact? *Geology*. **31**(5),pp.459–462.

Grotzinger, J.P., Fike, D.A. and Fischer, W.W. 2011. Enigmatic origin of the largest-known carbon isotope excursion in Earth's history. *Nature Geoscience*. **4**(5),pp.285–292.

Guilbaud, R., Poulton, S.W., Butterfield, N.J., Zhu, M. and Shields-Zhou, G.A. 2015. A global transition to ferruginous conditions in the early Neoproterozoic oceans. *Nature Geoscience*. **8**,pp.466–470.

Guilbaud, R., Slater, B.J., Poulton, S.W., Harvey, T.H.P., Brocks, J.J., Nettersheim, B.J., Butter and Group, T. 2018. Oxygen minimum zones in the early Cambrian ocean. *Geochemical Perspectives Letters*. **6**(February),pp.33–38.

Gumsley, A.P., Chamberlain, K.R., Bleeker, W., Söderlund, U., de Kock, M.O., Larsson, E.R. and Bekker, A. 2017. Timing and tempo of the Great Oxidation Event. *Proceedings of the National Academy of Sciences*. **114**(8),pp.1811–1816.

Guo, H., Du, Y., Kah, L.C., Huang, J., Hu, C., Huang, H. and Yu, W. 2013. Isotopic composition of organic and inorganic carbon from the Mesoproterozoic Jixian Group, North China: Implications for biological and oceanic evolution. *Precambrian Research*. **224**,pp.169–183.

Guo, Q., Strauss, H., Kaufman, A.J., Schröder, S., Gutzmer, J., Wing, B., Baker, M.A., Bekker, A., Jin, Q., Kim, S.T. and Farquhar, J. 2009. Reconstructing Earth's surface oxidation across the Archean-Proterozoic transition. *Geology*. **37**(5),pp.399–402.

Guo, Z., Peng, X., Czaja, A.D., Chen, S. and Ta, K. 2018. Cellular taphonomy of well-preserved Gaoyuzhuang microfossils : A window into the preservation of ancient cyanobacteria. *Precambrian Research*. **304**(May 2017),pp.88–98.

Habicht, K.S., Gade, M., Thamdrup, B., Berg, P. and Canfield, D.E. 2002. Calibration of Sulfate Levels in the Archean Ocean. *Science*. **298**(5602),pp.2372–2374.

Hannah, J.L., Bekker, A., Stein, H.J., Markey, R.J. and Holland, H.D. 2004. Primitive Os and 2316 Ma age for marine shale: Implications for Paleoproterozoic glacial events and the rise of atmospheric oxygen. *Earth and Planetary Science Letters*. **225**(1–2),pp.43–52.

Hardisty, D.S., Lu, Z., Bekker, A., Diamond, C.W., Gill, B.C., Jiang, G., Kah, L.C., Knoll, A.H., Loyd, S.J., Osburn, M.R., Planavsky, N.J., Wang, C., Zhou, X. and Lyons, T.W. 2017. Perspectives on Proterozoic surface

ocean redox from iodine contents in ancient and recent carbonate. *Earth and Planetary Science Letters*. **463**,pp.159–170.

Hardisty, D.S., Lyons, T.W., Riedinger, N., Isson, T.T., Owens, J.D., Aller, R.C., Rye, D.M., Planavsky, N.J., Reinhard, C.T., Gill, B.C., Masterson, A.L., Asael, D. and Johnston, D.T. 2018. An evaluation of sedimentary molybdenum and iron as proxies for pore fluid paleoredox conditions. *American Journal of Science*. **318**(5),pp.527–556.

Havig, J.R., McCormick, M.L., Hamilton, T.L. and Kump, L.R. 2015. The behavior of biologically important trace elements across the oxic/euxinic transition of meromictic Fayetteville Green Lake, New York, USA. *Geochimica et Cosmochimica Acta*. **165**,pp.389–406.

Hayes, J.M., Strauss, H. and Kaufman, A.J. 1999. The abundance of 13C in marine organic matter and isotopic fractionation in the global biogeochemical cycle of carbon during the past 800 Ma. *Chemical Geology*. **161**(1–3),pp.103–125.

Hedges, S.B., Blair, J.E., Venturi, M.L. and Shoe, J.L. 2004. A molecular timescale of eukaryote evolution and the rise of complex multicellular life. *BMC Evolutionary Biology*. **9**(4),pp.1–9.

Helz, G.R., Miller, C. V., Charnock, J.M., Mosselmans, J.F.W., Pattrick, R.A.D., Garner, C.D. and Vaughan, D.J. 1996. Mechanism of molybdenum removal from the sea and its concentration in black shales: EXAFS evidence. *Geochimica et Cosmochimica Acta*. **60**(19),pp.3631–3642.

Hensen, C., Zabel, M., Pfeifer, K., Schwenk, T., Kasten, S., Riedinger, N., Schulz, H.D. and Boetius, A. 2003. Control of sulfate pore-water profiles by sedimentary events and the significance of anaerobic oxidation of methane for the burial of sulfur in marine sediments. *Geochimica et Cosmochimica Acta*. **67**(14),pp.2631–2647.

Hetzel, A., Böttcher, M.E., Wortmann, U.G. and Brumsack, H.J. 2009. Paleo-redox conditions during OAE 2 reflected in Demerara Rise sediment geochemistry (ODP Leg 207). *Palaeogeography, Palaeoclimatology, Palaeoecology*. **273**(3–4),pp.302–328.

Hoefs, J. 2010. *Stable Isotope Geochemistry*.

Hoffman, P.F. 2013. The Great Oxidation and a Siderian snowball Earth: MIF-S based correlation of Paleoproterozoic glacial epochs. *Chemical Geology*. **362**,pp.143–156.

Holland, H.D. 1973. Systematics of the isotopic composition of sulfur in the oceans during the Phanerozoic and its implications for atmospheric oxygen. *Geochimica et Cosmochimica Acta*. **37**(12),pp.2605–2616.

Holland, H.D. 1984. *The chemical evolution of the atmosphere and oceans*. Princeton: Princeton University Press.

Holland, H.D. 2006. The Oxygenation of the Atmosphere and Oceans. *Philosophical transactions of the Royal Society of London. Series B, Biological sciences*. **361**(1470),pp.903–915.

Holland, H.D. 2002. Volcanic gases, black smokers, and the Great Oxidation Event. *Geochimica et Cosmochimica Acta*. **66**(21),pp.3811–3826.

Hollander, D.J. and Smith, M.A. 2001. Microbially mediated carbon cycling as a control on the δ13C of sedimentary carbon in eutrophic Lake Mendota (USA): New models for interpreting isotopic excursions in the sedimentary record. *Geochimica et Cosmochimica Acta*. **65**(23),pp.4321–4337.

Housecroft, C. and Sharpe, A. 2007. The group 16 elements *In*: *Inorganic Chemistry*., p. 520.

Hoyal Cuthill, J.F. and Han, J. 2018. Cambrian petalonamid Stromatoveris phylogenetically links Ediacaran biota to later animals J. Álvaro, ed. *Palaeontology*.,pp.1–11.

Huerta-Diaz, M.A. and Morse, J.W. 1992. Pyritization of trace metals in anoxic marine sediments. *Geochimica et Cosmochimica Acta*. **56**(7),pp.2681–2702.

Huminicki, D.M.C. and Rimstidt, J.D. 2009. Iron oxyhydroxide coating of pyrite for acid mine drainage control. *Applied Geochemistry*. **24**(9),pp.1626–1634.

Husson, J.M., Maloof, A.C., Schoene, B., Chen, C.Y. and Higgins, J.A. 2015. Stratigraphic expression of earth's deepest $\delta^{13}C$ excursion in the wonoka formation of South Australia. *American Journal of Science*. **315**(1),pp.1–45.

Iizuka, T., Horie, K., Komiya, T., Maruyama, S., Hirata, T., Hidaka, H. and Windley, B.F. 2006. 4.2 Ga zircon xenocryst in an Acasta gneiss from northwestern Canada: Evidence for early continental crust. *Geology*. **34**(4),pp.245–248.

Immenhauser, A. 2009. Estimating palaeo-water depth from the physical rock record. *Earth-Science Reviews*. **96**(1–2),pp.107–139.

Ingall, E.D., Bustin, R.M. and Van Cappellen, P. 1993. Influence of water column anoxia on the burial and preservation of carbon and phosphorus in marine shales. *Geochimica et Cosmochimica Acta*. **57**(2),pp.303–316.

Ingall, E.D. and Van Cappellen, P. 1990. Relation between sedimentation rate and burial of organic phosphorus and organic carbon in marine sediments. *Geochimica et Cosmochimica Acta*. **54**(2),pp.373–386.

Ivantsov, A.Y. and Malakhovskaya, Y.E. 2002. Giant traces of Vendian animals. *Doklady Earth Sciences*. **385A**(6),pp.618–622.

Izon, G., Zerkle, A.L., Zhelezinskaia, I., Farquhar, J., Newton, R.J., Poulton, S.W., Eigenbrode, J.L. and Claire, M.W. 2015. Multiple oscillations in Neoarchaean atmospheric chemistry. *Earth and Planetary Science Letters*. **431**,pp.264–273.

Jackson, T.A. 2015. Variations in the abundance of photosynthetic oxygen through Precambrian and Paleozoic time in relation to biotic evolution and mass extinctions: Evidence from Mn/Fe ratios. *Precambrian Research*. **264**,pp.30–35.

Javaux, E.J., Knoll, A.H. and Walter, M.R. 2004. TEM evidence for eukaryotic diversity in mid-Proterozoic oceans. *Geobiology*. **2**(3),pp.121–132.

Jenkins, R.J.F., McKirdy, D.M., Foster, C.B., O'Leary, T. and Pell, S.D. 1992. The record and stratigraphie implications of organic-walled microfossils

from the Ediacaran (terminal Proterozoic) of South Australia. *Geological Magazine*. **129**(4),pp.401–410.

Jensen, S., Saylor, B.Z., Gehling, J.G. and Germs, G.J.B. 2000. Complex trace fossils from terminal Proterozoic of Namibia. *Geology*. **28**(2),pp.143–146.

Jiang, G., Wang, X., Shi, X., Xiao, S., Zhang, S. and Dong, J. 2012. The origin of decoupled carbonate and organic carbon isotope signatures in the early Cambrian (ca. 542-520Ma) Yangtze platform. *Earth and Planetary Science Letters*. **317**–**318**,pp.96–110.

Jilbert, T. and Slomp, C.P. 2013. Iron and manganese shuttles control the formation of authigenic phosphorus minerals in the euxinic basins of the Baltic Sea. *Geochimica et Cosmochimica Acta*. **107**,pp.155–169.

Jilbert, T., Slomp, C.P., Gustafsson, B.G. and Boer, W. 2011. Beyond the Fe-P-redox connection: Preferential regeneration of phosphorus from organic matter as a key control on Baltic Sea nutrient cycles. *Biogeosciences*. **8**(6),pp.1699–1720.

Johnson, J.E., Gerpheide, A., Lamb, M.P. and Fischer, W.W. 2014. O2 constraints from Paleoproterozoic detrital pyrite and uraninite. *Bulletin of the Geological Society of America*. **126**(5–6),pp.813–830.

Johnston, D.T., Macdonald, F.A., Gill, B.C., Hoffman, P.F. and Schrag, D.P. 2012b. Uncovering the Neoproterozoic carbon cycle. *Nature*. **483**(7389),pp.320–323.

Johnston, D.T., Poulton, S.W., Dehler, C., Porter, S., Husson, J., Canfield, D.E. and Knoll, A.H. 2010. An emerging picture of Neoproterozoic ocean chemistry: Insights from the Chuar Group, Grand Canyon, USA. *Earth and Planetary Science Letters*. **290**(1–2),pp.64–73.

Johnston, D.T., Poulton, S.W., Goldberg, T., Sergeev, V.N., Podkovyrov, V., Vorob'eva, N.G., Bekker, A. and Knoll, A.H. 2012a. Late Ediacaran redox stability and metazoan evolution. *Earth and Planetary Science Letters*. **335**–**336**,pp.25–35.

Jones, C., Nomosatryo, S., Crowe, S.A., Bjerrum, C.J. and Canfield, D.E. 2015. Iron oxides, divalent cations, silica, and the early earth phosphorus crisis. *Geology*. **43**(2),pp.1–4.

Kah, L.C. and Bartley, J.K. 2011. Protracted oxygenation of the Proterozoic biosphere. *International Geology Review*. **53**(11–12),pp.1424–1442.

Kah, L.C., Lyons, T.W. and Frank, T.D. 2004. Low marine sulphate and protracted oxygenation of the Proterozoic biosphere. *Nature*. **431**(October),pp.834–837.

Kappler, A. and Newman, D.K. 2004. Formation of Fe(III)-minerals by Fe(II)-oxidizing photoautotrophic bacteria. *Geochimica et Cosmochimica Acta*. **68**(6),pp.1217–1226.

Karl, D.M. 2014. Microbially mediated transformations of phosphorus in the sea: new views of an old cycle. *Annual review of marine science*. **6**,pp.279–337.

Keller, B.M. and Chumakov, N.M. 1983. *The Riphean Stratotype: Stratigraphy and Geochronology*. Moscow.

Kendall, B., Gordon, G.W., Poulton, S.W. and Anbar, A.D. 2011. Molybdenum isotope constraints on the extent of late Paleoproterozoic ocean euxinia. *Earth and Planetary Science Letters*. **307**(3–4),pp.450–460.

Kendall, B., Reinhard, C.T., Lyons, T.W., Kaufman, A.J., Poulton, S.W. and Anbar, A.D. 2010. Pervasive oxygenation along late Archaean ocean margins. *Nature Geoscience*. **3**(9),pp.647–652.

Kennedy, M., Droser, M., Mayer, L., Pevear, D. and Mrofka, D. 2006. Late Precambrian Oxygenation; Inception of the Clay Mineral Factory. *Science*. **311**(5766),pp.1446–1449.

Kipp, M.A., Stüeken, E.E., Bekker, A. and Buick, R. 2017. Selenium isotopes record extensive marine suboxia during the Great Oxidation Event. *Proceedings of the National Academy of Sciences*. **114**(5),pp.875–880.

Kirschvink, J.L. and Kopp, R.E. 2008. Palaeoproterozoic ice houses and the evolution of oxygen-mediating enzymes: the case for a late origin of photosystem II. *Philosophical Transactions of the Royal Society B: Biological Sciences*. **363**(1504),pp.2755–2765.

Klar, J.K., Schlosser, C., Milton, J.A., Woodward, E.M.S., Lacan, F., Parkinson, I.J., Achterberg, E.P. and James, R.H. 2018. Sources of dissolved iron to oxygen minimum zone waters on the Senegalese continental margin in the tropical North Atlantic Ocean: Insights from iron isotopes. *Geochimica et Cosmochimica Acta*. **236**,pp.60–78.

Klein, C. 2005. Some Precambrian banded iron-formations (BIFs) from around the world: Their age, geologic setting, mineralogy, metamorphism, geochemistry, and origin. *American Mineralogist*. **90**(10),pp.1473–1499.

Klinkhammer, G.P. and Palmer, M.R. 1991. Uranium in the oceans: Where it goes and why. *Geochimica et Cosmochimica Acta*. **55**(7),pp.1799–1806.

Klunder, M.B., Laan, P., Middag, R., De Baar, H.J.W. and Bakker, K. 2012. Dissolved iron in the Arctic Ocean: Important role of hydrothermal sources, shelf input and scavenging removal. *Journal of Geophysical Research: Oceans*. **117**(4),pp.1–17.

Knauth, L.P. and Kennedy, M.J. 2009. The late Precambrian greening of the Earth. *Nature*.,pp.1–5.

Knoll, A.H. 1999. Early Animal Evolution: Emerging Views from Comparative Biology and Geology. *Science*. **284**(5423),pp.2129–2137.

Knoll, A.H. 2015. Paleobiological Perspectives on Early Microbial Evolution. *Cold Spring Harbor Perspectives in Biology*. **7**(7),p.a018093.

Knoll, A.H. 2011. The Multiple Origins of Complex Multicellularity. *Annual Review of Earth and Planetary Sciences*. **39**(1),pp.217–239.

Kondo, Y. and Moffett, J.W. 2015. Iron redox cycling and subsurface offshore transport in the eastern tropical South Pacific oxygen minimum zone. *Marine Chemistry*. **168**,pp.95–103.

Konhauser, K.O., Hamade, T., Raiswell, R., Morris, R.C., Ferris, F.G., Southam, G. and Canfield, D.E. 2002. Could bacteria have formed the Precambrian banded iron formations? *Geology*. **30**(12),pp.1079–1082.

Konhauser, K.O., Lalonde, S.V., Amskold, L. and Holland, H.D. 2007. Was

there really an Archean Phosphate Crisis? *Science*. **315**(5816),p.1234.

Konhauser, K.O., Lalonde, S.V., Planavsky, N.J., Pecoits, E., Lyons, T.W., Mojzsis, S.J., Rouxel, O.J., Barley, M.E., Rosìere, C., Fralick, P.W., Kump, L.R. and Bekker, A. 2011. Aerobic bacterial pyrite oxidation and acid rock drainage during the Great Oxidation Event. *Nature*. **478**(7369),pp.369–373.

Kraal, P., Dijkstra, N., Behrends, T. and Slomp, C.P. 2017. Phosphorus burial in sediments of the sulfidic deep Black Sea: key roles for adsorption by calcium carbonate and apatite authigenesis. *Geochimica et Cosmochimica Acta*. **204**,pp.140–158.

Kraal, P. and Slomp, C.P. 2014. Rapid and extensive alteration of phosphorus speciation during oxic storage of wet sediment samples. *PloS one*. **9**(5),p.e96859.

Kraal, P., Slomp, C.P., Forster, A. and Kuypers, M.M.M. 2010. Phosphorus cycling from the margin to abyssal depths in the proto-Atlantic during oceanic anoxic event 2. *Palaeogeography, Palaeoclimatology, Palaeoecology*. **295**(1–2),pp.42–54.

Kraal, P., Slomp, C.P., Forster, A., Kuypers, M.M.M. and Sluijs, A. 2009. Pyrite oxidation during sample storage determines phosphorus fractionation in carbonate-poor anoxic sediments. *Geochimica et Cosmochimica Acta*. **73**(11),pp.3277–3290.

Kraal, P., Slomp, C.P., Reed, D.C., Reichart, G. and Poulton, S.W. 2012. Sedimentary phosphorus and iron cycling in and below the oxygen minimum zone of the northern Arabian Sea. *Biogeosciences*. **9**,pp.2603–2624.

Krachler, R., Jirsa, F. and Ayromlou, S. 2005. Factors influencing the dissolved iron input by river water to the open ocean. *Biogeosciences*. **2**(4),pp.311–315.

Krasnobaev, A.A., Puchkov, V.N., Kozlov, V.I., Sergeeva, N.D., Busharina, S. V and Lepekhina, E.N. 2013. Zirconology of Navysh volcanic rocks of the Ai Suite and the problem of the age of the Lower Riphean boundary in the Southern Urals. *Doklady Earth Sciences*. **448**(2),pp.185–190.

Krom, M.D. and Berner, R.A. 1981. The diagenese of phosphorus in a nearshore marine sediment. *Geochimica et Cosmochimica Acta*. **45**(1976),pp.207–216.

Kump, L.R. and Arthur, M.A. 1999. Interpreting carbon-isotope excursions: Carbonates and organic matter. *Chemical Geology*. **161**(1),pp.181–198.

Kump, L.R. and Barley, M.E. 2007. Increased subaerial volcanism and the rise of atmospheric oxygen 2.5 billion years ago. *Nature*. **448**(7157),pp.1033–1036.

Kump, L.R., Fallick, A.E., Melezhik, V.A., Strauss, H. and Lepland, A. 2013. The Great Oxidation Event *In*: V. A. Melezhik, A. R. Prave, A. E. Fallick, E. J. Hanski, A. Lepland, L. R. Kump and H. Strauss, eds. *Reading the archive of Earth's Oxygenation: Volume 3: Global Events and the Fennoscandian Arctic Russia - Drilling Early Earth Project*., pp. 1517–1533.

Kurzweil, F., Drost, K., Pašava, J., Wille, M., Taubald, H., Schoeckle, D. and Schoenberg, R. 2015. Coupled sulfur, iron and molybdenum isotope data from black shales of the Teplá-Barrandian unit argue against deep ocean oxygenation during the Ediacaran. *Geochimica et Cosmochimica Acta*. **171**,pp.121–142.

Kurzweil, F., Wille, M., Gantert, N., Beukes, N.J. and Schoenberg, R. 2016. Manganese oxide shuttling in pre-GOE oceans – evidence from molybdenum and iron isotopes. *Earth and Planetary Science Letters*. **452**,pp.69–78.

Kusky, T.M. and Li, J. 2003. Paleoproterozoic tectonic evolution of the North China Craton. *Journal of Asian Earth Sciences*. **22**(4),pp.383–397.

Kusky, T.M., Li, J. and Tucker, R.D. 2001. The Archean Dongwanzi Ophiolite Complex, North China Craton: 2.505-Billion-Year-Old Oceanic Crust and Mantle. *Science*. **292**(May),pp.1142–1145.

Kusky, T.M. and Santosh, M. 2009. The Columbia connection in North China. *Geological Society, London, Special Publications*. **323**,pp.49–71.

Kuznetsov, A.B., Bekker, A., Ovchinnikova, G.V., Gorokhov, I.M. and Vasilyeva, I.M. 2017. Unradiogenic strontium and moderate-amplitude carbon isotope variations in early Tonian seawater after the assembly of Rodinia and before the Bitter Springs Excursion. *Precambrian Research*. **298**,pp.157–173.

Kuznetsov, A.B., Ovchinnikova, G. V, Semikhatov, M.A., Gorokhov, I.M., Kaurova, O.K., Krupenin, M.T., Vasil'eva, I.M., Gorokhovskii, B.M. and Maslov, A. V 2008. The Sr isotopic characterization and Pb-Pb age of carbonate rocks from the Satka formation, the Lower Riphean Burzyan Group of the southern Urals. *Stratigraphy and Geological Correlation*. **16**(2),pp.120–137.

Kuznetsov, A.B., Semikhatov, M.A., Gorokhov, I.M., Mel'nikov, N.N., Konstantinova, G. V and Kutyavin, E.P. 2003. Sr isotope composition in carbonates of the Karatau Group, southern Urals, and standard curve of 87Sr/86Sr variations in the Late Riphean Ocean. *Stratigraphy and Geological Correlation*. **11**(5),pp.415–449.

Kuznetsov, A.B., Semikhatov, M.A., Maslov, A. V., Gorokhov, I.M., Prasolov, E.M., Krupenin, M.T. and Kislova, I. V. 2006. New data on Sr-and C-isotopic chemostratigraphy of the Upper Riphean type section (Southern Urals). *Stratigraphy and Geological Correlation*. **14**(6),pp.602–628.

Kuznetsov, N.B., Belousova, E.A., Romanyuk, T. V., Degtyarev, K.E., Maslov, A. V., Gorozhanin, V.M., Gorozhanina, E.N. and Pyzhova, E.S. 2017. First results of U/Pb dating of detrital zircons from middle Riphean sandstones of the Zigalga Formation, South Urals. *Doklady Earth Sciences*. **475**(2),pp.863–867.

Lamb, D.M., Awramik, S.M., Chapman, D.J. and Zhu, S. 2009. Evidence for eukaryotic diversification in the ~1800 million-year-old Changzhougou Formation, North China. *Precambrian Research*. **173**(1–4),pp.93–104.

Lang, X., Shen, B., Peng, Y., Huang, K., Lv, J. and Ma, H. 2016. Ocean oxidation during the deposition of basal Ediacaran Doushantuo cap carbonates in the Yangtze Platform, South China. *Precambrian Research*.

281,pp.253–268.

Lau, K. V., Macdonald, F.A., Maher, K. and Payne, J.L. 2017. Uranium isotope evidence for temporary ocean oxygenation in the aftermath of the Sturtian Snowball Earth. *Earth and Planetary Science Letters*. **458**,pp.282–292.

Lee, C., Love, G.D., Fischer, W.W., Grotzinger, J.P. and Halverson, G.P. 2015. Marine organic matter cycling during the Ediacaran Shuram excursion. *Geology*. **43**(12),p.G37236.1.

Lenton, T.M., Boyle, R.A., Poulton, S.W., Shields-Zhou, G.A. and Butterfield, N.J. 2014. Co-evolution of eukaryotes and ocean oxygenation in the Neoproterozoic era. *Nature Geoscience*. **7**(4),pp.257–265.

Lenton, T.M. and Watson, A.J. 2000. Redfield revisited 1. Regulation of nitrate, phosphate, and oxygen in the ocean. *Global Biogeochemical Cycles*. **14**(1),pp.225–248.

Lewis, B.L. and Landing, W.M. 1991. The biogeochemistry of manganese and iron in the Black Sea. *Deep Sea Research Part A. Oceanographic Research Papers*. **38**,pp.S773–S803.

Li, C., Love, G.D., Lyons, T.W., Fike, D.A., Sessions, A.L. and Chu, X. 2010. A stratified redox model for the Ediacaran ocean. *Science (New York, N.Y.)*. **328**(5974),pp.80–3.

Li, C., Planavsky, N.J., Love, G.D., Reinhard, C.T., Hardisty, D., Feng, L., Bates, S.M., Huang, J., Zhang, Q., Chu, X. and Lyons, T.W. 2015a. Marine redox conditions in the middle Proterozoic ocean and isotopic constraints on authigenic carbonate formation: Insights from the Chuanlinggou Formation, Yanshan Basin, North China. *Geochimica et Cosmochimica Acta*. **150**,pp.90–105.

Li, C., Planavsky, N.J., Shi, W., Zhang, Z., Zhou, C., Cheng, M., Tarhan, L.G., Luo, G. and Xie, S. 2015b. Ediacaran Marine Redox Heterogeneity and Early Animal Ecosystems. *Scientific Reports*. **5**,pp.1–8.

Li, H., Li, H. and Lu, S. 1995. Grain zircon U Pb ages for volcanic rocks from Tuanshanzi Formation of Changcheng system and their geological implication. *Geochimica*. **24**(1),pp.43–48.

Li, H.K., Zhu, S.X., Xiang, Z.Q., Su, W.B., Lu, S.N., Zhou, H.Y., Geng, J.Z., Li, S. and Yang, F.J. 2010. Zircon U-Pb dating on tuff bed from Gaoyuzhuang Formation in Yanqing, Beijing: Further constraints on the new subdivision of the Mesoproterozoic stratigraphy in the northern North China Craton. *Acta Petrologica Sinica*. **26**(7),pp.2131–2140.

Li, Z.X.A. and Lee, C.T.A. 2004. The constancy of upper mantle fO2 through time inferred from V/Sc ratios in basalts. *Earth and Planetary Science Letters*. **228**(3–4),pp.483–493.

Little, S.H., Vance, D., Lyons, T.W. and McManus, J. 2015. Controls on trace metal authigenic enrichment in reducing sediments: Insights from modern oxygen-deficient settings. *American Journal of Science*. **315**(2),pp.77–119.

Liu, A.G., McIlroy, D. and Brasier, M.D. 2010. First evidence for locomotion in the Ediacara biota from the 565 Ma Mistaken Point Formation, Newfoundland. *Geology*. **38**(2),pp.123–126.

Logan, G. a., Summons, R.E. and Hayes, J.M. 1997. An isotopic biogeochemical study of Neoproterozoic and Early Cambrian sediments from the Centralian Superbasin, Australia. *Geochimica et Cosmochimica Acta*. **61**(24),pp.5391–5409.

Logan, G.A., Hayes, J.M., Hieshima, G.B. and Summons, R.E. 1995. Terminal Proterozoic reorganization of biogeochemical cycles. *Nature*. **376**,pp.53–56.

Love, G.D., Grosjean, E., Stalvies, C., Fike, D.A., Grotzinger, J.P., Bradley, A.S., Kelly, A.E., Bhatia, M., Meredith, W., Snape, C.E., Bowring, S. a, Condon, D.J. and Summons, R.E. 2009. Fossil steroids record the appearance of Demospongiae during the Cryogenian period. *Nature*. **457**(7230),pp.718–721.

Lovley, D. 2000. Fe(III) and Mn(IV) Reduction *In*: *Environmental Microbe-Metal Interactions*., pp. 3–30.

Lu, S., Zhao, G., Wang, H. and Hao, G. 2008. Precambrian metamorphic basement and sedimentary cover of the North China Craton: A review. *Precambrian Research*. **160**(1–2),pp.77–93.

Lu, S.N. and Li, H.M. 1991. A precise U–Pb single zircon age determination for the volcanics of the Dahongyu Formation, Changcheng System in Jixian. *Bulletin of Chinese Academia Geologica Scientia*. **22**,pp.137–145.

Lubnina, N. V., Pisarevsky, S.A., Bogdanova, S. V. and Sokolov, S.J. 2016. Late Paleoproterozoic Paleogeography of Baltica and Laurentia: New Paleomagnetic Data from 1.80–1.75 Ga Mafic Intrusions of Fennoscandia and Sarmatia. *Acta Geologica Sinica*. **90**(July),p.37.

Luo, G., Junium, C.K., Kump, L.R., Huang, J., Li, C., Feng, Q., Shi, X., Bai, X. and Xie, S. 2014. Shallow stratification prevailed for ~1700 to ~1300 Ma ocean: Evidence from organic carbon isotopes in the North China Craton. *Earth and Planetary Science Letters*. **400**,pp.219–232.

Lyons, T.W., Anbar, A.D., Severmann, S., Scott, C. and Gill, B.C. 2009. Tracking Euxinia in the Ancient Ocean: A Multiproxy Perspective and Proterozoic Case Study. *Annual Review of Earth and Planetary Sciences*. **37**,pp.507–534.

Lyons, T.W., Luepke, J.J., Schreiber, M.E. and Zieg, G.A. 2000. Sulfur geochemical constraints on Mesoproterozoic restricted marine deposition: Lower Belt Supergroup, northwestern United States. *Geochimica et Cosmochimica Acta*. **64**(3),pp.427–437.

Lyons, T.W., Reinhard, C.T. and Planavsky, N.J. 2014. The rise of oxygen in Earth's early ocean and atmosphere. *Nature*. **506**(7488),pp.307–315.

Lyons, T.W. and Severmann, S. 2006. A critical look at iron paleoredox proxies: New insights from modern euxinic marine basins. *Geochimica et Cosmochimica Acta*. **70**(23),pp.5698–5722.

Mapstone, N.B. and McIlroy, D. 2006. Ediacaran fossil preservation: Taphonomy and diagenesis of a discoid biota from the Amadeus Basin, central Australia. *Precambrian Research*. **149**(3–4),pp.126–148.

Martin, J.H. 1990. Glacial-interglacial CO2 change: The Iron Hypothesis. *Paleoceanography*. **5**(1),pp.1–13.

Martin, J.H., Knauer, G.A., Karl, D.M. and Broenkow, W.W. 1987. VERTEX: carbon cycling in the northeast Pacific. *Deep Sea Research Part A, Oceanographic Research Papers*. **34**(2),pp.267–285.

Martin, M.W. 2000. Age of Neoproterozoic Bilatarian Body and Trace Fossils, White Sea, Russia: Implications for Metazoan Evolution. *Science*. **288**(5467),pp.841–845.

März, C., Poulton, S.W., Beckmann, B., Küster, K., Wagner, T. and Kasten, S. 2008. Redox sensitivity of P cycling during marine black shale formation: Dynamics of sulfidic and anoxic, non-sulfidic bottom waters. *Geochimica et Cosmochimica Acta*. **72**(15),pp.3703–3717.

März, C., Poulton, S.W., Wagner, T., Schnetger, B. and Brumsack, H.J. 2014. Phosphorus burial and diagenesis in the central Bering Sea (Bowers Ridge, IODP Site U1341): Perspectives on the marine P cycle. *Chemical Geology*. **363**,pp.270–282.

März, C., Riedinger, N., Sena, C. and Kasten, S. 2018. Phosphorus dynamics around the sulphate-methane transition in continental margin sediments: Authigenic apatite and Fe(II) phosphates. *Marine Geology*. **404**(March),pp.84–96.

Maslov, A.V., Erdtmann, B.-D., Ivanov, K.S., Ivanov, S.N. and Krupenin, M.T. 1997. The main tectonic events, depositional history, and the palaeogeography of the southern Urals during the Riphean-early Palaeozoic. *Tectonophysics*. **276**(1–4),pp.313–335.

Maslov, A.V., Grazhdankin, D.V., Podkovyrov, V.N., Ronkin, Y.L. and Lepikhina, O.P. 2008. Composition of sediment provenances and patterns in geological history of the Late Vendian Mezen Basin. *Lithology and Mineral Resources*. **43**(3),pp.260–280.

Maslov, A.V., Podkovyrov, V.N. and Gareev, E.Z. 2012. Evolution of the paleogeodynamic settings of the formation of the Lower and Middle Riphean sedimentary sequences of the Uchur-Maya region and the Bashkir meganticlinorium. *Russian Journal of Pacific Geology*. **6**(5),pp.382–394.

Maslov, A. V 2002. Facies Associations of Riphean Sedimentary Sequences. *Lithology and Mineral Resources*. **37**(5),pp.462–474.

Maslov, A. V 2004. Riphean and Vendian sedimentary sequences of the Timanides and Uralides, the eastern periphery of the East European Craton. *Geological Society, London, Memoirs*. **30**(1),pp.19–35.

Maslov, A.V., Gareev, E.Z. and Podkovyrov, V.N. 2010. Upper Riphean and Vendian sandstones of the Bashkirian anticlinorium. *Lithology and Mineral Resources*. **45**(September 2015),pp.285–301.

Maslov, A.V. and Isherskaya, M.V. 2006. Variations of Eu/Eu* ratio in Vendian shales of the Volga-Ural region and the boundary traced between the Redkino and Kotlin Horizons. *Stratigraphy and Geological Correlation*. **14**(3),pp.275–282.

McCall, G.J.H. 2006. The Vendian (Ediacaran) in the geological record: Enigmas in geology's prelude to the Cambrian explosion. *Earth-Science Reviews*. **77**(1–3),pp.1–229.

McFadden, K.A., Huang, J., Chu, X., Jiang, G., Kaufman, A.J., Zhou, C., Yuan, X. and Xiao, S. 2008. Pulsed oxidation and biological evolution in the Ediacaran Doushantuo Formation. *Proceedings of the National Academy of Sciences*. **105**(9),pp.3197–3202.

McLennan, S.M. 2001. Relationships between the trace element composition of sedimentary rocks and upper continental crust. *Geochemistry, Geophysics, Geosystems*. **2**(4),pp.1–30.

Mei, M. 2008. Sedimentary features and Implications for the Precambrian Non-srtromatolitic Carbonate Succession: A Case Study of the Mesoproterozoic Gaoyuzhuang formation at the Qiangoa Section in Yanqing County of Beijing. *Acta Geologica Sinica*. **82**(2),pp.295–309.

Mei, M., Gao, J. and Meng, Q. 2009. MISS in Mesoproterozoic Nonstromatolitic Limestones: A Case Study of the Third Member of Gaoyuzhuang Formation at Qiangou Section in Beijing. *Earth Science Frontiers*. **16**(5),pp.207–218.

Mei, M., Meng, Q. and Gao, J. 2007. Microbial Sand Chips in Transgressive Sandstones of the Precambrian: An Example from the Late Paleoproterozoic Dahongyu Formation at the Huyu Section of Nankou Town, Beijing, China. *Earth Science Frontiers*. **14**(2),pp.197–204.

Mei, M. and Tucker, M. 2011. Molar Tooth Structure: a Contribution from the Mesoproterozoic Gaoyuzhuang Formation, Tianjin City, North China. *Acta Geologica Sinica*. **85**(5),pp.1084–1099.

Meng, Q.-R., Wei, H.-H., Qu, Y.-Q. and Ma, S.-X. 2011. Stratigraphic and sedimentary records of the rift to drift evolution of the northern North China craton at the Paleo- to Mesoproterozoic transition. *Gondwana Research*. **20**(1),pp.205–218.

Mens, K. and Pirrus, E. 1986. Stratigraphical characteristics and development of Vendian-Cambrian boundary beds on the East European Platform. *Geological Magazine*. **123**(4),pp.357–360.

Meyer, K.M. and Kump, L.R. 2008. Oceanic Euxinia in Earth History: Causes and Consequences. *Annual Review of Earth and Planetary Sciences*. **36**(1),pp.251–288.

Meyers, S.R. 2007. Production and preservation of organic matter: The significance of iron. *Paleoceanography*. **22**(4),p.n/a-n/a.

Miller, A.J., Strauss, J. V., Halverson, G.P., Macdonald, F.A., Johnston, D.T. and Sperling, E.A. 2017. Tracking the onset of Phanerozoic-style redox-sensitive trace metal enrichments: New results from basal Ediacaran post-glacial strata in NW Canada. *Chemical Geology*. **457**,pp.24–37.

Mills, D.B. and Canfield, D.E. 2014. Oxygen and animal evolution: Did a rise of atmospheric oxygen ‘trigger’ the origin of animals? *BioEssays*. **36**(12),pp.1145–1155.

Mills, D.B., Ward, L.M., Jones, C., Sweeten, B., Forth, M., Treusch, A.H. and Canfield, D.E. 2014. Oxygen requirements of the earliest animals. *Proceedings of the National Academy of Sciences of the United States of America*. **111**(11),pp.4168–72.

Mojzsis, S.J., Harrison, T.M. and Pidgeon, R.T. 2001. Oxygen-isotope evidence

from ancient zircons for liquid water at the Earth’s surface 4,300[thinsp]Myr ago. *Nature*. **409**(6817),pp.178–181.

Moore, K.R., Bosak, T., Macdonald, F.A., Lahr, D.J.G., Newman, S., Settens, C. and Pruss, S.B. 2017. Biologically agglutinated eukaryotic microfossil from Cryogenian cap carbonates. *Geobiology*. (June 2016),pp.499–515.

Morford, J.L. and Emerson, S. 1999. The geochemistry of redox sensitive trace metals in sediments. *Geochimica et Cosmochimica Acta*. **63**(11–12),pp.1735–1750.

Morford, J.L., Emerson, S.R., Breckel, E.J. and Kim, S.H. 2005. Diagenesis of oxyanions (V, U, Re, and Mo) in pore waters and sediments from a continental margin. *Geochimica et Cosmochimica Acta*. **69**(21),pp.5021–5032.

Morford, J.L., Martin, W.R., François, R. and Carney, C.M. 2009. A model for uranium, rhenium, and molybdenum diagenesis in marine sediments based on results from coastal locations. *Geochimica et Cosmochimica Acta*. **73**(10),pp.2938–2960.

Morin, G., Mangeret, A., Othmane, G., Stetten, L., Seder-Colomina, M., Brest, J., Ona-Nguema, G., Bassot, S., Courbet, C., Guillevic, J., Thouvenot, A., Mathon, O., Proux, O. and Bargar, J.R. 2016. Mononuclear U(IV) complexes and ningyoite as major uranium species in lake sediments. *Geochemical Perspectives Letters*. (Iv),pp.95–105.

Morris, A.W. 1975. Dissolved molybdenum and vanadium in the northeast Atlantic Ocean. *Dee*. **22**,pp.49–54.

Mort, H.P., Slomp, C.P., Gustafsson, B.G. and Andersen, T.J. 2010. Phosphorus recycling and burial in Baltic Sea sediments with contrasting redox conditions. *Geochimica et Cosmochimica Acta*. **74**(4),pp.1350–1362.

Mucci, A. 2004. The behavior of mixed Ca-Mn carbonates in water and seawater: Controls of manganese concentrations in marine porewaters. *Aquatic Geochemistry*. **10**(1–2),pp.139–169.

Mukherjee, I. and Large, R.R. 2016. Pyrite trace element chemistry of the Velkerri Formation, Roper Group, McArthur Basin: Evidence for atmospheric oxygenation during the Boring Billion. *Precambrian Research*. **281**,pp.13–26.

Muscente, A.D., Boag, T.H., Bykova, N. and Schiffbauer, J.D. 2018. Environmental disturbance, resource availability, and biologic turnover at the dawn of animal life. *Earth-Science Reviews*. **177**(November 2017),pp.248–264.

Myrow, P.M. 1995. Neoproterozoic rocks of the Newfoundland Avalon Zone. *Precambrian Research*. **73**(1–4),pp.123–136.

Nagy, R.M., Porter, S.M., Dehler, C.M. and Shen, Y. 2009. Biotic turnover driven by eutrophication before the Sturtian low-latitude glaciation. *Nature Geoscience*. **2**(6),pp.415–418.

Narbonne, G.M. 2004. Modular construction of early Ediacaran complex life forms. *Science*. **305**(5687),pp.1141–1144.

Narbonne, G.M. 2005. THE EDIACARA BIOTA: Neoproterozoic Origin of

Animals and Their Ecosystems. *Annual Review of Earth and Planetary Sciences*. **33**(1),pp.421–442.

Narbonne, G.M. and Gehling, J.G. 2003. Life after snowball: The oldest complex Ediacaran fossils. *Geology*. **31**(1),pp.27–30.

Narbonne, G.M., Kaufman, A.J. and Knoll, A.H. 1994. Integrated chemostratigraphy and biostratigraphy of the Windermere Supergroup, northwestern Canada: implications for Neoproterozoic correlations and the early evolution of animals. *Geological Society of America Bulletin*. **106**(10),pp.1281–1292.

Nealson, K.H. and Saffarini, D. 1994. Iron and Manganese in Anaerobic Respiration: Environmental Significance, Physiology, and Regulation. *Annual Review of Microbiology*. **48**(1),pp.311–343.

Newton, R. and Bottrell, S. 2007. Stable isotopes of carbon and sulphur as indicators of environmental change: past and present. *Journal of the Geological Society*. **164**(4),pp.691–708.

Ni, J., Lin, P., Zhen, Y., Yao, X. and Guo, L. 2015. Distribution, source and chemical speciation of phosphorus in surface sediments of the central Pacific Ocean. *Deep-Sea Research Part I: Oceanographic Research Papers*. **105**(November 2015),pp.74–82.

Nikishin, A.M., Ziegler, P.A., Stephenson, R.A., Cloetingh, S., Furne, A. V, Fokin, P.A., Ershov, A. V., Bolotov, S.N., Korotaev, M. V., Alekseev, A.S., Gorbachev, V.I., Shipilov, E. V, Lankreijer, A., Bembinova, E.Y. and Shalimov, I. V 1996. Late Precambrian to Triassic history of the East European Craton: dynamics of sedimentary basin evolution. *Tectonophysics*. **268**,pp.23–63.

Noffke, N. and Awramik, S.M. 2011. Stromatolites and MISS — Differences between relatives. *GSA Today*. **23**(9),pp.4–9.

Och, L.M., Müller, B., März, C., Wichser, A., Vologina, E.G. and Sturm, M. 2016. Elevated uranium concentrations in Lake Baikal sediments: Burial and early diagenesis. *Chemical Geology*. **441**,pp.92–105.

Och, L.M. and Shields-Zhou, G. a. 2012. The Neoproterozoic oxygenation event: Environmental perturbations and biogeochemical cycling. *Earth-Science Reviews*. **110**(1–4),pp.26–57.

Olson, S.L., Kump, L.R. and Kasting, J.F. 2013. Quantifying the areal extent and dissolved oxygen concentrations of Archean oxygen oases. *Chemical Geology*. **362**,pp.35–43.

Ovchinnikova, G.V., Kuznetsov, A.B., Vasil'eva, I.M., Gorokhov, I.M., Krupenin, M.T., Gorokhovskii, B.M. and Maslov, A.V. 2013. Pb-Pb age and Sr isotopic characteristic of the Middle Riphean phosphorite concretions: The Zigaza-Komarovo Formation of the South Urals. *Doklady Earth Sciences*. **451**(4),pp.798–802.

Ovchinnikova, G. V, Vasil'eva, I.M., Semikhatov, M.A., Gorokhov, I.M., Kuznetsov, A.B., Gorokhovskii, B.M. and Levskii, L.K. 2000. The Pb-Pb trail dating of carbonates with open U-Pb systems: The Min'yar Formation of the Upper Riphean stratotype, southern Urals. *Stratigraphy and Geological Correlation*. **8**(6),pp.529–543.

Papineau, D. 2010. Global biogeochemical changes at both ends of the proterozoic: insights from phosphorites. *Astrobiology*. **10**(2),pp.165–181.

Papineau, D., Mojzsis, S.J. and Schmitt, A.K. 2007. Multiple sulfur isotopes from Paleoproterozoic Huronian interglacial sediments and the rise of atmospheric oxygen. *Earth and Planetary Science Letters*. **255**(1–2),pp.188–212.

Parfrey, L.W., Lahr, D.J.G., Knoll, A.H. and Katz, L.A. 2011. Estimating the timing of early eukaryotic diversification with multigene molecular clocks. *Proceedings of the National Academy of Sciences*. **108**(33),pp.13624–13629.

Parnell, J., Spinks, S., Andrews, S., Thayalan, W. and Bowden, S. 2015. High Molybdenum availability for evolution in a Mesoproterozoic lacustrine environment. *Nature Communications*. **6**(May),p.6996.

Partin, C.A., Bekker, A., Planavsky, N.J. and Lyons, T.W. 2015. Euxinic conditions recorded in the ca. 1.93 Ga Bravo Lake Formation, Nunavut (Canada): Implications for oceanic redox evolution. *Chemical Geology*. **417**,pp.148–162.

Partin, C.A., Bekker, A., Planavsky, N.J., Scott, C.T., Gill, B.C., Li, C., Podkovyrov, V., Maslov, A., Konhauser, K.O., Lalonde, S. V., Love, G.D., Poulton, S.W. and Lyons, T.W. 2013. Large-scale fluctuations in Precambrian atmospheric and oceanic oxygen levels from the record of U in shales. *Earth and Planetary Science Letters*. **369**–**370**,pp.284–293.

Pasek, M.A., Gull, M. and Herschy, B. 2017. Phosphorylation on the early earth. *Chemical Geology*. **475**(August),pp.149–170.

Peng, X., Guo, Z., House, C.H., Chen, S. and Ta, K. 2016. SIMS and NanoSIMS analyses of well-preserved microfossils imply oxygen-producing photosynthesis in the Mesoproterozoic anoxic ocean. *Chemical Geology*. **441**,pp.24–34.

Peng, Y., Bao, H. and Yuan, X. 2009. New morphological observations for Paleoproterozoic acritarchs from the Chuanlinggou Formation, North China. *Precambrian Research*. **168**,pp.223–232.

Penny, A.M., Wood, R., Curtis, A., Bowyer, F., Tostevin, R. and Hoffman, K.H. 2014. Ediacaran metazoan reefs from the Nama Group, Namibia. *Science*. **344**(6191),pp.1504–1506.

Perkins, R.B. and Mason, C.E. 2015. The relative mobility of trace elements from short-term weathering of a black shale. *Applied Geochemistry*. **56**,pp.67–79.

Pirrus, E. 1992. Freshening of the Late Vendian Basin on the East European Craton. *Proceedings of the Estonian Academy of Sciences, Geology*. **41**(3),pp.115–123.

Pirrus, E. 1993. Sedimentological and Paleogeographic aspects of the Vendian-Cambrian Transition on the East European Platform. *Proceedings of the Estonian Academy of Sciences, Geology*. **42**(4),pp.141–147.

Planavsky, N.J. 2014. The elements of marine life. *Nature Geoscience*. **7**(12),pp.855–856.

Planavsky, N.J., Asael, D., Hofmann, A., Reinhard, C.T., Lalonde, S. V., Knudsen, A., Wang, X., Ossa Ossa, F., Pecoits, E., Smith, A.J.B., Beukes, N.J., Bekker, A., Johnson, T.M., Konhauser, K.O., Lyons, T.W. and Rouxel, O.J. 2014b. Evidence for oxygenic photosynthesis half a billion years before the Great Oxidation Event. *Nature Geoscience*. **7**(4),pp.283–286.

Planavsky, N.J., Cole, D.B., Reinhard, C.T., Diamond, C., Love, G.D., Luo, G., Zhang, S., Konhauser, K.O. and Lyons, T.W. 2016. No evidence for high atmospheric oxygen levels 1,400 million years ago. *Proceedings of the National Academy of Sciences*. **113**(19),pp.E2550–E2551.

Planavsky, N.J., McGoldrick, P., Scott, C.T., Li, C., Reinhard, C.T., Kelly, A.E., Chu, X., Bekker, A., Love, G.D. and Lyons, T.W. 2011. Widespread iron-rich conditions in the mid-Proterozoic ocean. *Nature*. **477**(7365),pp.448–451.

Planavsky, N.J., Reinhard, C.T., Wang, X., Thomson, D., Mcgoldrick, P., Rainbird, R.H., Johnson, T.M., Fischer, W.W. and Lyons, T.W. 2014a. Low Mid-Proterozoic atmospheric oxygen levels and the delayed rise of Animals. *Science*. **346**(6209),pp.635–638.

Planavsky, N.J., Rouxel, O.J., Bekker, A., Lalonde, S. V, Konhauser, K.O., Reinhard, C.T. and Lyons, T.W. 2010. The evolution of the marine phosphate reservoir. *Nature*. **467**(7319),pp.1088–90.

Planavsky, N.J., Slack, J.F., Cannon, W.F., O'Connell, B., Isson, T.T., Asael, D., Jackson, J.C., Hardisty, D.S., Lyons, T.W. and Bekker, A. 2018. Evidence for episodic oxygenation in a weakly redox-buffered deep mid-Proterozoic ocean. *Chemical Geology*. **483**,pp.581–594.

Podkovyrov, V.N., Grazhdankin, D. V and Maslov, A. V 2011. Lithogeochemistry of the Vendian Fine-Grained Clastic Rocks in the Southern Vychegda Trough. *Lithology and Mineral Resources*. **46**(5),pp.427–446.

Podkovyrov, V.N., Maslov, A. V., Kuznetsov, A.B. and Ershova, V.B. 2017. Lithostratigraphy and geochemistry of Upper Vendian–Lower Cambrian deposits in the northeastern Baltic monocline. *Stratigraphy and Geological Correlation*. **25**(1),pp.1–20.

Pogge von Strandmann, P.A.E., Stüeken, E.E., Elliott, T., Poulton, S.W., Dehler, C.M., Canfield, D.E. and Catling, D.C. 2015. Selenium isotope evidence for progressive oxidation of the Neoproterozoic biosphere. *Nature Communications*. **6**,p.10157.

Porter, S.M., Meisterfeld, R. and Knoll, A.H. 2003. Vase-Shaped Microfossils From the Neoproterozoic Chuar Group, Grand Canyon: a Classification Guided By Modern Testate Amoebae. *Journal of Paleontology*. **77**(3),pp.409–429.

Posth, N.R., Canfield, D.E. and Kappler, a. 2014. Biogenic Fe(III) minerals: From formation to diagenesis and preservation in the rock record. *Earth-Science Reviews*. **135**,pp.103–121.

Poulton, S.W. 2017. Biogeochemistry: Early phosphorus redigested. *Nature Geoscience*. **10**(2),pp.75–76.

Poulton, S.W. and Canfield, D.E. 2006. Co-diagenesis of iron and phosphorus in hydrothermal sediments from the southern East Pacific Rise: Implications for the evaluation of paleoseawater phosphate concentrations. *Geochimica et Cosmochimica Acta*. **70**(23),pp.5883–5898.

Poulton, S.W. and Canfield, D.E. 2005. Development of a sequential extraction procedure for iron: implications for iron partitioning in continentally derived particulates. *Chemical Geology*. **214**(3–4),pp.209–221.

Poulton, S.W. and Canfield, D.E. 2011. Ferruginous Conditions: A Dominant Feature of the Ocean through Earth's History. *Elements*. **7**(2),pp.107–112.

Poulton, S.W., Fralick, P.W. and Canfield, D.E. 2010. Spatial variability in oceanic redox structure 1.8 billion years ago. *Nature Geoscience*. **3**(7),pp.486–490.

Poulton, S.W., Fralick, P.W. and Canfield, D.E. 2004a. The transition to a sulphidic ocean ~1.84 billion years ago. *Nature*. **431**(September),pp.173–177.

Poulton, S.W., Henkel, S., März, C., Urquhart, H., Flögel, S., Kasten, S., Sinninghe Damsté, J.S. and Wagner, T. 2015. A continental-weathering control on orbitally driven redox-nutrient cycling during Cretaceous oceanic anoxic event 2. *Geology*. **43**(11),pp.963–966.

Poulton, S.W., Krom, M.D. and Raiswell, R. 2004b. A revised scheme for the reactivity of iron (oxyhydr)oxide minerals towards dissolved sulfide. *Geochimica et Cosmochimica Acta*. **68**(18),pp.3703–3715.

Poulton, S.W. and Raiswell, R. 2005. Chemical and physical characteristics of iron oxides in riverine and glacial meltwater sediments. *Chemical Geology*. **218**(3–4),pp.203–221.

Poulton, S.W. and Raiswell, R. 2002. The low-temperature geochemical cycle of iron: From continental fluxes to marine sediment deposition. *American Journal of Science*. **302**(9),pp.774–805.

Powell, R.T. and Wilson-Finelli, A. 2003. Importance of organic Fe complexing ligands in the Mississippi River plume. *Estuarine, Coastal and Shelf Science*. **58**(4),pp.757–763.

Puchkov, V.N. 1997. Structure and geodynamics of the Uralian orogen. *Geological Society, London, Special Publications*. **121**(121),pp.201–236.

Puchkov, V.N., Bogdanova, S. V., Ernst, R.E., Kozlov, V.I., Krasnobaev, A.A., Söderlund, U., Wingate, M.T.D., Postnikov, A. V. and Sergeeva, N.D. 2013. The ca. 1380Ma Mashak igneous event of the Southern Urals. *Lithos*. **174**,pp.109–124.

Qu, Y., Wang, J., Xiao, S., Whitehouse, M., Engdahl, A., Wang, G. and McLoughlin, N. 2017. Carbonaceous biosignatures of diverse chemotrophic microbial communities from chert nodules of the Ediacaran Doushantuo Formation. *Precambrian Research*. **290**,pp.184–196.

Qu, Y., Zhu, S., Whitehouse, M., Engdahl, A. and McLoughlin, N. 2018. Carbonaceous biosignatures of the earliest putative macroscopic multicellular eukaryotes from 1630 Ma Tuanshanzi Formation, north China. *Precambrian Research*. **304**(June 2017),pp.99–109.

Raiswell, R. and Canfield, D.E. 1996. Rates of reaction between silicate iron and dissolved sulfide in Peru Margin sediments. *Geochimica et Cosmochimica Acta*. **60**(15),pp.2777–2787.

Raiswell, R. and Canfield, D.E. 1998. Sources of iron for pyrite formation in marine sediments. *American Journal of Science*. **298**(3),pp.219–245.

Raiswell, R. and Canfield, D.E. 2012. The Iron Biogeochemical Cycle Past and Present. *Geochemical Perspectives*. **1**(1),pp.1–220.

Raiswell, R., Canfield, D.E. and Berner, R.A. 1994. A comparison of iron extraction methods for the determination of degree of pyritisation and the recognition of iron-limited pyrite formation. *Chemical Geology*. **111**,pp.101–110.

Raiswell, R., Newton, R., Bottrell, S.H., Coburn, P.M., Briggs, D.E.G., Bond, D.P.G. and Poulton, S.W. 2008. Turbidite depositional influences on the diagenesis of Beecher's Trilobite Bed and the Hunsrück Slate; sites of soft tissue pyritization. *American Journal of Science*. **308**(2),pp.105–129.

Raiswell, R., Tranter, M., Benning, L.G., Siegert, M., De'ath, R., Huybrechts, P. and Payne, T. 2006. Contributions from glacially derived sediment to the global iron (oxyhydr)oxide cycle: Implications for iron delivery to the oceans. *Geochimica et Cosmochimica Acta*. **70**(11),pp.2765–2780.

Rasmussen, B., Fletcher, I.R., Brocks, J.J. and Kilburn, M.R. 2008. Reassessing the first appearance of eukaryotes and cyanobacteria. *Nature*. **455**(7216),pp.1101–1104.

Redfield, A.C. 1958. The biological control of chemical factors in the environment. *American Scientist*. **46**(3),pp.205–221.

Reed, D.C., Slomp, C.P. and Gustafsson, B.G. 2011. Sedimentary phosphorus dynamics and the evolution of bottom-water hypoxia: A coupled benthic-pelagic model of a coastal system. *Limnology and Oceanography*. **56**(3),pp.1075–1092.

Reimink, J.R., Davies, J.H.F.L., Chacko, T., Stern, R.A., Heaman, L.M., Sarkar, C., Schaltegger, U., Creaser, R.A. and Pearson, D.G. 2016. No evidence for Hadean continental crust within Earth's oldest evolved rock unit. *Nature Geoscience*. **9**(10),pp.777–780.

Reinhard, C.T., Planavsky, N.J., Gill, B.C., Ozaki, K., Robbins, L.J., Lyons, T.W., Fischer, W.W., Wang, C., Cole, D.B. and Konhauser, K.O. 2016a. Evolution of the global phosphorus cycle. *Nature*.

Reinhard, C.T., Planavsky, N.J., Olson, S.L., Lyons, T.W. and Erwin, D.H. 2016b. Earth's oxygen cycle and the evolution of animal life. *Proceedings of the National Academy of Sciences*. **113**(32),pp.8933–8938.

Reinhard, C.T., Planavsky, N.J., Robbins, L.J., Partin, C.A., Gill, B.C., Lalonde, S. V, Bekker, A., Konhauser, K.O. and Lyons, T.W. 2013. Proterozoic ocean redox and biogeochemical stasis. *Proceedings of the National Academy of Sciences of the United States of America*. **110**,pp.5357–62.

Reinhard, C.T., Planavsky, N.J., Wang, X., Fischer, W.W., Johnson, T.M. and Lyons, T.W. 2014. The isotopic composition of authigenic chromium in anoxic marine sediments : A case study from the Cariaco Basin. *Earth and Planetary Science Letters*. **407**,pp.9–18.

Retallack, G.J. 2016. Ediacaran sedimentology and paleoecology of Newfoundland reconsidered. *Sedimentary Geology*. **333**,pp.15–31.

Rickard, D. and Luther, G.W. 2007. *Chemistry of iron sulfides*.

Riding, R., Fralick, P. and Liang, L. 2014. Identification of an Archean marine oxygen oasis. *Precambrian Research*. **251**,pp.232–237.

Rijkenberg, M.J.A., Middag, R., Laan, P., Gerringa, L.J.A., Van Aken, H.M., Schoemann, V., De Jong, J.T.M. and De Baar, H.J.W. 2014. The distribution of dissolved iron in the West Atlantic Ocean. *PLoS ONE*. **9**(6),pp.1–14.

Robbins, L.J., Lalonde, S. V., Planavsky, N.J., Partin, C.A., Reinhard, C.T., Kendall, B., Scott, C., Hardisty, D.S., Gill, B.C., Alessi, D.S., Dupont, C.L., Saito, M.A., Crowe, S.A., Poulton, S.W., Bekker, A., Lyons, T.W. and Konhauser, K.O. 2016. Trace elements at the intersection of marine biological and geochemical evolution. *Earth-Science Reviews*. **163**,pp.323–345.

Rogers, J.J.W. and Santosh, M. 2002. Configuration of Columbia, a Mesoproterozoic Supercontinent. *Gondwana Research*. **5**(1),pp.5–22.

Rogov, V., Marusin, V., Bykova, N., Goy, Y., Nagovitsin, K., Kochnev, B., Karlova, G. and Grazhdankin, D. 2012. The oldest evidence of bioturbation on Earth. *Geology*. **40**(5),pp.395–398.

Romanyuk, T.V., Maslov, A.V., Kuznetsov, N.B., Belousova, E.A., Ronkin, Y.L.Y., Krupenin, M.T., Gorozhanin, V.M., Gorozhanina, E.N. and Seregina, E.S. 2013. First data on LA-ICP-MS U/Pb zircon geochronology of Upper Riphean sandstones of the Bashkir Anticlinorium (South Urals). *Doklady Earth Sciences*. **452**(2),pp.997–1000.

Ronkin, Y.L., Maslov, A. V, Kazak, A.P., Matukov, D.I. and Lepikhina, O.P. 2007. The Lower-Middle Riphean boundary in the southern Urals: new isotopic U-Pb (SHRIMP II) constraints. *Doklady Earth Sciences*. **415**(2),pp.835–840.

Rosing, M.T. and Frei, R. 2004. U-rich Archaean sea-floor sediments from Greenland - indications of > 3700 Ma oxygenic photosynthesis. *Earth and Planetary Science Letters*. **217**(3–4),pp.237–244.

Ross, G.M., Bloch, J.D. and Krouse, H.R. 1995. Neoproterozoic strata of the southern Canadian Cordillera and the isotopic evolution of seawater sulfate. *Precambrian Research*. **73**(1–4),pp.71–99.

Rothman, D.H., Hayes, J.M. and Summons, R.E. 2003. Dynamics of the Neoproterozoic carbon cycle. *Proceedings of the National Academy of Sciences*. **100**(14),pp.8124–8129.

Ruttenberg, K.C. 1992. Development of a sequential extraction method for different forms of phosphorus in marine sediments. *Limnology and Oceanography*. **37**(7),pp.1460–1482.

Ruttenberg, K.C. 1993. Reassessment of the oceanic residence time of phosphorus. *Chemical Geology*. **107**(3–4),pp.405–409.

Ruttenberg, K.C. 2003. The Global Phosphorus Cycle. *Treatise on Geochemistry*. **8**,pp.585–643.

Ruttenberg, K.C. and Berner, R.A. 1993. Authigenic apatite formation and burial in sediments from non-upwelling, continental margin environments. *Geochimica et Cosmochimica Acta*. **57**(5),pp.991–1007.

Ruttenberg, K.C. and Goñi, M. 1997. Depth Trends in Phosphorus Distribution and C:N:P Ratios of Organic Matter in Amazon Fan Sediments: Indices of Organic Matter Source and Burial History. *Proceedings of the Ocean Drilling Program, Scientific Results*. **155**,pp.505–517.

Ryba, S.A. and Burgess, R.M. 2002. Effects of sample preparation on the measurement of organic carbon, hydrogen, nitrogen, sulfur, and oxygen concentrations in marine sediments. *Chemosphere*. **48**,pp.139–147.

Sahoo, S.K., Planavsky, N.J., Jiang, G., Kendall, B., Owens, J.D., Wang, X., Shi, X., Anbar, A.D. and Lyons, T.W. 2016. Oceanic oxygenation events in the anoxic Ediacaran ocean. *Geobiology*. **14**(5),pp.457–468.

Sahoo, S.K., Planavsky, N.J., Kendall, B., Wang, X., Shi, X., Scott, C., Anbar, A.D., Lyons, T.W. and Jiang, G. 2012. Ocean oxygenation in the wake of the Marinoan glaciation. *Nature*. **489**(7417),pp.546–9.

Saltzman, M.R. 2005. Phosphorus, nitrogen, and the redox evolution of the Paleozoic oceans. *Geology*. **33**(7),pp.573–576.

Saltzman, M.R. and Thomas, E. 2012. Carbon Isotope Stratigraphy. *The Geologic Time Scale 2012*. **1**–**2**,pp.207–232.

Schenau, S.J. and De Lange, G.J. 2001. Phosphorus regeneration vs. burial in sediments of the Arabian Sea. *Marine Chemistry*. **75**(3),pp.201–217.

Schenau, S.J., Slomp, C.P. and De Lange, G.J. 2000. Phosphogenesis and active phosphorite formation in sediments from the Arabian Sea oxygen minimum zone. *Marine Geology*. **169**(1–2),pp.1–20.

Schippers, A. and Jorgensen, B.B. 2002. Biogeochemistry of pyrite and iron sulfide oxidation in marine sediments. *Geochimica et Cosmochimica Acta*. **66**(1),pp.85–92.

Scholz, F. 2018. Identifying oxygen minimum zone-type biogeochemical cycling in Earth history using inorganic geochemical proxies. *Earth-Science Reviews*. **184**(August),pp.29-45.

Scholz, F., McManus, J. and Sommer, S. 2013. The manganese and iron shuttle in a modern euxinic basin and implications for molybdenum cycling at euxinic ocean margins. *Chemical Geology*. **355**,pp.56–68.

Schoonen, M.A. 2004. Mechanisms of sedimentary pyrite formation *In*: *Special Paper 379: Sulfur Biogeochemistry - Past and Present*. Geological Society of America, pp. 117–134.

Schrag, D.P., Higgins, J.A., Macdonald, F.A. and Johnston, D.T. 2013. Authigenic Carbonate and the History of the Global Carbon Cycle. *Science*. **339**(6119),pp.540–543.

Schulz, H.D. and Zabel, M. 2006. *Marine geochemistry*.

Schwarz, E. and Arnott, R.W.C. 2007. Anatomy and Evolution of a Slope Channel-Complex Set (Neoproterozoic Isaac Formation, Windermere Supergroup, Southern Canadian Cordillera): Implications for Reservoir Characterization. *Journal of Sedimentary Research*. **77**(2),pp.89–109.

Scott, C. and Lyons, T.W. 2012. Contrasting molybdenum cycling and isotopic properties in euxinic versus non-euxinic sediments and sedimentary rocks: Refining the paleoproxies. *Chemical Geology*. **324**–**325**,pp.19–27.

Scott, C., Lyons, T.W., Bekker, A., Shen, Y., Poulton, S.W., Chu, X. and Anbar, A.D. 2008. Tracing the stepwise oxygenation of the Proterozoic ocean. *Nature*. **452**(7186),pp.456–9.

Scott, C., Planavsky, N.J., Dupont, C.L., Kendall, B., Gill, B.C., Robbins, L.J., Husband, K.F., Arnold, G.L., Wing, B. a, Poulton, S.W., Bekker, A., Anbar, A.D., Konhauser, K.O. and Lyons, T.W. 2012. Bioavailability of zinc in marine systems through time. *Nature Geoscience*. **6**(2),pp.125–128.

Scott, C., Slack, J.F. and Kelley, K.D. 2017. The hyper-enrichment of V and Zn in black shales of the Late Devonian-Early Mississippian Bakken Formation (USA). *Chemical Geology*. **452**,pp.24–33.

Seilacher, A., Grazhdankin, D. and Legouta, A. 2003. Ediacaran biota: The dawn of animal life in the shadow of giant protists. *Paleontological Research*. **7**(1),pp.43–54.

Semikhatov, M.A., Kuznetsov, A.B. and Chumakov, N.M. 2015. Isotope age of boundaries between the general stratigraphic subdivisions of the Upper Proterozoic (Riphean and Vendian) in Russia: The evolution of opinions and the current estimate. *Stratigraphy and Geological Correlation*. **23**(6),pp.568–579.

Semikhatov, M.A., Kuznetsov, A.B., Maslov, A. V, Gorokhov, I.M. and Ovchinnikova, G. V 2009. Stratotype of the Lower Riphean, the Burzyan Group of the Southern Urals: Lithostratigraphy, paleontology, geochronology, Sr- and C-isotopic characteristics of its carbonate rocks. *Stratigraphy and Geological Correlation*. **17**(6),pp.574–601.

Sergeev, V.. and Seong-Joo, L. 2006. Real eukaryotes and precipitates first found in the Middle Riphean Stratotype, Southern Urals. *Stratigraphy and Geological Correlation*. **14**(1),pp.1–18.

Severmann, S., Lyons, T.W., Anbar, A., McManus, J. and Gordon, G. 2008. Modern iron isotope perspective on the benthic iron shuttle and the redox evolution of ancient oceans. *Geology*. **36**(6),pp.487–490.

Sharp, Z. 2017. *Principles of Stable Isotope Geochemistry* 2nd ed.

Shatsky, N.S. 1945. *Sketches on the tectonics of the Volga-Urals oil region and the adjacent part of the western slope of the South Urals*. Moscow.

Shatsky, N.V. 1960. Principles of stratigraphy of the Late Precambrian and volume of the Riphean Group *In*: *Stratigraphy of the Late Precambrian and Cambrian (IGC, XXI Session, Problem 8), AN SSSR*. Moscow.

Shemesh, A. 1990. Crystallinity and diagenesis of sedimentary apatites. *Geochimica et Cosmochimica Acta*. **54**,pp.2433–2438.

Shen, B., Dong, L., Xiao, S. and Kowalewski, M. 2008. The Avalon explosion: Evolution of Ediacara morphospace. *Science*. **319**(5859),pp.81–84.

Shen, Y., Canfield, D.E. and Knoll, A.H. 2002. Middle Proterozoic Ocean Chemistry: Evidence from the McArthur Basin, Northern Australia. *American Journal of Science*. **302**(February),pp.81–109.

Shen, Y., Knoll, A.H. and Walter, M.R. 2003. Evidence for low sulphate and anoxia in a mid-Proterozoic marine basin. *Nature*. **423**(June),pp.632–635.

Shields-Zhou, G. and Och, L. 2011. The case for a Neoproterozoic Oxygenation Event: Geochemical evidence and biological consequences. *GSA Today*. **21**(3),pp.4–11.

Shih, P.M., Hemp, J., Ward, L.M., Matzke, N.J. and Fischer, W.W. 2016. Crown group Oxyphotobacteria postdate the rise of oxygen. *Geobiology*. (February 2016),pp.19–29.

Slack, J.F. and Cannon, W.F. 2009. Extraterrestrial demise of banded iron formations 1.85 billion years ago. *Geology*. **37**(11),pp.1011–1014.

Slack, J.F., Grenne, T., Bekker, A., Rouxel, O.J. and Lindberg, P.A. 2007. Suboxic deep seawater in the late Paleoproterozoic: Evidence from hematitic chert and iron formation related to seafloor-hydrothermal sulfide deposits, central Arizona, USA. *Earth and Planetary Science Letters*. **255**(1–2),pp.243–256.

Slomp, C.P., Epping, E.H.G., Helder, W. and Raaphorst, W. Van 1996b. A key role for iron-bound phosphorus in authigenic apatite formation in North Atlantic continental platform sediments. *Journal of Marine Research*. **54**(6),pp.1179–1205.

Slomp, C.P., Van der Gaast, S.J. and Van Raaphorst, W. 1996a. Phosphorus binding by poorly crystalline iron oxides in North Sea sediments. *Marine Chemistry*. **52**(1),pp.55–73.

Slomp, C.P., Thomson, J. and De Lange, G.J. 2004. Controls on phosphorus regeneration and burial during formation of eastern Mediterranean sapropels. *Marine Geology*. **203**(1–2),pp.141–159.

Smith, M.D., Arnaud, E., Arnott, R.W.C. and Ross, G.M. 2011. Chapter 37 The record of Neoproterozoic glaciations in the Windermere Supergroup, southern Canadian Cordillera. *Geological Society, London, Memoirs*. **36**(1),pp.413–424.

Sokolov, B.S. and Iwanowski, A.B. 1985. *The Vendian System: Vol. 1 Paleontology*.

Song, H., Jiang, G., Poulton, S.W., Wignall, P.B., Tong, J., Song, H., An, Z., Chu, D., Tian, L., She, Z. and Wang, C. 2017. The onset of widespread marine red beds and the evolution of ferruginous oceans. *Nature Communications*. **8**(1),p.399.

Sorensen, J. and Jorgensen, B.B. 1987. Early diagenesis in sediments from Danish coastal waters: Microbial Activity and Mn-Fe S geochemistry. *Geochimica et Cosmochimica Acta*. **51**,pp.1583–1590.

Sperling, E.A., Halverson, G.P., Knoll, A.H., Macdonald, F.A. and Johnston, D.T. 2013. A basin redox transect at the dawn of animal life. *Earth and Planetary Science Letters*. **371**–**372**,pp.143–155.

Sperling, E.A., Peterson, K.J. and Laflamme, M. 2011. Rangeomorphs, Thectardis (Porifera?) and dissolved organic carbon in the Ediacaran oceans. *Geobiology*. **9**(1),pp.24–33.

Sperling, E.A., Rooney, A.D., Hays, L., Sergeev, V.N., Vorob’eva, N.G.,

Sergeeva, N.D., Selby, D., Johnston, D.T. and Knoll, A.H. 2014. Redox heterogeneity of subsurface waters in the Mesoproterozoic ocean. *Geobiology*. **12**(5),pp.373–86.

Sperling, E.A., Wolock, C.J., Morgan, A.S., Gill, B.C., Kunzmann, M., Halverson, G.P., Macdonald, F. a., Knoll, A.H. and Johnston, D.T. 2015. Statistical analysis of iron geochemical data suggests limited late Proterozoic oxygenation. *Nature*. **523**,pp.451–454.

Spinks, S.C., Schmid, S. and Pagès, A. 2016. Delayed euxinia in Paleoproterozoic intracontinental seas: Vital havens for the evolution of eukaryotes? *Precambrian Research*. **287**,pp.108–114.

Stanier, R.Y. and Niel, C.B. 1962. The concept of a bacterium. *Archiv fur Mikrobiologie*. **42**(1),pp.17–35.

Strickland, J.D.H. and Parsons, T.R. 1972. A Practical Handbook of Seawater Analysis. *A practical handbook of seawater analysis*. **167**,p.185.

Stüeken, E.E., Buick, R. and Anbar, A.D. 2015. Selenium isotopes support free O2 in the latest Archean. *Geology*. **43**(3),pp.259–262.

Sundby, B., Gobeil, C., Silverberg, N. and Mucci, A. 1992. The phosphorus cycle in coastal marine sediments. *Limnology and Oceanography*. **37**(September),pp.1129–1145.

Tang, D., Shi, X., Wang, X. and Jiang, G. 2016. Extremely low oxygen concentration in mid-Proterozoic shallow seawaters. *Precambrian Research*. **276**,pp.145–157.

Tarhan, L.G. 2018. The early Paleozoic development of bioturbation—Evolutionary and geobiological consequences. *Earth-Science Reviews*. **178**,pp.177–207.

Tarhan, L.G., Droser, M.L., Planavsky, N.J. and Johnston, D.T. 2015. Protracted development of bioturbation through the early Palaeozoic Era. *Nature Geoscience*. **8**(November),pp.865–869.

Taylor, S.R. and McLennan, S.M. 1995. The geochemical evolution of the continental crust. *Reviews of Geophysics*. **33**(2),pp.241–265.

Terlaky, V., Rocheleau, J. and Arnott, R.W.C. 2016. Stratal composition and stratigraphic organization of stratal elements in an ancient deep-marine basin-floor succession, Neoproterozoic Windermere Supergroup, British Columbia, Canada. *Sedimentology*. **63**(1),pp.136–175.

Tessier, A., Campbell, P.G.C. and Bisson, M. 1979. Sequential Extraction Procedure for the Speciation of Particulate Trace Metals. *Analytical Chemistry*. **51**(7),pp.844–851.

Theiling, B.P. and Coleman, M. 2015. Refining the extraction methodology of carbonate associated sulfate: Evidence from synthetic and natural carbonate samples. *Chemical Geology*. **411**,pp.36–48.

Thompson, J., Poulton, S.W., Guilbaud, R., Doyle, K.A. and Krom, M.D. *In prep*. Development of the SEDEX phosphorus speciation method for modern and ancient iron-rich sediments.

Thomson, D., Rainbird, R.H., Planavsky, N., Lyons, T.W. and Bekker, A. 2015. Chemostratigraphy of the Shaler Supergroup, Victoria Island, NW Canada:

A record of ocean composition prior to the Cryogenian glaciations. *Precambrian Research*. **263**,pp.232–245.

Tosca, N.J., Guggenheim, S. and Pufahl, P.K. 2016. An authigenic origin for Precambrian greenalite: Implications for iron formation and the chemistry of ancient seawater. *Bulletin of the Geological Society of America*. **128**(3–4),pp.511–530.

Tostevin, R., Wood, R.A., Shields, G.A., Poulton, S.W., Guilbaud, R., Bowyer, F., Penny, A.M., He, T., Curtis, A., Hoffmann, K.H. and Clarkson, M.O. 2016. Low-oxygen waters limited habitable space for early animals. *Nature Communications*. **7**,p.12818.

Tribovillard, N., Algeo, T.J., Baudin, F. and Riboulleau, A. 2012. Analysis of marine environmental conditions based on molybdenum-uranium covariation-Applications to Mesozoic paleoceanography. *Chemical Geology*. **324**–**325**,pp.46–58.

Tribovillard, N., Algeo, T.J., Lyons, T. and Riboulleau, A. 2006. Trace metals as paleoredox and paleoproductivity proxies: An update. *Chemical Geology*. **232**(1–2),pp.12–32.

Tribovillard, N., Riboulleau, A., Lyons, T. and Baudin, F. 2004. Enhanced trapping of molybdenum by sulfurized marine organic matter of marine origin in Mesozoic limestones and shales. *Chemical Geology*. **213**(4),pp.385–401.

Turekian, K.K. and Wedepohl, K.H. 1961. Distribution of the Elements in Some Major Units of the Earth's Crust. *Geological Society of America Bulletin*. **22**(February),pp.175–192.

Turner, E.C. and Bekker, A. 2016. Thick sulfate evaporite accumulations marking a mid-neoproterozoic oxygenation event (Ten Stone Formation, Northwest territories, Canada). *Bulletin of the Geological Society of America*. **128**(1–2),pp.203–222.

Tyrrell, T. 1999. The relative influences of nitrogen and phosohorus on oceanic primary production. *Nature*. **400**(6744),pp.525–531.

Ueno, Y., Johnson, M.S., Danielache, S.O., Eskebjerg, C., Pandey, A. and Yoshida, N. 2009. Geological sulfur isotopes indicate elevated OCS in the Archean atmosphere, solving faint young sun paradox. *Proceedings of the National Academy of Sciences*. **106**(35),pp.14784–14789.

Veis, A.F., Vorob'eva, N.G. and Golubkova, E.Y. 2006. The early Vendian microfossils first found in the Russian plate: Taxonomic composition and biostratigraphic significance. *Stratigraphy and Geological Correlation*. **14**(4),pp.368–385.

Vorob'eva, N.G., Sergeev, V.N. and Knoll, A.H. 2009a. Neoproterozoic microfossils from the margin of the East European Platform and the search for a biostratigraphic model of lower Ediacaran rocks. *Precambrian Research*. **173**(1–4),pp.163–169.

Vorob'eva, N.G., Sergeev, V.N. and Knoll, A.H. 2009b. Neoproterozoic Microfossils from the Northeastern Margin of the East European Platform. *Journal of Paleontology*. **83**(2),pp.161–196.

Vorob'eva, N.G., Sergeev, V.N. and Semikhatov, M.A. 2006. Unique lower

Vendian Kel'tma microbiota, Timan ridge: New evidence for the paleontological essence and global significance of the Vendian system. *Doklady Earth Sciences*. **410**(1),pp.1038–1043.

Wagner, M., Chappaz, A. and Lyons, T.W. 2017. Molybdenum speciation and burial pathway in weakly sulfidic environments: Insights from XAFS. *Geochimica et Cosmochimica Acta*. **206**,pp.18–29.

Wan, B., Windley, B.F., Xiao, W., Feng, J. and Zhang, J. 2015. Paleoproterozoic high-pressure metamorphism in the northern North China Craton and implications for the Nuna supercontinent. *Nature Communications*. **6**.

Wan, Y., Zhang, Q. and Song, T. 2003. SHRIMP ages of detrital zircons from the Changcheng System in the Ming Tombs area, Beijing: Constraints on the protolith nature and maximum depositional age of the Mesoproterozoic cover of the North China Craton. *Chinese Science Bulletin*. **48**(22).

Wang, D., and Sanudo Wilhelmy, S.A. 2009. Vanadium speciation and cycling in coastal waters. *Marine Chemistry*. **117**(1–4),pp.52–58.

Wang, L., Shi, X. and Jiang, G. 2012. Pyrite morphology and redox fluctuations recorded in the Ediacaran Doushantuo Formation. *Palaeogeography, Palaeoclimatology, Palaeoecology*. **333**–**334**,pp.218–227.

Wang, W., Cawood, P.A., Liu, S., Guo, R., Bai, X. and Wang, K. 2017b. Cyclic formation and stabilization of Archean lithosphere by accretionary orogenesis: Constraints from TTG and potassic granitoids, North China Craton. *Tectonics*. **36**(9),pp.1724–1742.

Wang, X., Zhang, S., Wang, H., Bjerrum, C.J., Hammarlund, E.U., Haxen, E.R., Su, J., Wang, Y. and Canfield, D.E. 2017a. Oxygen, climate and the chemical evolution of a 1400 million year old tropical marine setting. *American Journal of Science*. **317**(8),pp.861–900.

Wanty, R.B. and Goldhaber, M.B. 1992. Thermodynamics and kinetics of reactions involving vanadium in natural systems: Accumulation of vanadium in sedimentary rocks. *Geochimica et Cosmochimica Acta*. **56**(4),pp.1471–1483.

Wheat, C.G., Feely, R.A. and Mottl, M.J. 1996. Phosphate removal by oceanic hydrothermal processes: An update of the phosphorus budget in the oceans. *Geochimica et Cosmochimica Acta*. **60**(19),pp.3593–3608.

Wheat, C.G., McManus, J., Mottl, M.J. and Giambalvo, E. 2003. Oceanic phosphorus imbalance: Magnitude of the mid-ocean ridge flank hydrothermal sink. *Geophysical Research Letters*. **30**(17),pp5-1–5-4.

Whiticar, M.J. 1999. Carbon and hydrogen isotope systematics of bacterial formation and oxidation of methane. *Chemical Geology*. **161**(1–3),pp.291–314.

Wilde, P., Lyons, T.W. and Quinby-Hunt, M.S. 2004. Organic carbon proxies in black shales: Molybdenum. *Chemical Geology*. **206**(3–4),pp.167–176.

Wilde, S.A., Valley, J.W., Peck, W.H. and Graham, C.M. 2001. Evidence from detrital zircons for the existence of continental crust and oceans on the Earth 4.4 Gyr ago. *Nature*. **409**(6817),pp.175–178.

Williamson, M.A. and Rimstidt, J.D. 1994. The kinetics and electrochemical rate-determining step of aqueous pyrite oxidation. *Geochimica et Cosmochimica Acta*. **58**(24),pp.5443–5454.

Wood, D., Dalyrymple, R., Narbonne, G.M., Gehling, J.G. and Clapham, M.E. 2003. Paleoenvironmental analysis of the late Neoproterozoic Mistaken Point and Trepassey formations, southeastern Newfoundland. *Canadian Journal of Earth Sciences*. **40**(10),pp.1375–1391.

Wood, R., Ivantsov, A.Y. and Zhuravlev, A.Y. 2017. First macrobiota biomineralization was environmentally triggered. *Proceedings of the Royal Society B: Biological Sciences*. **284**(1851),p.20170059.

Wood, R.A., Poulton, S.W., Prave, A.R., Hoffmann, K.-H., Clarkson, M.O., Guilbaud, R., Lyne, J.W., Tostevin, R., Bowyer, F., Penny, A.M., Curtis, A. and Kasemann, S.A. 2015. Dynamic redox conditions control late Ediacaran metazoan ecosystems in the Nama Group, Namibia. *Precambrian Research*. **261**,pp.252–271.

Xiang, L., Schoepfer, S.D., Shen, S., Cao, C. and Zhang, H. 2017. Evolution of oceanic molybdenum and uranium reservoir size around the Ediacaran – Cambrian transition : Evidence from western Zhejiang , South China. *Earth and Planetary Science Letters*. **464**,pp.84–94.

Xiao, S., Droser, M., Gehling, J.G., Hughes, I. V., Wan, B., Chen, Z. and Yuan, X. 2013. Affirming life aquatic for the ediacara biota in China and Australia. *Geology*. **41**(10),pp.1095–1098.

Xiao, S. and Knoll, A.H. 2000. Phosphatized Animal Embryos From the Neoproterozoic Doushantuo Formation At Weng'an, Guizhou, South China. *Journal of Paleontology*. **74**(5),pp.767–788.

Xiao, S., McFadden, K.A., Peek, S., Kaufman, A.J., Zhou, C., Jiang, G. and Hu, J. 2012. Integrated chemostratigraphy of the Doushantuo Formation at the northern Xiaofenghe section (Yangtze Gorges, South China) and its implication for Ediacaran stratigraphic correlation and ocean redox models. *Precambrian Research*. **192**–**195**(1),pp.125–141.

Xiao, S., Zhang, Y. and Knoll, A.H. 1998. Three-dimensional preservation of algae and animal embryos in a Neoproterozoic phosphorite. *Nature*. **391**(February),pp.553–558.

Yang, H., Chen, Z. and Fang, Y. 2017b. Microbially induced sedimentary structures from the 1.64 Ga. *Palaeogeography, Palaeoclimatology, Palaeoecology*. **474**,pp.7–25.

Yang, S., Kendall, B., Lu, X., Zhang, F. and Zheng, W. 2017a. Uranium isotope compositions of mid-Proterozoic black shales: Evidence for an episode of increased ocean oxygenation at 1.36 Ga and evaluation of the effect of post-depositional hydrothermal fluid flow. *Precambrian Research*. **298**,pp.187–201.

Yang, W. and Holland, H.D. 2003. The Hekpoort paleosol profile in strata 1 at Gaborone, Botswana: Soil formation during the great oxidation event. *American Journal of Science*. **303**(3),pp.187–220.

Yin, L., Zhu, M., Knoll, A.H., Yuan, X., Zhang, J. and Hu, J. 2007. Doushantuo embryos preserved inside diapause egg cysts. *Nature*. **446**(7136),pp.661–

663.

Zahnle, K., Claire, M. and Catling, D. 2006. The loss of mass-independent fractionation in sulfur due to a Palaeoproterozoic collapse of atmospheric methane. *Geobiology*. **4**(4),pp.271–283.

Van Der Zee, C., Slomp, C.P. and Van Raaphorst, W. 2002. Authigenic P formation and reactive P burial in sediments of the Nazaré canyon on the Iberian margin (NE Atlantic). *Marine Geology*. **185**(3–4),pp.379–392.

Zerkle, A.L., Claire, M.W., Domagal-Goldman, S.D., Farquhar, J. and Poulton, S.W. 2012. A bistable organic-rich atmosphere on the Neoarchaean Earth. *Nature Geoscience*. **5**(5),pp.359–363.

Zhai, M., Hu, B., Zhao, T., Peng, P. and Meng, Q. 2015. Late Paleoproterozoic-Neoproterozoic multi-rifting events in the North China Craton and their geological significance: A study advance and review. *Tectonophysics*. **662**,pp.153–166.

Zhai, M., Shao, J., Hao, J. and Pengl, P. 2003. Geological Signature and Possible Position of the North China Block in the Supercontinent Rodinia. *Gondwana Research*. **6**(2),pp.171–183.

Zhai, M.G., Guo, J.H. and Liu, W.J. 2001. An exposed cross-section of early precambrian continental lower crust in North China Craton. *Physics and Chemistry of the Earth, Part A: Solid Earth and Geodesy*. **26**(9–10),pp.781–792.

Zhai, M.G. and Santosh, M. 2011. The early Precambrian odyssey of the North China Craton: A synoptic overview. *Gondwana Research*. **20**(1),pp.6–25.

Zhang, K., Zhu, X., Wood, R.A., Shi, Y., Gao, Z. and Poulton, S.W. 2018. COxygenation of the Mesoproterozoic ocean and the evolution of large multicellular eukaryotes. *Nature Geoscience*.,pp.1–21.

Zhang, K., Zhu, X., Wood, R.A., Shi, Y., Gao, Z. and Poulton, S.W. 2018. Oxygenation of the Mesoproterozoic ocean and the evolution of complex eukaryotes. *Nature Geoscience*. **11**(5),pp.345–350.

Zhang, S., Li, Z.X., Evans, D.A.D., Wu, H., Li, H. and Dong, J. 2012. Pre-Rodinia supercontinent Nuna shaping up: A global synthesis with new paleomagnetic results from North China. *Earth and Planetary Science Letters*. **353**–**354**,pp.145–155.

Zhang, S., Wang, X., Wang, H., Bjerrum, C.J., Hammarlund, E.U., Costa, M.M., Connelly, J.N., Zhang, B., Su, J. and Canfield, D.E. 2016. Sufficient oxygen for animal respiration 1,400 million years ago. *Proceedings of the National Academy of Sciences*. **113**(7),pp.1731–1736.

Zhao, G. 2001. Palaeoproterozoic assembly of the North China Craton. *Geological Magazine*. **138**(1),pp.87–91.

Zhao, G. and Cawood, P.A. 2012. Precambrian geology of China. *Precambrian Research*. **222**–**223**,pp.13–54.

Zhao, G., Cawood, P.A., Li, S., Wilde, S.A., Sun, M., Zhang, J., He, Y. and Yin, C. 2012. Amalgamation of the North China Craton: Key issues and discussion. *Precambrian Research*. **222**–**223**,pp.55–76.

Zhao, G., Cawood, P.A., Wilde, S.A. and Sun, M. 2002. Review of global 2.1-

1.8 Ga orogens: Implications for a pre-Rodinia supercontinent. *Earth-Science Reviews*. **59**(1–4),pp.125–162.

Zhao, G., Sun, M., Wilde, S.A. and Li, S. 2004. A Paleo-Mesoproterozoic supercontinent: assembly, growth and breakup. *Earth-Science Reviews*. **67**(1–2),pp.91–123.

Zhao, G., Sun, M., Wilde, S.A. and Sanzhong, L. 2005. Late Archean to Paleoproterozoic evolution of the North China Craton: key issues revisited. *Precambrian Research*. **136**(2),pp.177–202.

Zhao, G., Wilde, S.A., Cawood, P.A. and Sun, M. 2001. Archean blocks and their boundaries in the North China Craton: lithological, geochemical, structural and P–T path constraints and tectonic evolution. *Precambrian Research*. **107**(1–2),pp.45–73.

Zhao, G., Wilde, S.A., Sun, M., Guo, J., Kröner, A., Li, S., Li, X. and Zhang, J. 2008. SHRIMP U-Pb zircon geochronology of the Huai'an Complex: Constraints on Late Archean to Paleoproterozoic magmatic and metamorphic events in the Trans-North China Orogen. *American Journal of Science*. **308**(3),pp.270–303.

Zhu, S. and Chen, H. 1995. Megascopic Multicellular Organisms from the 1700-Million-Year-Old Tuanshanzi Formation in the Jixian Area, North China. *Science*. **270**(3–5),pp.620–622.

Zhu, S., Sun, S., Huang, X., He, Y., Zhu, G., Sun, L. and Zhang, K. 2000. Discovery of carbonaceous compressions and their multicellular tissues from the Changzhougou Formation (1800 Ma) in the Yanshan range, North China. *Chinese Science Bulletin*. **45**(9),pp.841–847.

Zhu, S., Zhu, M., Knoll, A.H., Yin, Z., Zhao, F., Sun, S., Qu, Y., Shi, M. and Liu, H. 2016. Decimetre-scale multicellular eukaryotes from the 1.56-billion-year-old Gaoyuzhuang Formation in North China. *Nature Communications*. **7**(May),pp.1–8.

Appendix A

Locality	Sample Number	Lithology
BMA, South Urals	767-1	Siltstone-Argillite
	767-4	Siltstone-Argillite
	767-5	Siltstone-Argillite
	767-11	Siltstone-Argillite
	767-20	Siltstone
	767-23	Siltstone-Argillite
	767-24	Dolomite/Limestone
	767-33	Sandstone
	768-10	Limestone
	768-12	Limestone
	768-14	Siltstone-Argillite
	768-15	Limestone
	768-16	Siltstone-Argillite
	768-20	Limestone
	768-21	Limestone
	768-22	Siltstone
	768-23	Siltstone
	768-25	Limestone
	768-26	Siltstone
	768-27	Siltstone-Argillite
	768-28	Limestone
	768-29	Siltstone-Argillite
	768-30	Limestone
	768-31	Limestone
	768-40	Muddy Limestone
	768-43	Stromatolitic Limestone
	768-44	Siltstone
	768-45	Limestone
	768-46	Limestone
	768-47	Limestone
	768-48	Limestone
	768-49	Muddy Limestone
	768-59	Dolomite
	768-61	Dolomite
	768-71	Dolomite
	773-2	Argillite
	773-3	Argillite
	773-4	Argillite
	773-6	Argillite
	773-7	Argillite
	773-8	Argillite
	773-10	Argillite
	773-13	Carbonate
	773-36	Siltstone-Argillite

	773-13	Carbonate
	773-14	Dolomite
	773-15	Dolomite
	773-16	Dolomite
	773-27	Dolomite
	773-29	Dolomite
	773-35	Dolomite
	773-36	Siltstone-Argillite
	773-37	Dolomite
	773-39	Dolomite
	773-47	Dolomite
	775-1	Argillite
	775-2	Argillite
	775-3	Siltstone
	775-3	Siltstone
	775-4	Siltstone
	775-5	Siltstone-Argillite
	775-6	Siltstone-Argillite
	775-7	Sandstone-Siltstone
	775-9	Siltstone
	775-11	Argillite
	775-15	Siltstone
	775-16	Siltstone-Argillite
	775-18	Sandstone-Siltstone
	775-19	Argillite
	775-20	Siltstone
	775-22	Siltstone-Argillite
	775-23	Siltstone-Argillite
	775-25	Carbonate
	775-26	Siltstone-Argillite
	775-27	Siltstone
	776-11	Dolomite
	776-14	Dolomite
	776-16	Dolomite
	776-17	Argillite
	776-18	Argillite
	758-5	Siltstone
	758-9	Siltstone
	758-12	Siltstone
	758-33	Argillite
	758-35	Argillite
	758-38	Siltstone
	758-40	Siltstone
	759-28	Argillite
	776-19	Argillite
	759-38	Siltstone
	776-23	Argillite with quartz inclusions
	776-28	Dolomite
	776-30	Siltstone
	776-39	Siltstone
	776-40	Dolomite
	776-44	Dolomite
	762-24	Argillite

	762-38	Argillite
	755-2	Argillite
	755-5	Siltstone
	755-8	Argillite
	755-9	Siltstone
	755-11	Sandstone
	755-12	Argillite
	755-14	Siltstone
	755-18	Siltstone
	755-20	Siltstone
	755-23	Siltstone
	755-26	Argillite
	755-27	Siltstone
	755-34	Argillite
	755-36	Argillite
	755-37	Limestone
	755-41	Argillite
	755-44	Dolomitic limestone
	755-46	Argillite
	755-47	Argillite
	755-48	Limestone
	755-50	Argillite
	755-51	Limestone
	755-53	Argillite
	755-54	Limestone
	755-58	Limestone
	755-59	Carbonate breccia
	755-60	Limestone
	755-63	Pelitic limestone
	755-65	Argillite
	755-67	Argillite
	755-69	Limestone
	755-70	Argillite
	755-72	Argillite
	755-76	Argillite
	755-77	Limestone
	755-79	Limestone
	755-80	Siltstone
	755-82	Siltstone
	755-83	Siltstone
	755-86	Argillite
	755-89	Argillite
	755-90	Siltstone
	755-92	Argillite
	755-96	Siltstone
	755-99	Siltstone
	755-101	Siltstone
	755-103	Siltstone
	755-104	Siltstone
	755-108	Siltstone
	755-109	Siltstone
	755-111	Argillite
	755-117	Siltstone
	755-118	Dolomite

	755-120	Muddy dolomite
	755-123	Dolomite
	755-138	Dolomite
	755-142	Dolomite
	761-3	Dolomite
	761-7	Dolomite
	740-12	Limestone
	740-15	Limestone
	740-40	Limestone
	740-44	Limestone
	740-45	Limestone
	761-56	Siltstone
	761-74	Muddy Limestone
	761-76	Muddy Limestone
	746-12	Argillite
	746-13	Siltstone
	746-14	Argillite
	746-22	Argillite
	761-93	Siltstone
	746-29	Argillite
	761-103	Limestone
	761-105	Limestone
	746-33	Argillite
	761-108	Carbonate
	746-35	Argillite
	761-110	Siltstone
	746-38	Limestone
	761-114	Dolomite
	761-115	Carbonate (grey)
	746-41	Siltstone
	761-119	Siltstone
	761-121	Carbonate (grey)
	746-43	Argillite
	746-44	Limestone
	746-45	Limestone
	742-3	Limestone
	742-5	Limestone
	742-20	Limestone
	742-22	Limestone
	742-48	Limestone
North China Craton	ADS-1	Sandstone
	ADS-2	Sandstone
	ADS-3	Sandstone
	ADS-4	Sandstone
	ADS-5	Shale
	ADS-6	Shale
	ADS-7	Shale
	ADS-8	Shale
	ADS-9	Shale
	ADS-10	Shale
	ADS-11	Shale
	ADS-12	Shale
	ADS-13	Shale

	ADS-14	Shale
	ADS-15	Shale
	ADS-16	Shale
	ADS-17	Shale
	ADS-18	Shale
	ADS-19	Shale
	ADS-20	Shale
	ADS-21	Shale
	ADS-22	Shale
	ADS-23	Shale
	ADS-24	Shale
	ADS-25	Shale
	ADS-26	Shale
	ADS-27	Shale
	ADS-28	Shale
	ADS-29	Shale
	ADS-30	Shale
	ADS-31	Shale
	ADS-32	Shale
	ADS-33	Shale
	ADS-34	Shale
	ADS-35	Shale
	ADS-36	Shale
	ADS-37	Shale
	JSZG-1	Cherty dolostone
	JSZG-2	Cherty dolostone
	JSZG-3	Cherty dolostone
	JSZG-4	Cherty dolostone
	JSZZ-1	Limestone
	JSZZ-2	Limestone
	JSZZ-3	Limestone
	JSZZ-4	Limestone
	JSZZ-5	Limestone
	PCZ-1	Limestone
	PCZ-2	Limestone
	PCZ-3	Limestone
	PCZ-4	Limestone
	PCZ-5	Limestone
	HXSZ-6	Limestone
	HXSZ-5	Limestone
	HXSZ-4	Limestone
	HXSZ-3	Limestone
	HXSZ-2	Limestone
	HXSZ-1	Limestone
	CH1	Limestone
	SSAZ-1	Limestone
	SSAZ-2	Limestone
	SSAZ-3	Limestone
	SSAZ-4	Limestone
	SSAZ-5	Limestone
	SSAZ-6	Limestone
	SSAZ-7	Limestone
	SSAZ-8	Limestone
	SSAZ-9	Limestone

	SSAZ-10	Limestone
	SSAZ-11	Limestone
	SSAZ-12	Limestone
	SSAZ-13	Limestone
	SSAZ-14	Limestone
	SSAZ-15	Limestone
	SSAZ-16	Limestone
	SSAZ-17	Limestone
	SSAZ-18	Limestone
	SSAZ-19	Limestone
	SSAZ-20	Limestone
	SSAZ-21	Limestone
	HXS-1	Cherty dolomite
	HXS-2	Cherty dolomite
	HXS-3	Cherty dolomite
	HXS-4	Cherty dolomite
	HXS-5	Cherty dolomite
	HXS-6	Cherty dolomite
	HXS-7	Cherty dolomite
	HXS-8	Cherty dolomite
	HXS-9	Cherty dolomite
	HXS-10	Cherty dolomite
	HXS-11	Cherty dolomite
	HXS-12	Cherty dolomite
	HXS-13	Cherty dolomite
	HXS-14	Cherty dolomite
	HXS-15	Cherty dolomite
Kel'tma Core, Russia	K-1	Black shale
	K-2	Black shale
	K-3	Black shale
	K-4	Black shale
	K-5	Grey shale
	K-6	Grey shale
	K-7	Grey shale
	K-8	Black shale
	K-9	Black shale
	K-10	Black shale
	K-11	Black shale
	K-12	Black shale
	K-13	Black shale
	K-14	Black shale
	K-15	Black shale
	K-16	Black shale
	K-17	Black shale
	K-18	Black shale
	K-19	Black shale
	K-20	Black shale
	K-21	Dark grey shale
	K-22	Dark grey shale
	K-23	Dark grey shale
	K-24	Dark grey shale
	K-25	Dark grey shale
	K-26	Dark grey shale
	K-27	Dark grey shale

	K-28	Dark grey shale
	K-29	Dark grey shale
	K-30	Dark grey shale
	K-31	Dark grey shale
	K-32	Dark grey shale
	K-33	Dark grey shale
	K-34	Dark grey shale
	K-35	Dark grey shale
	K-36	Dark grey shale
	K-37	Dark grey shale
	K-38	Dark grey shale
	K-39	Dark grey shale
	K-41	Grey siltstone
	K-43	Grey siltstone
	K-44	Dark grey shale
	K-48	Dark grey shale
	K-111	Muddy limestone
	K-111B	Muddy limestone
	K-112	Muddy limestone
	K-114	Muddy limestone
	K-115	Muddy limestone
	K-116	Limestone
	K-116B	Limestone
	K-119	Dolomite
	K-120	Dolomite
	K-121	Dolomite
	K-123	Argillaceous carbonate
	K-124	Argillaceous carbonate
	K-125	Argillaceous carbonate
	K-127	Dark marl
	K-128	Dark marl
	K-129	Dark marl
	K-131	Limestone
	K-132	Limestone
	K-133	Marl
	K-137	Marl
	K-137B	Marl
	K-139	Limestone
	K-140	Marl-limestone
Kostovo-13 core, Russia	KS-57	Fine, green siltstone
	KS-58	Unlithified pale grey silt
	KS-59	Unlithified pale grey silt
	KS-60	Coarse siltstone
	KS-61	Coarse siltstone with dark laminations
	KS-62	Siltstone
	KS-63	Siltstone with interlayers of shale
	KS-65	Laminated siltstone
	KS-66	Laminated siltstone
	KS-68	Siltstone
	KS-69	Siltstone
	KS-70	Siltstone
	KS-71	Siltstone

	KS-73	Siltstone
	KS-74	Siltstone
	KS-75	Siltstone
	KS-76	Shale
	KS-77	Shale
	KS-78	Shale
	KS-79	Shale
	KS-80	Shale
	KS-81	Shale
	KS-83	Shale
	KS-84	Shale
	KS-85	Shale
	KS-86	Shale with darker laminations
	KS-87	Shale with darker laminations
	KS-89	Shale, fewer laminations
	KS-91	Laminated shale with organic sheets
	KS-94	Siltstone
	KS-95	Siltstone
	KS-96	Siltstone
	KS-97	Siltstone
	KS-98	Siltstone
	KS-99	Siltstone with organic sheets
	KS-101	Siltstone with organic sheets
	KS-102	Shale
	KS-103	Shale
	KS-104	Shale
	KS-105	Shale with organic sheets
	KS-106	Shale, fine laminations
	KS-109	Very finely laminated shale
	KS-110	Shale with organic sheets
	KS-111	Shale with organic sheets
	KS-112	Shale with organic sheets
	KS-113	Finely laminated shale
	KS-114	Shale with large organic layer
	KS-115	Shale with large organic layer
	KS-116	Shale with large organic layer
	KS-118	Shale with large organic layer
	KS-119	Shale with large organic layer
	KS-123	Shale
	KS-125	Shale with organic rich nodule
	KS-126	Shale
	KS-127	Siltstone
	KS-128	Green siltstone
	KS-129	Green siltstone
	KS-130	Mica-rich green siltstone
	KS-131	Green siltstone
	KS-132	Purple/Green siltstone

	KS-133	Purple/Green siltstone
	KS-134	Siltstone
	KS-135	Red clay/silt
	KS-136	Red clay/silt
	KS-137	Red clay/silt
	KS-138	Red clay/silt
	KS-139	Green sandstone
Avalon Peninsula, Newfoundland	DEC-05-108	Mudstone
	DEC-05-109	Mudstone
	DEC-05-39	Interbedded red-silt turbidite
	DEC-05-40	Interbedded red-silt turbidite
	DEC-05-41	Interbedded red-silt turbidite
	DEC-05-42	Interbedded red-silt turbidite
	DEC-05-43	Interbedded red-silt turbidite
	DEC-05-45	Interbedded red-silt turbidite
	DEC-05-136	Shale
	DEC-05-137	Shale
	DEC-05-140	Shale
	DEC-05-141	Shale
	DEC-05-142	Shale
	DEC-05-145	Shale
	DEC-05-75	Mudstone
	DEC-05-76	Mudstone
	DEC-05-77	Mudstone
	DEC-05-78	Mudstone
	DEC-05-79	Mudstone
	DEC-05-80	Mudstone
	DEC-05-84	Mudstone
	DEC-05-85	Mudstone
	DEC-05-86	Laminated mudstone
	DEC-05-87	Laminated mudstone
	DEC-05-88	Laminated mudstone
	DEC-05-89	Laminated mudstone
	DEC-05-90	Laminated mudstone
	DEC-05-91	Laminated mudstone
	DEC-05-68	Mudstone
	DEC-05-69	Mudstone
	DEC-05-70	Mudstone
	DEC-05-71	Mudstone
	DEC-05-72	Mudstone
	DEC-05-73	Mudstone
Cariboo Mountains, Canada	DEC-04-27	Sandstone
	DEC-04-28	Sandstone
	DEC-04-29	Siltstone turbidite
	DEC-04-30	Siltstone
	DEC-04-31	Siltstone
	DEC-04-41	Siltstone
	DEC-04-42	Sandstone
	DEC-04-43	Silt interbedded sand
	DEC-04-44	Siltstone
	DEC-04-46	Sandstone
	DEC-04-47	Sandstone

	DEC-04-48	Siltstone
	DEC-04-49	Siltstone
	DEC-04-50	Sandstone
	DEC-04-54	Siltstone turbidite
	DEC-04-55	Siltstone turbidite
	DEC-04-56	Siltstone turbidite
	DEC-04-57	Siltstone turbidite
	DEC-04-58	Sandstone
	DEC-04-59	Siltstone
	DEC-04-65	Siltstone
	DEC-04-66	Siltstone
	DEC-04-68	Siltstone
	DEC-04-72	Siltstone
	DEC-04-73	Siltstone/ferruginous sandstone
	DEC-04-74	Siltstone/ferruginous sandstone
	DEC-04-136	Siltstone
	DEC-04-137	Siltstone
	DEC-04-138	Siltstone
	DEC-04-147	Siltstone
	DEC-04-148	Siltstone
	DEC-04-149	Siltstone
	DEC-04-150	Siltstone
	DEC-04-151	Pyritic sandstone
	DEC-04-152	Siltstone
	DEC-04-161	Siltstone
	DEC-04-162	Siltstone
	DEC-04-163	siltstone
Narana Formation, Officer Basin, Australia	1108840	Fine mudstone within limestone beds
	1108841	Fine mudstone within limestone beds
	1108842	Fine mudstone within limestone beds
	1108843	Fine mudstone within limestone beds
	1108844	Fine mudstone within limestone beds
	1108845	Fine mudstone within limestone beds
	1108846	Calcareous mudstone
	1108847	Calcareous mudstone
	1108848	Calcareous mudstone
	1108849	Calcareous mudstone
	1108850	Calcareous mudstone
	1108851	Calcareous mudstone
	1108852	Calcareous mudstone
	1108853	Dark grey-green silty shale
	1108854	Dark grey-green silty shale
	1108855	Dark grey-green silty shale
	1108856	Dark grey-green silty shale
	1108857	Dark grey-green silty shale
	1108858	Dark grey-green silty shale
	1108859	Dark grey-green silty shale

	1108860	Dark grey-green silty shale
	1108861	Dark grey-green silty shale
	1108862	Dark grey-green silty shale
	1108863	Dark grey-green silty shale
	1108864	Dark grey-green silty shale
	1108865	Dark grey-green silty shale
	1108866	Dark grey-green silty shale
	1108867	Dark grey-green silty shale
	1108868	Dark grey-green silty shale
	1108869	Dark grey-green silty shale
	1108870	Dark grey-green silty shale
	1108871	Dark grey-green silty shale
	1108872	Dark grey-green silty shale
	1108873	Dark grey-green silty shale
	1108874	Dark grey-green silty shale
	1108875	Dark grey-green silty shale
	1108876	Dark grey-green silty shale
	1108877	Dark grey-green silty shale
	1108878	Dark grey-green silty shale
	1108879	Dark grey-green silty shale
	1108880	Dark grey-green silty shale
	1108881	Dark grey-green silty shale
	1108882	Dark grey-green silty shale
	1108883	Dark grey-green silty shale
	1108884	Dark grey-green silty shale
	1108885	Dark grey-green silty shale
	1108886	Dark grey-green silty shale
	1108887	Dark grey-green silty shale
	1108888	Dark grey-green silty shale

Appendix B

Results for the Bashkir Meganticlinorium

Table B.1 illustrates the iron speciation, TOC, TIC and $\delta^{34}S_{py}$ results

Table B.2 shows Mn, Mo, U, and Al concentrations

Table B.1 Iron speciation, TOC, TIC and $\delta^{34}S_{py}$ results for the Bashkir Meganticlinorium sedimentary succession

#	Height (m)	Fe_{CARB} wt%	Fe_{OX} wt%	Fe_{MAG} wt%	Fe_{PY} wt%	Fe_{T} wt%	Fe_{PRS} wt%	TOC wt%	TIC wt%	$\delta^{34}S_{py}$ ‰
Burzyan Group, *Ai Formation*										
767-1	618.2	0.124	0.225	0.189	0.006	1.756	0.790	0.027	0.555	
767-4	672.7	0.254	0.903	0.595	0.006	4.132	1.664	0.035	0.482	
767-5	690.9	0.158	0.236	0.221	0.012	1.305	0.382	0.029	0.538	28.052
767-11	800.0	0.102	0.106	0.291	0.005	3.789	2.448	0.038	0.426	
767-20	963.6	0.066	0.057	0.335	0.003	3.358	1.566	0.052	0.662	
767-23	1018.2	0.100	0.141	0.059	0.008	0.662	0.127	0.003	0.246	
767-24	1036.4	0.210	0.260	0.022	0.004	0.519	<LOD	0.001	0.120	
767-33	1200.0	0.314	0.380	0.420	0.030	2.003	0.571	0.002	0.355	21.97

Satka Formation										
#	Height (m)	Fe_{CARB} wt%	Fe_{OX} wt%	Fe_{MAG} wt%	Fe_{PY} wt%	Fe_{T} wt%	Fe_{PRS} wt%	TOC wt%	TIC wt%	$\delta^{34}S_{py}$ ‰
768-10	1352.54	0.619	0.013	0.040	0.002	0.883	0.079		9.964	
768-12	1383.05	1.828	0.026	0.084	0.010	2.156	0.134		11.413	
768-14	1413.56	0.106	0.170	0.210	0.005	1.507	0.316	0.015	0.361	
768-15	1428.81	0.527	0.008	0.047	0.003	0.721	0.058		10.203	-1.53
768-16	1444.07	0.104	0.344	0.319	0.003	2.296	0.874	0.018	0.502	
768-20	1505.08	0.187	0.035	0.039	0.003	0.784	0.293		9.999	
768-21	1520.34	0.509	0.049	0.088	0.006	1.205	0.222	0.164	9.419	4.03
768-22	1535.59	0.407	0.158	0.296	0.002	2.452	0.561	0.018	1.539	17.17
768-23	1550.85	0.182	0.148	0.492	0.000	3.287	1.264	0.005	0.242	
768-25	1581.36	0.467	0.016	0.017	0.002	0.742	0.121	0.129	10.174	1.33

#	Height (m)	Fe_{CARB} wt%	Fe_{OX} wt%	Fe_{MAG} wt%	Fe_{PY} wt%	Fe_{T} wt%	Fe_{PRS} wt%	TOC wt%	TIC wt%	$\delta^{34}S_{py}$ ‰
768-26	1596.61	0.109	0.118	0.218	0.000	2.678	0.740	0.005	0.272	
768-27	1611.86	0.193	0.119	0.045	0.000	1.118	0.180	0.041	2.216	
768-28	1627.12	1.246	0.053	0.097	0.002	1.903	0.200	0.225	8.234	
768-29	1642.37	0.108	0.139	0.123	0.000	2.285	0.957	0.022	0.484	
768-30	1657.63	0.438	0.186	0.164	0.004	1.624	0.532		8.230	
768-31	1672.88	0.553	0.007	0.022	0.002	0.643	<LOD			
768-40	1810.17	0.382	0.020	0.056	0.014	0.635	0.085		10.172	
768-43	1855.93	0.359	0.002	0.074	0.002	0.541	0.035	0.093	6.047	
768-44	1871.19	0.266	0.122	0.392	0.000	3.893	1.439	0.005	0.234	
768-45	1886.44	2.136	0.102	0.169	0.001	3.126	0.375	0.114	8.894	10.47

#	Height (m)	Fe_{CARB} wt%	Fe_{OX} wt%	Fe_{MAG} wt%	Fe_{PY} wt%	Fe_{T} wt%	Fe_{PRS} wt%	TOC wt%	TIC wt%	$\delta^{34}S_{py}$ ‰
768-46	1901.69	0.651	0.005	0.027	0.001	0.749	<LOD		10.346	
768-47	1916.95	0.587	0.001	0.039	0.000	0.732	0.072	0.055	8.046	
768-48	1932.20	1.005	0.005	0.079	0.000	1.135	0.044	0.081	9.198	
768-49	1947.46	0.968	0.005	0.036	0.000	1.056	<LOD		10.442	
768-59	2100.00	0.456	0.003	0.075	0.000	0.574	<LOD		11.992	
768-61	2125.81	0.771	0.021	0.058	0.000	0.996	0.121	0.207	9.539	
768-71	2267.77	0.674	0.030	0.047	0.000	1.205	0.163	0.115	9.037	
773-2	3130.27	0.241	0.785	0.872	0.006	5.786	2.452	0.030	0.694	
773-3	3142.77	0.159	0.671	0.772	0.003	4.740	1.711	0.054	7.05	
773-4	3155.27	0.331	0.990	0.870	0.003	4.630	1.893		0.628	

#	Height (m)	Fe_{CARB} wt%	Fe_{OX} wt%	Fe_{MAG} wt%	Fe_{PY} wt%	Fe_{T} wt%	Fe_{PRS} wt%	TOC wt%	TIC wt%	$\delta^{34}S_{py}$ ‰
773-6	3186.52	0.380	0.990	0.975	0.002	6.157	3.083	0.040	12.68	
773-7	3205.27	0.244	0.751	0.945	0.005	5.273	2.871	0.011	10.27	
773-8	3217.77	0.139	0.203	0.591	0.003	4.421	2.667		0.234	
773-10	3242.77	0.397	0.387	0.709	0.006	4.252	2.228		0.206	
773-13	3365.91	0.118	0.366	0.631	0.009	3.581	1.921	0.009	0.225	
773-36	3910.22	0.066	0.430	0.168	0.005	1.742	0.406		0.961	
773-13	4065.91	0.118	0.366	0.631	0.009	3.581	1.921	0.010	0.22	
773-14	4072.98	0.076	0.293	0.248	0.003	2.369	0.844	0.016	0.410	
773-15	4080.05	0.435	0.003	0.021	0.001	0.505	<LOD		12.0	
773-16	4087.12	0.393	0.005	0.018	0.002	0.468	0.066		12.0	

#	Height (m)	Fe_{CARB} wt%	Fe_{OX} wt%	Fe_{MAG} wt%	Fe_{PY} wt%	Fe_{T} wt%	Fe_{PRS} wt%	TOC wt%	TIC wt%	$\delta^{34}S_{py}$ ‰
773-27	4273.03	0.573	0.010	0.041	0.001	0.725	0.060	0.271	9.758	
773-29	4311.20	0.538	0.064	0.421	0.002	1.505	0.162		8.719	22.23
773-35	4578.41	1.069	0.039	0.193	0.001	1.764	0.186		9.773	13.22
773-36	4610.22	0.066	0.430	0.168	0.005	1.742	0.406	0.045	0.942	9.37
773-37	4719.30	0.104	0.009	0.025	0.008	0.155	0.023		12.0	
773-39	4773.84	0.077	0.005	0.014	0.004	0.118	0.021		12.0	
773-47	4937.46	0.423	0.008	0.105	0.002	0.569	0.051	0.465	9.581	
Bakal Formation										
775-1	4947.46	0.178	0.944	0.719	0.006	5.139	2.706	0.043	6.49	
775-2	4952.46	0.212	1.264	0.750	0.005	4.519	2.207	0.029	6.82	

#	Height (m)	Fe_{CARB} wt%	Fe_{OX} wt%	Fe_{MAG} wt%	Fe_{PY} wt%	Fe_{T} wt%	Fe_{PRS} wt%	TOC wt%	TIC wt%	$\delta^{34}S_{py}$ ‰
775-3	4957.46	0.276	1.002	0.789	0.005	4.920	2.569	0.042	0.581	
775-3	4957.46	0.276	1.002	0.789	0.005	4.920	2.569		0.622	
775-4	4987.46	0.216	1.286	0.778	0.005	4.952	2.767	0.016	0.289	
775-5	4987.46	0.245	0.899	0.712	0.007	4.850	2.829	0.023	7.11	
775-6	5007.46	0.194	0.817	0.562	0.007	4.224	2.226	0.023	0.488	
775-7	5007.46	0.159	0.870	0.364	0.005	4.445	2.738	0.010	5.9	
775-9	5047.46	0.189	0.308	0.600	0.023	3.549	1.392	0.021	0.532	7.11
775-11	5047.46	0.216	0.595	0.676	0.004	4.027	1.763	0.025	0.582	
775-15	5097.46	0.124	0.705	0.515	0.004	3.107	1.525	0.018	0.418	
775-16	5117.46	0.165	0.457	0.577	0.006	3.401	1.638		12.0	

#	Height (m)	Fe_{CARB} wt%	Fe_{OX} wt%	Fe_{MAG} wt%	Fe_{PY} wt%	Fe_{T} wt%	Fe_{PRS} wt%	TOC wt%	TIC wt%	$\delta^{34}S_{py}$ ‰
775-18	5137.46	0.233	1.170	0.676	0.003	4.576	2.207	0.040	0.543	
775-19	5152.46	0.140	0.411	1.432	0.003	4.514	<LOD	0.018	0.368	
775-20	5167.46	0.333	0.915	0.838	0.009	5.098	2.702	0.043	0.553	
775-22	5207.46	0.137	0.804	0.712	0.006	4.515	2.496	0.023	0.470	
775-23	5247.46	0.200	0.495	0.638	0.007	4.111	2.414	0.026	0.560	
775-25	5257.46	0.117	0.312	1.387	0.002	4.807	2.719	0.020	0.460	
775-26	5267.46	0.281	0.573	0.633	0.006	4.079	2.311	0.019	0.360	
775-27	5277.46	0.165	0.291	0.378	0.007	2.441	1.034	0.015	4.56	
776-11	5853.86	1.522	1.623	0.532	0.002	7.410	2.672		1.49	
776-14	6011.06	0.403	0.012	0.182	0.003	0.623	<LOD		0.140	18.87

#	Height (m)	Fe_{CARB} wt%	Fe_{OX} wt%	Fe_{MAG} wt%	Fe_{PY} wt%	Fe_{T} wt%	Fe_{PRS} wt%	TOC wt%	TIC wt%	$\delta^{34}S_{py}$ ‰
776-16	6115.86	0.550	0.039	1.071	0.003	4.179	<LOD	0.003	0.135	9.35
776-17	6168.26	0.125	0.035	0.368	0.002	1.251	<LOD	0.005	0.129	9.84
776-18	6220.66	0.189	0.023	0.166	0.011	0.419	<LOD	0.001	0.107	7.73
Yurmatau Group, *Mashak Formation*										
758-5	6365.66	0.073	0.297	0.121	0.000	4.923	3.547	0.001	0.113	
758-9	6395.66	0.314	0.301	0.161	0.002	4.769	2.687	0.002	0.139	
758-12	6425.66	0.335	1.803	0.258	0.002	10.887	3.068	0.005	0.486	
758-33	6510.66	0.378	0.220	0.605	0.026	7.389	1.898	0.035	0.488	9.74
758-35	6539.66	0.251	0.267	0.314	0.003	6.190	2.146	0.020	0.332	9.74
758-38	6570.66	0.039	0.182	0.091	0.001	6.978	4.054		0.139	9.74

#	Height (m)	Fe_{CARB} wt%	Fe_{OX} wt%	Fe_{MAG} wt%	Fe_{PY} wt%	Fe_{T} wt%	Fe_{PRS} wt%	TOC wt%	TIC wt%	$\delta^{34}S_{py}$ ‰
758-40	6585.66	0.089	0.129	0.420	0.004	6.816	4.507	0.001	0.129	
759-28	6771.66	0.068	0.490	0.225	0.001	7.222	4.439	0.001	0.159	
Zigalga Formation										
776-19	8869.26	0.051	0.729	0.020	0.019	1.008	0.065	0.015	2.407	13.87
759-38	9203.08	0.084	0.111	0.350	0.003	4.421	2.540	0.001	0.16	
776-23	8871.13	0.124	0.038	0.572	0.003	5.883	<LOD	0.003	0.221	30.92
Zigazino-Komarovo Formation										
776-28	8878.63	1.533	0.083	0.219	0.003	3.075	0.255	0.031	1.964	-1.44
776-30	8906.76	0.469	0.011	0.056	0.003	3.159	0.203	0.008	0.485	
776-39	9075.51	0.126	0.152	0.100	0.003	2.988	0.686	0.007	0.409	

#	Height (m)	Fe_{CARB} wt%	Fe_{OX} wt%	Fe_{MAG} wt%	Fe_{PY} wt%	Fe_{T} wt%	Fe_{PRS} wt%	TOC wt%	TIC wt%	$\delta^{34}S_{py}$ ‰
776-40	9094.26	0.420	0.047	0.057	0.000	1.514	4.080		11.129	
776-44	9169.26	0.445	0.034	0.089	0.003	1.507	1.980	0.003	0.155	
762-24	9563.01	0.068	0.620	0.018	0.000	1.013	0.126	0.087	0.02	
762-38	9786.73	0.089	0.475	0.484	0.000	3.121	0.583	0.024	0.675	
755-2	9810.30	0.117	0.951	0.353	0.054	3.137	0.474	0.034	0.758	20.14
755-5	9845.65	0.592	0.048	0.089	0.000	2.822	0.224	0.023	0.134	
755-8	9881.01	0.233	0.543	0.304	1.726	3.837	0.476	0.022	0.450	20.06
755-9	9892.80	0.177	0.143	0.272	2.649	4.641	0.484	0.013	0.382	16.39
755-11	9916.37	0.273	0.965	0.081	0.015	6.164	4.339	0.005	0.186	17.76
755-12	9928.15	0.665	0.919	0.450	0.251	4.658	1.143	0.053	1.463	9.00

#	Height (m)	Fe_{CARB} wt%	Fe_{OX} wt%	Fe_{MAG} wt%	Fe_{PY} wt%	Fe_{T} wt%	Fe_{PRS} wt%	TOC wt%	TIC wt%	$\delta^{34}S_{py}$ ‰
755-14	9951.73	0.084	0.188	0.208	0.000	2.260	0.657	0.008	0.399	
755-18	9998.87	0.192	0.156	0.489	0.004	4.655	1.844	0.022	0.418	11.63
755-20	10022.4	0.209	0.302	0.462	0.000	3.788	0.777	0.011	0.342	
755-23	10057.8	0.934	0.021	0.023	0.000	1.905	0.906	0.026	0.278	
755-26	10093.15	0.207	0.081	0.079	0.001	1.749	0.742	0.019	0.420	
755-27	10104.94	0.085	0.210	0.019	0.137	1.659	0.061	0.003	0.249	30.61
Avzyan Formation										
755-34	10397.05	0.031	0.467	0.061	0.003	3.288	0.068	0.018	0.308	18.68
755-36	10414.24	1.215	0.025	0.071	0.012	1.732	<LOD	0.057	0.394	
755-37	10422.83	0.616	0.006	0.301	0.003	0.951	<LOD	0.072	7.654	

#	Height (m)	Fe_{CARB} wt%	Fe_{OX} wt%	Fe_{MAG} wt%	Fe_{PY} wt%	Fe_{T} wt%	Fe_{PRS} wt%	TOC wt%	TIC wt%	$\delta^{34}S_{py}$ ‰
755-41	10457.19	0.103	0.351	0.302	0.006	2.380	0.395	0.010	0.324	24.03
755-44	10482.97	0.716	0.092	0.096	0.001	9.230	<LOD			
755-46	10500.15	0.136	0.087	0.377	0.002	3.604	0.642	0.013	0.422	
755-47	10508.74	0.272	0.205	0.518	0.008	6.086	0.346	0.025	0.473	12.43
755-48	10517.33	0.037	0.124	1.500	0.000	6.445	<LOD		11.059	
755-50	10534.52	0.319	0.334	0.796	0.006	4.367	1.707	0.032	0.475	13.69
755-51	10543.11	1.312	0.155	0.216	0.033	7.138	<LOD	0.013	0.357	
755-53	10560.29	0.087	0.319	0.228	0.010	1.503	0.769	0.017	0.560	21.58
755-54	10568.88	1.127	0.058	0.098	0.283	4.400	0.022	1.427	10.208	12.33
755-58	10603.25	0.184	0.138	0.347	1.604	3.187	0.424	0.022	0.504	6.96

#	Height (m)	Fe_{CARB} wt%	Fe_{OX} wt%	Fe_{MAG} wt%	Fe_{PY} wt%	Fe_{T} wt%	Fe_{PRS} wt%	TOC wt%	TIC wt%	$\delta^{34}S_{py}$ ‰
755-59	10611.84	0.301	0.008	0.017	0.021	2.597	0.358		11.660	
755-60	10620.43	0.421	0.013	0.047	0.000	3.482	0.435		11.227	
755-63	10646.21	0.303	0.006	0.176	0.064	3.019	0.562		10.881	
755-65	10663.39	0.158	0.285	0.293	0.290	2.719	0.042	0.068	1.605	15.02
755-67	10680.57	0.094	0.095	0.134	0.323	2.080	<LOD	0.012	0.463	14.36
755-69	10697.76	0.998	0.015	0.140	0.004	3.280	<LOD	0.027	1.285	
755-70	10706.35	0.082	0.560	0.176	0.006	3.260	0.128	0.000	0.556	
755-72	10723.53	0.105	0.473	0.222	0.228	2.861	<LOD	0.041	7.05	5.66
755-76	10757.9	0.126	0.395	0.330	0.046	3.722	0.211	0.013	0.480	15.25
755-77	10766.49	0.332	0.012	0.089	0.000	4.929	0.985		11.736	

#	Height (m)	Fe_{CARB} wt%	Fe_{OX} wt%	Fe_{MAG} wt%	Fe_{PY} wt%	Fe_{T} wt%	Fe_{PRS} wt%	TOC wt%	TIC wt%	$\delta^{34}S_{py}$ ‰
755-79	10783.67	0.241	0.019	0.194	0.002	4.625	0.662		12.00	
755-80	10792.26	0.139	0.437	0.313	0.022	3.194	<LOD	0.062	1.293	10.39
755-82	10809.45	0.139	0.441	0.488	0.000	7.150	0.538	0.035	0.688	
755-83	10818.04	0.578	0.547	0.822	0.008	5.908	2.296	0.013	12.00	
755-86	10843.81	0.335	0.103	0.632	0.001	2.684	0.342	0.037	0.636	
755-89	10869.59	0.072	0.379	0.210	0.004	7.537	0.482	0.020	0.577	
755-90	10878.18	0.289	0.765	0.438	0.005	4.362	1.797	0.046	1.591	
755-92	10895.36	0.329	0.290	0.572	0.005	2.490	2.198	0.018	0.461	
755-96	10929.73	0.152	0.278	0.397	0.003	4.205	1.503	0.028	6.61	
755-99	10955.5	0.072	0.535	0.253	0.004	5.526	2.595	0.015	0.400	

#	Height (m)	Fe_{CARB} wt%	Fe_{OX} wt%	Fe_{MAG} wt%	Fe_{PY} wt%	Fe_{T} wt%	Fe_{PRS} wt%	TOC wt%	TIC wt%	$\delta^{34}S_{py}$ ‰
755-101	10972.69	0.206	0.618	0.676	0.005	6.441	2.165	0.021	0.304	
755-103	10989.87	0.082	0.435	0.367	0.019	3.895	3.370	0.013	0.255	2.11
755-104	10998.46	0.176	0.152	0.577	0.002	3.187	2.793	0.014	0.371	
755-108	11032.83	0.271	0.260	0.288	0.001	3.795	1.248	0.001	0.192	
755-109	11041.42	0.163	0.051	0.279	0.000	1.536	0.963	0.006	0.268	
755-111	11058.6	0.163	0.101	0.047	0.117	4.625	0.827	0.012	0.380	
755-117	11110.15	0.074	0.105	0.168	0.005	5.614	0.775	0.003	0.337	
755-118	11118.74	0.032	0.038	0.895	0.007	3.508	3.271		9.918	
755-120	11135.93	0.103	0.396	0.396	0.011	3.102	2.334	0.098	0.279	16.87
755-123	11161.7	0.429	0.107	0.112	1.233	3.734	4.201		11.332	

#	Height (m)	Fe_{CARB} wt%	Fe_{OX} wt%	Fe_{MAG} wt%	Fe_{PY} wt%	Fe_{T} wt%	Fe_{PRS} wt%	TOC wt%	TIC wt%	$\delta^{34}S_{py}$ ‰
755-138	11290.57	0.287	0.294	0.089	0.025	3.520	<LOD	0.070	6.901	
755-142	11324.94	0.223	0.054	0.494	0.000	2.329	<LOD	0.009	2.334	
761-3	10167.44	0.209	0.257	0.280	0.000	5.948	0.468		0.012	
761-7	10250.77	0.105	0.128	0.115	0.000	3.714	0.143		0.013	
Karatau Group, Zilmerdak Formation										
761-15	333.33	0.377	0.062	0.010		0.519	0.011		0.198	
761-19	425.33	0.291	2.000	0.124		3.259	0.694		0.152	
740-5	666	0.220	0.595	0.641	0.012	3.739	1.287	0.013	0.703	
761-22	494.33	0.079	0.122	2.196		4.747	1.030	0.005	0.243	
761-25	563.33	0.071	0.166	2.149		3.768	1.273	0.003	0.169	

#	Height (m)	Fe_{CARB} wt%	Fe_{OX} wt%	Fe_{MAG} wt%	Fe_{PY} wt%	Fe_{T} wt%	Fe_{PRS} wt%	TOC wt%	TIC wt%	$\delta^{34}S_{py}$ ‰
761-29	655.33	0.045	0.204	0.949		4.402	1.474	0.002	0.177	
761-33	747.33	0.058	0.902	0.253		5.514	2.340			
761-35a	793.33	0.233	0.085	0.010		0.375	0.070		0.140	
761-40	908.33	0.012	1.335	0.231	0.003	6.213	2.516			
740-12	1021	0.104	0.373	0.267	0.006	2.452	0.662	0.019	0.188	4.89
740-15	1021	1.854	0.889	0.163		3.892	0.765	0.003	10.012	
740-40	1728	0.539	0.205	0.542	0.009	3.526	1.066	0.048	1.549	-4.9
740-44	1728	1.006	0.163	0.081	0.044	1.585	0.108	0.006	2.466	-31.84
740-45	1728	0.270	0.067	0.040	0.010	0.493	<LOD	0.028	2.122	4.46
761-56	1276.33	0.105	0.203	0.847		3.483	1.458	0.004	0.201	

#	Height (m)	Fe_{CARB} wt%	Fe_{OX} wt%	Fe_{MAG} wt%	Fe_{PY} wt%	Fe_{T} wt%	Fe_{PRS} wt%	TOC wt%	TIC wt%	$\delta^{34}S_{py}$ ‰
761-74	1690.33	0.131	0.236	0.777		1.580	1.604	0.009	0.223	
761-76	1736.33	0.149	0.333	0.804		1.283	1.533	0.015	0.286	
746-12	2350	0.122	0.336	0.468	0.009	2.965	1.401		0.331	
746-13	2363.8	0.311	0.389	0.229	0.005	3.683	2.217	0.006	0.114	
746-14	2377.6	0.128	0.227	1.013	0.003	3.561	1.051	0.020	0.329	
746-22	2488	0.257	0.279	0.459	0.004	3.489	1.347	0.004	0.147	
761-93	2127.33	0.260	0.286	0.226		1.328	1.395	0.008	0.368	
746-29	2584.6	0.102	0.336	1.051	0.005	1.672	2.288	0.005	0.511	
761-103	2357.33	0.215	0.343	0.232	0.028	2.205	1.527	0.006	0.251	
761-105	2403.33	1.383	0.146	0.166	0.069	2.341	0.021	0.030	12.00	-7.33

#	Height (m)	Fe_{CARB} wt%	Fe_{OX} wt%	Fe_{MAG} wt%	Fe_{PY} wt%	Fe_{T} wt%	Fe_{PRS} wt%	TOC wt%	TIC wt%	$\delta^{34}S_{py}$ ‰
746-33	2639.8	0.439	0.239	0.686	0.001	3.107	1.659	0.022	2.578	
761-108	2472.33	1.972	0.042	0.134	0.006	2.228	0.198		10.404	
746-35	2667.4	0.076	0.300	0.680		1.606	2.108	0.006	0.355	
761-110	2518.33	0.211	0.161	0.187	0.003	0.928	0.847	0.025	0.772	
746-38	2708.8	1.454	0.125	0.436	0.001	3.381	1.219		8.971	
761-114	2610.33	2.208	0.010	0.095	0.017	1.942	<LOD			
761-115	2633.33	0.448	0.081	0.330	0.062	1.818	0.241	0.003	0.400	-12.17
746-41	2750	0.111	0.092	0.265		3.846	0.590		8.677	
761-119	2725.33	0.192	0.188	0.281	0.048	0.969	1.576	0.007	0.309	
761-121	2771.33	0.758	0.356	0.293	0.019	3.108	0.194	0.035	3.532	-23.84

#	Height (m)	Fe_{CARB} wt%	Fe_{OX} wt%	Fe_{MAG} wt%	Fe_{PY} wt%	Fe_{T} wt%	Fe_{PRS} wt%	TOC wt%	TIC wt%	$\delta^{34}S_{py}$ ‰
746-43	2777.8	0.110	0.140	0.471		2.994	0.807		6.882	
746-44	2791.6	0.364	0.032	0.033		3.088	0.121		11.325	
746-45	2805.4	0.177	0.050	0.173		2.097	0.280		10.433	
Inzer Formation										
742-3	3122.5	0.157	0.605	0.710		4.977	2.054	0.005	0.234	
742-5	3093.5	0.135	0.408	0.472		3.984	1.737	0.006	0.189	
742-20	3540	0.222	0.434	0.376	0.004	1.925	0.517	0.004	0.129	
742-22	3569	0.099	0.706	0.597		6.146	2.140	0.008	0.260	
742-48	3946	0.334	0.385	0.200	0.010	1.947	0.417	0.003	0.673	
743-1	3950	0.372	1.160	0.033	0.011	4.761	<LOD	0.006	1.282	

Table B.2 Mn, Mo, U and Al results for the Bashkirian Meganticlinorium

Sample #	Weight g	Mn ppm	Mo ppm	U ppm	Al wt%
767-1	0.0597	152.866	4.820	2.195	6.27
767-4	0.0669	295.880	5.181	2.033	7.90
767-5	0.067	77.233	4.465	2.885	5.98
767-11	0.0617	297.024	4.646	1.193	7.70
767-20	0.0623	218.190	4.516	1.988	6.98
767-23	0.0677	19.572	4.227	2.470	6.51
767-24	0.0556	27.540	5.103	1.203	4.92
767-33	0.0681	315.251	4.226	3.408	6.27
768-10	0.0549	167.189	3.642	0.457	1.51
768-12	0.0665	1759.890	2.512	0.323	1.05
768-14	0.0588	40.021	4.897	1.610	8.25
768-15	0.0503	239.979	3.409	0.595	1.39
768-16	0.0539	92.929	5.534	1.537	8.93
768-20	0.0705	177.650	2.320	0.575	1.68
768-21	0.0501	232.910	2.530	0.579	1.83
768-22	0.0734	114.960	3.815	1.137	7.56
768-23	0.0647	39.576	4.256	1.331	9.02
768-25	0.0548	260.281	2.369	0.588	1.32
768-26	0.0504	35.248	5.193	1.050	9.78
768-27	0.0607	104.857	4.627	2.079	7.62
768-28	0.0582	410.463	2.659	1.052	2.53
768-29	0.0518	90.777	5.391	1.710	9.05
768-30	0.052	342.583	1.993	0.542	2.75
768-31	0.0764	227.664	1.266	0.373	0.69
768-40	0.0533	193.566	1.865	0.395	1.86

Sample #	Weight g	Mn ppm	Mo ppm	U ppm	Al wt%
768-43	0.0668	158.271	1.910	2.026	5.20
768-44	0.063	65.849	4.420	1.317	8.99
768-45	0.078	891.890	1.797	0.538	2.15
768-46	0.0536	238.615	2.737	0.387	1.52
768-47	0.0738	304.037	1.818	1.038	2.84
768-48	0.0504	443.414	2.087	0.676	2.09
768-49	0.0517	390.652	2.399	0.591	1.38
768-59	0.0666	127.942	1.224	0.244	0.69
768-61	0.0563	232.052	0.000	0.721	1.94
768-71	0.0608	226.453	0.000	0.603	2.78
773-2	0.0552	312.369	5.371	2.486	11.65
773-3	0.061	365.007	4.742	1.905	11.81
773-4	0.0563	308.350	4.846	1.864	10.05
773-6	0.0639	332.367	4.518	1.603	10.20
773-7	0.0628	368.215	4.699	2.120	9.99
773-8	0.0662	314.038	4.579	2.155	7.60
773-10	0.0555	133.259	4.757	0.558	5.00
773-13	0.0614	78.808	4.634	1.150	5.63
773-36	0.0522	41.347	7.028	3.045	8.28
773-13	0.0614	78.808	4.634	1.150	5.63
773-14	0.0619	108.821	0.000	1.483	9.11
773-15	0.0798	260.840	0.000	0.302	0.19
773-16	0.0664	245.815	0.000	0.199	0.17
773-27	0.0587	141.748	0.000	0.551	1.33
773-29	0.0525	283.248	0.000	1.608	2.40
773-35	0.0684	423.510	0.000	0.954	2.03

Sample #	Weight g	Mn ppm	Mo ppm	U ppm	Al wt%
773-36	0.0522	41.347	7.028	3.045	8.28
773-37	0.0599	121.217	0.000	0.486	0.17
773-39	0.0646	101.002	0.000	0.309	0.11
773-47	0.0677	113.623	0.000	0.789	1.48
775-1	0.0533	64.688	5.982	2.182	10.08
775-2	0.0551	68.022	5.659	1.837	8.86
775-3	0.059	54.849	5.213	1.356	7.50
775-3	0.059	54.849	5.213	1.356	7.50
775-4	0.0761	123.290	3.809	1.345	8.07
775-5	0.0547	115.525	5.061	1.817	9.00
775-6	0.0601	58.756	4.848	2.060	10.54
775-7	0.0543	67.662	5.192	1.869	8.58
775-9	0.0755	121.992	4.068	1.807	11.16
775-11	0.0654	257.719	4.247	1.521	9.85
775-15	0.0547	97.624	4.991	2.333	10.53
775-16	0.0698	118.352	0.000	0.000	9.23
775-18	0.0521	65.045	5.477	1.991	9.56
775-19	0.0775	163.365	0.000	2.102	8.19
775-20	0.055	121.830	5.164	1.535	8.99
775-22	0.0639	128.485	4.517	1.560	10.82
775-23	0.0533	105.679	5.744	2.357	10.94
775-25	0.083	171.695	0.000	1.654	8.39
775-26	0.0563	67.104	4.997	1.357	9.16
775-27	0.0622	62.681	4.447	1.274	8.48
776-11	0.0536	697.442	0.000	1.733	8.25
776-14	0.0603	68.548	1.784	0.224	0.27

Sample #	Weight g	Mn ppm	Mo ppm	U ppm	Al wt%
776-16	0.0588	78.789	2.823	0.285	0.16
776-17	0.0616	60.885	0.000	0.242	0.10
776-18	0.054	35.231	0.000	0.229	0.27
758-5	0.0581	61.459	4.277	1.500	8.58
758-9	0.0627	696.819	0.000	0.685	5.03
758-12	0.0558	2820.072	0.000	0.466	8.52
758-33	0.0515	817.461	5.225	3.588	10.13
758-35	0.0618	869.411	4.538	1.511	10.04
758-38	0.079	407.536	3.423	1.712	8.97
758-40	0.0755	280.480	0.000	1.621	6.77
759-28	0.0621	60.800	4.083	1.509	10.72
776-19	0.0491	29.128	5.184	2.233	10.16
759-38	0.0752	31.246	0.000	3.035	7.07
776-23	0.0537	101.792	0.269	1.202	9.62
776-28	0.0536	39.389	0.200	1.604	9.47
776-30	0.0647	35.226	0.195	2.192	9.96
776-39	0.0535	28.077	0.307	1.804	10.36
776-40	0.0537	33.489	0.641	2.972	8.92
776-44	0.0605	31.795	0.274	2.254	8.33
762-24	0.0554	<LOD	6.074	4.874	8.58
762-38	0.056	51.602	4.636	1.807	9.08
755-2	0.0591	45.475	4.460	1.075	9.72
755-5	0.0552	67.434	0.392	2.012	9.59
755-8	0.0456	72.863	5.625	1.829	8.93
755-9	0.0677	117.553	3.864	1.877	8.56
755-11	0.0654	18.740	4.001	0.447	3.48

Sample #	Weight g	Mn ppm	Mo ppm	U ppm	Al wt%
755-12	0.0558	761.138	4.563	1.232	7.97
755-14	0.0552	45.929	4.480	1.601	9.55
755-18	0.059	182.518	4.234	0.966	8.45
755-20	0.0513	177.229	4.987	1.689	10.03
755-23	0.0542	193.023	0.839	2.192	7.57
755-26	0.0792	145.460	0.441	2.126	6.28
755-27	0.0599	31.974	4.300	2.113	8.02
755-34	0.0656	26.987	4.144	1.718	10.10
755-36	0.0625	34.727	0.000	3.235	8.46
755-37	0.0507	20.124	2.159	5.036	8.75
755-41	0.0716	24.210	3.614	1.464	6.91
755-44	0.0797	1579.353	0.920	0.292	6.38
755-46	0.0521	43.661	4.990	1.671	10.07
755-47	0.0571	39.838	4.502	1.101	9.14
755-48	0.0568	96.792	0.520	1.680	11.22
755-50	0.057	904.283	4.590	1.668	12.43
755-51	0.0629	41.851	0.498	1.916	9.86
755-53	0.0726	331.965	3.836	<LOD	0.45
755-54	0.0659	566.483	4.036	1.051	7.71
755-58	0.0558	41.485	4.463	1.017	7.19
755-59	0.0504	67.686	0.813	2.556	12.16
755-60	0.052	68.701	0.438	2.238	11.65
755-63	0.0523	67.184	0.418	2.014	11.37
755-65	0.0499	44.896	5.378	1.640	11.55
755-67	0.0643	19.961	3.927	1.108	7.73
755-69	0.0625	16.657	0.257	2.038	11.57

Sample #	Weight g	Mn ppm	Mo ppm	U ppm	Al wt%
755-70	0.0529	178.489	5.215	2.204	11.90
755-72	0.0653	65.534	3.997	1.136	8.11
755-76	0.0565	31.660	4.613	1.609	10.18
755-77	0.057	79.978	1.059	2.298	10.83
755-79	0.0495	70.020	1.118	2.083	10.14
755-80	0.0632	54.774	4.370	1.138	8.99
755-82	0.054	42.953	4.749	0.735	7.39
755-83	0.0484	316.500	5.289	1.482	12.62
755-86	0.067	68.212	3.786	1.420	9.44
755-89	0.0638	28.008	<LOD	1.201	8.83
755-90	0.0753	305.869	3.317	1.287	7.97
755-92	0.0674	148.949	3.897	1.508	8.60
755-96	0.0512	41.499	4.802	1.546	9.93
755-99	0.0491	73.447	5.258	1.634	10.80
755-101	0.0636	60.444	4.017	1.623	10.31
755-103	0.0763	90.951	3.245	1.186	8.91
755-104	0.062	462.246	3.971	1.211	5.17
755-108	0.0638	459.889	3.450	1.506	10.50
755-109	0.0731	171.377	3.467	1.257	6.87
755-111	0.0505	54.059	5.209	2.068	8.90
755-117	0.0685	55.164	0.335	1.632	10.05
755-118	0.0696	96.267	2.914	1.909	10.92
755-120	0.0743	118.765	0.665	1.026	8.30
755-123	0.0725	108.705	2.920	1.607	9.54
755-138	0.0512	359.689	0.519	2.110	9.86
755-142	0.059	83.331	0.662	1.273	8.45

Sample #	Weight g	Mn ppm	Mo ppm	U ppm	Al wt%
740-12	0.0502	145.186	5.118	1.867	8.50
740-15	0.0566	2086.858	4.562	<LOD	1.51
761-56	0.0607	113.182	0.378	0.541	5.02
761-74	0.0624	37.260	1.855	3.190	8.74
740-40	0.0599	937.514	0.000	0.000	5.64
740-44	0.0576	1932.431	4.937	<LOD	1.40
740-45	0.0649	27.604	4.028	<LOD	1.49
761-76	0.0713	226.498	0.186	1.136	3.74
761-93	0.0796	34.995	0.244	1.579	7.52
746-12	0.0835	211.750	0.118	1.400	8.20
761-103	0.0719	46.664	3.935	1.160	5.53
746-13	0.069	102.463	0.166	1.781	10.83
746-14	0.0834	112.948	0.439	1.525	4.67
761-105	0.0575	1377.014	4.609	2.156	4.78
761-108	0.0545	29.204	0.161	1.130	9.60
746-22	0.0623	94.351	0.229	1.627	10.36
761-110	0.0636	100.949	0.186	2.237	7.74
746-29	0.0774	104.956	0.385	1.994	3.69
761-114	0.0573	87.281	0.159	1.884	9.06
761-115	0.0619	196.932	4.191	0.773	3.62
746-33	0.0586	26.691	0.708	2.840	11.52
746-35	0.0737	17.797	0.370	2.081	9.67
746-38	0.0571	41.165	0.151	2.276	11.78
761-119	0.0682	155.683	0.127	1.224	5.81
746-41	0.0872	30.780	0.493	3.158	10.34
761-121	0.0494	1105.698	5.170	2.530	7.17

Sample #	Weight g	Mn ppm	Mo ppm	U ppm	Al wt%
746-43	0.0823	26.391	0.182	2.274	9.24
746-44	0.0556	21.025	0.274	2.865	10.10
746-45	0.0832	2648.158	0.446	0.603	3.49
742-3	0.0497	143.805	5.053	2.496	7.80
742-5	0.0563	219.408	4.727	2.152	7.97
742-20	0.0538	518.003	4.769	0.849	3.28
742-22	0.0529	130.633	5.068	4.505	10.36
742-48	0.0624	542.680	4.234	1.098	4.65
743-1	0.0679	1199.632	8.472	4.669	9.09

Appendix C

Yanshan Basin, North China Craton Results

Table C.1 gives all C, Al, Mn, Fe_T and iron speciation (Fe_{CARB}, Fe_{OX}, Fe_{MAG}, Fe_{PY}) results

Table C.2 gives all trace metal (Mo,V, U, Cr) data

Table C.3 displays all P speciation results

Table C.1 TOC, TIC, Al, Mn, Fe_T, Fe_{CARB}, Fe_{OX}, Fe_{MAG}, Fe_{PY}, Fe_{PRS} and $\delta^{13}C_{org}$ values for Yanshan Basin, North China

Sample	TOC	TIC	Al	Mn	Fe_T	Fe_{CARB}	Fe_{OX}	Fe_{MAG}	Fe_{PY}	Fe_{PRS}	$\delta^{13}C_{org}$
	wt%	wt%	wt%	wt%	wt%	wt%	wt%	wt%	wt%	wt%	‰
	Changzhougou Formation										
ADS-1	0.000	0.009	5.048	0.005	1.046	0.038	0.100	0.032	0.001	0.316	-29.6
ADS-2	0.000	0.009	3.118	0.003	0.641	0.033	0.071	0.028	0.003	0.292	-30.3
ADS-3	0.009	0.000	5.828	0.010	1.513	0.046	0.140	0.058	0.001	0.558	-30.2
ADS-4	0.013	0.000	6.373	0.011	3.051	0.098	0.316	0.184	0.001	1.861	-28.2
ADS-5	0.142	0.009	12.777	0.012	2.565	0.025	0.658	0.091	0.002	0.624	-30.3
ADS-6	0.146	0.000	9.299	0.012	2.629	0.048	0.649	0.165	0.001	1.514	-30.3
ADS-7	0.131	0.000	12.496	0.011	2.489	0.015	0.519	0.071	0.002	0.382	-31.0
ADS-8	0.123	0.000	12.125	0.019	3.064	0.037	0.713	0.190	0.002	1.272	-30.4
ADS-9	0.092	0.000	9.571	0.018	4.034	0.077	0.570	0.304	0.001	2.336	-28.9
	Chuanlinggou Formation										
ADS-10	0.203	0.000	11.150	0.012	2.267	0.025	0.365	0.077	0.001	0.705	-31.5

Sample	TOC	TIC	Al	Mn	Fe_T	Fe_{CARB}	Fe_{OX}	Fe_{MAG}	Fe_{PY}	Fe_{PRS}	$\delta^{13}C_{org}$
	wt%	wt%	wt%	wt%	wt%	wt%	wt%	wt%	wt%	wt%	‰
ADS-11	0.084	0.266	11.730	0.071	4.597	0.748	0.098	0.417	0.025	1.313	
ADS-12	0.211	0.000	11.439	0.007	3.725	0.055	1.097	0.244	0.001	1.579	-31.2
ADS-13	0.231	0.000	11.740	0.016	4.096	0.236	0.074	0.281	0.049		-32.2
ADS-14	0.287	0.041	11.405	0.023	3.597	0.213	0.056	0.199	0.078	0.684	-32.8
ADS-15	0.400	0.056	11.157	0.030	4.014	0.292	0.075	0.265	0.100	0.903	-32.6
ADS-16	0.299	0.058	10.899	0.036	5.063	0.445	0.103	0.422	0.086	1.731	-32.4
ADS-17	0.547	0.010	11.567	0.010	3.556	0.179	0.055	0.193	0.108	0.836	-33.4
ADS-18	0.425	0.079	10.161	0.028	4.047	0.351	0.085	0.316	0.196	1.055	-33.3
ADS-19	0.538	0.168	10.263	0.069	5.142	0.518	0.115	0.456	0.140	1.791	-33
ADS-20	0.532	0.122	11.249	0.058	4.202	0.406	0.139	0.345	0.129	1.066	-33
ADS-21	0.600	0.097	11.119	0.048	4.221	0.393	0.121	0.329	0.124	2.194	-33
ADS-22	0.637	0.164	10.862	0.076	4.933	0.499	0.150	0.458	0.160	2.542	-33
ADS-23	0.330	0.046	10.861	0.028	3.971	0.258	0.125	0.207	0.054	2.134	-31.9
ADS-24	0.608	0.482	10.005	0.117	4.579	1.093	0.059	0.517	0.244	1.594	-33.2

Sample	TOC	TIC	Al	Mn	Fe_T	Fe_{CARB}	Fe_{OX}	Fe_{MAG}	Fe_{PY}	Fe_{PRS}	$\delta^{13}C_{org}$
	wt%	wt%	wt%	wt%	wt%	wt%	wt%	wt%	wt%	wt%	‰
ADS-25	0.959	0.575	8.707	0.053	3.521	0.823	0.094	0.451	0.348	0.896	-33.7
ADS-27	0.990	0.237	10.093	0.008	2.125	0.210	0.057	0.114	0.260	0.371	-33.4
ADS-28	1.015	0.385	10.496	0.031	2.681	0.565	0.116	0.272	0.338	0.573	-33.4
ADS-29	1.057	0.310	9.447	0.053	3.480	0.500	0.114	0.296	0.414	0.961	-33.5
ADS-30	2.059	0.066	11.548	0.041	3.143	0.069	0.892	0.107	0.065	1.184	-34
ADS-31	2.113	0.029	11.769	0.006	2.576	0.087	0.728	0.064	0.089	0.559	-34
ADS-32	1.362	0.031	9.778	0.014	3.646	0.265	0.110	0.184	0.821	1.211	-33.6
ADS-33	1.352	0.026	10.488	0.008	2.116	0.020	0.246	0.076	0.015	0.644	-33.5
ADS-34	0.895	0.035	8.840	0.004	1.519	0.019	0.223	0.081	0.012	0.417	-33.5
ADS-35	1.192	0.022	10.773	0.008	1.734	0.011	0.271	0.030	0.017	0.338	-33.4
ADS-36	1.109	0.035	10.262	0.006	2.222	0.009	0.781	0.054	0.010	0.436	-33.6
ADS-37	1.564	0.026	8.448	0.005	1.979	0.021	0.315	0.049	0.018	0.455	-33.7
	Gaoyuzhuang Formation										
JSZG-1	0.000	5.078	0.048	0.079	0.130						

Sample	TOC	TIC	Al	Mn	Fe_T	Fe_{CARB}	Fe_{OX}	Fe_{MAG}	Fe_{PY}	Fe_{PRS}	$\delta^{13}C_{org}$
	wt%	wt%	wt%	wt%	wt%	wt%	wt%	wt%	wt%	wt%	‰
JSZG-2	0.039	0.694	0.274	0.031	0.096						
JSZG-3	0.020	8.650	0.234	0.453	0.326						-29
JSZG-4	0.022	9.681	0.148	0.737	0.254						-27.2
JSZZ-1	0.000	7.952	0.863	0.108	0.187						
JSZZ-2	0.033	9.028	0.148	0.041	0.061						
JSZZ-3	0.004	5.967	0.637	0.008	0.270						
JSZZ-4	0.041	6.698	0.188	0.008	0.177						
JSZZ-5	0.027	5.765	2.217	0.016	1.193	0.523	0.016	0.014	1.193	0.002	
PCZ-1	0.137	4.329	4.287	0.027	0.937	0.447	0.015	0.003	0.937	0.003	-31.4
PCZ-2	0.130	5.359	0.987	0.014	0.683	0.326	0.009	0.000	0.683	0.016	-32.4
PCZ-3	0.086	7.640	0.649	0.023	0.538	0.183	0.005	0.000	0.538		-32.4
PCZ-4	0.086	7.196	0.836	0.019	0.643	0.252	0.007	0.000	0.643		-32
PCZ-5	0.000	3.905	3.156	0.017	0.818	0.153	0.013	0.000	0.818		-32.2
HXSZ-6	0.084	8.250	0.426	0.004	0.148						-32.1

Sample	TOC	TIC	Al	Mn	Fe_T	Fe_{CARB}	Fe_{OX}	Fe_{MAG}	Fe_{PY}	Fe_{PRS}	$\delta^{13}C_{org}$
	wt%	wt%	wt%	wt%	wt%	wt%	wt%	wt%	wt%	wt%	‰
HXSZ-5	0.072	8.500	0.479	0.004	0.272						-31.9
HXSZ-4	0.063	7.395	0.439	0.004	0.163						-32.3
HXSZ-3	0.040	8.275	0.389	0.004	0.177						-32.6
HXSZ-2	0.105	7.970	0.269	0.004	0.126						-31.5
HXSZ-1	0.020	7.672	0.799	0.004	0.297						-33
CH1	0.426	4.097	4.370	0.027	0.956	0.438	0.015	0.001	0.930	0.01	-31.6
SSAZ-1	0.022	6.938	1.618	0.060	1.069	0.046	0.007	0.001	1.069		
SSAZ-2	0.049	4.684	2.572	0.019	0.386						
SSAZ-3	0.275	6.801	1.358	0.054	1.137	0.053	0.010	0.000	0.841		-32.1
SSAZ-4	0.055	0.915	4.960	0.009	1.156	0.124	0.031	0.002	0.989	0.11	-33.6
SSAZ-5	0.416	6.475	1.829	0.056	1.048	0.067	0.017	0.001	0.984	0.041	-32.1
SSAZ-6	0.023	0.616	7.316	0.010	1.822	0.249	0.039	0.001	1.407	0.339	-33.4
SSAZ-7	0.508	6.339	1.481	0.049	0.934	0.054	0.010	0.001	1.496		
SSAZ-8	0.007	0.809	7.225	0.012	1.070	0.375	0.044	0.002	1.352	0.321	-33.6

Sample	TOC	TIC	Al	Mn	Fe_T	Fe_{CARB}	Fe_{OX}	Fe_{MAG}	Fe_{PY}	Fe_{PRS}	$\delta^{13}C_{org}$
	wt%	wt%	wt%	wt%	wt%	wt%	wt%	wt%	wt%	wt%	‰
SSAZ-9	0.044	6.540	0.617	0.020	0.299						
SSAZ-10	0.038	5.903	2.060	0.040	1.138	0.088	0.013	0.001	0.838	0.027	-31.8
SSAZ-11	0.002	7.320	1.479	0.057	0.654	0.037	0.003	0.001	1.015		-31.5
SSAZ-12	0.007	8.291	0.156	0.019	0.108						
SSAZ-13	0.009	7.325	0.556	0.024	0.183						
SSAZ-14	0.012	7.698	0.334	0.019	0.170						
SSAZ-15	0.001	7.150	0.438	0.036	0.620	0.022	0.002	0.000	0.552		
SSAZ-16	0.070	8.817	0.298	0.022	0.184						
SSAZ-17	0.076	3.197	3.637	0.015	0.745	0.180	0.028	0.000	0.650	0.142	
SSAZ-18	0.001	8.351	0.819	0.037	0.332						-33.2
SSAZ-19	0.018	6.103	0.184	0.015	0.115						
SSAZ-20	0.033	8.005	0.243	0.022	0.500						-31.5
SSAZ-21	0.084	7.909	0.884	0.026	0.299						-32.2
HXS-1	0.000	9.320			0.000						

Sample	TOC	TIC	Al	Mn	Fe_T	Fe_{CARB}	Fe_{OX}	Fe_{MAG}	Fe_{PY}	Fe_{PRS}	$\delta^{13}C_{org}$
	wt%	wt%	wt%	wt%	wt%	wt%	wt%	wt%	wt%	wt%	‰
HXS-2	0.000	9.271			0.004						
HXS-3	0.000	9.411			0.001						
HXS-4	0.000	9.053			0.028						
HXS-5	0.000	9.158			0.005						
HXS-6	0.000	9.248			0.003						
HXS-7	0.000	9.323			0.009						
HXS-8	0.000	10.072			0.005						
HXS-9	0.000	9.885			0.002						
HXS-10	0.011	10.053			0.007						
HXS-11	0.033	9.817			0.016						
HXS-12	0.004	9.295			0.004						
HXS-13	0.041	9.345			0.023						
HXS-14	0.027	10.028			0.006						
HXS-15	0.000	9.958			0.012						

Table C.2 Trace metal (Mo, V, U, Cr) results for Yanshan Basin in ppm

Sample Name	Mo	V	U	Cr
	ppm	ppm	ppm	ppm
ADS-1	0.158	<LOD	0.961	27.608
ADS-2	0.192	<LOD	0.487	10.103
ADS-3	0.152	<LOD	0.621	26.968
ADS-4	0.196	<LOD	1.051	31.811
ADS-5	0.562	100.037	2.495	109.078
ADS-6	1.316	57.765	2.163	59.000
ADS-7	0.475	113.516	3.305	109.252
ADS-8	0.585	124.506	3.973	121.569
ADS-9	0.264	76.611	2.772	80.161
ADS-10	0.548	85.141	2.705	91.361
ADS-11	0.647	108.751	2.904	111.633
ADS-12	0.561	111.995	2.492	111.998
ADS-13	0.233	118.806	1.964	118.164
ADS-14	0.240	104.622	2.111	103.072
ADS-15	0.217	108.842	1.818	112.364
ADS-16	0.293	99.282	1.823	103.089
ADS-17	0.208	123.537	2.385	117.428
ADS-18	0.265	103.602	2.104	103.807
ADS-19	0.266	100.981	1.839	98.076
ADS-20	0.632	102.351	2.299	106.920
ADS-21	0.402	110.830	2.398	110.041
ADS-22	0.362	100.996	2.026	102.477
ADS-23	0.265	108.860	2.501	112.290
ADS-24	0.425	94.099	1.847	100.182
ADS-25	0.418	76.015	1.551	80.721
ADS-27	0.553	98.992	1.850	96.385
ADS-28	0.970	101.930	1.835	104.291
ADS-29	0.975	89.655	2.148	92.152
ADS-30	1.389	124.896	2.672	117.408
ADS-31	0.905	103.154	1.970	103.677
ADS-32	1.148	92.816	1.880	89.453
ADS-33	0.760	94.829	1.479	99.031
ADS-34	0.769	68.458	1.122	70.488
ADS-35	0.572	93.365	1.434	99.236
ADS-36	0.801	88.593	1.937	87.388
ADS-37	0.935	83.920	1.572	83.344
JSZG-1	0.000	<LOD	0.086	<LOD
JSZG-2	0.108	<LOD	0.266	<LOD
JSZG-3	0.132	<LOD	0.297	<LOD
JSZG-4	0.107	<LOD	0.203	<LOD
JSZZ-1	0.116	<LOD	0.328	<LOD
Sample Name	**Mo**	**V**	**U**	**Cr**

	ppm	ppm	ppm	ppm
JSZZ-2	0.000	<LOD	0.234	<LOD
JSZZ-3	0.186	<LOD	0.346	<LOD
JSZZ-4	0.094	<LOD	0.199	<LOD
JSZZ-5	0.521	<LOD	0.984	9.407
PCZ-1	0.550	<LOD	2.450	<LOD
PCZ-2	0.463	<LOD	0.631	<LOD
PCZ-3	0.124	<LOD	0.534	<LOD
PCZ-4	0.189	<LOD	0.559	<LOD
PCZ-5	0.213	<LOD	1.693	<LOD
HXSZ-6	0.150	<LOD	0.589	<LOD
HXSZ-5	0.304	<LOD	0.702	<LOD
HXSZ-4	0.120	<LOD	0.390	<LOD
HXSZ-3	0.173	<LOD	0.644	<LOD
HXSZ-2	0.297	<LOD	0.538	<LOD
HXSZ-1	0.271	<LOD	0.710	<LOD
CH1	0.554	<LOD	2.623	<LOD
SSAZ-1	0.183	<LOD	0.763	6.994
SSAZ-2	0.132	<LOD	0.983	12.145
SSAZ-3	0.126	<LOD	0.756	7.036
SSAZ-4	0.175	46.637	1.800	31.242
SSAZ-5	0.152	<LOD	0.798	9.792
SSAZ-6	0.220	77.617	2.745	54.606
SSAZ-7	0.115	<LOD	0.560	8.023
SSAZ-8	0.454	66.678	3.193	43.974
SSAZ-9	0.072	<LOD	0.282	<LOD
SSAZ-10	0.142	<LOD	0.728	11.928
SSAZ-11	0.120	<LOD	0.605	<LOD
SSAZ-12	0.172	<LOD	0.224	<LOD
SSAZ-13	0.328	<LOD	0.349	<LOD
SSAZ-14	0.117	<LOD	0.185	<LOD
SSAZ-15	1.290	<LOD	0.341	<LOD
SSAZ-16	0.099	<LOD	0.355	<LOD
SSAZ-17	0.545	36.977	1.567	18.355
SSAZ-18	0.563	<LOD	0.644	<LOD
SSAZ-19	0.153	<LOD	0.223	<LOD
SSAZ-20	0.317	<LOD	0.674	<LOD
SSAZ-21	2.665	<LOD	0.518	<LOD

Table C.3 Phosphorus speciation results for the North China unit

Sample	P_{auth}	P_{det}	P_{mag}	P_{org}	P_{Tot}
	wt%	wt%	wt%	wt%	wt%
ADS-1	0.002	0.008	1.74E-05	2.79E-04	0.015
ADS-2	0.010	0.024	1.40E-05	1.29E-04	0.034
ADS-3	0.019	0.037	5.82E-05	0.003	0.065
ADS-4	0.007	0.009	1.23E-04	0.006	0.030
ADS-5	0.000	0.001	3.79E-05	0.006	0.028
ADS-6	0.002	0.004	1.08E-03	0.003	0.020
ADS-7	0.003	0.005	8.31E-04	0.007	0.036
ADS-8	0.009	0.009	3.82E-05	0.009	0.047
ADS-9	0.012	0.013	1.23E-03	0.007	0.036
ADS-10	0.012	0.010	4.25E-04	0.008	0.038
ADS-11	0.019	0.025	5.09E-04	0.014	0.065
ADS-12	0.007	0.005	2.53E-04	0.012	0.037
ADS-13	0.005	0.008	2.90E-04	0.012	0.035
ADS-14	0.005	0.012	4.02E-04	0.010	0.037
ADS-15	0.003	0.011	2.95E-04	0.010	0.034
ADS-16	0.006	0.012	7.36E-04	0.010	0.038
ADS-17	0.005	0.010	1.98E-03	0.009	0.036
ADS-18	0.005	0.015	1.21E-03	0.008	0.039
ADS-19	0.004	0.014	1.22E-03	0.009	0.038
ADS-20	0.008	0.013	1.95E-04	0.011	0.042
ADS-21	0.007	0.009	2.59E-04	0.012	0.040
ADS-22	0.006	0.013	3.32E-04	0.010	0.041
ADS-23	0.008	0.012	2.78E-04	0.010	0.042
ADS-24	0.003	0.018	4.87E-04	0.009	0.043
ADS-25	0.003	0.014	3.99E-04	0.010	0.036

Sample	P_{auth}	P_{det}	P_{mag}	P_{org}	P_{Tot}
	wt%	wt%	wt%	wt%	wt%
ADS-27	0.008	0.008	7.06E-05	0.006	0.036
ADS-28	0.001	0.013	7.09E-04	0.008	0.036
ADS-29	0.008	0.021	3.53E-04	0.009	0.050
ADS-30	0.005	0.009	4.50E-04	0.011	0.045
ADS-31	0.006	0.008	9.64E-04	0.008	0.046
ADS-32	0.004	0.009	6.03E-04	0.010	0.039
ADS-33	0.001	0.001	1.30E-03	0.009	0.029
ADS-34	0.000	0.001	5.51E-04	0.008	0.019
ADS-35	0.001	0.001	7.03E-04	0.012	0.029
ADS-36	4.33E-04	0.001	1.01E-03	0.009	0.033
ADS-37	6.23E-04	0.001	4.56E-04	0.015	0.026

Appendix D

Table D.1 Iron speciation, Al and TOC results for the Kel'tma core taken from Johnston et al. (2012)

Table D.2 Phosphorus speciation results for the Kel'tma core

Table D.3 Kostovo core iron speciation, TOC and Al results supplied by Romain Guilbaud

Table D.4 Kostovo core phosphorus speciation results

Table D.5 Iron speciation, TOC and Al (wt%) results for the Avalon Peninsula taken from Canfield et al. (2007)

Table D.6 Phosphorus speciation results for samples chosen from the Avalon Peninsula

Table D.7 Cariboo Mountain iron speciation, TOC and Al results. Taken from Canfield et al. (2008)

Table D.8 Cariboo Mountain phosphorus speciation results

Table D.9 Narana Formation iron speciation and TOC results determined by Rachel Beaumont at University of Leeds. Al results measured in this research

Table D.10 Phosphorus speciation results for the Narana Formation, Upper Ungoolya Group, Officer Basin

Table D.1 Iron speciation, Al and TOC results for the Kel'tma core taken from Johnston et al. (2012)

Sample	Depth	Fe_{CARB}	Fe_{OX}	Fe_{MAG}	Fe_T	Fe_{PY}	Fe_{HR}/Fe_T	Fe_{PY}/Fe_{HR}	Al	TOC
	m	wt%	wt%	wt%	wt%	wt%			wt%	%
1	1370.0	0.18	0.64	0.46	6.23	0.00	0.21	0.00	7.66	0.09
2	1372.0	0.30	0.64	0.48	5.39	0.01	0.26	0.01	6.64	0.07
3	1374.0	0.26	0.58	0.48	4.98	0.00	0.27	0.00	6.68	0.08
4	1376.0	0.18	0.86	0.54	6.77	0.00	0.23	0.00	7.23	0.08
5	1412.0	0.19	0.43	0.45	5.36	0.00	0.20	0.00	6.54	0.05
6	1415.8	0.20	0.43	0.42	4.79	0.01	0.22	0.01	7.33	0.08
7	1417.0	0.26	0.92	0.67	6.52	0.01	0.28	0.00	7.75	0.09
8	1454.6	0.58	0.27	0.87	5.61	0.09	0.32	0.05	7.10	0.08
9	1457.3	0.44	0.33	0.67	6.02	0.01	0.24	0.01	6.88	0.07
10	1461.2	0.58	0.39	0.82	5.67	0.00	0.32	0.00	6.34	0.07
11	1497.3	0.20	0.53	0.51	5.69	0.00	0.22	0.00	7.15	0.07
12	1503.3	0.18	0.31	0.42	4.61	0.01	0.20	0.01	7.15	0.07
13	1542.0	0.38	0.29	0.57	5.19	0.00	0.24	0.00	7.20	0.06

Sample	Depth	Fe_{CARB}	Fe_{OX}	Fe_{MAG}	Fe_T	Fe_{PY}	Fe_{HR}/Fe_T	Fe_{PY}/Fe_{HR}	Al	TOC
	m	wt%	wt%	wt%	wt%	wt%			wt%	%
14	1545.7	0.39	0.26	0.54	5.17	0.01	0.23	0.01	5.99	0.04
15	1581.3	0.31	0.08	0.37	4.64	0.01	0.17	0.02	7.16	0.05
16	1584.0	0.34	0.29	0.52	5.39	0.01	0.21	0.01	7.38	0.07
17	1587.3	0.40	0.28	0.62	5.03	0.00	0.26	0.00	6.61	0.07
18	1623.7	0.41	0.19	0.56	4.58	0.00	0.25	0.00	7.04	0.09
19	1629.2	0.48	0.23	0.67	4.45	0.00	0.31	0.00	5.90	0.07
20	1666.5	0.44	0.20	0.59	4.21	0.00	0.29	0.00	6.75	0.08
21	1670.7	0.42	0.20	0.57	4.00	0.00	0.30	0.00	6.40	0.07
22	1711.0	0.51	0.22	0.72	5.57	0.03	0.26	0.02	7.11	0.08
23	1751.0	0.57	0.12	0.73	4.92	0.04	0.30	0.02	6.81	0.08
24	1754.3	0.76	0.17	0.87	6.62	0.04	0.28	0.02	7.00	0.08
25	1783.7	0.63	0.16	0.79	5.46	0.04	0.30	0.02	7.30	0.09
26	1786.7	0.70	0.16	0.88	6.18	0.02	0.28	0.01	7.14	0.09
27	1829.0	0.71	0.18	0.87	6.49	0.01	0.27	0.01	7.55	0.10

Sample	Depth	Fe_{CARB}	Fe_{OX}	Fe_{MAG}	Fe_T	Fe_{PY}	Fe_{HR}/Fe_T	Fe_{PY}/Fe_{HR}	Al	TOC
	m	wt%	wt%	wt%	wt%	wt%			wt%	%
28	1870.0	0.62	0.23	0.75	5.97	0.01	0.27	0.01	7.21	0.10
29	1899.0	0.78	0.21	0.68	6.36	0.01	0.26	0.01	7.66	0.10
30	1902.4	0.60	0.17	0.60	5.48	0.05	0.26	0.04	6.56	0.09
31	1906.0	0.62	0.19	0.56	5.52	0.04	0.25	0.03	7.03	0.09
32	1956.2	0.76	0.25	0.71	5.86	0.05	0.30	0.03	7.52	0.22
33	1997.0	0.87	0.20	0.72	5.61	0.03	0.32	0.01	7.49	0.10
34	2034.0	0.61	0.18	0.64	5.37	0.05	0.27	0.03	7.04	0.14
35	2042.0	0.79	0.17	0.66	6.02	0.09	0.29	0.05	7.20	0.10
36	2081.0	0.80	0.18	0.57	5.84	0.12	0.29	0.07	7.73	0.14
37	2123.0	0.55	0.28	0.73	5.30	0.01	0.30	0.00	7.18	0.09
38	2162.0	0.40	0.12	0.45	4.57	0.18	0.25	0.16	6.88	0.10
39	2204.0	0.35	0.16	0.47	4.52	0.02	0.22	0.02	7.14	0.07
40	2205.0	0.36	0.13	0.45	4.42	0.04	0.22	0.04	8.85	0.08
41	2209.0	0.28	0.08	0.35	3.49	0.01	0.21	0.01	4.55	0.11

Sample	Depth	Fe_{CARB}	Fe_{OX}	Fe_{MAG}	Fe_T	Fe_{PY}	Fe_{HR}/Fe_T	Fe_{PY}/Fe_{HR}	Al	TOC
	m	wt%	wt%	wt%	wt%	wt%			wt%	%
43	2251.0	0.32	0.09	0.37	3.70	0.01	0.21	0.01	5.60	0.07
44	2291	0.28	0.36	0.52	5.05	0	0.23	0	8.54	0.11
48	2302.5	0.26	0.22	0.40	4.81	0.01	0.18	0.01	8.23	0.07
111	3946.0	0.62	0.01	0.01	1.38	0.16	0.58	0.20	0.44	0.04
112	3951.3	0.40	0.01	0.01	0.50	0.01	0.84	0.03	0.41	0.04
114	3994.5	0.49	0.02	0.01	1.33	0.18	0.53	0.26	1.00	0.12
115	4032				0.54	0.01	0.96	0.02	0.25	0.04
116	4107.0	0.22	0.02	0.02	0.59	0.12	0.66	0.31	0.66	0.07
121	4307.0	1.07	0.02	0.02	1.77	0.10	0.68	0.08	2.23	0.27
123	4352.0	0.03	1.25	0.42	4.72	0.00	0.36	0.00	6.37	0.03
124	4386.0	1.19	0.03	0.02	1.82	0.02	0.69	0.01	1.63	0.24
125	4387.0	0.12	0.04	0.04	2.49	0.00	0.08	0.02	8.22	0.37
127	4462.0	0.22	0.00	0.01	0.60	0.04	0.44	0.14	1.61	0.07
128	4502.0	0.19	0.01	0.01	0.77	0.01	0.28	0.04	1.78	0.22

Sample	Depth	Fe_{CARB}	Fe_{OX}	Fe_{MAG}	Fe_T	Fe_{PY}	Fe_{HR}/Fe_T	Fe_{PY}/Fe_{HR}	Al	TOC
	m	wt%	wt%	wt%	wt%	wt%			wt%	%
129	4553.5	0.22	0.01	0.01	0.75	0.04	0.37	0.16	1.17	0.11
132	4640.0	0.22	0.00	0.00	0.44	0.04	0.61	0.16	4.19	0.27
133	4640.5	0.21	0.10	0.17	2.57	0.00	0.19	0.01	4.63	0.05
137	4824.7	0.24	0.04	0.12	3.00	0.00	0.13	0.00	5.46	0.07
139	4852.5	0.41	0.02	0.04	1.09	0.01	0.45	0.03	1.93	0.11
140	4901.0	0.32	0.02	0.02	0.99	0.01	0.37	0.02	1.80	0.07

Table D.2 Phosphorus speciation results for the Kel'tma core

Sample	Depth	P_{Tot}	P_{Fe}	P_{auth}	P_{det}	P_{mag}	P_{org}
	m	wt%	ppm	ppm	ppm	ppm	ppm
1	1370	0.078	0.98	278.78	176.97	11.74	22.71
2	1372	0.070	0.28	163.45	233.59	10.02	18.27
3	1374	0.070	7.51	205.40	191.89	7.84	13.80
4	1376	0.078	0.00	313.35	146.65	7.16	21.61
5	1412	0.060	0.19	214.02	170.44	0.44	15.53
6	1415.8	0.069	0.10	254.55	186.28	8.22	16.78
7	1417	0.103	0.06	465.04	363.60	22.80	29.73
8	1454.6	0.072	0.11	170.77	261.13	15.33	20.91
9	1457.3	0.065	0.13	167.90	193.63	9.43	15.84
10	1461.2	0.053	0.13	101.35	225.72	9.71	12.77
11	1497.3	0.076	2.39	261.46	201.90	10.53	20.42
12	1503.3	0.072	0.60	265.69	228.74	11.01	17.31
13	1542	0.071	0.06	249.14	244.65	11.59	12.78
14	1545.7	0.069	0.22	109.01	289.64	10.96	6.62
15	1581.3	0.066	0.17	266.60	196.48	9.65	12.48
16	1584	0.067	0.12	236.93	182.87	8.22	7.54
17	1587.3	0.061	0.18	88.49	276.73	11.16	8.08
18	1623.7	0.067	0.29	195.29	219.99	9.12	8.97
19	1629.2	0.073	0.10	102.74	422.44	11.38	5.73
20	1666.5	0.065	0.06	170.96	253.14	10.65	9.43
21	1670.7	0.058	0.10	115.21	244.52	9.80	8.04
22	1711	0.073	16.01	134.24	278.75	12.96	15.86
23	1751	0.072	10.87	127.47	335.62	11.45	16.13
24	1754.3	0.077	18.24	95.87	371.90	13.70	15.24

Sample	Depth	P_{Tot}	P_{Fe}	P_{auth}	P_{det}	P_{mag}	P_{org}
	m	wt%	ppm	ppm	ppm	ppm	ppm
25	1783.7	0.077	16.49	152.49	346.53	13.61	23.62
26	1786.7	0.087	13.01	109.76	461.71	17.80	20.32
27	1829	0.087	15.74	162.09	362.72	16.17	23.40
28	1870	0.072	15.20	113.38	360.89	15.76	28.62
29	1899	0.090	15.41	165.10	420.63	15.75	35.98
30	1902.4	0.058	18.35	50.76	269.41	10.68	29.95
31	1906	0.066	18.11	67.51	282.50	14.46	34.72
32	1956.2	0.076	17.53	88.34	293.82	15.42	35.44
33	1997	0.086	16.86	97.51	423.71	21.46	28.21
34	2034	0.065	14.59	72.54	253.11	0.36	28.96
35	2042	0.088	20.18	68.33	401.79	18.83	33.48
36	2081	0.097	21.62	127.76	383.54	16.71	49.31
37	2123	0.068	16.25	103.49	213.61	12.11	35.42
38	2162	0.063	13.48	128.42	263.00	12.29	39.80
39	2204	0.057	16.10	111.41	147.97	9.26	36.68
41	2209	0.048	0.19	47.21	125.61	0.88	29.73
43	2251	0.082	0.00	89.63	147.04	0.45	54.38
44	2291	0.060	0.12	271.69	221.08	15.95	34.53
48	2302.5	0.007	0.00	152.10	133.43	10.74	59.89
111	3946	0.007	0.10	16.68	51.35	0.26	21.73
111B	3946	0.037	0.11	18.15	56.89	0.34	17.13
112	3951.3	0.062	0.10	35.41	267.58	0.15	6.97
114	3994.5	0.008	0.16	24.08	483.80	1.10	12.20
115	4032	0.016	0.10	14.79	64.87	0.31	28.46
116	4107	0.015	0.06	33.46	125.66	0.18	47.70

Sample	Depth	P_{Tot}	P_{Fe}	P_{auth}	P_{det}	P_{mag}	P_{org}
	m	wt%	ppm	ppm	ppm	ppm	ppm
116B	4107	0.004	0.60	29.49	126.71	0.55	53.65
119	4258	0.062	0.06	10.85	59.20	0.06	5.72
120	4304.5	0.014	0.13	32.73	632.39	11.86	49.35
121	4307	0.043	0.45	12.90	112.48	0.40	60.18
123	4352	0.006	0.06	74.72	114.12	0.31	61.90
124	4386	0.017	0.28	11.70	64.78	1.24	48.05
125	4387	0.023	0.23	12.61	64.81	1.05	17.69
127	4462	0.011	0.00	19.83	171.26	0.06	58.80
128	4502	0.026	0.68	12.91	72.85	0.97	60.53
129	4553.5	0.058	0.11	18.85	205.68	0.54	48.46
131	4605	0.044	0.06	24.51	549.07	0.11	48.34
132	4640	0.102	8.94	27.63	323.70	0.74	40.03
133	4640.5	0.185	0.06	66.82	705.67	18.48	75.83
137	4824.7	0.175	0.00	63.35	1408.63	23.27	52.49
137B	4824.7	0.061	0.06	54.12	1664.61	28.28	60.73
139	4852.5	0.043	0.25	33.65	545.91	0.25	56.01
140	4901	0.044	0.12	32.13	303.52	0.12	11.13

Table D.3 Kostovo core iron speciation, TOC and Al results supplied by Romain Guilbaud

Sample	Depth	Fe_T	Fe_{CARB}	Fe_{OX}	Fe_{MAG}	Fe_{PY}	Fe_{HR}/Fe_T	Fe_{PY}/Fe_{HR}	TOC	Al
	m	wt%	wt%	wt%	wt%	wt%			wt%	wt%
KS-57	244.50	3.34	0.72	0.19	0.48	0.01	0.42	0.01	0.08	8.2
KS-58	246.50	4.78	1.67	0.20	1.13	0.02	0.63	0.01	0.17	6.1
KS-59	252.60	5.43	0.91	0.28	1.29	0.03	0.46	0.01	0.23	7.4
KS-60	253.00	4.29	0.94	0.27	0.82	0.05	0.49	0.03	0.13	6.8
KS-61	253.90	3.59	0.53	0.15	0.46	0.00	0.32	0.00	0.18	8.2
KS-62	254.40	4.06	0.61	0.16	0.58	0.02	0.34	0.01	0.42	8.5
KS-63	257.50	2.54	0.33	0.11	0.24	0.01	0.27	0.01	0.40	7.7
KS-65	258.20	4.06	0.72	0.22	0.77	0.01	0.42	0.01	0.38	7.7
KS-66	259.20	3.81	0.62	0.19	0.58	0.04	0.37	0.03	0.81	7.6
KS-68	263.40	3.31	0.63	0.18	0.54	0.07	0.43	0.05	0.30	7.4
KS-69	263.80	5.18	1.44	0.50	0.63	0.10	0.52	0.04	1.14	9.1
KS-70	264.40	4.30	0.78	0.21	0.69	0.03	0.40	0.02	0.49	8.8
KS-71	265.40	4.54	0.95	0.25	0.85	0.01	0.45	0.00	0.52	9.6

Sample	Depth	Fe_T	Fe_{CARB}	Fe_{OX}	Fe_{MAG}	Fe_{PY}	Fe_{HR}/Fe_T	Fe_{PY}/Fe_{HR}	TOC	Al
	m	wt%	wt%	wt%	wt%	wt%			wt%	wt%
KS-73	267.50	4.95	0.90	0.25	1.00	0.06	0.45	0.03	0.51	9.3
KS-74	268.50	5.31	1.38	0.48	0.73	0.04	0.50	0.02	0.92	9.4
KS-75	271.20	4.60	0.88	0.25	0.80	0.08	0.43	0.04	0.84	9.5
KS-76	272.20	4.17	0.69	0.21	0.65	0.06	0.39	0.04	1.37	9.6
KS-77	276.00	3.87	0.89	0.21	0.75	0.03	0.49	0.02	0.45	8.1
KS-78	279.20	3.56	0.58	0.17	0.48	0.01	0.35	0.01	0.21	8.4
KS-79	279.50	4.44	1.06	0.24	0.79	0.06	0.48	0.03	0.58	8.4
KS-80	285.20	3.23	0.64	0.14	0.49	0.05	0.41	0.03	0.54	6.2
KS-81	287.90	3.44	0.63	0.16	0.51	0.03	0.38	0.02	0.48	8.1
KS-83	293.20	3.68	0.62	0.17	0.53	0.04	0.37	0.03	0.60	8.8
KS-84	298.30	4.34	0.61	0.18	0.62	0.05	0.34	0.04	0.81	9.9
KS-85	301.20	3.72	0.50	0.16	0.47	0.01	0.31	0.01	0.64	9.0
KS-86	307.50	3.93	0.70	0.15	0.55	0.05	0.37	0.04	0.71	8.6
KS-87	308.40	3.86	0.51	0.18	0.38	0.01	0.28	0.01	0.51	10.5

Sample	Depth	Fe_T	Fe_{CARB}	Fe_{OX}	Fe_{MAG}	Fe_{PY}	Fe_{HR}/Fe_T	Fe_{PY}/Fe_{HR}	TOC	Al
	m	wt%	wt%	wt%	wt%	wt%			wt%	wt%
KS-89	309.40	3.80	0.34	0.16	0.40	0.01	0.24	0.01	0.41	8.3
KS-91	313.30	3.49	0.46	0.23	0.48	0.10	0.36	0.08	0.82	6.2
KS-94	322.40	4.29	0.34	0.20	0.38	0.07	0.23	0.07	0.34	5.7
KS-95	323.00	4.31	0.41	0.17	0.47	0.03	0.25	0.03	0.58	6.2
KS-96	323.80	4.32	0.33	0.16	0.46	0.10	0.25	0.10	0.84	5.8
KS-97	326.70	3.46	0.65	0.34	0.54	0.02	0.45	0.01	0.55	8.2
KS-98	329.90	3.63	0.32	0.15	0.34	0.01	0.23	0.02	0.41	6.8
KS-99	332.30	4.22	0.39	0.16	0.41	0.07	0.25	0.07	0.98	6.5
KS-101	335.00	5.53	0.90	0.56	0.64	0.08	0.39	0.04	0.93	7.1
KS-102	340.00	3.89	0.24	0.13	0.33	0.02	0.19	0.03	0.68	9.1
KS-103	344.20	7.35	2.03	0.49	1.99	0.06	0.62	0.01	0.52	5.0
KS-104	348.00	3.53	0.21	0.11	0.24	0.01	0.16	0.02	0.43	5.8
KS-105	349.80	22.09	7.34	1.42	6.49	0.05	0.69	0.00	0.39	2.9
KS-106	350.80	5.75	0.48	0.19	0.44	0.08	0.21	0.07	0.93	9.1

Sample	Depth	Fe_T	Fe_{CARB}	Fe_{OX}	Fe_{MAG}	Fe_{PY}	Fe_{HR}/Fe_T	Fe_{PY}/Fe_{HR}	TOC	Al
	m	wt%	wt%	wt%	wt%	wt%			wt%	wt%
KS-109	358.50	*41.46*	0.15	38.66	1.37	0.01	0.97	0.00	0.30	1.5
KS-110	358.60	3.65	0.47	0.21	0.30	0.10	0.30	0.10	1.07	5.3
KS-111	360.50	*30.47*	5.67	8.01	5.12	0.05	0.62	0.00	0.23	3.4
KS-112	368.00	7.58	4.64	0.46	1.40	0.02	0.86	0.00	0.22	3.8
KS-113	371.20	2.87	0.19	0.10	0.22	0.03	0.18	0.05	0.27	8.1
KS-114	372.80	46.58	0.82	1.60	0.48	0.03	0.06	0.01	0.38	6.7
KS-115	377.40	2.75	0.39	0.12	0.29	0.01	0.30	0.01	0.20	5.4
KS-116	379.00	24.53	0.04	21.30	0.65	0.02	0.90	0.00	0.29	4.7
KS-118	383.80	*34.89*	0.33	33.96	0.88	0.00	1.01	0.00	0.20	2.4
KS-119	383.90	4.25	0.43	0.27	0.70	0.03	0.34	0.02	0.53	8.1
KS-123	390.00	3.21	0.31	0.27	0.29	0.04	0.28	0.04	0.41	5.2
KS-125	393.00	*35.99*	3.75	24.44	3.49	0.09	0.88	0.00	0.17	1.9
KS-126	396.10	3.56	1.26	0.28	0.58	0.04	0.61	0.02	0.15	4.3
KS-127	407.00	3.52	0.45	0.18	0.62	0.00	0.36	0.00	0.17	7.8

Sample	**Depth**	**Fe_T**	**Fe_{CARB}**	**Fe_{OX}**	**Fe_{MAG}**	**Fe_{PY}**	**Fe_{HR}/Fe_T**	**Fe_{PY}/Fe_{HR}**	**TOC**	**Al**
	m	**wt%**	**wt%**	**wt%**	**wt%**	**wt%**			**wt%**	**wt%**
KS-128	409.50	5.62	0.66	0.58	1.31	0.01	0.45	0.00	0.10	7.1
KS-129	411.40	7.15	1.00	0.32	1.90	0.09	0.46	0.03	0.09	8.1
KS-130	416.60	8.30	1.29	0.79	2.30	0.03	0.53	0.01	0.08	9.1
KS-131	418.40	1.94	0.22	0.06	0.19	0.00	0.24	0.00	0.12	8.6
KS-132	422.50	7.15	0.33	2.12	1.32	0.00	0.53	0.00	0.12	10.7
KS-133	423.20	6.48	0.19	2.47	0.93	0.00	0.55	0.00	0.14	9.8
KS-134	427.10	4.65	0.30	0.53	0.67	0.11	0.35	0.07	0.09	8.3
KS-135	429.90	4.93	0.20	1.11	0.50	0.08	0.38	0.04	0.16	7.4
KS-136	434.50	5.19	0.26	0.86	0.52	0.09	0.33	0.05	0.11	8.5
KS-137	435.70	4.91	0.32	1.05	0.58	0.00	0.40	0.00	0.14	8.0
KS-138	437.10	4.54	0.21	1.26	0.33	0.28	0.46	0.13	0.15	8.1
KS-139	441.30	*3.58*	0.44	0.14	0.53	0.00	0.31	0.00	0.12	8.4

Table D.4 Kostovo core phosphorus speciation results

Sample	Depth	P_{Tot}	P_{Fe}	P_{auth}	P_{det}	P_{mag}	P_{org}
	m	wt%	ppm	ppm	ppm	ppm	ppm
KS-57	244.5	0.023	1.164	88.107	55.654	7.703	14.969
KS-58	246.5	0.038	0.384	215.647	74.298	6.304	23.463
KS-59	252.6	0.012	0.284	11.925	27.413	0.568	20.672
KS-61	253.9	0.024	0.288	87.129	61.634	7.296	27.850
KS-62	254.4	0.019	0.712	46.392	51.560	6.650	36.395
KS-63	257.5	0.014	31.173	14.159	33.146	0.698	19.335
KS-65	258.2	0.014	32.411	14.304	35.218	1.127	22.070
KS-66	259.2	0.013	1.530	20.665	38.002	6.308	30.485
KS-68	263.4	0.013	1.789	17.949	38.572	0.740	33.201
KS-69	263.8	0.018	18.583	27.620	45.678	6.900	34.035
KS-70	264.4	0.018	0.984	33.515	54.909	7.614	35.048
KS-71	265.4	0.044	0.571	219.035	128.899	14.531	34.825
KS-73	267.5	0.024	1.218	78.375	77.110	8.658	30.752

Sample	Depth	P_{Tot}	P_{Fe}	P_{auth}	P_{det}	P_{mag}	P_{org}
	m	wt%	ppm	ppm	ppm	ppm	ppm
KS-74	268.5	0.021	19.157	34.377	66.264	7.822	40.232
KS-75	271.2	0.017	1.089	26.587	45.973	0.666	25.381
KS-76	272.2	0.020	0.961	44.949	63.070	8.445	35.785
KS-77	276	0.016	0.832	28.966	57.346	8.156	31.773
KS-78	279.2	0.011	0.296	10.211	21.118	0.237	22.995
KS-79	279.5	0.017	1.066	27.521	67.028	7.925	31.405
KS-80	285.2	0.013	0.555	25.594	46.355	0.493	24.885
KS-81	287.9	0.014	0.495	23.701	43.053	6.296	28.572
KS-83	293.2	0.016	1.835	23.661	40.497	0.779	33.894
KS-84	298.3	0.016	0.684	22.699	32.469	0.513	45.547
KS-85	301.2	0.015	0.360	15.122	24.673	0.480	40.805
KS-86	307.5	0.021	1.024	22.796	53.120	6.862	41.416
KS-87	308.4	0.017	0.870	18.137	30.995	0.497	38.375
KS-89	309.4	0.015	0.557	21.583	36.156	0.724	30.865

Sample	Depth	P_{Tot}	P_{Fe}	P_{auth}	P_{det}	P_{mag}	P_{org}
	m	wt%	ppm	ppm	ppm	ppm	ppm
KS-91	313.3	0.012	1.287	24.717	32.418	0.702	50.016
KS-94	322.4	0.020	0.756	66.673	63.234	8.987	41.532
KS-95	323	0.017	0.932	30.955	41.818	0.995	46.246
KS-96	323.8	0.015	0.635	30.853	54.309	7.974	44.251
KS-97	326.7	0.014	0.914	19.483	29.833	0.514	42.037
KS-98	329.9	0.014	1.017	33.291	51.828	0.890	38.242
KS-99	332.3	0.015	1.749	25.548	35.993	1.108	53.529
KS-102	340	0.014	1.566	19.495	26.335	0.636	41.826
KS-103	344.2	0.014	0.913	13.562	64.650	7.130	35.738
KS-104	348	0.012	0.910	22.999	20.754	0.963	38.119
KS-106	350.8	0.017	0.817	63.459	47.096	2.742	36.938
KS-109	358.5	0.050	152.527	14.265	1.528	22.855	5.729
KS-110	358.6	0.017	1.643	15.456	23.068	1.007	32.295
KS-111	360.5	0.043	201.675	22.452	144.313	0.395	10.276

Sample	**Depth**	**P_{Tot}**	**P_{Fe}**	**P_{auth}**	**P_{det}**	**P_{mag}**	**P_{org}**
	m	**wt%**	**ppm**	**ppm**	**ppm**	**ppm**	**ppm**
KS-113	371.2	0.013	0.646	10.550	28.123	0.538	23.436
KS-114	372.8	0.017	32.751	18.083	37.262	0.680	19.459
KS-115	377.4	0.012	0.367	7.669	24.065	0.734	21.990
KS-119	383.9	0.030	118.122	31.569	44.563	6.848	44.979
KS-123	390	0.015	0.313	22.362	22.820	0.752	27.781
KS-125	393	0.068	477.850	19.304	144.875	0.608	8.316
KS-126	396.1	0.017	0.094	20.587	49.524	6.252	36.864
KS-127	407	0.013	0.115	18.008	15.013	0.345	37.760
KS-129	411.4	0.015	0.000	13.258	22.389	0.298	29.852
KS-130	416.6	0.021	0.065	39.516	28.758	0.649	32.353
KS-131	418.4	0.018	0.411	22.745	13.433	0.977	36.635
KS-133	423.2	0.048	38.232	170.589	73.678	11.157	103.511
KS-134	427.1	0.021	0.616	30.501	41.195	0.504	52.268
KS-135	429.9	0.019	0.098	29.366	34.218	6.959	51.326

Sample	Depth	P_{Tot}	P_{Fe}	P_{auth}	P_{det}	P_{mag}	P_{org}
	m	wt%	ppm	ppm	ppm	ppm	ppm
KS-136	434.5	0.067	5.278	115.117	176.169	16.568	44.042
KS-137	435.7	0.022	0.100	30.302	53.379	7.788	49.029
KS-138	437.1	0.043	74.555	130.229	118.604	10.340	44.476
KS-139	441.3	0.022	0.051	50.584	24.778	0.462	47.931

Table D.5 Iron speciation, TOC and Al (wt%) results for the Avalon Peninsula taken from Canfield et al. (2007)

Sample I.D.	Age	Fe_T	Fe_{CARB}	Fe_{OX}	Fe_{MAG}	Fe_{PY}	Fe_{HR}/Fe_T	Fe_{PY}/Fe_{HR}	TOC	Al
	Ma	wt%	wt%	wt%	wt%	wt%			wt%	wt%
DEC-05-108	560	5.36	0.51	0.26	0.33	0.01	0.21	0.00	0.00	8.80
DEC-05-109	560	4.88	0.35	0.20	0.27	0.01	0.17	0.01	0.00	8.40
DEC-05-39	559.41	4.39	0.32	0.30	0.30	0.02	0.21	0.02	0	7.53
DEC-05-40	559.35	4.31	0.35	0.32	0.33	0.00	0.23	0.00	0	7.85
DEC-05-41	559.29	3.77	0.31	0.32	0.25	0.14	0.27	0.14	0.003	7.33
DEC-05-42	559.24	3.34	0.31	0.35	0.30	0.01	0.29	0.01	0	7.00
DEC-05-43	559.18	3.30	0.29	0.27	0.25	0.00	0.25	0.00	0	6.75
DEC-05-45	559.06	5.05	0.32	0.28	0.29	0.36	0.25	0.29	0.01	8.19
DEC-05-136	558.7	4.71	0.24	0.20	0.21	0.09	0.16	0.12	0.151	8.38
DEC-05-137	558.5	4.72	0.21	0.23	0.20	0.21	0.18	0.25	0.114	8.83

Sample I.D.	Age	Fe_T	Fe_{CARB}	Fe_{OX}	Fe_{MAG}	Fe_{PY}	Fe_{HR}/Fe_T	Fe_{PY}/Fe_{HR}	TOC	Al
	Ma	wt%	wt%	wt%	wt%	wt%			wt%	wt%
DEC-05-140	557.9	4.46	0.23	0.32	0.21	0.01	0.18	0.01	0	8.39
DEC-05-141	557.7	4.44	0.21	0.16	0.18	0.05	0.13	0.08	0	9.09
DEC-05-142	557.5	4.27	0.26	0.28	0.21	0.17	0.22	0.18	0	7.97
DEC-05-145	556.9	4.40	0.23	0.25	0.21	0.02	0.16	0.03	0	9.20
DEC-05-75	555.88	5.04	0.37	0.25	0.22	0.40	0.25	0.32	0.051	8.20
DEC-05-76	555.76	4.58	0.29	0.27	0.21	0.00	0.17	0.00	0.044	8.60
DEC-05-77	555.65	4.70	0.27	0.23	0.18	0.23	0.19	0.25	0.113	8.62
DEC-05-78	555.53	3.64	0.28	0.26	0.15	0.08	0.21	0.10	0.082	7.57
DEC-05-79	555.41	3.93	0.33	0.45	0.24	0.08	0.28	0.08	0.026	6.81
DEC-05-80	555.29	4.23	0.31	0.39	0.23	0.14	0.25	0.13	0.045	7.71
DEC-05-84	554.82	4.23	0.27	0.22	0.23	0.02	0.17	0.03	0.00	8.51

Sample I.D.	Age	Fe_T	Fe_{CARB}	Fe_{OX}	Fe_{MAG}	Fe_{PY}	Fe_{HR}/Fe_T	Fe_{PY}/Fe_{HR}	TOC	Al
	Ma	wt%	wt%	wt%	wt%	wt%			wt%	wt%
DEC-05-85	554.7	4.44	0.31	0.25	0.22	0.02	0.18	0.03	0.00	8.65
DEC-05-86	554.58	4.59	0.31	0.23	0.24	0.06	0.18	0.07	0.00	8.60
DEC-05-87	554.47	4.48	0.30	0.25	0.25	0.02	0.18	0.02	0.00	8.60
DEC-05-88	554.35	4.66	0.29	0.34	0.24	0.02	0.19	0.02	0.00	8.37
DEC-05-89	554.23	4.58	0.29	0.30	0.24	0.04	0.19	0.04	0.13	8.41
DEC-05-90	554.11	4.40	0.29	0.24	0.23	0.04	0.18	0.05	0.12	8.45
DEC-05-91	553.99	4.96	0.28	0.26	0.27	0.08	0.18	0.09	0.12	8.73
DEC-05-68	553.5	4.26	0.29	0.21	0.21	0.13	0.19	0.15	0.013	8.43
DEC-05-69	553.3	4.43	0.33	0.24	0.22	0.14	0.21	0.15	0	6.42
DEC-05-70	553.1	4.66	0.29	0.28	0.21	0.08	0.19	0.09	0	8.89
DEC-05-71	552.9	4.37	0.33	0.44	0.18	0.04	0.23	0.04	0	8.40
DEC-05-72	552.7	4.24	0.30	0.27	0.19	0.12	0.21	0.14	0.01	8.24
DEC-05-73	552.5	2.30	0.34	0.18	0.06	0.55	0.49	0.49	0	5.79

Table D.6 Phosphorus speciation results for samples chosen from the Avalon Peninsula

Sample I.D.	Age	P_{Tot}	P_{Fe}	P_{auth}	P_{det}	P_{mag}	P_{org}
	Ma	wt%	ppm	ppm	ppm	ppm	ppm
DEC-05-108	560	0.056	1723.06	30.63	493.18	16.56	0.32
DEC-05-109	560	0.062	20272.09	40.23	440.54	15.04	41.86
DEC-05-39	559.41	0.063	10879.94	14.25	495.75	15.06	1.80
DEC-05-40	559.35	0.059	11504.81	10.22	492.38	13.61	1.49
DEC-05-41	559.29	0.049	34123.30	46.82	306.39	11.99	0.37
DEC-05-42	559.24	0.040	25070.87	60.81	248.41	10.51	0.33
DEC-05-43	559.18	0.048	30600.13	47.33	304.25	10.23	0.67
DEC-05-45	559.06	0.226	22418.87	83.43	1428.51	51.79	0.70
DEC-05-136	558.7	0.060	757.06	30.87	429.84	14.10	0.32
DEC-05-137	558.5	0.140	344.64	55.28	1073.73	22.83	0.45
DEC-05-140	557.9	0.033	652.50	73.84	110.49	8.35	0.46
DEC-05-141	557.7	0.056	356.97	134.18	255.81	13.89	0.21
DEC-05-142	557.5	0.079	853.46	15.87	565.22	21.20	0.12

Sample I.D.	Age	P_{Tot}	P_{Fe}	P_{auth}	P_{det}	P_{mag}	P_{org}
	Ma	wt%	ppm	ppm	ppm	ppm	ppm
DEC-05-145	556.9	0.183	4850.33	366.14	1298.63	40.44	0.68
DEC-05-75	555.88	0.128	971.89	23.60	990.85	32.85	0.50
DEC-05-76	555.76	0.070	31203.55	83.97	426.70	19.24	2.34
DEC-05-77	555.65	0.073	10217.80	40.06	487.69	15.16	0.32
DEC-05-78	555.53	0.073	95112.20	117.66	390.35	15.46	0.23
DEC-05-79	555.41	0.109	6491.79	56.07	783.06	28.42	0.22
DEC-05-80	555.29	0.053	776.90	55.10	320.93	19.07	0.12
DEC-05-84	554.82	0.062	39829.98	40.29	374.44	13.56	0.21
DEC-05-85	554.7	0.069	36841.40	44.06	427.84	15.15	0.72
DEC-05-86	554.58	0.069	1336.00	61.13	443.10	15.84	0.21
DEC-05-87	554.47	0.077	1499.07	54.73	574.12	19.56	1.86
DEC-05-88	554.35	0.099	700.05	51.43	751.14	22.42	0.21
DEC-05-89	554.23	0.074	12626.77	53.08	519.78	15.02	0.24
DEC-05-90	554.11	0.094	1139.68	51.00	717.35	20.98	0.31

Sample I.D.	Age	P_{Tot}	P_{Fe}	P_{auth}	P_{det}	P_{mag}	P_{org}
	Ma	wt%	ppm	ppm	ppm	ppm	ppm
DEC-05-91	553.99	0.070	12572.22	48.11	507.41	18.86	0.48
DEC-05-68	553.5	0.095	22316.03	100.79	706.02	20.95	0.38
DEC-05-69	553.3	0.067	437.42	19.54	504.13	16.37	0.25
DEC-05-70	553.1	0.100	1126.03	44.40	698.50	22.79	0.61
DEC-05-71	552.9	0.089	7738.74	47.84	620.64	22.63	0.53
DEC-05-72	552.7	0.098	25467.65	76.89	736.57	24.65	0.46
DEC-05-73	552.5	0.073	12797.62	40.03	520.32	17.37	0.55

Table D.7 Cariboo Mountain iron speciation, TOC and Al results. Taken from Canfield et al. (2008)

Sample I.D.	Age	Fe_T	Fe_{CARB}	Fe_{OX}	Fe_{MAG}	Fe_{PY}	Fe_{HR}/Fe_T	Fe_{PY}/Fe_{HR}	TOC	Al
	Ma	wt%	wt%	wt%	wt%	wt%	wt%		wt%	wt%
DEC-04-27	593.88	2.81	0.34	0.02	0.18	0.02	0.20	0.04	0.01	2.75
DEC-04-28	593.67	4.00	0.70	0.03	0.18	0.01	0.23	0.01	0.04	4.12
DEC-04-29	593.46	5.36	0.13	0.00	0.05	0.00	0.03	0.01	0.04	10.26
DEC-04-30	593.25	5.67	0.23	0.03	0.08	0.18	0.09	0.36	0.06	9.03
DEC-04-31	593.10	7.52	0.24	0.03	0.11	0.05	0.06	0.11	0.03	8.22
DEC-04-41	591.65	7.14	0.29	0.03	0.13	0.01	0.06	0.02	0.02	7.68
DEC-04-42	591.50	3.84	0.25	0.01	0.15	0.02	0.11	0.05	0.04	5.43
DEC-04-43	591.36	11.61	0.32	0.00	0.14	0.17	0.05	0.27	0.03	8.42
DEC-04-44	591.21	6.44	0.17	0.07	0.06	0.09	0.06	0.24	0.02	8.86
DEC-04-46	590.92	2.85	0.42	0.01	0.17	0.04	0.22	0.06	0.02	3.11
DEC-04-47	590.77	2.98	0.11	0.00	0.07	0.46	0.21	0.72	0.03	6.41
DEC-04-48	590.63	4.25	0.10	0.08	0.04	0.05	0.06	0.19	0.02	9.89
DEC-04-49	590.48	6.15	0.30	0.02	0.14	0.46	0.15	0.50	0.02	6.12

Sample I.D.	Age	Fe_T	Fe_{CARB}	Fe_{OX}	Fe_{MAG}	Fe_{PY}	Fe_{HR}/Fe_T	Fe_{PY}/Fe_{HR}	TOC	Al
	Ma	wt%	wt%	wt%	wt%	wt%	wt%		wt%	wt%
DEC-04-50	590.34	3.71	0.23	0.00	0.16	0.01	0.11	0.01	0.02	4.66
DEC-04-54	589.75	6.00	0.17	0.02	0.07	0.10	0.06	0.27	0.06	9.08
DEC-04-55	589.55	6.01	0.27	0.03	0.07	0.27	0.10	0.43	0.10	9.38
DEC-04-56	589.36	5.12	0.40	0.01	0.14	0.30	0.17	0.35	0.02	5.02
DEC-04-57	589.16	8.92	0.24	0.01	0.11	0.01	0.04	0.03	0.09	9.63
DEC-04-58	588.97	7.23	0.22	0.02	0.10	0.26	0.08	0.44	0.04	8.14
DEC-04-59	588.77	5.50	0.32	0.09	0.15	0.11	0.12	0.16	0.08	10.49
DEC-04-65	587.60	7.21	0.30	0.39	0.12	0.30	0.15	0.27	0.05	6.21
DEC-04-66	587.40	8.18	0.57	0.08	0.09	0.24	0.12	0.24	0.07	7.66
DEC-04-68	587.01	6.88	0.33	0.06	0.07	0.01	0.07	0.03	0.07	9.51
DEC-04-72	586.23	6.64	0.18	0.10	0.08	0.08	0.07	0.18	0.08	9.01
DEC-04-73	586.03	5.84	0.13	0.22	0.05	0.07	0.08	0.16	0.09	10.61
DEC-04-74	585.84	6.40	0.29	0.06	0.06	0.03	0.07	0.06	0.08	8.98
DEC-04-136	569.50	4.28	0.45	0.01	0.12	0.23	0.19	0.28	0.19	7.20

Sample I.D.	**Age**	**Fe_T**	**Fe_{CARB}**	**Fe_{OX}**	**Fe_{MAG}**	**Fe_{PY}**	**Fe_{HR}/Fe_T**	**Fe_{PY}/Fe_{HR}**	**TOC**	**Al**
	Ma	**wt%**	**wt%**	**wt%**	**wt%**	**wt%**	**wt%**		**wt%**	**wt%**
DEC-04-137	569.20	4.50	0.53	0.19	0.10	0.52	0.30	0.39	0.21	8.65
DEC-04-138	568.90	2.20	0.48	0.14	0.16	0.32	0.49	0.29	0.07	7.86
DEC-04-147	566.50	4.37	0.27	0.04	0.12	0.43	0.20	0.50	0.13	8.06
DEC-04-148	566.25	4.94	0.52	0.09	0.16	0.42	0.24	0.36	0.10	7.49
DEC-04-149	566.00	3.49	0.33	0.05	0.11	0.13	0.18	0.21	0.12	8.51
DEC-04-150	565.75	4.36	0.36	0.27	0.13	0.08	0.19	0.09	0.10	7.11
DEC-04-151	565.50	5.17	0.71	0.05	0.18	0.07	0.20	0.07	0.07	5.53
DEC-04-152	565.25	6.47	0.27	0.09	0.10	0.11	0.09	0.19	0.09	5.96
DEC-04-161	563.13	4.55	0.18	0.12	0.08	0.09	0.10	0.19	0.04	8.38
DEC-04-162	562.78	5.38	0.27	0.10	0.11	0.16	0.12	0.25	0.05	8.61
DEC-04-163	562.44	5.17	0.27	0.18	0.12	0.83	0.27	0.59	0.05	7.74

Table D.8 Cariboo Mountain phosphorus speciation results

Sample I.D.	Age	P_{Tot}	P_{Fe}	P_{auth}	P_{det}	P_{mag}	P_{org}
	Ma	wt%	ppm	ppm	ppm	ppm	ppm
DEC-04-27	593.88	0.010	0.411	6.968	57.564	1.767	0.000
DEC-04-28	593.67	0.016	0.833	10.729	93.040	5.144	1.022
DEC-04-29	593.46	0.033	12.217	18.853	271.399	8.650	1.088
DEC-04-30	593.25	0.041	0.149	2.149	351.401	9.483	0.517
DEC-04-31	593.10	0.026	0.146	6.649	214.896	7.324	1.528
DEC-04-41	591.65	0.017	0.396	7.468	126.812	4.487	5.262
DEC-04-42	591.50	0.013	0.289	6.886	91.481	3.361	4.120
DEC-04-43	591.36	0.017	0.230	1.358	134.186	5.951	7.017
DEC-04-46	590.92	0.006	0.303	4.736	30.376	1.305	2.002
DEC-04-47	590.77	0.013	7.255	1.703	95.574	2.571	2.100
DEC-04-48	590.63	0.022	15.433	6.284	168.347	3.846	3.405
DEC-04-49	590.48	0.013	0.412	0.917	97.795	2.961	2.148
DEC-04-50	590.34	0.011	0.246	5.224	85.716	2.193	1.849

Sample I.D.	Age	P_{Tot}	P_{Fe}	P_{auth}	P_{det}	P_{mag}	P_{org}
	Ma	wt%	ppm	ppm	ppm	ppm	ppm
DEC-04-54	589.75	0.041	0.170	2.390	386.473	8.228	2.725
DEC-04-55	589.55	0.043	0.458	1.432	407.856	9.490	4.675
DEC-04-56	589.36	0.010	0.327	1.124	47.275	1.680	2.142
DEC-04-57	589.16	0.013	0.290	2.047	78.028	3.132	7.260
DEC-04-58	588.97	0.014	0.540	0.825	97.530	3.153	5.074
DEC-04-59	588.77	0.025	0.195	1.810	220.200	5.386	3.247
DEC-04-65	587.60	0.011	1.622	1.140	66.768	2.339	5.754
DEC-04-66	587.40	0.012	0.411	1.204	70.689	3.077	2.820
DEC-04-68	587.01	0.056	6.342	1.464	474.432	10.528	4.450
DEC-04-72	586.23	0.041	0.372	7.685	338.177	9.101	4.942
DEC-04-73	586.03	0.016	1.752	2.585	99.142	4.720	6.866
DEC-04-74	585.84	0.035	0.449	2.693	231.521	8.084	5.523
DEC-04-137	569.20	0.035	9.606	3.050	219.663	8.260	16.989
DEC-04-138	568.90	0.018	0.718	3.302	126.926	4.306	1.373

Sample I.D.	Age	P_{Tot}	P_{Fe}	P_{auth}	P_{det}	P_{mag}	P_{org}
	Ma	wt%	ppm	ppm	ppm	ppm	ppm
DEC-04-147	566.50	0.042	0.441	1.357	359.935	9.553	5.419
DEC-04-148	566.25	0.030	0.492	23.624	284.069	6.383	2.968
DEC-04-149	566.00	0.064	0.611	5.157	566.306	11.752	1.391
DEC-04-150	565.75	0.034	0.667	41.844	290.965	6.577	2.583
DEC-04-151	565.50	0.020	0.221	3.459	134.656	2.849	2.420
DEC-04-152	565.25	0.034	0.191	1.673	235.644	4.809	51.665
DEC-04-161	563.13	0.038	25.777	1.876	270.917	6.360	8.806
DEC-04-162	562.78	0.048	12.460	39.989	370.398	10.864	4.857
DEC-04-163	562.44	0.038	0.241	26.642	330.856	8.317	4.220

Table D.9 Narana Formation iron speciation and TOC results determined by Rachel Beaumont at University of Leeds. Al results measured in this research

Sample	Depth	Fe_T	Fe_{CARB}	Fe_{OX}	Fe_{MAG}	Fe_{PY}	Fe_{AVS}	Fe_{HR}/Fe_T	Fe_{PY}/Fe_{HR}	TOC	Al
	m	wt%	wt%	wt%	wt%	wt%	wt%			wt%	wt%
1108840	905.4	1.61	0.42	0.06	0.05	0.25	0	0.48	0.32	0.21	2.41
1108841	910	1.21	0.37	0.07	0.03	0.22	0	0.57	0.31	0.30	1.72
1108842	916.4	1.75	0.45	0.08	0.05	0.34	0.0015	0.53	0.36	0.25	2.79
1108843	921	1.10	0.34	0.05	0.02	0.14	0.0044	0.51	0.25	0.20	1.47
1108844	930.6	1.49	0.41	0.07	0.04	0.22	0	0.50	0.29	0.18	2.43
1108845	937.2	1.56	0.39	0.06	0.05	0.19	0	0.44	0.27	0.16	2.40
1108846	949.3	1.68	0.32	0.08	0.06	0.22	0	0.40	0.33	0.46	2.81
1108847	953.2	2.35	0.41	0.10	0.08	0.33	0	0.40	0.36	0.55	3.64
1108848	959	2.36	0.39	0.08	0.08	0.31	0.0074	0.36	0.35	0.29	3.60
1108849	964.7	3.55	0.26	0.17	0.13	0.46	0	0.29	0.45	0.21	5.29
1108850	972.4	2.01	0.71	0.10	0.07	0.26	0	0.56	0.23	0.27	2.91
1108851	976.4	3.08	0.62	0.12	0.11	0.37	0	0.40	0.30	0.37	4.88

Sample	Depth	Fe_T	Fe_{CARB}	Fe_{OX}	Fe_{MAG}	Fe_{PY}	Fe_{AVS}	Fe_{HR}/Fe_T	Fe_{PY}/Fe_{HR}	TOC	Al
	m	wt%	wt%	wt%	wt%	wt%	wt%			wt%	wt%
1108852	987.7	2.40	0.41	0.11	0.11	0.21	0	0.35	0.25	0.33	3.79
1108853	998.4	3.61	0.14	0.11	0.22	0.09	0	0.15	0.16	0.15	5.84
1108854	1002.3	2.86	0.16	0.10	0.17	0.02	0	0.15	0.04	0.13	5.05
1108855	1010	3.15	0.14	0.20	0.15	0.07	0.0030	0.18	0.11	0.23	5.39
1108856	1022.6	3.22	0.25	0.10	0.15	0.19	0	0.21	0.28	0.11	4.56
1108857	1025.3	3.40	0.25	0.12	0.20	0.08	0	0.19	0.12	0.11	4.86
1108858	1029.2	3.16	0.21	0.10	0.16		0	0.15		0.26	4.58
1108859	1039	3.07	0.19	0.11	0.19	0.07	0	0.18	0.13	0.13	4.70
1108860	1047.1	2.95	0.20	0.12	0.17	0.05	0	0.18	0.10	0.14	5.08
1108861	1049.8	2.95	0.24	0.12	0.18	0.09	0	0.21	0.15	0.10	4.62
1108862	1057.3	2.78	0.33	0.10	0.18	0.03	0	0.23	0.05	0.11	4.62
1108863	1066.2	3.48	0.22	0.09	0.20	0.18	0	0.20	0.26	0.16	4.95
1108864	1067.5	3.45	0.21	0.31	0.21	0.05	0	0.23	0.06	0.11	5.12
1108865	1074	3.96	0.16	0.15	0.29	0.01	0	0.15	0.02	0.17	5.90

Sample	Depth	Fe_T	Fe_{CARB}	Fe_{OX}	Fe_{MAG}	Fe_{PY}	Fe_{AVS}	Fe_{HR}/Fe_T	Fe_{PY}/Fe_{HR}	TOC	Al
	m	wt%	wt%	wt%	wt%	wt%	wt%			wt%	wt%
1108866	1078.1	2.96	0.18	0.11	0.22	0.01	0	0.18	0.02	0.12	5.13
1108867	1087.2	3.57	0.27	0.10	0.22	0.04	0	0.18	0.06	0.28	4.62
1108868	1092.7	3.90	0.18	0.10	0.27	0.01	0	0.15	0.02	0.17	5.25
1108869	1097.7	4.01	0.21	0.24	0.24	0.59	0.0059	0.32	0.46	0.22	5.73
1108870	1097.8	3.86	0.30	0.24	0.23	0.56	0.0180	0.35	0.41	0.24	5.63
1108871	1103.6	3.80	0.00	0.12	0.31	0.04	0	0.12	0.08	0.26	5.14
1108872	1108.7	3.17	0.25	0.11	0.18	0.33	0.0030	0.27	0.38	0.17	4.89
1108873	1119	4.03	0.27	0.16	0.36	0.02	0	0.20	0.02	0.17	5.33
1108874	1123.3	3.30	0.22	0.09	0.19	0.13	0	0.19	0.20	0.17	5.08
1108875	1134.85	2.93	0.15	0.11	0.17	0.10	0	0.18	0.19	0.19	4.93
1108876	1143.4	2.29	0.24	0.12	0.13	0.41	0	0.39	0.46	0.18	3.75
1108877	1150	2.71	0.16	0.09	0.10	0.19	0	0.20	0.36	0.14	4.56
1108878	1156.3	1.19	0.18	0.04	0.03	0.37	0	0.51	0.60	0.10	1.80
1108879	1155.3	0.78	0.10	0.04	0.01	0.23	0	0.49	0.61	0.07	1.26

Sample	Depth	Fe_T	Fe_{CARB}	Fe_{OX}	Fe_{MAG}	Fe_{PY}	Fe_{AVS}	Fe_{HR}/Fe_T	Fe_{PY}/Fe_{HR}	TOC	Al
	m	wt%	wt%	wt%	wt%	wt%	wt%			wt%	wt%
1108880	1157.3	0.91	0.12	0.03	0.02	0.36	0	0.58	0.69	0.10	1.60
1108881	1157.8	1.06	0.14	0.08	0.03	0.33	0	0.55	0.56	0.11	1.80
1108882	1158.2	1.21	0.12	0.10	0.04	0.13	0	0.32	0.33	0.10	2.29
1108883	1158.9	2.84	0.08	0.83	0.20	0.00	0	0.39	0.00	0.09	3.43
1108884	1161.2	2.02	0.02	0.72	0.08	0.00	0	0.41	0.00	0.12	2.53
1108885	1163.3	1.39	0.00	0.64	0.03	0.00	0	0.48	0.00	0.08	1.97
1108886	1165.8	0.98	0.01	0.42	0.03	0.00	0	0.46	0.00	0.16	1.45
1108887	1166	0.86	0.01	0.40	0.02	0.00	0	0.51	0.00	0.06	1.42
1108888	1166.8	1.32	0.01	0.24	0.04	0.00	0	0.22	0.00	0.11	1.90

Table D.10 Phosphorus speciation results for the Narana Formation, Upper Ungoolya Group, Officer Basin

Sample	Depth	P_{Tot}	P_{Fe}	P_{auth}	P_{det}	P_{mag}	P_{org}
	m	wt%	ppm	ppm	ppm	ppm	ppm
1108840	905.4	0.039	0.260	75.250	290.948	8.294	4.520
1108841	910	0.034	0.750	75.711	245.522	0.600	3.168
1108842	916.4	0.046	0.473	86.916	319.166	8.724	3.740
1108843	921	0.028	0.327	81.440	188.822	4.630	2.156
1108844	930.6	0.039	0.163	80.651	276.921	7.871	3.451
1108845	937.2	0.038	0.220	92.014	263.311	7.723	3.917
1108846	949.3	0.046	0.618	187.348	271.789	8.541	4.075
1108847	953.2	0.052	0.526	183.433	347.341	11.139	5.414
1108848	959	0.050	0.404	97.373	259.740	11.402	0.000
1108849	964.7	0.043	0.560	98.449	244.790	11.553	0.701
1108850	972.4	0.047	0.778	96.744	267.793	7.964	0.000
1108851	976.4	0.068	0.577	102.466	481.556	17.566	0.000
1108852	987.7	0.069	0.612	173.215	415.170	14.345	3.513

Sample	Depth	P_{Tot}	P_{Fe}	P_{auth}	P_{det}	P_{mag}	P_{org}
	m	wt%	ppm	ppm	ppm	ppm	ppm
1108853	998.4	0.051	0.114	50.103	379.283	15.948	0.000
1108854	1002.3	0.062	0.239	68.676	489.817	17.277	11.693
1108855	1010	0.054	0.659	46.658	434.980	15.846	1.261
1108856	1022.6	0.054	0.143	9.036	430.542	13.789	1.191
1108857	1025.3	0.057	0.159	6.416	454.150	15.691	1.215
1108858	1029.2	0.053	0.280	4.852	402.933	13.590	1.362
1108859	1039	0.055	0.265	10.809	448.879	15.931	1.656
1108860	1047.1	0.056	0.279	19.026	424.020	15.498	1.514
1108861	1049.8	0.054	0.194	13.010	447.654	16.421	1.825
1108862	1057.3	0.054	0.224	14.415	392.695	11.943	1.757
1108863	1066.2	0.052	0.142	15.446	399.075	14.163	0.989
1108864	1067.5	0.053	0.147	3.340	447.265	15.947	1.638
1108865	1074	0.052	0.057	57.875	379.027	16.871	2.022
1108866	1078.1	0.052	0.296	18.723	386.463	14.046	2.225

Sample	Depth	P_{Tot}	P_{Fe}	P_{auth}	P_{det}	P_{mag}	P_{org}
	m	wt%	ppm	ppm	ppm	ppm	ppm
1108867	1087.2	0.057	0.213	7.056	500.978	18.491	0.889
1108868	1092.7	0.052	0.157	12.177	415.679	16.195	1.528
1108869	1097.7	0.048	0.376	35.530	370.957	15.749	1.794
1108870	1097.8	0.064	0.282	79.709	482.813	19.855	1.768
1108871	1103.6	0.050	0.242	5.066	382.396	14.380	1.386
1108872	1108.7	0.053	0.248	15.380	438.572	14.477	2.383
1108873	1119	0.053	0.584	14.901	426.585	16.858	3.874
1108874	1123.3	0.050	0.104	9.113	405.796	17.698	1.949
1108875	1134.85	0.058	0.258	44.867	470.407	16.198	2.583
1108876	1143.4	0.068	0.482	13.406	556.302	15.432	1.341
1108877	1150	0.058	0.094	7.447	484.303	17.784	1.866
1108878	1156.3	0.044	0.193	100.803	258.691	5.696	0.202
1108879	1155.3	0.040	5.362	136.235	175.586	0.094	0.098
1108880	1157.3	0.062	5.114	88.988	449.164	8.141	0.098

Sample	Depth	P_{Tot}	P_{Fe}	P_{auth}	P_{det}	P_{mag}	P_{org}
	m	wt%	ppm	ppm	ppm	ppm	ppm
1108881	1157.8	0.067	0.112	170.060	417.908	9.007	0.233
1108882	1158.2	0.076	0.092	128.472	509.771	13.248	0.384
1108883	1158.9	0.107	5.375	129.850	802.393	26.259	0.942
1108884	1161.2	0.062	6.376	134.614	422.581	10.384	0.235
1108885	1163.3	0.067	0.110	302.446	268.401	8.511	0.804
1108886	1165.8	0.044	0.048	199.596	151.093	0.145	0.402
1108887	1166	0.044	0.340	153.778	184.611	0.170	0.354
1108888	1166.8	0.052	0.094	140.442	271.471	8.084	1.966